

INTERACTIONS OF DARK AND BARYONIC MATTER IN DWARF GALAXIES

David R. Cole

Submitted in fulfillment of the requirements for the degree of
Doctor of Philosophy

Theoretical Astrophysics Group, Department of Physics & Astronomy, University of
Leicester, Leicester, LE1 7RH

March 2012

Theoretical Astrophysics Group
Department of Physics and Astronomy
University of Leicester

Interactions of Dark and Baryonic Matter in Dwarf Galaxies

by

David R. Cole

The Λ CDM model for structure formation in the universe has been successful on large scales, however there are outstanding problems on the scale of galaxies. In this thesis we study a number of processes where baryonic and dark matter (DM) interact on the scale of galaxies in order to provide a greater understanding of how such processes can explain observations. One significant issue for Λ CDM is the prediction of cusped density profiles for DM halos. In Chapter 2 we consider the infall of a massive baryonic clump into a dark-matter halo and demonstrate that the baryons need to transfer only a small fraction of their initial energy to the dark matter via dynamical friction to explain the discrepancy between predicted dark-matter density profiles and those inferred from observations. The observational evidence for density cores in local dwarf galaxies is still disputed. In Chapter 3 we consider what the existence of five globular clusters (GCs) tells us about the dynamical history of the Fornax dSph system and the implications for its density profile. We find that if Fornax has an extended dark matter core (as opposed to a density cusp) then its GCs remain close to their currently observed locations for long times. In Chapter 4 we study the effect of a Central Mass Concentration (CMC) on the development of a bar in a galactic disc with differing density profiles for its DM halo. We find the relative density of the DM halo affects the potency of the CMC in suppressing the growth of a bar.

Preface

The work described in this thesis was carried out between October 2008 and February 2012 whilst the author was a research student under the supervision of Prof. Walter Dehnen and Dr. Mark Wilkinson in the Department of Physics and Astronomy at the University of Leicester. Chapter 2 has been published in the form of a paper,

Cole, D. R., Dehnen, W. and Wilkinson, M. I., 2011, MNRAS, 416, 1118

None of this material in this thesis has been submitted previously to a degree of the University of Leicester or at any other University. The work of others has been duly acknowledged.

The copyright of this thesis rests with the author. No quotation from it should be published without his prior written consent and information derived from it should be acknowledged.

Acknowledgements

The time I have spent at Leicester has been a very happy and rewarding one. I have been continually surprised by the warmth and friendliness of the people I have met during my studies. It is very difficult to express my gratitude for all the help and encouragement I have received but I will make my best attempt. I would particularly like to express my thanks to my supervisor, Walter Dehnen, for all his help, insights, guidance and instant tutorials which taught me a great deal. I also want to thank Mark Wilkinson for his calm and optimistic encouragement and good humour. My thanks also to my other collaborators; Justin Read for his enthusiasm and patience (and a great trip to Zurich); to Lia Athanassoula for sharing her deep knowledge and help (and a great trip to Marseilles); to Chris Power for many conversations when my spirits were flagging (but no trip to Perth yet!). I want to give a special thanks to Wyn Evans for his support which has been invaluable. Also I want to express my gratitude to others whom I have worked with and for their friendship; to Alex Hobbs for useful conversations about physics (as well as tips on dancing) and to Jean-Charles Lambert for his help with glnemo (and tips on running). I want to make a special mention of Celine Combet who have provided much support and help as well as tea and sympathy! Also deep thanks to Sarah Bryan for interesting conversations about work and valued friendship. Special thanks too to Albert Bosma and David Maurin.

I want to say a special thank you to Lisa Brant for all her very practical help. Thank you to all the members of staff in the Theoretical Astrophysics group, Andrew King, Sergei Nayakshin, Graham Wynn, Richard Alexander, Andreas Koch and Sung Hoon Cha. Many thanks too to Gary Gilchrist for helping to sort out computer conundrums.

Special thanks to all the other Theoretical Astrophysics PhD students Patrick Deegan, Jalpesh Sachania, Ugur Ural, Peter Cossins, Fergus Wilson, Lee Cullen, Fabrizio Pedes, Chris Nixon, Kastytis Zubovas, Alex Dunhill, Gillian James, Suzan Dogan and to the

PhD students from the wider Physics and Astronomy Department; Amy Scott, Antonia Rowlinson, Pippa Molyneux, Lucy Heil, Nathan Dickinson, Owen Littlejohns, Katherine Lawrie, Victoria Heard, Kate Dutson, Will Alston, Kim Tibbetts-Harlow and Suzy Jones for help support and many relaxing chats at afternoon tea!

Finally and most importantly I want to express my deep gratitude and thanks to my wife Margaret for her forbearance, patience, support, encouragement and love during a difficult period in her own career. Without her I could not have begun or completed this work.

“Mathematics is the language with which God has written the universe.”

Galileo Galilei (1564 - 1642)

“I have no doubt that in reality the future will be vastly more surprising than anything I can imagine. Now my own suspicion is that the Universe is not only queerer than we suppose, but queerer than we can suppose.”

Possible Worlds and Other Papers (1927), p. 286 J. B. S. Haldane (1892 - 1964)

“The secret to creativity is knowing how to hide your sources.”

Albert Einstein (1879 - 1955)

Contents

Abstract	1
1 Introduction	13
1.1 Λ CDM	13
1.2 Evidence for Dark Matter	19
1.2.1 Zwicky and Missing Mass	19
1.2.2 Galactic Rotation Curves	19
1.2.3 Strong Lensing	21
1.3 The Growth of Structure - Simulations	21
1.4 Λ CDM at galactic scales	24
1.5 The missing satellite problem	25
1.6 The core/cusp problem of DM halos	26
1.7 The Dynamics of Discs and Bars	27
2 Weakening dark-matter cusps by baryonic infall	29
2.1 Introduction	29
2.2 Theoretical arguments	33
2.3 Modelling approach	38
2.3.1 The halo model	40
2.3.2 Orbital and other parameters of the infalling clump	41
2.3.3 Technicalities	44

2.4	Orbital decay	46
2.4.1	Initial orbital decay	46
2.4.2	Late orbital decay	48
2.5	Effect on the Halo	49
2.5.1	Halo expansion	50
2.5.2	Halo shape	54
2.6	Effect of halo velocity anisotropy	55
2.6.1	Halo phase-space structure and vulnerability	56
2.6.2	Change in velocity anisotropy	58
2.6.3	Effect on orbital decay and final halo	60
2.7	Cosmologically motivated halo	64
2.7.1	Orbital Decay	65
2.7.2	Effect on halo structure	66
2.7.3	Effect on halo shape	67
2.8	Varying satellite mass and size	67
2.8.1	Varying satellite mass	69
2.8.2	Varying satellite size	71
2.9	The Effect of satellite removal	72
2.10	Summary	75
2.10.1	Orbital evolution	75
2.10.2	Effect on Halo	76
2.11	Discussion	77
2.11.1	Dark-matter contraction vs. expansion	78
2.11.2	Application to dSph and GCs	79
3	The mass distribution of the Fornax dSph	81
3.1	Introduction	81

3.2	Modelling Approach	86
3.2.1	Observations of the Fornax globular clusters	87
3.2.2	Technicalities	89
3.2.3	Theoretical modelling	90
3.2.4	Establishing the globular cluster distribution	92
3.2.5	Numerical convergence	97
3.2.6	N-body simulations	99
3.3	Results	99
3.3.1	Main simulations	99
3.3.2	Mass follows the light model	102
3.3.3	Initial GC position at the tidal radius of Fornax	106
3.3.4	Triaxial mass model	108
3.4	Conclusions	116
4	Can CMCs prevent galactic bars?	121
4.1	Introduction	121
4.2	Modelling approach	124
4.2.1	The galaxy models	124
4.2.2	Technicalities	128
4.3	Results	134
4.3.1	Bar Formation with a CMC present from the start	134
4.3.2	Effect of a CMC grown in a disc with an existing bar	138
4.3.3	Comparison of methods of CMC growth	141
4.3.4	Pattern speed CMC present from the start	142
4.3.5	Pattern speed CMC is grown in a disc with an existing bar	144
4.3.6	Evolution with a CMC vs CMC introduction	146
4.4	Bar Morphology	147

4.4.1	Development of bars with no CMC	147
4.4.2	Development of bars with a CMC	152
4.4.3	Evolution of Bars when a CMC introduced	154
4.5	Evolution of Disc Parameters	156
4.5.1	Disc buckling and velocity dispersion	156
4.5.2	Evolution of angular momentum	163
4.6	Discussion and Conclusions	167
5	Conclusions	170
A	Generating Fornax's Globular Cluster Distribution	176
A.1	Transformation of coordinates	176
A.1.1	Separation of variables	178
A.1.2	Generation of the velocity distribution	180
A.2	Velocity structure	180
	REFERENCES	182

List of Figures

1.1	Image of M101	14
1.2	Image of NGC1300	15
1.3	Image of the Milky Way satellite dwarf spheroidal galaxy Fornax	15
1.4	The history of the universe since the Big Bang	17
1.5	Temperature fluctuations in the CMB	18
1.6	Rotation curve for NGC3198	20
1.7	Image of 1E0657-558, the Bullet Cluster	22
1.8	The “Cosmic Web”	23
2.1	Predictions for the ratio of the maximum excavated mass	35
2.2	Time evolution of the satellite orbits and halo Lagrange radii	45
2.3	Radial profile of clump infall effects	48
2.4	Radial profiles of axis ratios	53
2.5	Differential energy distributions for the four different halo models	57
2.6	Radial profiles of halo velocity anisotropy parameter β	59
2.7	Dependence on initial halo velocity anisotropy	61
2.8	Dependence on initial halo velocity anisotropy for cosmological halos	62
2.9	Final halo radial profiles; initially parabolic orbit	63
2.10	Variation of results with satellite mass	68
2.11	Variation with satellite size	70
2.12	Effect on halo including satellite removal	73

2.13	Secondary orbital decay	74
3.1	The mass structure for each halo used in our simulations	93
3.2	The observed stellar velocity dispersion for Fornax	94
3.3	Results at different resolutions	98
3.4	Results for uniform LOS distribution: 2Gyr	103
3.5	Results for uniform LOS distribution: 10Gyr	104
3.6	Evolution of apocentres	105
3.7	Results for mass follows light distribution: 2Gyr	109
3.8	Results for mass follows light distribution: 10Gyr	110
3.9	Results starting at the tidal radius: 2Gyr	111
3.10	Results starting at the tidal radius: 10Gyr	112
3.11	Results starting at the tidal radius: 10Gyr comparison	113
3.12	Results for triaxial model: 2Gyr	114
3.13	Results for triaxial model: 10Gyr	115
4.1	Rotation curves; Model MD (“maximum disc”)	125
4.2	Rotation curves; Model MH (“maximum halo”)	126
4.3	Surface density contours; CMC grown 1	129
4.4	Surface density contours; CMC grown 2	130
4.5	Surface density contours; CMC present 1	131
4.6	Surface density contours; CMC present 2	132
4.7	Evolution of the $m = 2$ Fourier component; CMC present	135
4.8	Evolution of the $m = 2$ Fourier component; CMC grown	140
4.9	Evolution of pattern speed; CMC present	143
4.10	Evolution of pattern speed; CMC grown	145
4.11	Density maps; MD00i 1	148
4.12	Density maps; MD00i 2	149

4.13	Density maps; MH00i 1	150
4.14	Density maps; MH00i 2	151
4.15	Density maps; MD02i	153
4.16	Density maps; MH02i	155
4.17	Evolution of the vertical buckling amplitude; MD00i	157
4.18	Evolution of the vertical buckling amplitude; MD02i	158
4.19	Evolution of the vertical buckling amplitude; MH00i	160
4.20	Evolution of the vertical buckling amplitude; MH01i	161
4.21	Evolution of the vertical buckling amplitude; MH02i	162
4.22	Evolution of angular momentum; model MD	164
4.23	Evolution of angular momentum; model MH	165
4.24	Final value of the second Fourier component of the surface density	168
A.1	Coordinate axes for our models	177

List of Tables

2.1	Initial conditions and results for bound clumps	42
2.2	Initial conditions and results for zero energy clumps	43
3.1	Data for the Fornax system	87
3.2	Kinematic data for the Fornax dSph	88
3.3	Data for halos used in the simulations	95
4.1	Parameters of the two galaxy models used	133
4.2	Table of simulations with CMC present a start	134
4.3	Simulations with CMC present from the start	138

1

Introduction

1.1 Λ CDM

Few can have looked at some of the many images of galaxies taken by modern telescopes and not wondered how and when these great assemblages of stars, gas, dust and plasma formed and how they have evolved to take their present forms (see Figures 1.1,1.2 and 1.3). It is clear from observations that galaxy formation is a process which continues to the present and that galaxies are continually undergoing dynamic and sometimes violent evolution. A principal objective of any galaxy formation theory must be to understand how the underlying physics gives rise to the varied processes observed in galaxies. In addition modern galaxy formation theory is set within the context of a larger scale cosmological model and the currently favoured theory is called the Λ Cold Dark Matter (Λ CDM) model of the Big Bang theory.



Figure 1.1: M101, a giant spiral disk of stars, dust and gas is 62 kpc across, or nearly twice the diameter of our Milky Way galaxy. M101 is estimated to contain at least one trillion stars.

Credit for Hubble Image: NASA, ESA, K. Kuntz (JHU), F. Bresolin (University of Hawaii), J. Trauger (Jet Propulsion Lab), J. Mould (NOAO), Y.-H. Chu (University of Illinois, Urbana), and STScI

Credit for CFHT Image: Canada-France-Hawaii Telescope/ J.-C. Cuillandre/Coelum

Credit for NOAO Image: G. Jacoby, B. Bohannan, M. Hanna/ NOAO/AURA/NSF



Figure 1.2: NGC 1300 is considered to be prototypical of barred spiral galaxies (see Chapter 4).

Credit: HubbleSite and STScI, Acknowledgment: P. Knezek (WIYN observatory)



Figure 1.3: The Fornax dwarf spheroidal galaxy (see Chapter 3).

Credit: ESO/Digitized Sky Survey 2.

A minimal six parameter Λ CDM model of the Big Bang theory is very successful at explaining the observed state of the universe on cosmological scales (Komatsu et al., 2011). Here Λ is the cosmological term in Einstein's field equations

$$R_{\mu\nu} - \frac{1}{2}g_{\mu\nu}R + \Lambda g_{\mu\nu} = 8\pi G T_{\mu\nu} \quad (1.1)$$

where $R_{\mu\nu}$ is the Ricci tensor, R is the Ricci scalar, $g_{\mu\nu}$ is the metric, G is the gravitational constant and $T_{\mu\nu}$ is the energy momentum tensor. Λ was originally proposed by Einstein to achieve a static universe but he later rejected it when the Hubble redshift was observed and the expansion of the universe was discovered. Λ became necessary again when observations of type Ia supernovae made in the late 1990s (Perlmutter et al., 1999) indicated that the expansion of the universe is accelerating which is consistent with a positive value for Λ .

Big Bang theory predicts that the universe began in a hot dense state approximately 13.8 billion years ago (Komatsu et al., 2011). which then expanded and cooled. Figure 1.4 shows the history of the universe from the Big Bang onwards. Radiation and matter existed as a hot plasma which pervaded the universe until this plasma cooled sufficiently for the matter and radiation to decouple. At this time, after about 350 thousand years, the photons no longer had sufficient energy to ionise the matter in the universe and the universe became transparent. The neutral hydrogen and helium gas was no longer supported by radiation pressure and could collapse due to gravity. Big Bang theory predicts that there were Gaussian perturbations to the primordial matter density field which were imprinted on the CMB at its last scattering surface, that is when the photons and baryons decoupled. Such fluctuations were detected by the COBE satellite in 1992 (Smoot et al., 1992). More recently the the Wilkinson Microwave Anisotropy Probe (WMAP) which launched in June 2001 has provided an even more accurate picture of these fluctuations (see Figure 1.5).

The most recent findings from the Wilkinson Microwave Anisotropy Probe (Komatsu et al.,

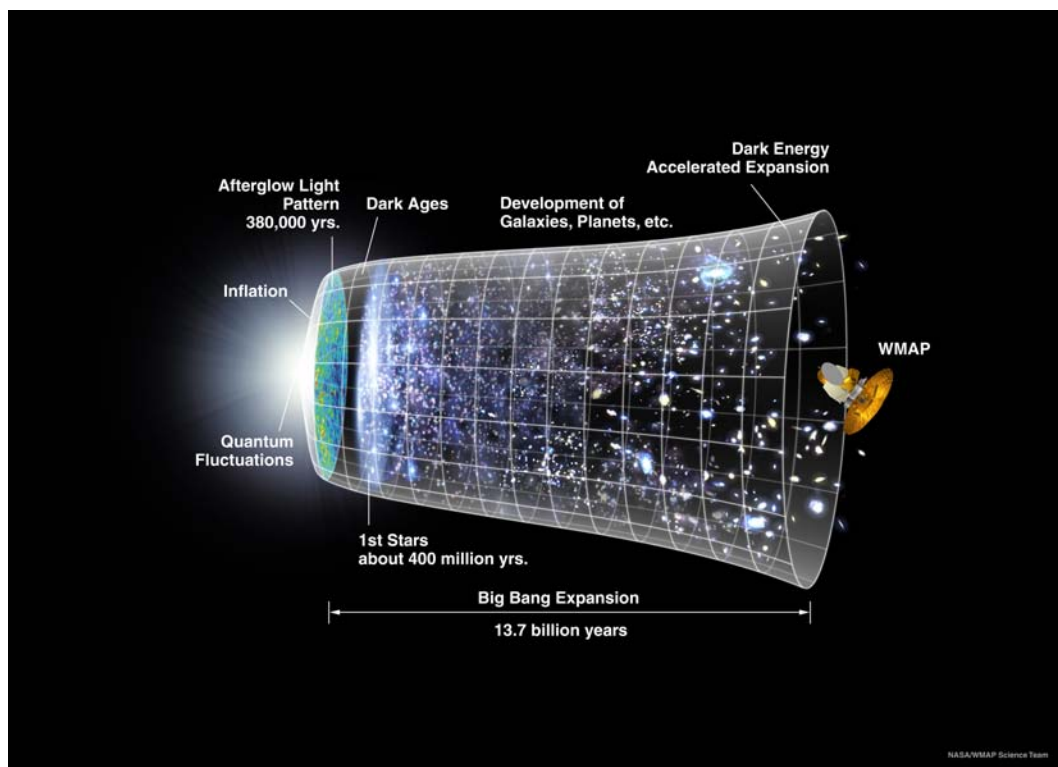


Figure 1.4: A representation of the evolution of the universe over 13.7 billion years. The far left depicts the earliest moment we can now probe, when a period of "inflation" produced a burst of exponential growth in the universe. (Size is depicted by the vertical extent of the grid in this graphic.) For the next several billion years, the expansion of the universe gradually slowed down as the matter in the universe pulled on itself via gravity. More recently, the expansion has begun to speed up again as the repulsive effects of dark energy have come to dominate the expansion of the universe. The afterglow light seen by WMAP was emitted about 380,000 years after inflation and has traversed the universe largely unimpeded since then. The conditions of earlier times are imprinted on this light; it also forms a backlight for later developments of the universe. Credit: NASA / WMAP Science Team.

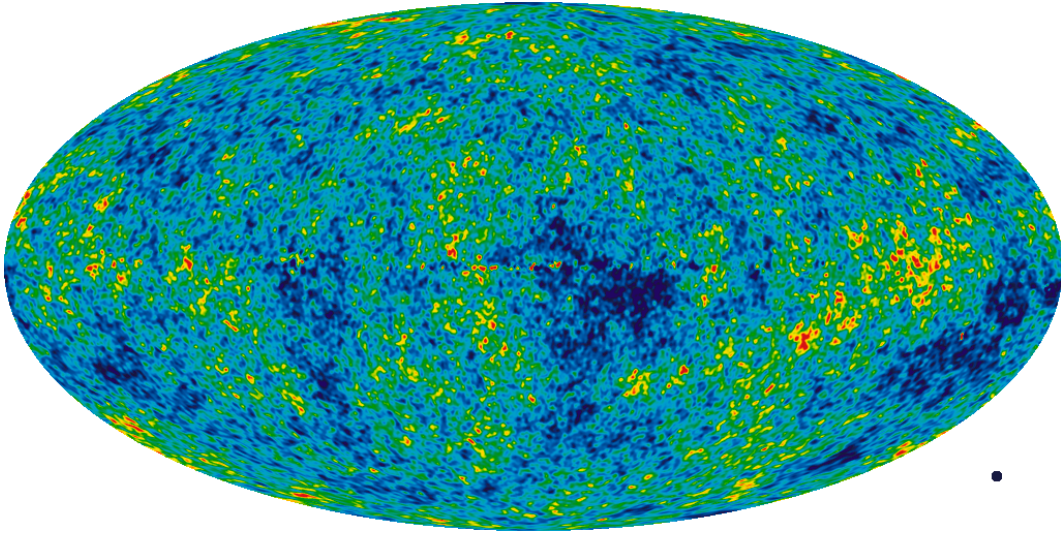


Figure 1.5: The detailed, all-sky picture of the infant universe created from seven years of WMAP data. The image reveals 13.7 billion year old temperature fluctuations (shown as colour differences) that correspond to the seeds that grew to become the galaxies. The signal from our Galaxy was subtracted using the multi-frequency data. This image shows a temperature range of 200 microKelvin.

Credit: NASA / WMAP Science Team.

2011; Bennett et al., 2011) give the following values for the fraction of baryonic matter, dark matter (DM) and Dark Energy in the universe¹:

$$\Omega_{\Lambda} \approx 72.9\%$$

$$\Omega_{\text{darkmatter}} \approx 22.6\%$$

$$\Omega_{\text{baryons}} \approx 4.5\%$$

These density fluctuations formed the basis for the growth of structure in the universe. Structure in the universe grew by gravitational instability based on these density field fluctuations which expanded with the universe before decoupling, gravitationally collapsing and virialising to form DM halos. These original halos then underwent further mergers and accreted baryonic matter. Thus DM dominates the matter content of the universe and so initially structure formation is dominated by DM. Gas then settles in the dense central

¹Note that $\Omega = \Omega_{\Lambda} + \Omega_{\text{darkmatter}} + \Omega_{\text{baryons}} = 1$ implying that the universe has a flat topology.

regions of the DM halos eventually cooling and forming stars. Despite the success of the Λ CDM model it does not provide an explanation of the nature of DM. This remains one of the key questions facing fundamental physics and cosmology today.

1.2 Evidence for Dark Matter

1.2.1 Zwicky and Missing Mass

Observations of the Coma cluster of galaxies by Zwicky (Zwicky, 1933, 1937) in the 1930s implied that there was unseen mass in the cluster needed to account for the velocities of the constituent galaxies. This was the first evidence for DM. Zwicky used the virial theorem to deduce that there is greater mass in the Coma galaxy cluster than in its visible components implying some form of DM.

1.2.2 Galactic Rotation Curves

There is early evidence for mass in excess of the stellar component in galaxies from work carried out on the circular velocities in galaxies by Freeman in the 1970s (Freeman, 1970). This became much more emphatic following the work of Bosma (Bosma and van der Kruit, 1979) and Rubin (Rubin et al., 1980). Figure 1.6 shows a rotation curve taken by van Albada et al. (1985) who looked at the rotation curve of NGC 3198 by looking at the Doppler shift of the HI 21cm hydrogen line. It can be seen that the the velocity is flat with radius. If the matter distribution was spherical then the circular velocity would be given by:

$$v_c = \sqrt{\frac{GM(R)}{R}} \quad (1.2)$$

If v_c is constant then

$$M(R) \propto R \quad (1.3)$$

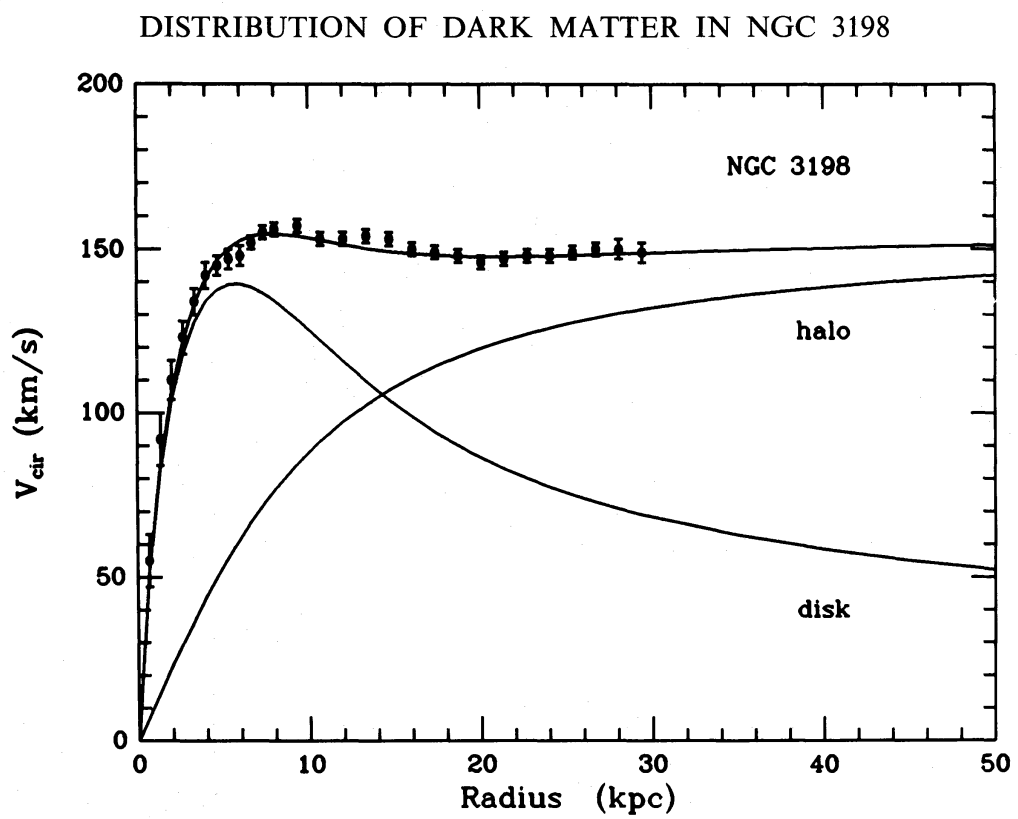


Figure 1.6: Rotation curve for NGC3198 showing the data fit to a model with a significant DM halo (van Albada et al., 1985).

whereas the light falls off exponentially. This was a further clear indication of missing mass.

1.2.3 Strong Lensing

General relativity predicts that massive objects will warp spacetime and deflect the path of light as it passes close to the object. Therefore massive objects such as clusters of galaxies can act as a gravitational lens and warp the images of objects. This can be observed in images of a background object such as a quasar. The geometry of the resulting image can be used to calculate the mass of the lensing object. The first time this effect was used to measure the mass of a galaxy cluster was with the cluster Abell 1689 (Taylor et al., 1998). Masses derived from strong lensing depend on the effects of general relativity and so are not dependant on dynamics for estimating mass.

An excellent example of the use of lensing to demonstrate the presence of DM is the Bullet Cluster (Figure 1.7). This is an interacting cluster 1E0657-558 where a smaller cluster has fallen into the main cluster and passed through to emerge after its first infall (Clowe et al., 2004; Markevitch et al., 2004). The hot intra-cluster gas has been separated from the galaxies by ram-pressure stripping and is observable through its X-ray emissions. The detected mass peaks found by gravitational lensing for the two clusters are in good agreement with the clusters' galaxies and offset from the X-ray emissions. The X-ray gas is the major visible component of the two clusters and its observed offsets from the lensing mass peaks provide direct evidence of the presence of DM in this cluster.

1.3 The Growth of Structure - Simulations

Studies of cosmological simulations such as the Millennium Simulation (Springel et al., 2005, and references therein) (see Figure 1.8) reveal that DM clumps begin to collapse

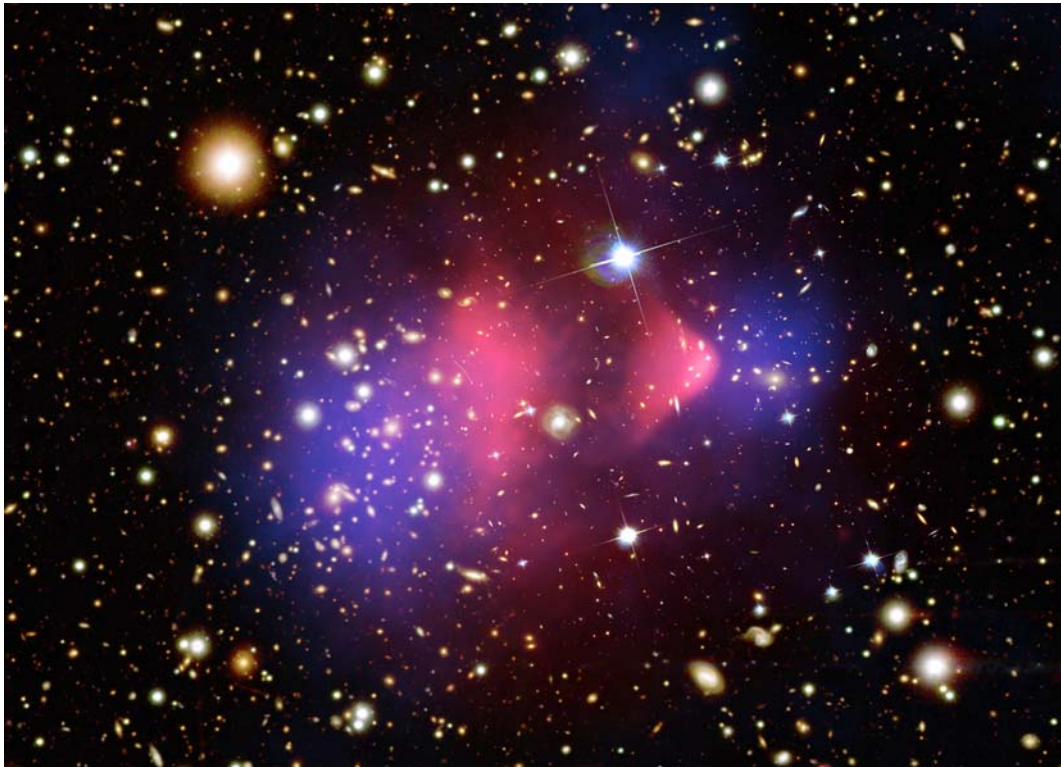


Figure 1.7: Hot gas detected by Chandra in X-rays is seen as two pink clumps in the image and contains most of the baryonic matter in the two clusters. The bullet-shaped clump on the right is the hot gas from one cluster, which passed through the hot gas from the other larger cluster during the collision. An optical image from Magellan and the Hubble Space Telescope shows the galaxies in orange and white. The blue areas in this image depict where lensing detects most of the mass in the clusters.

Credit: X-ray: NASA/CXC/M.Markevitch et al.

Optical: NASA/STScI; Magellan/U.Arizona/D.Clowe et al.

Lensing Map: NASA/STScI; ESO WFI; Magellan/U.Arizona/D.Clowe et al.

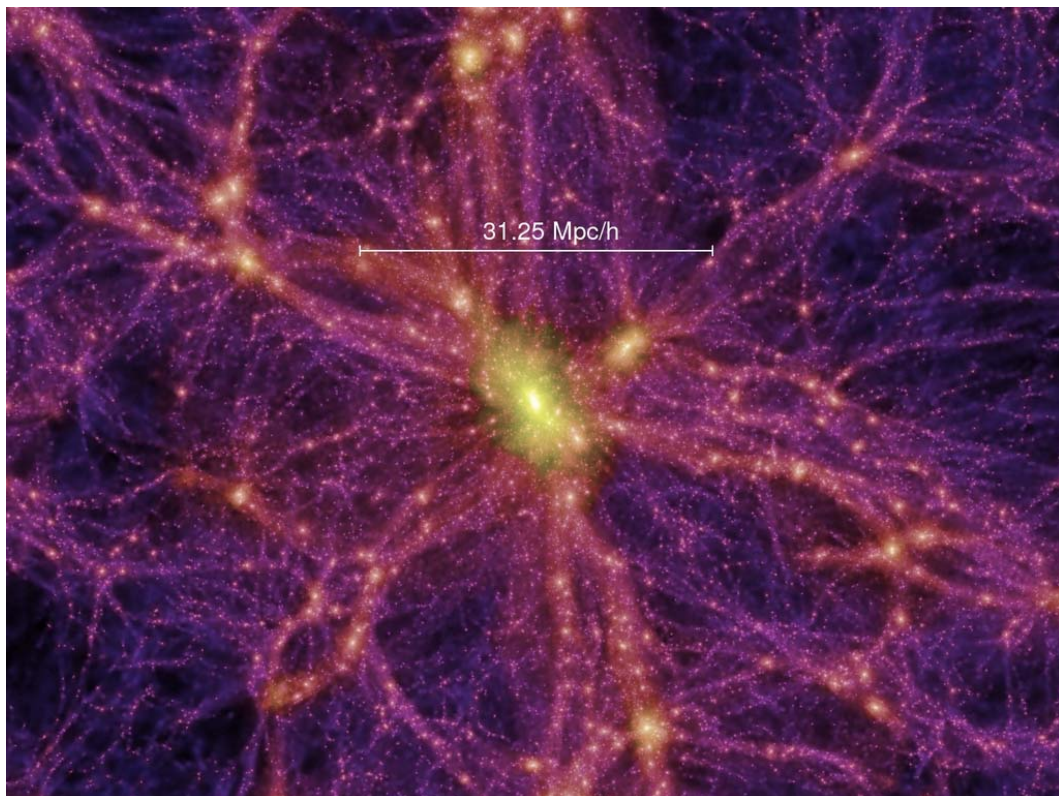


Figure 1.8: The Millennium Run used more than 10 billion particles to trace the evolution of the matter distribution in a cubic region of the Universe over 2 billion light-years on a side. Credit: Springel et al. (2005).

gravitationally to form halos as the primordial density fluctuations grow. These then merge due to gravitational attraction to form larger objects which can in turn go through further mergers in a process known as hierarchical structure formation. These mergers can be mapped using merger trees which provide a pictorial history of a DM halo (Lacey and Cole, 1993). By $z = 0$ a filamentary structure (the cosmic web) has formed made up of DM halos whose spatial distribution is in good agreement with observed large scale structure in the universe. On large scales gravitational attraction is the dominant physical process governing the growth of structure.

The form of the density profiles of DM halos from cosmological simulations has been extensively studied. Navarro et al. (1997, 1996b) showed that halos on a range of mass scales had similar profiles, with the density in the innermost regions exhibiting an $\rho(r) \propto r^{-1}$ cusp independent of mass, initial density fluctuation spectrum and cosmological parameters. More recent work has found that the profile can be better represented by profiles with either slightly shallower inner cusp slopes (Dehnen and McLaughlin, 2005; Navarro et al., 2009) or continuously varying slope, for example the Einasto and Einasto (1972) profile (Navarro et al., 2004).

1.4 Λ CDM at galactic scales

The success of the Λ CDM paradigm of cosmological structure formation in reproducing the observed structure of the universe on scales $\gtrsim 1$ Mpc is now well-established (see e.g. Springel et al., 2006, and references therein). However, on the scale of individual galaxies ($\lesssim 100$ kpc) two potentially significant issues have been raised. One central tenet of Λ CDM cosmology is that the DM is cold which means that the non-baryonic particles were non-relativistic at the time of decoupling. This leads to the following implications:

1. As noted above simulated DM halos are cusped (White and Frenk, 1991) though other theories such as Warm DM predict cusped halos.

2. There is an abundance of low mass halos whose space density increases with decreasing mass.² Cosmological simulations predict increasing substructure down to the mass limit of their resolution (Klypin et al., 1999; Moore et al., 1999; Gao et al., 2004; Diemand et al., 2007). In contrast cosmological simulations where the small scale power spectrum is suppressed (as shown in studies of Warm DM e.g. Knebe et al. (2002)) show reduced substructure although halo density profiles remain cusped.

1.5 The missing satellite problem

The hierarchical structure formation model predicts that small DM halos are accreted and merged with larger ones to form the galactic halos we observe today. This continuing process is not 100% efficient. High resolution cosmological simulations predict that a halo the size of our galaxy should have approximately 50 DM satellites with mass greater than $3 \times 10^8 M_{\odot}$. This is considerably more than has been known though recently fainter dwarf spheroidal galaxies have been discovered providing the possibility that further discoveries may bring observation into line with theory (Klypin et al., 1999; Gilmore et al., 2007). The recent discoveries of previously undetected satellite galaxies in orbit around the Milky Way (Willman et al., 2005; Zucker et al., 2006a,b; Belokurov et al., 2006, 2007; Irwin et al., 2007; Walsh et al., 2007) based on data from the Sloan Digital Sky Survey (York et al., 2000) may significantly reduce the former discrepancy. As Tollerud et al. (2008) have shown, the extension of current results to the whole sky, coupled with the deeper photometry of upcoming surveys, may indeed resolve the so-called “satellite crisis” completely.

Additionally there are a number of reasons why we may observe fewer low mass galaxies than predicted by Λ CDM. Galaxy formation is predicted to be inefficient in the

²Halo space density $\propto M^{-\alpha}$ where $\alpha \approx 2.0$ (Reed et al., 2007; Lukić et al., 2007) and may extend down to masses as small as $\approx 10^{-6} M_{\odot}$ (Green et al., 2004).

shallow potential wells of low mass DM halos (Efstathiou, 1992; Thoul and Weinberg, 1996). Galaxies form when gas contracts onto a DM halo which is massive enough to support efficient cooling. Cooling is inefficient in gas with primordial composition (zero metallicity) in halos with a virial temperature $\lesssim 10^4 K$ which implies that halos with a mass $\lesssim 10^9 M_\odot$ will not have formed galaxies at redshift $z=0$ (Efstathiou, 1992). In addition the universe underwent a period of reionization at $z \gtrsim 6$ during which a high flux of UV and X-ray radiation caused universal reionization which also inhibited galaxy formation. This would have prevented the collapse of gas onto low mass DM halos and in addition radiative cooling and star formation would have been suppressed in galaxies that formed prior to reionization (Benson et al., 2002).

Currently therefore it seems likely that the apparent discrepancy between theory and observations of the number of satellite galaxies may not be a significant issue for the Λ CDM paradigm.

1.6 The core/cusp problem of DM halos

There is mounting observational evidence that real galaxies occupy DM haloes with almost uniform density cores at their centres. Low surface brightness galaxies offer the strongest evidence for cored DM halos (see Oh et al., 2008; de Blok, 2010, for a recent review). Although there have been fewer such studies in high surface brightness spirals, recent work by Spano et al. (2008) has shown that in these galaxies also cored haloes are favoured. Even in low-luminosity, pressure supported systems such as the dwarf spheroidal satellite galaxies surrounding the Milky Way, there is circumstantial evidence that their halo profiles are not cusped (Gilmore et al., 2007).

However, baryons play an important role in the formation and early evolution of galaxies but the predictions of cusped profiles are based on purely DM simulations. The introduction of baryons can have a profound effect on halo structure, but detailed predic-

tions are very difficult because the physics of galaxy formation is still poorly understood. Therefore cosmological simulations are not very useful for developing insight and it is better to use controlled simulations, that allow you to study parts of a problem in detail and to build the physical understanding of how a particular process works.

One idea first proposed by El-Zant et al. (2001) is that clumpy gas inflow could lead to the removal of the DM cusp by transferring of energy to the DM halo through dynamical friction. A second proposal is that heating due to impulsive gas outflows pumps heat into the DM halo thus removing the density cusp (Navarro et al., 1996a; Read and Gilmore, 2005; Pontzen and Governato, 2011). Pontzen and Governato (2011) show that this is most likely what is happening in recent cosmological simulations that (owing to strong simulated stellar feedback) have a very bursty star formation history (Mashchenko et al., 2008; Governato et al., 2010).

In Chapter 2 we investigate in detail the effect of clumps of baryons falling into a initially cusped DM halo and the effects on the halo and in Chapter 3 we investigate what the existence and location of the Fornax dwarf spheroidal galaxy's globular clusters implies about the density profile and evolutionary history of this system.

1.7 The Dynamics of Discs and Bars

The interaction of DM and baryons can have other significant effects on the evolution of galaxies. A significant proportion of disc galaxies have galactic bars. It is clear that dynamical resonances between the baryons in the disc and the DM halo play a significant role in the formation and evolution of a bar (Athanasoula, 1996, 2002, 2003; Holley-Bockelmann et al., 2005; Ceverino and Klypin, 2007). Also disc galaxies often harbour central mass concentrations (CMCs) in form of super-massive black holes, central discs, and dense central star clusters. The effect of a CMC on an *existing* galactic bar has been studied using N -body simulations (Norman et al., 1996; Shen and Sellwood,

2004; Athanassoula et al., 2005) with the result that a CMC affects the structure and appearance of the bar and, if it reaches several percent of the mass of the stellar disc itself, may even effectuate the destruction of the bar. Thus, while it is plausible that a growing CMC affects and weakens an established galactic bar, its destruction via secular growth of a CMC seems rather unlikely, albeit this may be possible when (bar-driven) gas-inflow creates a sufficiently massive CMCs (Berentzen et al., 2007).

In Chapter 4 we investigate the effect of a *pre-existing* CMC has on the *formation* of a bar. This is motivated by the very real possibility that a CMC has been in place well before a stellar disc (and hence any possible bar) is established within a galaxy's inner few kpc.

2

Weakening dark-matter cusps by clumpy baryonic infall

2.1 Introduction

As was stated in our introduction the Λ CDM paradigm of cosmological structure formation is successful in reproducing the observed structure of the universe on large scales. However, on the scale of individual galaxies ($\lesssim 100\text{kpc}$) the density profiles of dark matter haloes pose a potentially significant problem. The form of these profiles in the absence of baryonic physics has been extensively studied by means of numerical simulations. Dubinski and Carlberg (1991) and Navarro et al. (1997) showed that haloes on a range of mass scales have similar profiles, with the density in the innermost regions exhibiting an $\rho \propto r^{-1}$ cusp and more recent work showing that the haloes can be better represented by

profiles with either slightly shallower inner cusp slopes (Dehnen and McLaughlin, 2005; Navarro et al., 2010) or continuously varying slope, for example the Einasto and Einasto (1972) profile (Navarro et al., 2004).

However, as stated in our introduction, there is observational evidence that galaxies occupy dark-matter halos with density cores with the strongest evidence coming from low surface brightness galaxies (de Blok, 2010) with supporting evidence from high surface brightness spirals (Spano et al., 2008) and from the low-luminosity dwarf spheroidal satellite galaxies surrounding the Milky Way (Gilmore et al., 2007).

It is important to remember however, that the ignorance of baryonic physics in the aforementioned simulations constitutes a significant limitation with regard to any discussion of the inner halo profiles. The inclusion of baryon physics is widely recognised as a crucial, albeit extremely technically challenging prerequisite for further progress in understanding galaxy formation.

There are multiple ways in which the baryons can affect the density profile of a dark matter halo. First, a cloud of gas which initially extends throughout a cusped dark matter halo can dissipate energy by radiation and contract to the centre of the halo. As the dark matter responds to the deeper gravitational potential, this in turn leads to a steepening of the dark matter cusp, known as adiabatic contraction (Blumenthal et al., 1986). This is not necessarily the end of the story, however, as baryons also have the ability to generate mass outflows driven by stellar winds and supernovae produced as a result of star formation. Depending on the efficiency of star formation, such processes can expel a significant fraction of the baryonic mass from the central regions of a galaxy, resulting in a large-scale rearrangement of the dark matter. Using semi-analytic arguments, Gnedin and Zhao (2002) found that when stellar mass loss was preceded by adiabatic contraction, the resulting halo distribution was almost unchanged from its original cusped profile. Read and Gilmore (2005), however, subsequently showed that repeated episodes

of adiabatic contraction followed by rapid mass expulsion could give rise to a reduction in the central density and hence produce cored haloes. This occurs because although the initial infall/outflow produces the same mass density profile, the velocity structure of the dark matter halo after the outflow is biased towards radial orbits. As a result, subsequent events are able to lower the inner density more easily.

Another way in which the baryonic component of a galaxy can transfer energy to the dark matter halo is by means of a stellar bar. Weinberg and Katz (2002) proposed that the rotation of bars is decelerated by the exchange of energy and angular momentum with dark-matter particles on orbits in resonance with the bar's rotation. While further work by Athanassoula (2002, 2003) confirmed this conclusion, the size required for a stellar bar to significantly change the mass distribution in the inner regions of a dark-matter halo was found to be much larger than those observed in barred galaxies. Hence, this mechanism is thought to be of limited importance for the majority of dark-matter haloes, though the deceleration process is certainly affecting the evolution of galactic bars.

However, galaxy formation also involves violent processes, where baryonic inflow is neither smooth nor adiabatic. Gas accretion is likely to occur during galaxy mergers, when it takes the form of clumpy infall rather than the slow contraction of a smooth cloud. Although a baryonic clump falling into the centre of a dark halo will add to the gravitational potential there (and thus increase the binding energy of the dark halo), it can, during this process, lose its orbital energy via dynamical friction. El-Zant et al. (2001) showed that the energy thus gained (i.e. binding energy lost) by the dark matter can produce an observable impact on the dark matter density profile. El-Zant et al. (2004) and Nipoti et al. (2004) extended this work by performing N -body simulations of galaxy clusters, where the infalling galaxies play the role of clumps. They found that the initial dark-matter cusp can be softened through the transfer of energy from the baryonic clumps to the dark-matter though the overall density profile, including the baryonic component, remained

cusped.

Attempts have also been made to add full baryonic physics to the studies of sinking clumps mainly based on the results of cosmological simulations, which try to model the effect of cooling, metal enrichment and supernova feedback (e.g. Gnedin et al. 2004; Romano-Diaz et al. 2008; Pedrosa et al. 2009; Johansson et al. 2009). These simulations confirmed the transfer of energy and angular momentum from baryons to the dark-matter, while the results on the dark-matter density reduction were conflicting. This is presumably because of varying amounts, depending on the details of the respective model, of contraction owed to the additional gravitational pull from the accreted baryons.

Despite these promising attempts, a truly realistic modelling of baryonic physics is still beyond contemporary simulation techniques, not least because important baryonic processes, such as re-ionisation as well as primordial and ordinary star-formation, are themselves not sufficiently understood. Therefore, it is important to understand more quantitatively the purely stellar dynamical aspect of this mechanism, which alone affects the dark-matter distribution. Some progress towards this goal has been made recently by Jardel and Sellwood (2009) and Goerdt et al. (2010). However, a complete understanding of the pure stellar dynamical problem is still missing, but seems essential before attempting to interpret the results of simulations which include baryons. In the present chapter, we build on this previous work to explore the impact of clumpy baryonic infall more broadly. We consider more realistic initial conditions. In particular, we focus on clumps initially on parabolic orbits, which may become bound to a halo during a merger event, and haloes with anisotropic velocity distributions, the expected situation to obtain within the hierarchical structure formation scenario of CDM.

The outline of the chapter is as follows. In Section 2.2 we consider analytical estimates for the damage done to the halo by the energy transfer from the satellite orbit. Section 4.2 gives our modelling approach for the N -body simulations, while Sections 2.4 and 2.5

describe the resulting orbital decay and typical changes induced in the simulated haloes. Sections 2.6 and 2.7 discuss the effect of halo velocity anisotropy on both orbital decay and damage to the halo, while Section 2.8 considers the effect of satellite mass and size. In Section 2.9 we demonstrate the effect of removing the accreted clump, corresponding to a galactic wind subsequent. Finally, Sections 2.10 and 2.11 summarise and discuss our findings, respectively.

2.2 Theoretical arguments

Chandrasekhar's (1943) dynamical friction formula for systems with a Maxwellian velocity distribution of dispersion σ (eq. 8.7 of Binney and Tremaine, 2008)

$$\frac{d\mathbf{v}_s}{dt} \simeq -\hat{\mathbf{v}}_s \frac{4\pi G^2 m_s \rho \ln \Lambda}{v_s^2} \left[\operatorname{erf}(x) - \frac{2x}{\sqrt{\pi}} e^{-x^2} \right]_{x=v_s/\sqrt{2}\sigma} \quad (2.1)$$

($\ln \Lambda$ is the Coulomb logarithm, m_s and \mathbf{v}_s are the mass and velocity of the clump or satellite, and ρ is the mass density of dark-matter particles) shows that the deceleration is proportional to m_s , such that the time for the orbit to decay $t_{\text{infall}} \propto m_s^{-1}$. In particular, for this orbital decay to occur within (less than) a Hubble time, a mass of $m_s \sim 10^{6-8} M_\odot$, depending on the size of the dark-matter halo, is required. Chandrasekhar's formula also suggests that the drag force is strongest for small v_s (because this increases the interaction time between perturber and dark-matter particles) and/or for large ρ .

However, the formula cannot be used to assess the effect the infalling clump has on the dark matter. A simple estimate for the mass removed from the inner parts of the dark-matter halo can be obtained from the following argument originally due to (Goerdet et al., 2010, preprint version). Assuming a circular orbit for the perturber, the specific energy lost when sinking from radius $r + \delta r$ to r is

$$\delta \varepsilon_s = \frac{d}{dr} \left[\frac{GM(r)}{2r} + \Phi(r) \right] \delta r = 2\pi G r \left(\frac{\bar{\rho}}{3} + \rho \right) \delta r \quad (2.2)$$

with $\bar{\rho}(r)$ the mean density interior to radius r . Assuming this energy is injected into the spherical shell at radius r , each dark-matter particle at that radius gains specific energy $(\delta\varepsilon_s/\delta r)(m_s/4\pi\rho r^2)$. A density core forms and the sinking of the clump stalls (Read et al., 2006a) as soon as this energy equals the specific kinetic energy of each particle, which may be estimated as $v_{\text{circ}}^2/2 = GM(r)/2r$. With (2.2), this yields (with $\gamma = -d \ln \rho / d \ln r$)

$$M(r) \sim \left[1 + \frac{\bar{\rho}(r)}{3\rho(r)} \right] m_s \simeq \frac{4-\gamma}{3-\gamma} m_s. \quad (2.3)$$

This argument suggests (i) that the mass ejected by the perturber is comparable to its own mass, and (ii) that the density core which forms in response to the heating induced by the sinking baryonic clump has radius comparable to that at which the originally enclosed mass equals m_s .

Strictly speaking, this argument only applies to circular orbits, which are not very realistic, and the assessment of the heating required to turn a cusp into a core is rather crude. We now present a more quantitative estimate based on the exact energy difference between initial and final halo and on the assumption that the orbital energy lost by the clump is absorbed by (the inner parts of) the halo.

Assuming spherical symmetry, let $M_i(r)$ and $M_f(r)$ denote the cumulative mass profiles of the initial and final halo. At large radii the halo is hardly altered, i.e. $M_f(r) \approx M_i(r)$, while at small radii the halo has been heated resulting in an expansion and hence $M_f(r) < M_i(r)$. A quantitative relation between the change in $M(r)$ and the mass m_s of the clump can be obtained by considering the total energy budget. By virtue of the virial theorem, the total energy of the initial equilibrium halo is half its potential energy V_i , to which the kinetic energy of the clump and the interaction energy between clump and halo must be added to obtain the total energy of the initial state (neglecting the clump self-energy)

$$E_i = \frac{m_s}{2} \left(v_i^2 + 2\Phi_i(r_i) \right) + \frac{1}{2} V_i. \quad (2.4)$$

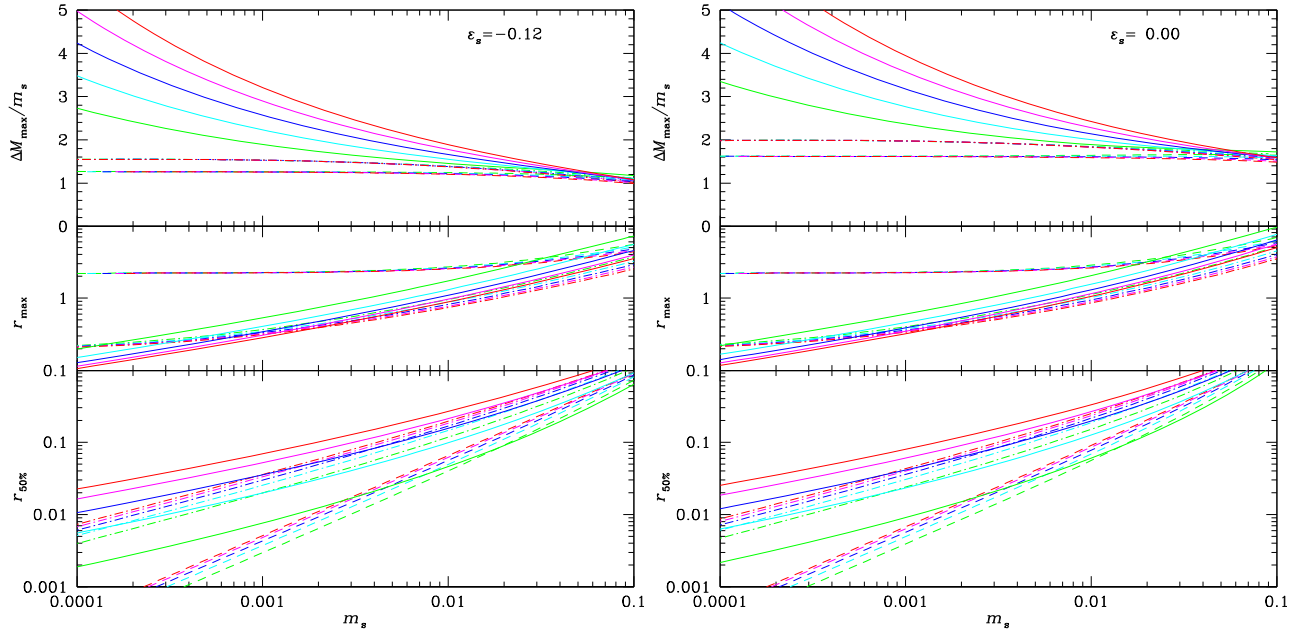


Figure 2.1: Predictions, using equation (2.8), for the ratio of the maximum excavated mass to the mass of the infalling clump (*top*), the radius at which this occurs (*middle*), and the radius inside of which half the mass has been removed (*bottom*; in units of halo scale radius) as function of the mass of the accreted clump. The clump was assumed to be initially either on a bound orbit with energy equal to that of the circular orbit at halo half-mass radius (*left*) or on a parabolic orbit (*right*). The initial halo is modelled to have density distribution (4.2) also used in our simulations, while for the final halo we used the models of equation (2.11) (*solid*) or (2.10) (*dashed*: $\eta = 0.9$ or *dash-dotted*: $\eta = 1.5$). The different lines correspond to inner density slopes for the final halo between $\gamma_0 = 0$ (*red*) and $\gamma_0 = 0.4$ (*green*), while along each line the scale radii r_0 of the final model are varied (and m_s obtained from equation 2.8).

with r_i and v_i the initial radius and speed of the clump and $\Phi_i(r)$ the potential due to the initial halo. Expressing this in terms of the initial specific orbital energy $\varepsilon_s \equiv \frac{1}{2}v_i^2 + \Phi_i(r_i)$ of the clump and the cumulative mass profile gives

$$E_i = m_s \varepsilon_s - \frac{G}{4} \int_0^\infty \frac{M_i^2(r)}{r^2} dr, \quad (2.5)$$

where we have used the relation $V = -\frac{G}{2} \int_0^\infty M^2(r) r^{-2} dr$. For the final state (halo in equilibrium with the clump at rest in the centre) we have

$$E_f = m_s \Phi_f(0) - \frac{G}{4} \int_0^\infty \frac{M_f^2(r)}{r^2} dr \quad (2.6)$$

– this is obtained as $E = V/2$ using $M(r) = m_s + M_f(r)$ (assuming a point-mass clump) and ignoring the clump self-energy. If the clump is extended with cumulative mass profile $m_s(r)$, then $\Phi_f(0)$ in equation (2.6) has to be replaced by

$$\tilde{\Phi}_f(0) = -\frac{G}{m_s} \int_0^\infty \frac{m_s(r)M_f(r)}{r^2} dr. \quad (2.7)$$

Equating $E_i = E_f$ and re-arranging gives

$$m_s (\varepsilon_s - \tilde{\Phi}_f(0)) = \frac{G}{4} \int_0^\infty \frac{M_i^2(r) - M_f^2(r)}{r^2} dr > 0. \quad (2.8)$$

This equation relates the clump mass and its initial conditions with the change in the halo mass profile. Because this latter is a one-dimensional function, while relation (2.8) provides only a single constraint, it can be satisfied by many possible functional forms for the final mass profile $M_f(r)$. However, using some simple yet reasonable models for the final mass profile $M_f(r)$ we can obtain some quantitative estimates for the amount of mass excavated

$$\Delta M(r) \equiv M_i(r) - M_f(r), \quad (2.9)$$

in particular its maximum and the radius at which it occurs, and their dependence on clump mass and initial specific energy ε_s .

In order to compare directly to our simulations, we chose the same initial halo density profile, given in equation (4.2) below, as used in the simulations. For the final halo we assume two different families of models; the first have mass profile

$$M_f(r) = \left(\frac{r}{x}\right)^{\gamma_i - \gamma_0} M_i(r) \quad \text{with } x^\eta = r^\eta + r_0^\eta, \quad (2.10)$$

where γ_i is the central density slope of the initial halo. These models have a $\rho \propto r^{-\gamma_0}$ density cusp at small radii. The second family of models also have the central density slope γ_0 and scale radius r_0 as free parameter and are given by

$$M_f(r) = M_i(r)(1 - \exp(-[r/r_0]^{\gamma_i - \gamma_0})). \quad (2.11)$$

The top panels of Fig. 2.1 show the resulting relations between clump mass m_s , obtained for the above models from equation (2.8), and the ratio of the maximum excavated mass over the clump mass, $\Delta M_{\max}/m_s$ for a clump on an orbit with initial specific energy of $\varepsilon_s = -0.12$ (*left*, corresponding to a circular orbit at the halo half-mass radius), or an initially parabolic orbit ($\varepsilon_s = 0$, *right*) decaying in a halo with initial density (4.2), as used in our N -body simulations below. While these two types of models result in a range of values for the excavated mass, both models suggest that a clump of 1% of the halo mass can excavate about 1.7 times its own mass for $\varepsilon_s = -0.12$ and twice its own mass for $\varepsilon_s = 0$. The models of equation (2.11) also indicate that a less massive clump is relatively more efficient in that it removes a larger multiple of its own mass.

The radius r_{\max} at which $\Delta M(r)$ becomes maximal (and hence $\rho_i = \rho_f$) is shown in the middle panels of Fig. 2.1, again as function of clump mass m_s . For a clump of only 1% of the halo mass, this radius can easily reach the dark-matter scale radius. We also plot in the bottom panels the radius $r_{50\%}$ inside of which half the mass has been removed, i.e. $M_f(r_{50\%}) = \frac{1}{2}M_i(r_{50\%})$, which is readily measured from our N -body simulations below and provides a more direct measure of the size of any possible density core. The rankings between the models of equation (2.11) (*solid* curves in Fig. 2.1) w.r.t. r_{\max} and $r_{50\%}$ are

opposite to each other: the model with the smallest $r_{50\%}$ has the largest r_{\max} and γ_0 and vice versa. While both $r_{50\%}$ and r_{\max} clearly increase with m_s , as one would expect, this dependence is rather weak, approximately $r \propto m_s^{0.6}$ for the models of equation (2.11) near $m_s = 0.01M_{\text{halo}}$.

Note that in obtaining these estimates we have assumed that the final halo is spherical and in perfect equilibrium. In reality, the momentum of the infalling clump is absorbed by the inner halo, which as a consequence moves slightly w.r.t. its outer parts. This motion is only weakly damped and it takes some time before its energy is transformed into internal heat. This implies that the estimates for ΔM_{\max} from equation (2.8) (as used in Fig. 2.1) are possibly somewhat too high, depending on the amount of energy absorbed into such oscillations. The inner asphericity resulting from the absorbed momentum also implies that the simple spherical model over-estimates ΔM_{\max} (because it under-estimates E_f given M_f).

2.3 Modelling approach

The above energy argument is only suggestive and cannot predict the final mass profiles and its dependence on the details of the satellite orbit and the initial halo equilibrium. To this end numerical (N -body) simulations are required. Recently, Jardel and Sellwood (2009) performed such simulations for a satellite starting on a circular orbit at the half-mass radius of a spherical dark-matter halo model with a Navarro et al. (1995) density profile and isotropic velocities. They found that the orbital decay of a satellite with 1% of the halo mass heats the dark matter and results in a density core of radius $\sim 0.2r_2$, where r_2 is the initial scale radius of the halo, the radius at which $\gamma(r) \equiv -d \ln \rho / d \ln r = 2$.

A study by Goerdt et al. (2010) also considered satellites on circular orbits, but for a variety of halo density profiles with different inner density slope γ . These authors were especially interested in the stalling of the orbital decay (Goerdt et al., 2006; Read et al.,

2006a), which depends sensitively on γ .

Assuming a circular orbit for the satellite may simplify some analytical arguments, but is certainly not very realistic. Similarly, the assumption of velocity isotropy for the dark matter is not justified and made only for convenience (so that initial conditions are easily prepared), though simulations by Arena and Bertin (2007) indicate that velocity anisotropy plays no significant role.

The aim of the present study is to extend the aforementioned simulations to more realistic initial conditions. In particular, we are interested in non-circular satellite orbits and cosmologically motivated velocity anisotropy for the dark matter. Our energy-based argument of §2.2 shows that the total amount of heating induced by the decaying satellite orbit only depends on the satellite orbit's energy, but not on its eccentricity. However, where the satellite dumps its energy, and consequently which halo particles gain energy and angular momentum, will depend on eccentricity. In order to differentiate these effects, we will present two sets of N -body simulations with satellite orbits of the same energy. The first set essentially extends the simulations of Jardel and Sellwood by considering satellite orbits of varying eccentricity, but same initial radius and energy as used by those authors. The second set of simulations considers parabolic orbits, whose initial orbital energy just vanishes. If it were not for dynamical friction, these orbits would just pass by the dark-matter halo and never return. However, due to dynamical friction they become bound and decay to the halo centre if initially aimed sufficiently close. We consider isotropic velocities for the dark matter as well as velocity anisotropy of various degree and radial dependence. Furthermore, we investigate the effects from changing the satellite mass and/or its adopted size.

2.3.1 The halo model

For the density profile of the dark-matter halo, we adopt a truncated spherical Dehnen and McLaughlin (2005) model, which gives an excellent fit to simulated CDM halos and has density

$$\rho(r) \propto r^{-7/9} \left(r^{4/9} + s^{4/9} \right)^{-6} \operatorname{sech}(r/r_t). \quad (2.12)$$

For $r_t \rightarrow \infty$, this profile asymptotes to $\rho \propto r^{-7/9}$ and $r^{-31/9}$ at small and large radii, respectively, with a very smooth transition. Here s is a scale factor but we identify the scale radius with the radius at which $\gamma(r) = 2$ (in the limit $r_t \rightarrow \infty$), which for these models is given by $r_2 = (11/13)^{9/4} s \approx 0.687s$ and set the truncation radius to $r_t = 10r_2$, which we identify with the virial radius. We consider various velocity anisotropy profiles; in particular models for which

$$\beta \equiv 1 - \frac{\sigma_\theta^2 + \sigma_\phi^2}{2\sigma_r^2} \quad (2.13)$$

is constant and models for which

$$\beta(r) = \beta_\infty \frac{r^{4/9}}{s^{4/9} + r^{4/9}}. \quad (2.14)$$

These latter models are isotropic in the centre and become increasingly radially anisotropic (for $\beta_\infty > 0$) at large radii, again with a very smooth transition, and are excellent descriptions of N -body CDM haloes (Dehnen and McLaughlin, 2005).

To generate initial N -body conditions for the halo, we sample positions from (2.12) and velocities from self-consistent distribution functions of the form $L^{-2\beta} f(\varepsilon)$ for constant β models with $f(\varepsilon)$ obtained from an Abel inversion (Cuddeford, 1991). For models with $\beta(r)$ as in equation (2.14), we generate initial conditions using the made-to-measure N -body method of Dehnen (2009).

For models with constant β , the resolution in the inner parts is enhanced by increasing the sampling probability by a factor $g(\varepsilon)^{-1}$ which is compensated by setting particle masses μ_i proportional to $g(\varepsilon_i)$. We used

$$g(\varepsilon) \propto \frac{1 + q r_{\text{circ}}^{4/9}(\varepsilon)}{r_{\text{circ}}^{4/9}(\varepsilon) + s^{4/9}} \quad (2.15)$$

with $q = 10$ the ratio between maximum and minimum particle mass and $r_{\text{circ}}(\varepsilon)$ the radius of the circular orbit with specific energy ε . The gravitational forces were computed using a softening kernel with density profile given in equation (3.5) below and r_s replaced by the softening length $\epsilon = 0.005$. Testing this method for our particular purposes we found that it allows a reduction of N to half at the same central resolution without any adverse effects.

We use a unit system where $G = M = r_2 = 1$, which implies a time unit of $15.5 \text{ Myr} (r_2/500\text{pc})^{3/2} (M/10^8 M_\odot)^{-1/2}$.

2.3.2 Orbital and other parameters of the infalling clump

Henceforth, we shall use the term ‘satellite’ for the infalling baryonic clump, which we model as a single massive extended (softened) particle. For the satellite mass m_s we considered 0.3%, 1%, and 3% of the total halo mass (only 77% of which is inside r_t associated with the virial radius), while the satellite size r_s was taken to be 0.01, 0.03, or 0.1 times the halo scale radius. This means that the satellite is effectively modelled to have spherical density profile

$$\rho_s(r) = \frac{15}{8\pi} \frac{r_s^4 m_s}{(r^2 + r_s^2)^{7/2}}. \quad (2.16)$$

We considered a large range of initial satellite orbits, but report here only on two sets of simulations. The simulations of the first set, summarised in table 2.1, all start from $r = 4$, the radius containing 40% of the total or 54% of the mass within r_t , and have specific orbital energy $\varepsilon_s = -0.12$ equal to that of the circular orbit at that radius. The only remaining free parameter of these orbits is the pericentric radius of the initial orbit—owing to dynamical friction, the actual trajectory of the satellite may have a slightly smaller first pericentric radius. These simulations thus extend those reported by Jardel and Sellwood (2009) to non-zero eccentricity and also anisotropic halo velocity distributions. The second set of simulations, summarised in table 2.2, employs parabolic orbits, i.e. with initial

Table 2.1: Initial conditions and results for our simulations. Initial conditions are specified by the satellite size r_s and mass m_s , which default to $r_s = 0.03$ and $m_s = 0.01$, respectively; the peri-centric radius r_{peri} of the initial satellite orbit; and the halo initial velocity anisotropy β_i , which is either constant or $\beta(r)$ given by equation (2.14) with $\beta_\infty = 1$. As results we list the time t_{infall} for the satellite to fall to the centre of the halo (defined in Section 2.4.1); the radius r_{max} of maximum halo-mass reduction ΔM_{max} (compared to the control simulation); the radius $r_{50\%}$ where the cumulative mass is reduced to 50% compared to the control simulation; the radius $r_{M=m_s}$ within which the final halo mass equals m_s ; and the maximum (over all radii) of ρ/σ^3 for the final halo.

simulations started at $r_i = 4$ and run until $t = 1000$								
r_s, m_s	r_{peri}	β_i	t_{infall}	r_{max}	ΔM_{max}	$r_{50\%}$	$r_{M=m_s}$	$\max\left\{\frac{\rho}{\sigma^3}\right\}$
default	0.00	-0.43	44.1	0.704	0.0157	0.330	0.315	1.36
default	1.03	-0.43	111.4	1.351	0.0104	0.119	0.253	4.16
default	2.44	-0.43	169.8	1.864	0.0085	0.100	0.247	4.80
default	4.01	-0.43	198.0	2.052	0.0081	0.109	0.247	4.44
default	0.00	0	43.5	0.646	0.0139	0.324	0.312	1.14
default	1.03	0	99.9	0.778	0.0106	0.165	0.266	2.84
default	2.44	0	163.1	0.783	0.0086	0.100	0.250	3.88
default	4.01	0	193.6	0.779	0.0084	0.097	0.249	3.57
default	0.00	0.3	43.2	0.563	0.0139	0.350	0.325	0.84
default	1.03	0.3	87.1	0.644	0.0104	0.242	0.287	1.42
default	2.44	0.3	145.9	0.641	0.0088	0.127	0.262	2.46
default	4.01	0.3	178.8	0.665	0.0082	0.128	0.257	2.37
$r_s = 0.01$	4.01	0	181.8	0.802	0.0084	0.048	0.247	4.67
$r_s = 0.1$	4.01	0	231.1	0.464	0.0076	0.215	0.272	2.60
$m_s = 0.003$	4.01	0	491.4	1.932	0.0028	0.042	0.116	13.38
$m_s = 0.03$	4.01	0	90.3	1.278	0.0210	0.257	0.541	0.88

orbital energy $\varepsilon_s = 0$, started at $r = r_t$, corresponding to the halo virial radius. Again, the only free orbital parameter is the pericentric radius of the initial orbit.

Within either set of simulations the specific energy of the initial orbit is the same. This choice was motivated by the analytic argument of section 2.2, which suggested that orbital energy is the main parameter affecting the amount of ‘damage’ done to the halo. Thus keeping this energy fixed and varying orbital eccentricity or, equivalently, the pericentric radius, we can study the influence of this secondary orbital parameter.

Table 2.2: Initial conditions and results for our simulations. Initial conditions are specified by the satellite size r_s and mass m_s , which default to $r_s = 0.03$ and $m_s = 0.01$, respectively; the peri-centric radius r_{peri} of the initial satellite orbit; and the halo initial velocity anisotropy β_i , which is either constant or $\beta(r)$ given by equation (2.14) with $\beta_\infty = 1$. As results we list the time t_{infall} for the satellite to fall to the centre of the halo (defined in Section 2.4.1); the radius r_{max} of maximum halo-mass reduction ΔM_{max} (compared to the control simulation); the radius $r_{50\%}$ where the cumulative mass is reduced to 50% compared to the control simulation; the radius $r_{M=m_s}$ within which the final halo mass equals m_s ; and the maximum (over all radii) of ρ/σ^3 for the final halo.

simulations started at $r_i = 10$ and run until $t = 2000$								
r_s, m_s	r_{peri}	β_i	t_{infall}	r_{max}	ΔM_{max}	$r_{50\%}$	$r_{M=m_s}$	$\max\left\{\frac{\rho}{\sigma^3}\right\}$
default	0.0	-0.43	225	0.802	0.0243	0.530	0.384	0.86
default	0.4	-0.43	460	0.891	0.0208	0.393	0.332	1.26
default	0.8	-0.43	835	1.271	0.0180	0.207	0.280	2.96
default	1.3	-0.43	1365	1.922	0.0163	0.094	0.256	4.32
default	0.0	0	215	0.701	0.0229	0.515	0.378	0.69
default	0.4	0	408	0.734	0.0197	0.447	0.352	0.82
default	0.8	0	774	0.906	0.0167	0.331	0.315	1.20
default	1.3	0	1319	1.288	0.0138	0.265	0.294	1.62
default	0.0	0.3	202	0.710	0.0220	0.511	0.380	0.57
default	0.4	0.3	388	0.721	0.0193	0.445	0.355	0.69
default	0.8	0.3	700	0.750	0.0178	0.389	0.339	0.88
default	1.3	0.3	1165	0.853	0.0160	0.358	0.329	0.84
default	0.0	$\beta(r)$	183	0.858	0.0187	0.445	0.372	0.52
default	0.4	$\beta(r)$	320	0.812	0.0182	0.435	0.368	0.53
default	0.8	$\beta(r)$	593	0.807	0.0157	0.379	0.350	0.66
default	1.3	$\beta(r)$	947	0.844	0.0159	0.372	0.348	0.65
$r_s = 0.01$	0.4	$\beta(r)$	249	0.834	0.0174	0.412	0.360	0.58
$r_s = 0.1$	0.4	$\beta(r)$	566	0.822	0.0177	0.415	0.360	0.65
$m_s = 0.003$	0.4	$\beta(r)$	1902	0.406	0.0064	0.207	0.180	2.02
$m_s = 0.03$	0.4	$\beta(r)$	95	1.149	0.0427	0.871	0.762	0.16

2.3.3 Technicalities

The N -body simulations are performed using the public N -body code `gyrfalcON` which uses the $\mathcal{O}(N)$ force solver `falcON` (Dehnen, 2002) with minimum opening parameter $\theta_{\min} = 0.5$ and employs an adaptive time-stepping scheme.

The simulations were run for 1000 or 2000 time units for the first and second set of simulations, respectively. The energy conservation was typically 1 part in 10^4 (more accurate control simulations obtained the same results). Halo models with constant β had 1 Mio particles selected using the resolution-enhancement method of Section 2.3.1, while for halo models with $\beta(r)$ as in equation (2.14) 2 Mio equal-mass particles were used. In order to ensure a careful modelling of the satellite, it was integrated with a shorter time step than most halo particles and the mutual forces with the halo particles were approximated with a much reduced opening angle. One simulation over 1000 time units (16 000 block steps or 256 000 shortest time steps) took about 190 CPU hours (single CPU, $N = 1$ Mio), including some of the analysis.

After each time step the position and velocity of the halo centre was estimated from the position of the most bound particles¹. Snapshots are stored at regular intervals and analysed in terms of their radial profiles using two different approaches. The first employs simple averages over radial shells, assuming the centre to coincide with the one found from the most bound particles. The second estimates for each particle the density as a kernel estimate from its 32 nearest neighbours and then computes the centre, radius, and other properties from density bins. This latter method is more robust in case the configuration is non-spherical, either because of flattening or because of a spatial or velocity offset of the inner w.r.t. outer regions.

For all except one halo model, simulations in isolation maintained the original density

¹Let ϕ denote a halo particle's specific potential energy due to all other halo particles (but not the satellite), then we first find the particle with the smallest (most negative) ϕ and its $K = 256$ spatially nearest neighbours. Then we obtain the centre position and velocity as weighted average from the $K/4$ most bound particles (with largest $|\phi|$) using the weights $|\phi_{K/4} - \phi_i|^3$.

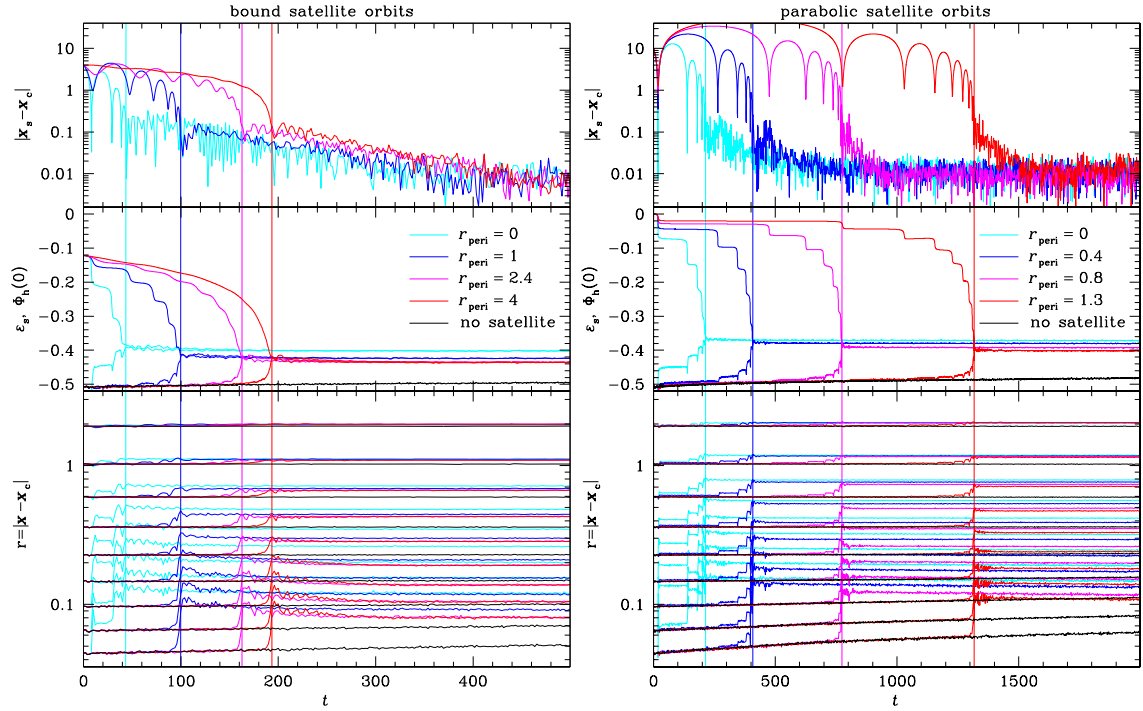


Figure 2.2: Time evolution of the satellite orbits and halo Lagrange radii for four bound (*left*) and four parabolic satellite orbits (*right*) decaying in a halo with isotropic velocity distribution – note the different time scales. The *top* and *middle* panels show the evolution of the satellite distance to the halo centre and the satellite orbital energy ε_s , respectively. Also shown in the middle panel is the halo’s central potential depth $\Phi_h(0)$ (lower curves). The thin vertical lines indicate the time at which the difference $\varepsilon_s - \Phi_h(0)$ is reduced by a factor 50. The *bottom* panel shows the evolution of the halo Lagrange radii (w.r.t. the halo centre) containing 0.08%, 0.16%, etc. up to 20.48% of the halo mass. Within each set of orbits the initial orbital energy is the same, namely $\varepsilon_s = 0$ for the parabolic orbits and $\varepsilon_s = -0.12$ for the bound orbits, equivalent to that of the circular orbit at the halo half-mass radius (which is in fact the *red* orbit in the left panels). The purely radial orbits of both sets are plotted in *cyan*, while the colour sequence to *red* corresponds to ever less eccentric orbits, reaching $e = 0$ (circular) for the family of bound orbits, corresponding to larger pericentric radii as indicated.

profile over 2000 time units, except for the very inner parts, where artificial two-body relaxation and force softening result in a slight expansion. More quantitatively, the Lagrange radii containing $\lesssim 1 \times 10^{-3}$ of the total mass expand noticeably (see bottom panels of Fig. 2.2), which is more pronounced in halo models with radially biased velocity distributions. The exception is the halo model with initial $\beta(r)$ following equation (2.14) with $\beta_\infty = 1$. This model turned out to be unstable to the radial-orbit instability and spontaneously re-arranges into a triaxial configuration within ~ 200 time units. In the course of this process the radial mass distribution is also slightly altered even without infalling satellite. In order to minimize the effects of these problems when interpreting our results, we compare each simulation with infalling satellite to a control simulation without satellite but identical initial halo. Tables 2.1 and 2.2 shows a numerical summary of our results.

2.4 Orbital decay

In Fig. 2.2, we plot the time evolution of the satellite orbital radius and energy (top and middle panels) and the halo Lagrange radii (bottom panels) for both sets of satellite orbits in a dark-matter halo with isotropic velocities. In all these simulations the satellite mass and size are at their default values of $m_s = 0.01$ and $r_s = 0.03$.

2.4.1 Initial orbital decay

We like to start our discussion by comparing the circular orbit starting at $r = 4$ (*red* in the left panels), which is similar to that used by Jardel and Sellwood (2009), and a plunging, almost radial, orbit with vanishing orbital energy (*blue* in the right panels of Fig. 2.2). While both orbits decay to the centre, their evolution is clearly different. The circular orbit decays first slowly then faster, whereby remaining near-circular. The rate of decay,

as indicated by the energy loss, is continuously increasing as the orbit comes closer to the centre. This is qualitatively consistent with Chandrasekhar’s formula (2.1), since the halo density is steeply increasing inwards.

The plunging parabolic orbit (*blue* in the right panels) on the other hand, suffers noticeable energy loss only near peri-centre, undergoing a stepped rather than steady decay of orbital energy. At the first peri-centric passage, the satellite loses enough orbital energy to find itself on a bound but highly eccentric orbit which returns to the inner parts of the halo within about 4 halo half-mass dynamical times. The energy loss at the second peri-centric passage is larger, resulting in a quick orbital decay thereafter. The time scale (note the different the time axes in the left and right panels of Fig. 2.2) for the decay of this orbit is only about twice as long as that of the circular orbit starting much closer (a circular orbit starting at r_t does not decay within 1000 time units). Thus, even though more energy has to be lost for this orbit, the dynamical friction at peri-centre is so strong that the decay is still quite fast, even though the orbit spends about half its time well outside the halo virial radius.

During the first few periods, the peri-centric radius for this plunging orbit is hardly decaying. This is expected if dynamical friction causes a near-instantaneous deceleration at peri-centre, which transfers the satellite to an orbit with the same pericentric radius. The apparent decay of the peri-centric radius after two periods is not because dynamical friction away from pericentre becomes significant, as the closest approach to the origin (as opposed to the halo centre) is in fact increasing, but because the centre of the halo has moved, as a consequence of the satellite interaction.

For all orbits, we identify as the orbital decay or infall time t_{infall} the time at which the difference $\varepsilon_s - \Phi_h(0)$ first obtains 2% of its original value. There is a systematic trend of the infall time to decrease for higher eccentricities (smaller r_{peri} within each set of simulations), which is easily understood by the fact that dynamical friction is stronger for

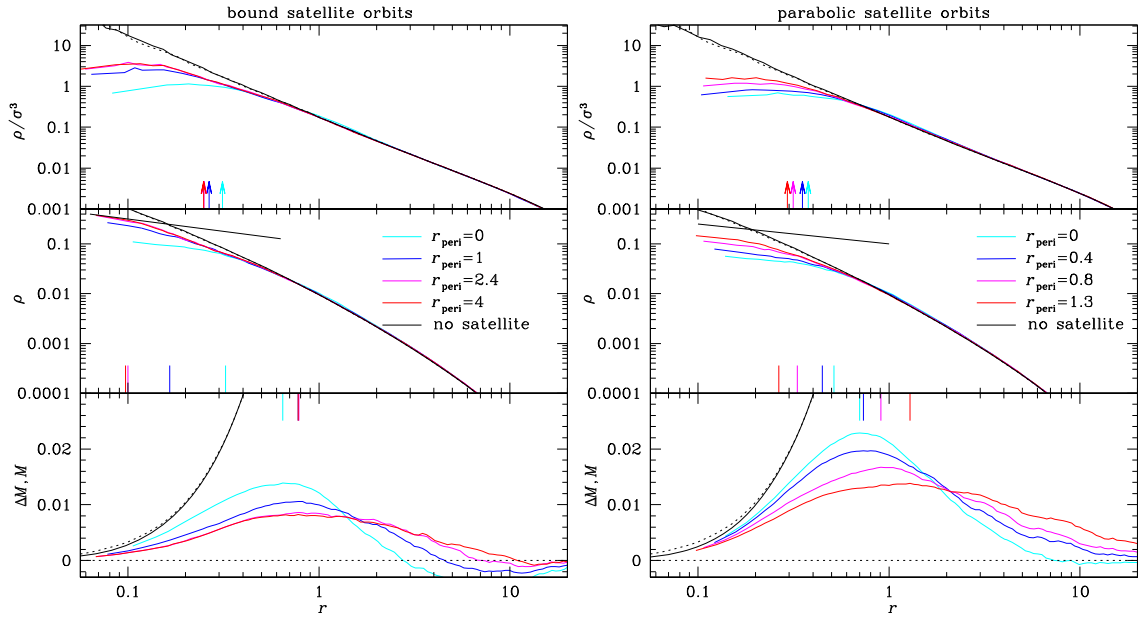


Figure 2.3: Radial profiles of the halo’s pseudo phase-space density ρ/σ^3 (top), density ρ (middle), and the change in cumulative halo mass ΔM (bottom) at $t = 1000$ and 2000 for simulations of the decay of bound (left) and parabolic (right) satellite orbits, respectively. The simulations and colour coding are the same as in Fig. 2.2. For each model, the vertical lines in the middle and bottom panels indicate the locations of $r_{50\%}$ and r_{max} , respectively, while the arrows in the top panels indicate the radius $r_{M=m_s}$ within which the dark mass equals the satellite mass. The dotted curves correspond to the situation before satellite infall ($t = 0$), while the solid black curves represent the control simulation (no satellite). In the bottom panels, the black curves give $M(r)$, not $\Delta M(r)$. The thin black lines in the middle panels are power-laws $r^{-0.5}$ (left) and $r^{-0.4}$ (right).

the higher density at smaller radii.

2.4.2 Late orbital decay

Interestingly, after the initial decay, when the orbital energy has almost reached its final value, the satellite and the halo centre are still orbiting each other at a distance of initially $r \sim 0.1$. In other words, the orbital decay was incomplete and has stalled. Unlike the situation investigated by previous authors, this stalling occurs at a radius which contains much less dark mass than the satellite mass m_s and it seems more apt to say the halo centre orbits the satellite.

This small orbit remains inert only for a short while (when $|\mathbf{x}_s - \mathbf{x}_c|$ remains constant or even increases at ~ 0.1 , see also Fig. 2.13), which is longer for high eccentricities of the initial orbit, while for the initially circular orbit ($r_{\text{peri}} = 4$) there is hardly any such stalling. After this brief pause, the orbit decays very nearly exponentially with radial e-folding time of ~ 90 time units for the bound orbits (*left* panels of Fig. 2.2), which is discernable for over two e-foldings until the orbital radius reaches the noise level. In case of initially parabolic satellite orbits (*right*), the stalled orbits are more eccentric and their decay more erratic (but qualitatively similar) with a longer decay time (e-folding time of ~ 160).

Remarkably, the secondary decay times are very similar between orbits within either set of simulation, but differ between them. This implies that the eccentricity of the initial and also the stalled orbit are not affecting the process responsible for this phenomenon. The differences in secondary decay times may be caused by differences, induced by the orbital decay, in the structure of the central halo, as discussed below.

This secondary decay is not associated with any significant orbital energy loss and has no measurable effect on the final halo density profile (except perhaps for the innermost 0.1% of the halo mass), which is the main interest of our study. However, it is certainly an interesting stellar dynamical phenomenon deserving further investigation.

2.5 Effect on the Halo

We now discuss the changes induced by the satellite's orbital decay in the dark-matter halo, concentrating mostly on the spatial distribution, while the changes to the velocity structure are mostly discussed in the next section.

2.5.1 Halo expansion

The middle panels of Fig. 2.2 also show the evolution of the central halo potential $\Phi_h(0)$ (lower curves; not including the contribution of the satellite), which at late time coincides with the satellite’s orbital energy. In all simulations, the final central potential depth of the halo is considerably shallower than initially, indicating a significant reduction of the central dark-matter concentration. A comparison between the various simulations also shows that this reduction is more pronounced for parabolic than for bound satellite orbits, exactly as our analytic arguments of Section 2.2 predicted, as well as for more eccentric orbits.

In the bottom panels of Fig. 2.2, we plot the time evolution of the halo Lagrange radii, while Fig. 2.3 shows for the same simulations the halo density ρ before and after the satellite infall, as well as the change (2.9) in the cumulative halo mass profile and in the pseudo phase-space density ρ/σ^3 . From the time evolution of the Lagrange radii, we see that the expansion of the inner halo occurs rather suddenly at the time when the satellite settles in the core², in particular for the initially circular orbit (*red* in the left panels of Fig. 2.2). For more eccentric orbits, the early peri-centre passages result in some minor expansion of the halo at radii comparable to the peri-centre radius, but hardly affect the innermost halo.

The mass $\Delta M(r)$ removed from inside radius r (compared to the control simulation³) has different radial profiles for the various simulations. Its amplitude is generally larger after the decay of a parabolic than a bound orbit, which is due to the larger orbital energy of the former leading to stronger heating of the dark-matter particles. In fact, the maximum mass excavated ΔM_{\max} is about twice the satellite mass if the latter is decaying on a plunging parabolic orbit, consistent with our models of Section 2.2, while for a circular

²The initial slow rise of the innermost Lagrange radii is entirely due to artificial two-body relaxation and not present in simulations with ten times the number of halo particles, see also the last paragraph of § 2.3.3.

³For the simulations, $\Delta M(r)$ is always measured this way, rather than against the initial model (as in equation 2.9), in order to account for halo evolution in absence of any satellite.

orbit decaying from $r = 4$, corresponding to the situation studied by Jardel and Sellwood (2009), $\Delta M_{\max} < m_s$. This difference between ΔM_{\max} obtained for orbits with $\varepsilon_s = 0$ (parabolic) $\varepsilon_s = -0.12$ (bound) is even more pronounced than for the analytical models of Fig. 2.1.

Within each set of orbits $\Delta M(r)$ is most peaked for the purely radial orbit, while it widens for lower eccentricities. This is presumably because a satellite on a highly eccentric orbit loses its energy to a narrow range of dark-matter particles close to its peri-centre, while less eccentric orbits lead to a distribution over a wider range.

Central density reduction

The density profiles in the middle panels of Fig. 2.3 confirm earlier results that the infall of a baryonic clump can considerably weaken the central dark-matter cusp. The final halo mass profiles (not shown) are noticeably perturbed interior to the radius r_{\max} (indicated by the vertical lines in the bottom panels of Fig. 2.3), at which by definition the final halo density equals that of the control simulation without satellite. In order to quantify further the properties of the inner halo density profiles, we also calculate the radius $r_{50\%}$ (indicated by the vertical lines in the middle panels of Fig. 2.3) interior to which the dark mass mass is reduced to 50% compared to the control simulation. In general, $r_{50\%}$ is smaller than r_{\max} and marks the radius at which significant changes to the halo density profile are evident.

There is a clear trend for more eccentric orbits to more strongly reduce the central density and hence result in a larger radial range over which the density has been significantly reduced: $r_{50\%}$ is larger for smaller r_{peri} . The opposite is true for the radius r_{\max} . This contrasting behaviour of $r_{50\%}$ and r_{\max} can be understood in terms of the different shapes of the excavated mass distribution $\Delta M(r)$, which becomes broader with increasing r_{peri} , presumably because the energy input is spread over a larger radial range.

Such an anti-correlation between $r_{50\%}$ and r_{\max} for simulations with the same initial satellite orbital energy ε_s was also present in the analytic models in Fig. 2.1. For those analytic models the effect was generated by assuming different central density slopes $\gamma_0 = -d \ln \rho / d \ln r|_{r=0}$. However, the central density slope of the final N -body models (middle panel in Fig. 2.3) are remarkably similar at around $\gamma_0 = 0.4 - 0.5$ at radii $r \lesssim r_{50\%}$. We should stress, however, that the inner regions of these halo models are gravitationally dominated by the sunken satellite, and hence cannot be sensibly compared to the dark-matter haloes of galaxies.

Central phase-space density reduction

We also show in Fig. 2.3 the radii $r_{M=m_s}$ at which the enclosed dark mass equals that of the satellite (arrows in the top panels). Evidently, these radii do not differ much from $r_{50\%}$, implying that the innermost final dark-matter profiles are not self-gravitating: their gravity is dominated by the accreted satellite. Since the satellite size $r_s = 0.03$ is about ten times smaller than the radius inside of which it dominates the dynamics, it is effectively acting like a central point mass. A tracer population orbiting a point mass has a cusp $\rho \propto r^{-3/2}$ if its phase-space density is constant. However, the simulations have much shallower central cusps, suggesting that the actual dark-matter phase-space density has a central depression, decreasing towards the highest binding energies.

This is also borne out by the plots of the pseudo phase-space density ρ/σ^3 in the top panels of Fig. 2.3: while initially and in the control simulations (dotted and solid black curves) these follow a pure power law (this is how these models are actually constructed, see Dehnen and McLaughlin, 2005), the final profiles show a strong central depression, suggesting a considerable reduction of dark-matter phase-space density. The corresponding reduction in spatial density is much weaker, because the available phase space is increased above that from the self-gravitating cusp by the deeper central potential due to

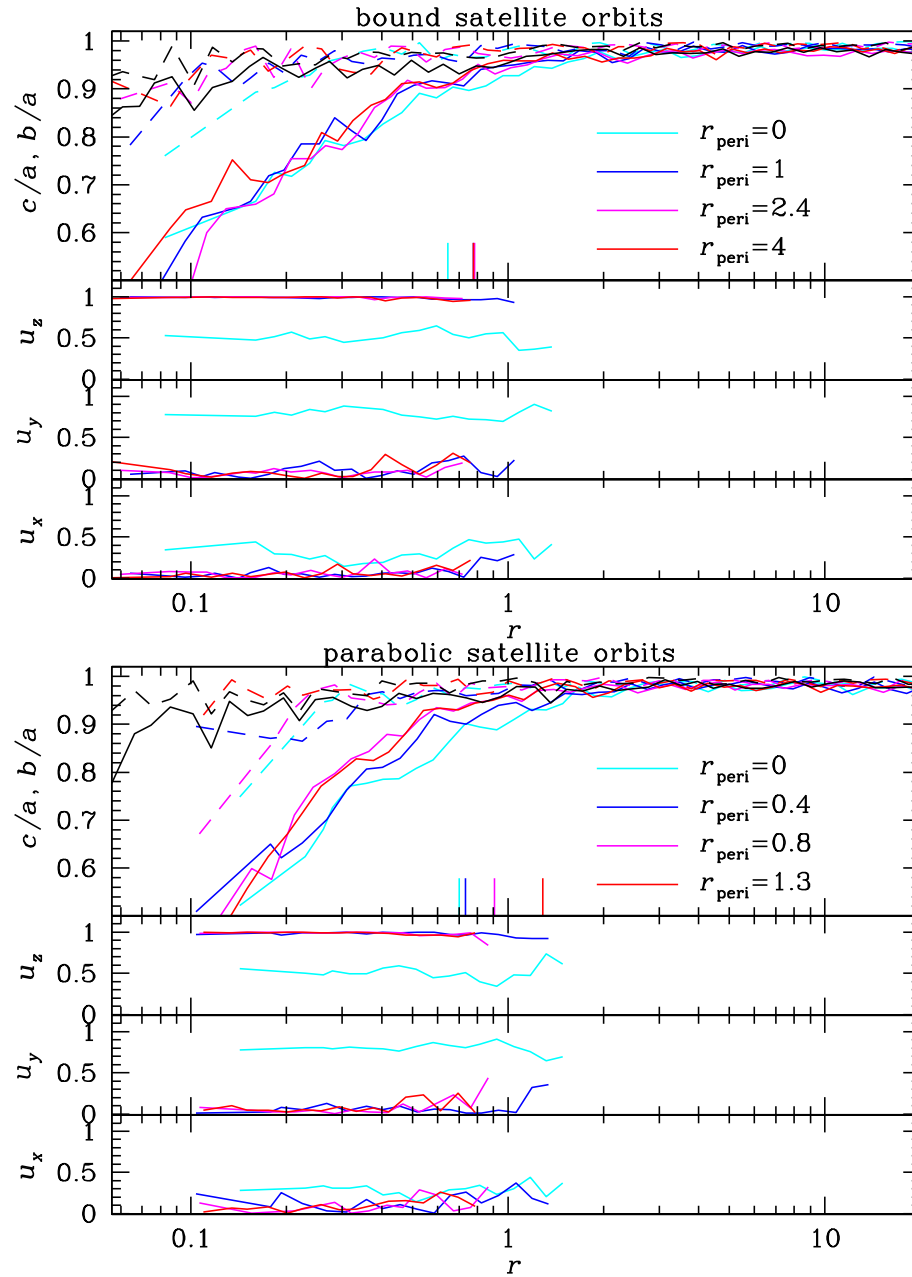


Figure 2.4: Radial profiles of the intermediate-to-major (b/a , *dashed*) and minor-to-major (c/a , *solid*) axis ratios, as well as the direction of the minor axis, provided as the x , y , and z components of the unit vector along the minor axis (plotted where $c/a < 0.95$) for the final halo in the same simulations as in Figs. 2.2 and 2.3. The vertical lines in the top panel indicate for each model the location of r_{\max} .

the accreted satellite.

The central velocity dispersion initially decreases towards $r = 0$ as $\sigma^2 \propto r^{\min(\gamma, 2-\gamma)}$ for a self-gravitating $\rho \propto r^{-\gamma}$ cusp. In all simulations, the final halo has $\sigma(r)$ increasing towards smaller radii (not shown, but evident from the strong central depression in ρ/σ^3 compared to that in ρ), inside the radius $r_{M=m_s}$, as is required for any equilibrium system dominated by a central mass concentration.

2.5.2 Halo shape

In all our simulations, the dark matter halo is initially spherical. The top panels of Fig. 2.4 show the run of the final halo's principal axis ratios for the same simulations as in Figs. 2.2 and 2.3. At $r \lesssim 1.5 > r_{\max}$ the final dark matter distribution is near-oblate in all cases, becoming flatter towards the centre reaching $c/a \sim 0.5$ at the smallest measurable radius. The bottom panels of the same figure show the direction cosines of the minor axis. Note that the satellite initially orbits in the xy plane, starting at $y = 0$ and $x = r_i$. For all but the purely radial orbits the halo minor axis is perpendicular to the initial orbital plane of the satellite. This is easily understood to originate from the transfer of orbital angular momentum from the satellite to inner halo particles during peri-centric passages, which presumably also generates the oblate inner halo shape.

For the purely radial satellite orbits (cyan), which start off with zero orbital angular momentum, the final halo minor axis does not align with the satellite orbit, but appears to point in some random direction (though it is self-aligned). This behaviour is counter-intuitive as the initial models for these simulations are completely symmetric w.r.t. the infall axis. However, such a break of symmetry is the natural behaviour of radial orbits in the gravitational potentials of a density cusp. This is best explained by considering the limit of vanishing peri-centre radius for the change in azimuth $\Delta\phi$ occurring over one radial period from apo-centre to apo-centre. For a harmonic potential, corresponding to

$\gamma = 0$, the radial orbit just passes straight through ($\Delta\phi = \pi$), while in the potential generated by a point mass, corresponding to $\gamma = 3$, the radial orbit is reflected ($\Delta\phi = 2\pi$). For mass distributions with intermediate values of γ , such as dark-matter haloes, $\Delta\phi$ is between these two extremes, and the symmetry of the initial orbit is broken⁴.

This deflection of the satellite orbit is compensated by an equal and opposite momentum to the inner halo, such that the subsequent relative orbit of the two is no longer radial. The further evolution follows the same pattern as for the non-radial orbits: the halo flattens perpendicular to the angular momentum axis of this orbit. Note that for both radial orbit simulations shown in Fig. 2.4 the minor axis is near-perpendicular to the original infall direction (x -axis). This is explained by the fact that $\Delta\phi$ for a shallow cusp is only slightly larger than the value π for the harmonic potential, implying that the orbit is only weakly deflected from its original infall trajectory, which is indeed what we see in our simulations.

There is also some hint of triaxiality at small radii, in particular for the radial bound orbit. This is somewhat surprising as it mostly occurs within the region where the satellite dominates the enclosed mass and hence the potential is near-spherical. We suspect that this very central triaxiality is generated during the secondary orbital decay if the small decaying orbit is eccentric.

2.6 Effect of halo velocity anisotropy

So far, we have discussed the results from eight simulations, which differed only in the satellite orbit, but had the same initial halo model with velocity isotropy. We are now

⁴Strictly speaking, the radial orbit with $L = 0$ is never deflected ($\Delta\phi = \pi$) as no transverse forces act on it. However, in the limit $L \rightarrow 0$ one gets $\Delta\phi > \pi$ (except for the harmonic potential), i.e. $\Delta\phi$ is discontinuous at $L = 0$ or, equivalently, $r_{\text{peri}} = 0$. In our simulations, the halo potential is modelled from the softened particle potentials and deviates from the power-law form at $r \lesssim \epsilon = 0.005$, where it becomes harmonic and the discontinuity at $r_{\text{peri}} = 0$ is removed such that $\Delta\phi \approx \pi$ for $r_{\text{peri}} \lesssim \epsilon$. However, even the simulations with initially purely radial satellite orbits have actual $r_{\text{peri}} > \epsilon$ at first passage (see Fig. 2.2), such that the simulated satellite orbit is actually deflected.

investigating initially anisotropic dark-matter velocity distributions. Since parabolic orbits are more realistic for infalling clumps, we restrict our discussion to the four satellite orbits with initially vanishing orbital energy $\varepsilon_s = 0$ and various eccentricities. Most of our general conclusion are, however, at least qualitatively also valid for bound orbits.

In addition to the halo model with velocity isotropy, used in Sections 2.4 and 2.5, we consider three initially anisotropic models. Two of these have constant anisotropy parameter of $\beta = 0.3$ and $\beta = -0.43$, respectively, which corresponds to the same level of anisotropy in the sense of $|\ln \sigma_r / \sigma_t|$ (with the tangential velocity dispersion $\sigma_t^2 \equiv [\sigma_\phi^2 + \sigma_\theta^2]/2$). The third anisotropic halo model is motivated by simulations of galaxy halo formation, which generally predict that the velocity distribution of the dark matter within haloes is outwardly increasing radially anisotropic (Hansen and Moore, 2006). We use the anisotropy profile of equation (2.14) with $\beta_\infty = 1$. This halo model is quite different from the others, as it undergoes a radial orbit instability, and we discuss it in some more detail in section 2.7.

2.6.1 Halo phase-space structure and vulnerability

Before we discuss the simulations, let us consider an important difference between these four models. Haloes with more radially biased velocities have more mass on eccentric orbits, which spend most of their time near apo-centre, but contribute significantly to the density near their respective peri-centres, in particular if the density increases more slowly than r^{-2} (because of geometrical effects) as it does in the inner regions of dark-matter haloes. Consequently, much of the dark matter in the innermost region of a halo with radial velocity anisotropy is on orbits which spend most of their time outside the innermost halo and have lower binding energies than the local circular orbits. Thus the more radially biased the velocities, the less mass is at high binding energies, as demonstrated in Fig. 2.5, which shows the differential energy distributions dM/dE for our four

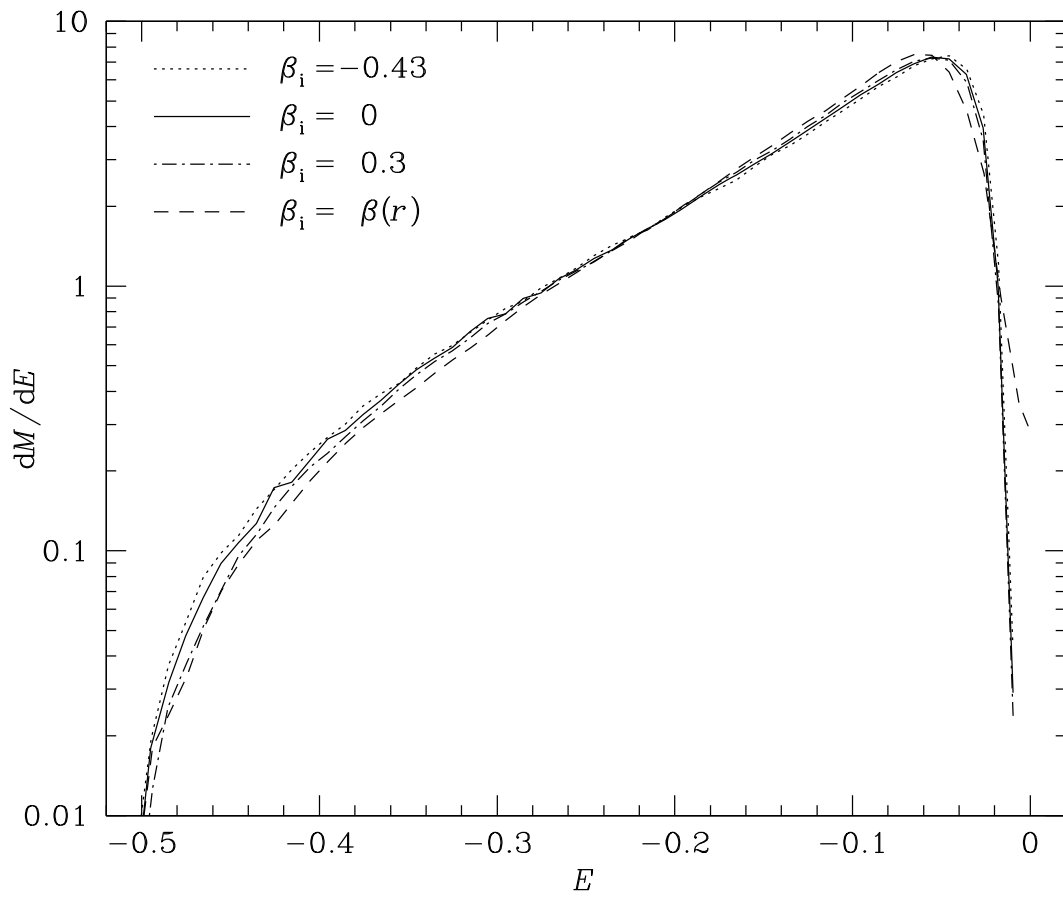


Figure 2.5: Differential energy distributions for the four different halo models considered, which only differ in their velocity anisotropy profiles.

halo models (computed from N -body data; for a cleaner plot of the same effect but for different models see Fig. 4.5 of Binney and Tremaine, 2008).

The relative lack of highly bound orbits in haloes with radial velocity anisotropy has immediate consequences for the responsiveness and hence vulnerability of the central regions to perturbations, such as an infalling massive satellite (see also Binney and Tremaine, 2008, p. 299). Highly bound orbits are confined to the central regions, which makes them relatively inert to external perturbations, in particular if their orbital period is short compared to the time scale of the perturbation (adiabatic invariance). The eccentric orbits in haloes with radial velocity anisotropy, on the other hand, have longer periods and hence are not adiabatically protected in the same way. Moreover, the infalling satellite can relatively easily perturb dark-matter particles near the apo-centres of such orbits, increasing their angular momenta and hence peri-centric radius, and thereby reducing the central density of the halo.

These arguments also suggest that the difference in vulnerability between haloes with isotropic and radially anisotropic velocities is more pronounced for perturbation by a satellite passing at larger peri-centric radius, which affects eccentric orbits contributing to the centre, but hardly the innermost orbits. A satellite falling in on a purely radial orbit, on the other hand, will affect dark-matter orbits at all radii, regardless of halo anisotropy.

2.6.2 Change in velocity anisotropy

In Fig. 2.6, we plot the radial β profiles of the final halo in simulations of the decay of the four different parabolic satellite orbits (colour coded as in Figs. 2.2 to 2.4) in each of the three different halo models with constant initial β .

In case of initial velocity isotropy the final velocity distribution is isotropic too, while in all of the initially anisotropic cases, the halo velocity distribution evolves towards isotropy in the inner regions. This evolution is partly driven by (artificial) two-body

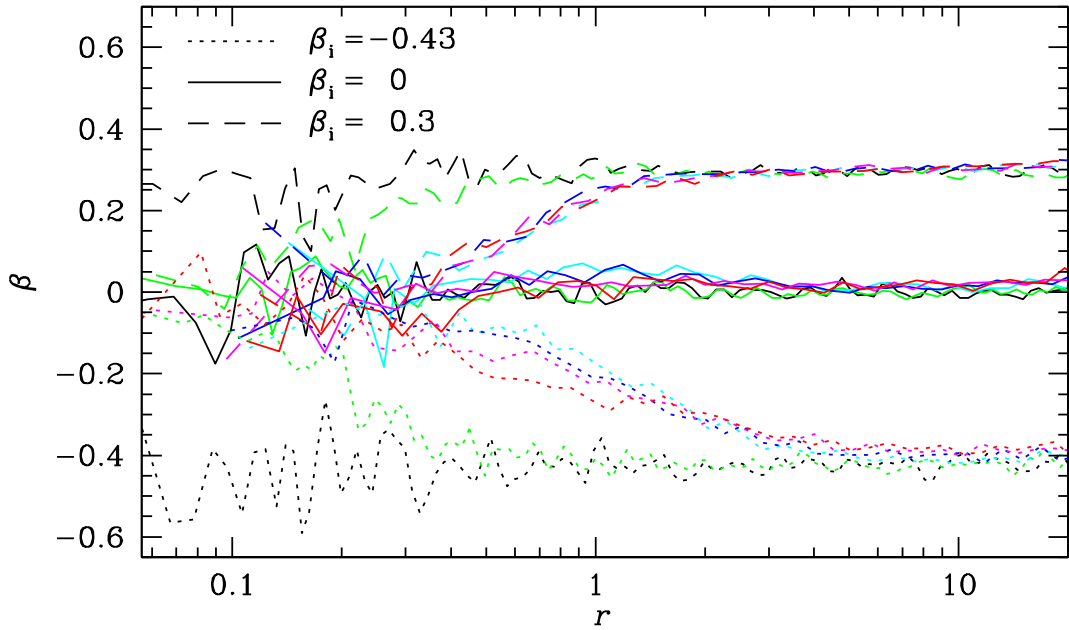


Figure 2.6: Radial profiles of the final (at $t = 2000$) halo velocity anisotropy parameter β for 4×3 simulations: four parabolic satellite orbits (as shown in the right panels of Figs. 2.2 to 2.4 with the same colour coding) decaying in three halo models with different constant initial anisotropy (line style as indicated). The black and green curves are the radial anisotropy profiles (obtained in the same way from N -body data) of the initial conditions and the control simulations, respectively. The satellite mass and size are $m_s = 0.01$ and $r_s = 0.03$ (as for all simulations presented sofar).

relaxation, as evident from the control simulations (green in Fig. 2.6), which results in velocity isotropy at $r \lesssim 0.1$. However, for the simulations with decaying satellite orbit, this isotropisation occurs to larger radii, which is essentially independent of the orbital eccentricity of the decaying orbit, and is only a function of the initial halo anisotropy.

This radius is larger by about a factor 3 for the models with initially constant tangential velocity anisotropy than for the models with initially constant radial velocity anisotropy. This is somewhat surprising in view of the discussion in the previous subsection. One speculation is that a system with tangential velocity anisotropy is not well-mixed in the sense of Tremaine et al. (1986) and Dehnen (2005), such that violent relaxation, induced by the perturbation, promotes evolution towards isotropy, while perhaps the opposite is true for radial velocity anisotropy.

It is also interesting to note that the evolution of the anisotropy profile is complete by the time of the first qualitative change in the orbit (i.e. essentially at $t = t_{\text{infall}}$). Thereafter, the final secondary decay of the satellite orbit takes place without further modification of the halo velocity distribution.

2.6.3 Effect on orbital decay and final halo

Instead of showing detailed figures, similar to Figs. 2.2 to 2.4, of the time evolution and radial profiles of density, axis ratios, etc. for the final halo of all the 4×4 simulations, we summarise the effects of different initial halo anisotropy in Fig. 2.7, which shows, for each simulation, the infall time t_{infall} as well as several properties of the final halo (at $t = 2000$). Apart from $\Delta M_{\text{max}}/m_s$, r_{max} , and $r_{50\%}$, already used in previous sections, we also plot the maximum value for the pseudo phase-space density ρ/σ^3 and the radius inside of which the minor-to-major axis ratio $c/a < 0.8$.

There is a systematic trend of shorter infall times for initially more radial dark-matter velocity anisotropy, exactly as expected from the arguments of Section 2.6.1: the inner

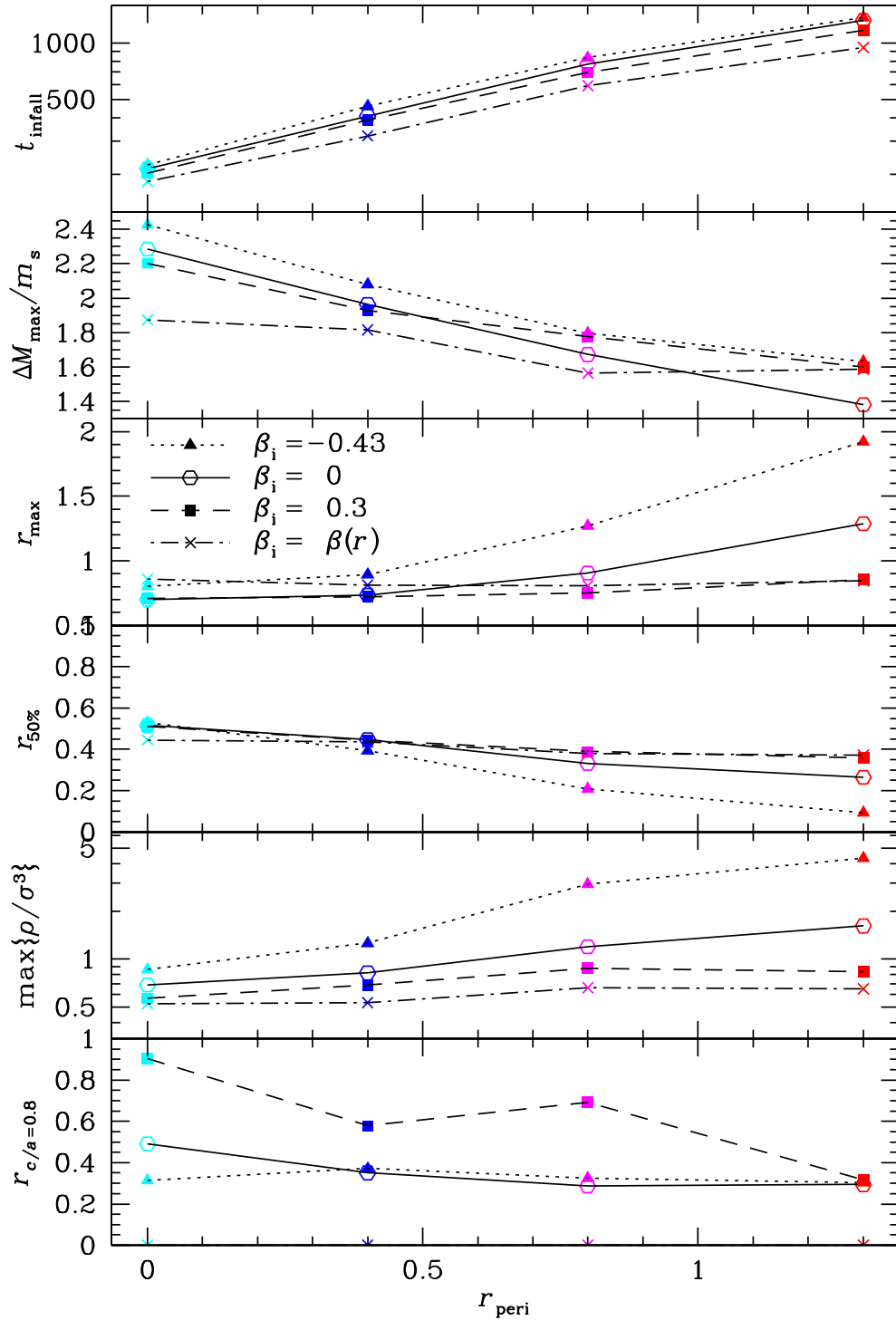


Figure 2.7: Dependence of orbital decay time t_{infall} and several properties of the final halo (the bottom panel plots the radius inside of which the minor-to-major axis ratio $c/a < 0.8$) on initial halo velocity anisotropy (line style as in Fig. 2.6) and initial pericentre for parabolic orbits with satellite of mass $m_s = 0.01$ and size $r_s = 0.03$. Symbol colours match those in Figs. 2.2 to 2.4.

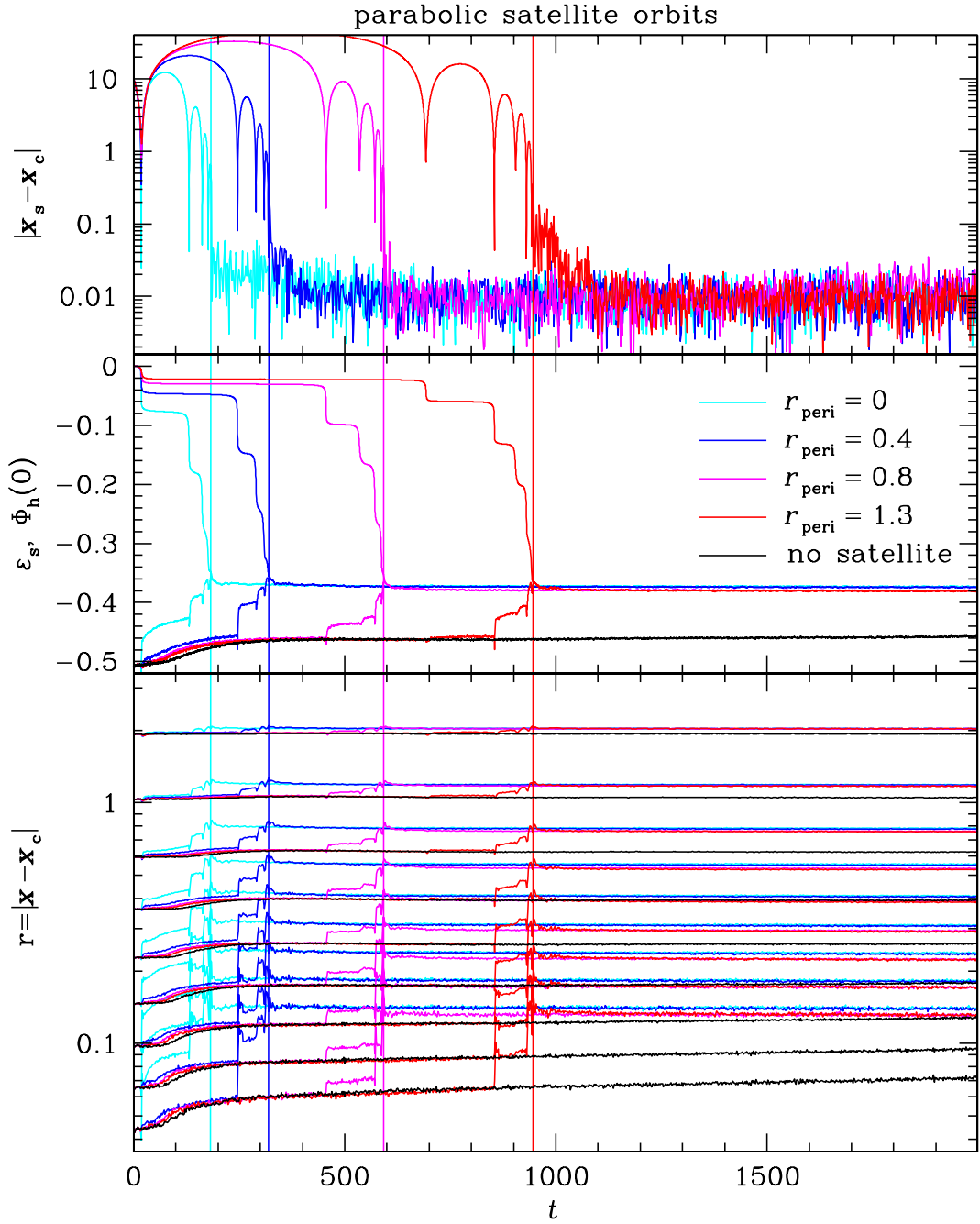


Figure 2.8: Like the right panels of Fig. 2.2, but for an initial halo with cosmologically motivated velocity anisotropy profile.

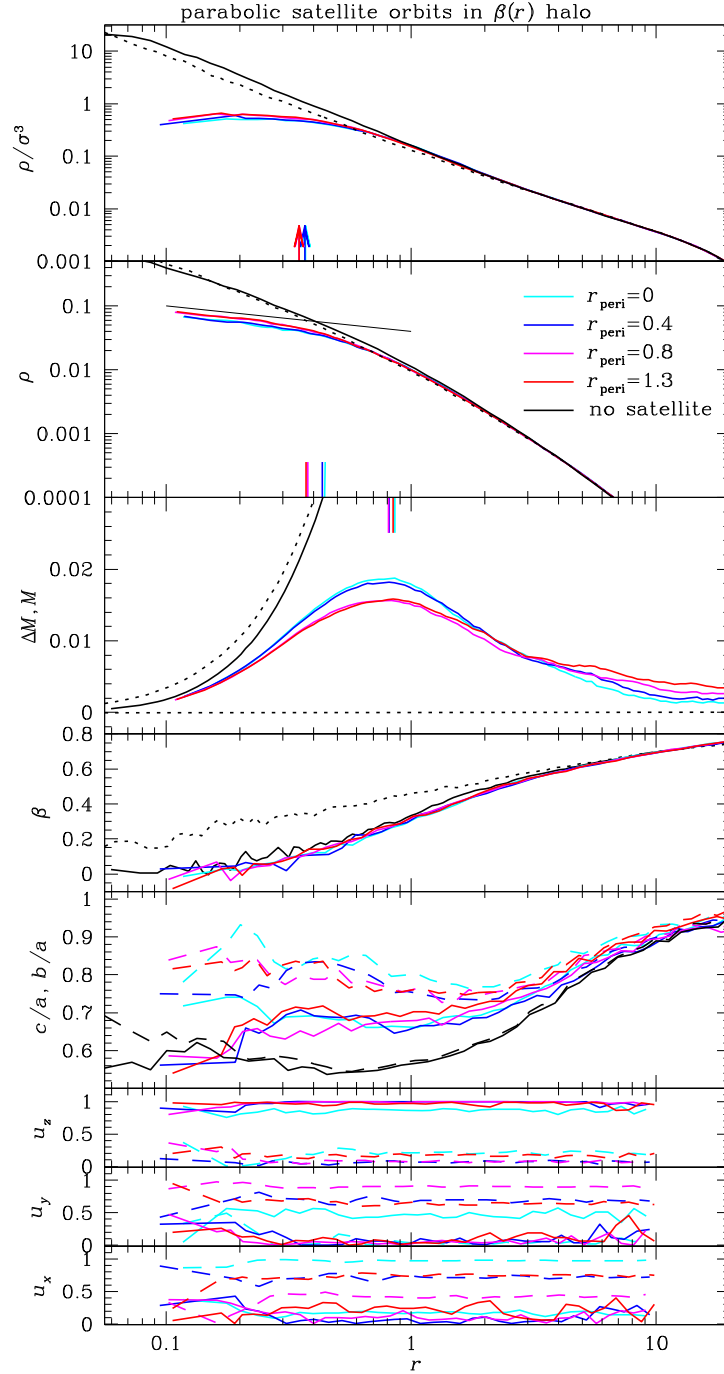


Figure 2.9: Final halo radial profiles after the infall of a satellite on an initially parabolic orbit into a halo with initially radially increasing velocity anisotropy $\beta(r)$ as in equation 2.14 with $\beta_\infty = 1$. The plots are equivalent to Figs. 2.3 and 2.4 (the thin line in the density plot is $r^{-0.4}$), except that in the bottom three panels we plot not only the minor-axis direction cosines (*solid*), but also the major axis direction cosines (*dashed*). For this halo model the control simulation (*black*) also undergoes some evolution driven by a radial-orbit instability, most evident from the changes in anisotropy and shape, see text for details.

parts of haloes with radially biased velocities are more responsive to and vulnerable by the infalling satellite. This is also the reason for the behaviour of $r_{50\%}$ and $\max\{\rho/\sigma^3\}$, which demonstrate that haloes with initially more radial velocity anisotropy suffer the strongest reduction in their central density and phase-space density. As argued in Section 2.6.1, the effects of initial halo velocity anisotropy are most pronounced for satellite orbits with large r_{peri} and least for a purely radial satellite orbit.

Again, the radius r_{max} at which $\Delta M(r)$ peaks anti-correlates with the radius $r_{50\%}$, indicating that the distribution $\Delta M(r)$ becomes more peaked (not shown) for more radially biased velocities and that this peak occurs at smaller radii. Both of these are natural consequences of the difference in orbital structure as outlined above.

There is also a systematic effect on the halo shape. For each model with initially constant β , the bottom panel of Fig. 2.7 plots the radius inside of which the minor-to-major axis ratio $c/a < 0.8$. The halo with tangential velocity anisotropy becomes flattened in a region comparable to that of the halo with isotropic velocities. For the halo with $\beta = 0.3$, the flattening is more pronounced, reaching out to about twice as far, and the shape is near-oblate (not shown) with the same characteristic as for the halo with initial velocity isotropy, discussed in Section 2.5.2. This is again expected, as the satellite's orbital angular momentum absorbed by the halo is relatively more important for dark-matter on low-angular-momentum orbits, as for radial velocity anisotropy.

2.7 Halo with cosmologically motivated velocity anisotropy

The situation with a outwardly increasing radial velocity anisotropy as in equation (2.14) is typical for dark-matter haloes emerging from simulations of large-scale structure formation (Hansen and Moore, 2006). As already mentioned in section 2.3.3, our spherical halo model with such an anisotropy profile undergoes a radial-orbit instability and quickly settles into a prolate configuration. While this instability somewhat complicates the in-

terpretation of any results, the corresponding simulations are presumably most realistic concerning the halo structure.

2.7.1 Orbital Decay

For the four simulations of initially parabolic satellite orbits in this halo model, we plot in Fig. 2.8 the orbital decay and time evolution of the halo Lagrange radii, similar to the right panels of Fig. 2.2. First note that the control simulation (black) undergoes an initial expansion within the first ~ 200 time units. This expansion is largely driven by the violent relaxation during the re-arrangement to a prolate configuration (due to the radial-orbit instability), while the expansion seen in the other control simulations (see Fig. 2.2) was solely driven by (artificial) two-body relaxation.

The orbital decay is faster than for any other halo model considered (see top panel of Fig. 2.7), because of the more efficient transfer of satellite orbital energy and angular momentum to the halo particles (as outlined in Section 2.6.1) during the very first peri-centric passages, when the halo density is not yet diminished by the instability-driven expansion. The associated heating of the innermost halo results in a slightly faster expansion in the simulations with satellite than in the control simulation even at $r < r_{\text{peri}}$.

The same is true to a lesser degree for the halo with $\beta = 0.3$ (not shown), while for the halo with isotropic velocities (Fig. 2.2), the Lagrange radii at $r < r_{\text{peri}}$ were hardly affected by the early peri-centric passages. This different response of the innermost halo to the satellite's first peri-centric passage can be attributed to the predominance of eccentric dark-matter orbits in the innermost halo, which are perturbed by the passing satellite at their respective apo-centres, as outlined in Section 2.6.1.

2.7.2 Effect on halo structure

Fig. 2.9 shows the radial profiles of ρ/σ^3 , ρ , ΔM , β , c/a , b/a and the direction cosines of the minor and major axes (similar to the right panels of Figs. 2.3 and 2.4) for the four simulations with decaying satellite orbits (coloured), the initial model (dotted), and control simulation (black). All these radial profiles after satellite orbit decay are quite similar, the strongest difference is 15% between the amplitudes of $\Delta M(r)$. This similarity is also expected from our discussion in Section 2.6.1: the halo is so responsive that the exact satellite orbit does not matter too much.

The pseudo phase-space density, ρ/σ^3 (top panel), of the control simulation is even larger than initially, although the density is reduced at $r \lesssim 0.15$. The reason for this counter-intuitive behaviour is that the isotropisation (evident from the runs of β) has reduced the velocity dispersion σ in the inner parts. However, after the orbital decay of the satellite, ρ/σ^3 is substantially reduced and necessarily also the true phase-space density. The maximum pseudo phase-space density is a factor 2-3 smaller than for simulations with initial velocity isotropy, and the density a factor ~ 2 . This represents the strongest central halo reduction in all models (for the default values of satellite mass and size), which makes sense in view of the vulnerability due to the radial velocity anisotropy.

The mass ΔM excavated compared to the control simulation is slightly less for the purely radial orbit (but slightly more for the orbit with $r_{\text{peri}} = 1.3$) than in case of an isotropic halo (Fig. 2.3). However, such a comparison is not quite adequate in view of the different behaviour of the respective halo models in isolation, and the picture that stronger radial velocity anisotropy results in larger an effect on the halo remains valid.

In all simulations the final halo is more isotropic than initially at $r \lesssim 3$, but still retains significant radial anisotropy. In fact, the β profiles are identical to that of the control simulation, presumably because this profile corresponds to a well-mixed state, attained after the initial violent relaxation phase, and hardly affected by any further relaxation

due to satellite interaction. Such radially anisotropic velocity distributions are likely the inevitable property of triaxial and prolate equilibria, because of the predominance of low-angular-momentum orbits, such as box orbits (Dehnen, 2009).

2.7.3 Effect on halo shape

Obviously, the final halo shapes are completely different from those obtained in simulations with any other initial halo model. As a result of the radial-orbit instability, the control simulation obtains a strongly flattened purely prolate shape with axis ratio < 0.6 at $r \lesssim 2$ (and some random orientation). This is in remarkable agreement with the fact that dark-matter haloes in gravity-only simulations of large-scale structure formation tend to have near-prolate shapes (Warren et al., 1992). After the satellite infall, however, the halo shape becomes less flattened and triaxial in the inner parts. The changes in halo shape compared to the control simulation extend to about $r \sim 5$, much farther than the changes in halo density or velocity anisotropy.

As the direction cosines indicate, the orientation of the principal axes of the triaxial shape is constant with radius, as one expects for an equilibrium system. The minor axis is always perpendicular to the original satellite orbit, while the major axis is somewhere in the initial orbital plane (except for the purely radial orbit for which such a plane cannot be defined).

2.8 Varying satellite mass and size

All simulations presented so far have the same satellite mass $m_s = 0.01$ and size $r_s = 0.03$. We are now investigating effects of larger and smaller values for these parameters.

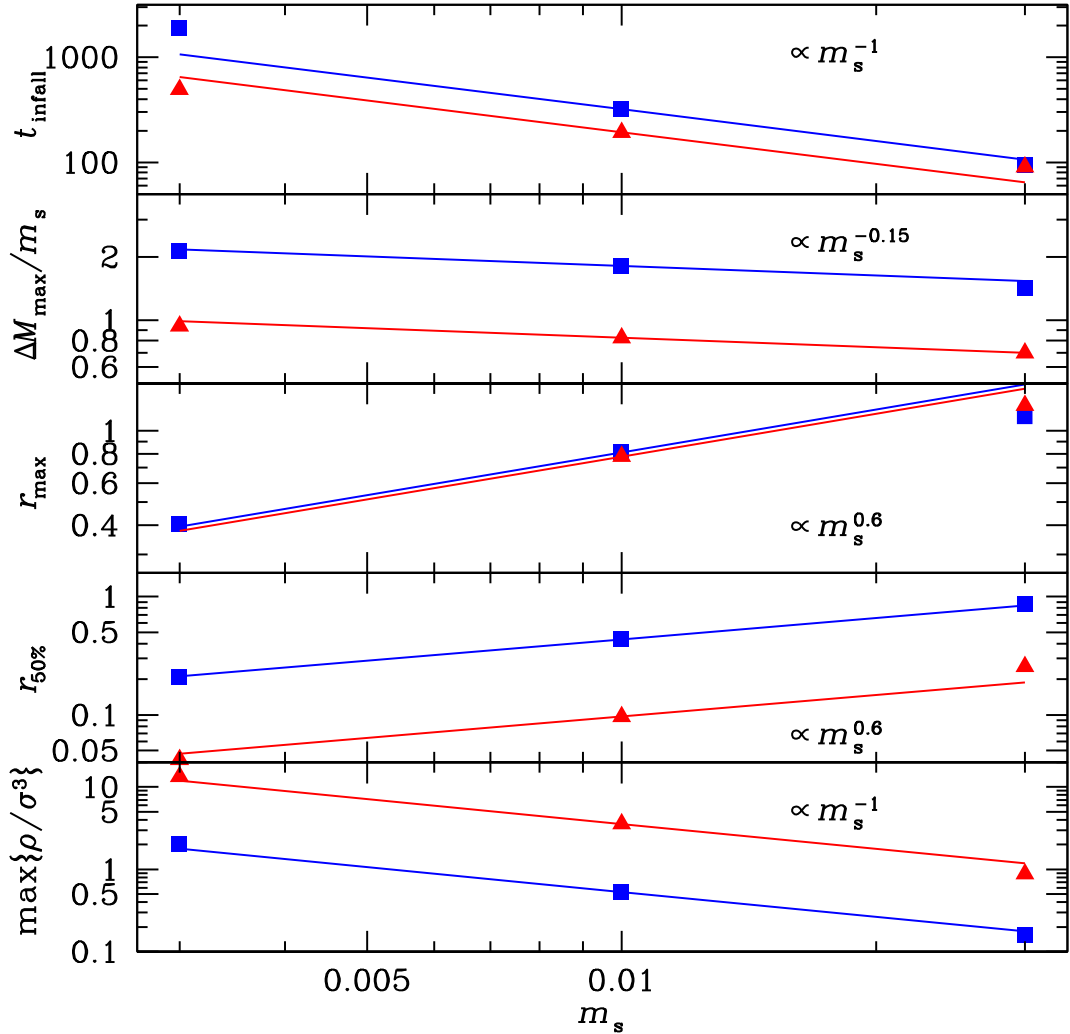


Figure 2.10: The variation with satellite mass of t_{infall} , ΔM_{max} , r_{max} , $r_{50\%}$, and the maximum (over all radii) of ρ/σ^3 after the decay of a circular satellite orbit starting at $r_i = 4$ in a halo with isotropic velocities (*red*) or after the decay of a parabolic satellite orbit with $r_{\text{peri}} = 0.4$ starting at $r_i = 10$ in a halo with outwardly increasing radial velocity anisotropy (*blue*). The lines are power-laws with exponent as indicated.

2.8.1 Varying satellite mass

Fig. 2.10 shows the effect of varying m_s by a factor of 3 up and down for a satellite initially on a circular orbit in a halo with isotropic velocities (*red*) and for a satellite on a parabolic with $r_{\text{peri}} = 0.4$ in a halo with cosmologically motivated $\beta(r)$. As expected, more massive satellites reach the centre more rapidly, and cause more damage to the inner halo. In agreement with Fig. 2.1, r_{max} , $r_{50\%}$, and ΔM_{max} are largest for the most massive satellite, and decrease systematically as the satellite mass is decreased. As the figure shows, the scaling of r_{max} and $r_{50\%}$ with satellite mass is close to scaling $r \propto m_s^{0.6}$ (solid lines) also found for our analytic models in Fig. 2.1.

The most interesting result from this study of varying satellite mass is that low mass satellites are more efficient at displacing mass than high mass satellites: in agreement with the analytic models the *relative* excavated mass $\Delta M_{\text{max}}/m_s$ increases towards smaller satellite masses.

According to Chandrasekhar's dynamical friction formula (2.1), the drag on the satellite is proportional to its mass m_s and would therefore naively expect the infall time to scale inversely with satellite mass: $t_{\text{infall}} \propto m_s^{-1}$. This is in fact the scaling indicated by the solid lines in the top panel of Fig. 2.10. However, the actual infall time measured for our simulations differ from this expectation. For the simple situation of an initially circular satellite orbit in a stable halo with isotropic velocities (red triangles), the infall time scales more like $t_{\text{infall}} \propto m_s^{-0.9}$. This difference is most likely caused by the re-adjustment of the halo during the satellite infall, an effect we ignored when deducing $t_{\text{infall}} \propto m_s^{-1}$, which therefore only applies in the limit $m_s \rightarrow 0$. The fact that this limit is not applicable even for $m_s/M_{\text{halo}} = 0.01$ may seem surprising, but is not in view of the fact that only a small fraction of the total halo mass accounts for most of its binding energy, which in turn enables such a feeble satellite to inflict significant damage to the halo.

The orbital decay into the halo model with radially increasing $\beta(r)$ (blue squares) is

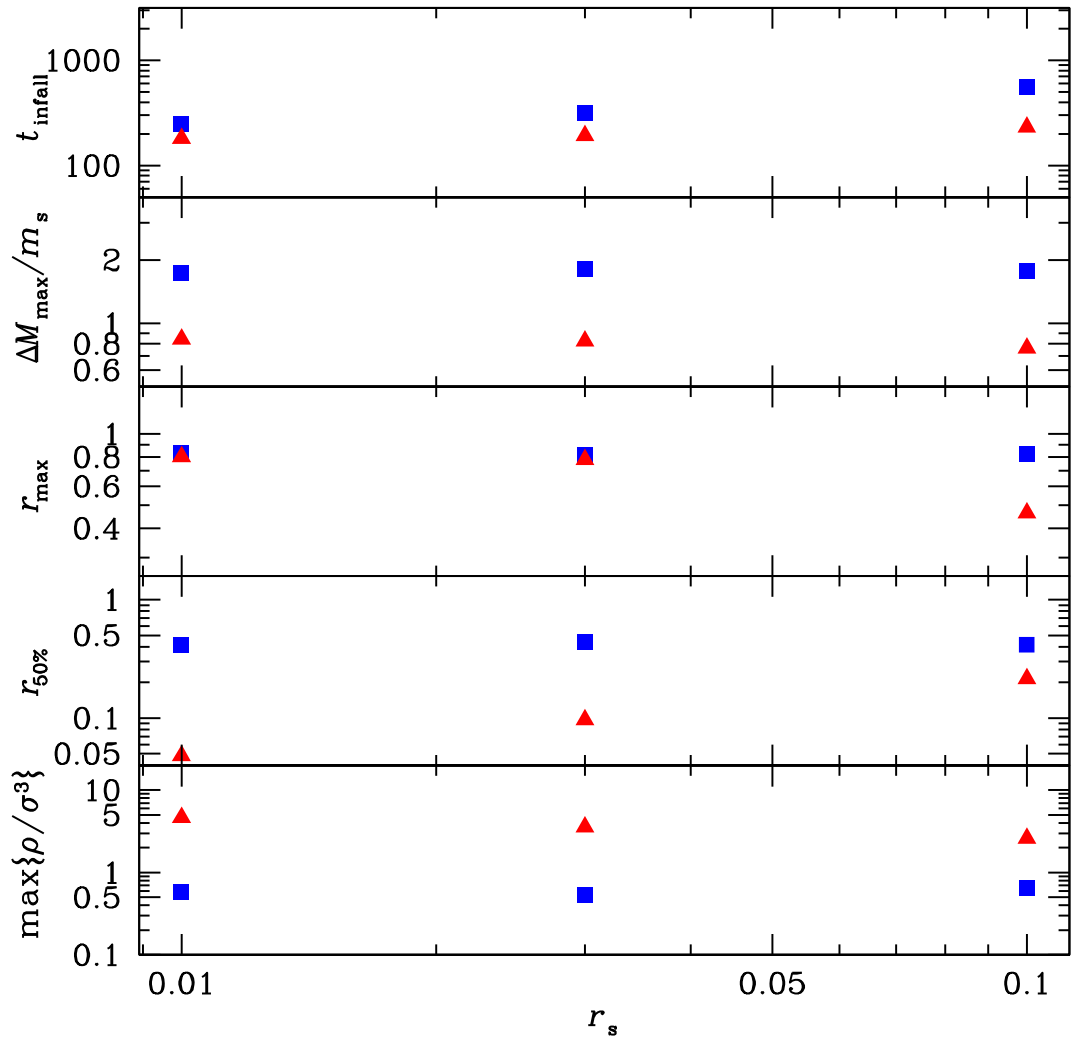


Figure 2.11: Like Fig. 2.10, except that satellite size r_s is varied and $m_s = 0.01$. kept constant.

complicated by the fact that the halo simultaneously undergoes a radial-orbit instability. The slight central density reduction driven by this instability increases the infall time compared to the original halo within the first ~ 200 time units. In our simulations, this sets up a race between satellite infall and instability-driven halo evolution. A more massive satellite sinks more quickly than this evolution and t_{infall} of the original halo applies, while for a low-mass satellite the longer infall time after the instability-driven halo evolution applies. Clearly, this race scenario is an artifact of our simulation setup, and we expect, based on the arguments given above, that in general t_{infall} scales slightly shallower than m_s^{-1} .

2.8.2 Varying satellite size

In Fig. 2.11 we vary the size r_s of the satellite by a factor 3 up and down, while holding its mass fixed for a circular satellite orbit in an isotropic halo (red triangles) and a parabolic satellite orbit with $r_{\text{peri}} = 0.4$ in a halo with cosmologically motivated $\beta(r)$. There is a systematic trend that more compact satellites lose energy more quickly and hence exhibit more rapid orbital decay. This is reasonable as more compact satellites are more efficient at scattering background particles and thus lose energy to the halo more rapidly.

The panels of Fig. 2.11 show that the cumulative effect of the satellite on the halo is almost independent of its size – the values of $\Delta M_{\text{max}}/m_s$, r_{max} , and $\max\{\rho/\sigma^3\}$ are virtually unchanged as the size of the satellite is changed by an order of magnitude, in particular for the parabolic orbit in the $\beta(r)$ halo. This is not very surprising in view of the analytical models of Section 2.2: the orbital energy of the satellite is essentially independent of r_s (as long as $r_s \ll r_2$).

However, for the circular satellite orbit decaying in a $\beta = 0$ halo, there is a systematic trend of larger $r_{50\%}$ with larger r_s and the halo profile is more significantly flattened by a more extended satellite. This is also seen in the evolution of the Lagrange radii and

is reasonable since the more extended the satellite, the less energy it loses at large radii and therefore has more energy to impart to the innermost halo. More extended satellites on near-circular orbits carry more energy to the inner regions and hence perturb the halo profile to a greater degree (for highly eccentric orbits this picture does not apply, as they affect the innermost halo already at their first peri-centric passage).

The evolution produced by satellites on bound orbits in isotropic haloes is qualitatively the same as that for parabolic orbits, although the magnitude of the effects is reduced. In particular, the infall time differs by only 30% between the largest and smallest satellites, compared to the factor of three for the parabolic satellite orbit in the halo with increasing $\beta(r)$. This again may be caused by the increased vulnerability and responsiveness of haloes with radial velocity anisotropy, as discussed in Section 2.6.1.

2.9 The Effect of satellite removal

In our modelling so far we have ignored the additional halo expansion following the possible loss of baryons in a feedback-driven galactic wind. At the final time in the models, the gravitational potential inside $\sim 0.1r_2$ is dominated by the satellite. Therefore the central potential is still quite deep, even though for most of our models the satellite mass is somewhat smaller than the removed dark mass. This implies that the bound phase-space volume available for the dark matter at the centre is almost unchanged.

In order to study the effect of baryon outflow on the dark-matter, we extend one of our models by removing the satellite. The model concerned is the one with an initially parabolic satellite orbit with $r_{\text{peri}} = 0.4$ falling into a halo with isotropic velocities (*blue* curves in the right panels of Figs. 2.2 and 2.3). In Fig. 2.12, the resulting radial profiles for ρ/σ^3 , ρ , and ΔM are shown for the situation (i) after satellite accretion (same as the curves in Fig. 2.3; *blue*), (ii) further 1000 time units after instant satellite removal (corresponding to a fast wind; *magenta*), and (iii) after a slow satellite removal (over 250 times units

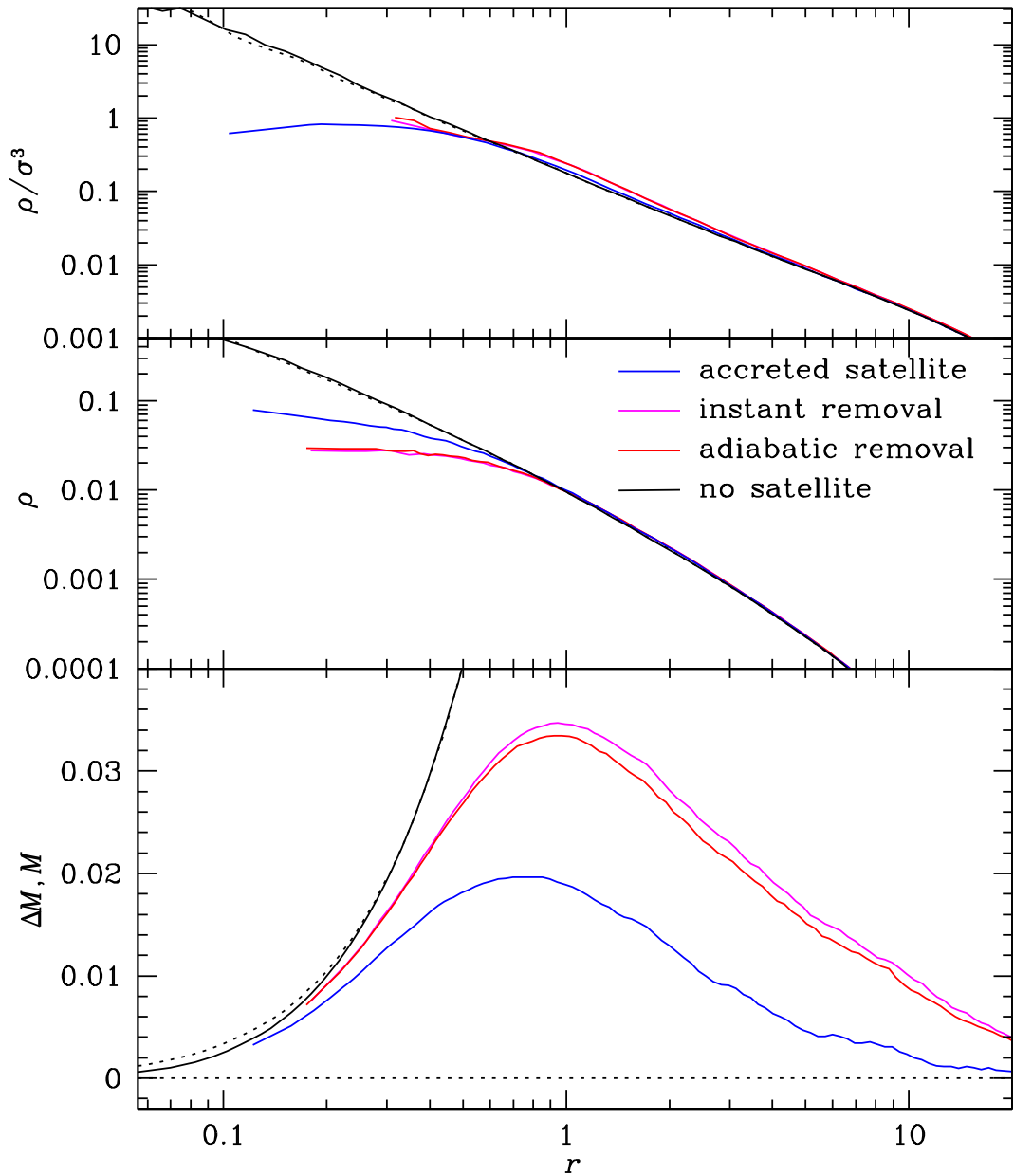


Figure 2.12: As Fig. 2.3, but also including the removal of the satellite. The *blue* curves refer to the same model as the *blue* curves in Fig. 2.3. The *magenta* curves are obtained from this model after instant removal of the satellite; while for the *red* model the satellite has been slowly removed.

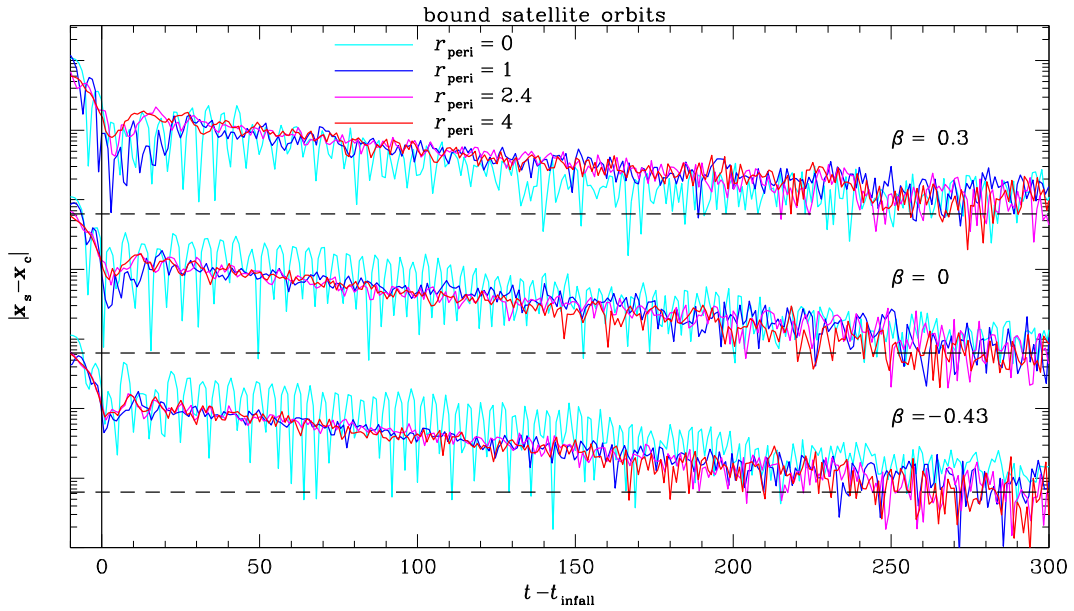


Figure 2.13: Secondary orbital decay: time evolution of the distance between satellite and halo centre for the 300 time units after the infall time (vertical line) for the bound satellite orbits in halo models with various velocity anisotropy as indicated (the curves for different halo models are offset by 2dex from each other). The horizontal dashed lines indicate the noise level measured at much later times.

followed by another 250 time units without satellite; *red*). Not surprisingly, the satellite removal has a dramatic effect on the central halo density: the total mass excavated has almost doubled compared to the situation prior to satellite removal and the density has become clearly cored with a central density ~ 10 times smaller than the initial density at the radius where initially $m_s = M(r)$.

The most intriguing plot, however, is that of the pseudo phase-space density ρ/σ^3 (*top* panel of Fig. 2.12). While the re-distribution of material to larger radii has shifted the inner profile somewhat, the overall distribution and the maximum value for ρ/σ^3 remained unaffected by the satellite removal. For the slow-wind model this is, of course, expected, since the (true coarse-grained) phase-space density is conserved. Therefore, the additional reduction of ρ and ΔM in this case is entirely owed to the reduction in available phase-space effected by the removal of the satellite potential. Of course, this is a non-linear process because the reduction in central dark-matter density itself leads to a

further decrease in the potential depth. This explains why the additional mass removed by the satellite departure (the difference between the *red/magenta* and *blue* curves) is quite substantial, exceeding the satellite mass.

Somewhat unexpectedly, the fast-wind model is only slightly more efficient at removing dark-matter. This strongly suggests that even a fast galactic wind is nearly adiabatic, i.e. has little effect on the (true coarse-grained) phase-space density (which is unaffected by a slow wind).

2.10 Summary

We have modelled, using N -body simulations, the decay of satellite orbits in spherical dark-matter halo models with various degrees of velocity anisotropy.

2.10.1 Orbital evolution

The evolution of the satellite orbits has several phases. First there is a steady decline in the radius of the orbit with almost constant peri-centric radius, driven by dynamical friction near peri-centre. This is followed by a period of rapid shrinkage of the peri-centre coinciding with significant expansion of the innermost halo, as evident from the evolution of the Lagrange radii in Figs. 2.2 and 2.8.

At this stage the evolution of the halo, driven by the transfer of energy and angular momentum from the decaying satellite orbit, is more or less complete. The time required for this process scales as $t_{\text{infall}} \propto m_s^{-0.9}$ with satellite mass, somewhat shallower than the inverse scaling expected from Chandrasekhar's dynamical-friction formula. We also find that t_{infall} is significantly shorter for decay in haloes with radial velocity anisotropy, because the orbital structure of such haloes makes them more susceptible to perturbations.

The orbital evolution shows some interesting and unexpected behaviour after t_{infall} .

The most bound region of the halo and the satellite form a sort of binary, dominated in mass by the satellite, which is modelled as a single softened particle with size (softening length) $r_s = 0.03$ (our unit of length is the halo scale radius). Initially, this secondary orbit has binary separation $\approx 0.1 > r_s$, but after a brief period of apparent growth decays very nearly exponentially with e-folding time of 90 time units.

This is clearly visible in Fig. 2.13, which plots for all 12 simulations of bound satellite orbits the late time evolution of the distance $|\mathbf{x}_s - \mathbf{x}_c|$ between halo centre and satellite after the initial infall of the satellite. In all these cases the secondary orbital decay occurs. The secondary orbit may be eccentric (as for $r_{\text{peri}} = 0$ in Fig. 2.13) or near-circular, when the decay appears more regular. In the case of parabolic satellite orbits (not shown), the secondary decay does not always occur or is much more noisy and less regular.

We are not sure about the cause and dynamics of this phenomenon, and whether it is a numerical artifact or not. It may be related to the form of the softened satellite potential, though the secondary orbital amplitude decays from $\sim 0.2 > r_s$ to $\sim 0.007 < r_s$, such that the harmonic inner parts of the softened potential become relevant only in the late stages.

2.10.2 Effect on Halo

Even though the assumed satellite mass was only 1% of the total halo mass, the damage done to the halo is significant: the inner parts of the halo are substantially reduced in density and phase-space density (as indicated by the behaviour of ρ/σ^3), when the satellite has displaced up to twice its own mass from the innermost halo. The satellite also affects the velocity structure of the inner halo making it more isotropic. Finally, the halo shape becomes triaxial in its inner parts.

We find that the efficiency with which the satellite can affect the halo, e.g. the amount of central density reduction, is increased for haloes with radial velocity anisotropy. This is understandable in terms of the orbital structure of such haloes, making them more

vulnerable (see Section 2.6.1), and relevant, as real dark-matter haloes are expected, from simulations of large-scale structure formation, to be radial anisotropic.

One of our most interesting findings is that satellites of smaller mass are relatively more efficient in damaging the halo: the ratio $\Delta M_{\max}/m_s$ of the maximum displaced halo mass over the satellite mass increases towards smaller satellite masses m_s (though the orbital decay time decreases, of course), as in fact predicted by the analytic energy arguments presented in Section 2.2.

2.11 Discussion

In this study we have ignored the details of baryonic physics and instead used the simple model of a compact baryonic clump falling into a dark-matter halo. Of all possible scenarios for the effect of baryonic physics on the structure of dark-matter haloes this is likely the most efficient. This process proved to be highly effective in altering the structure of the dark-matter halo in its inner parts, where the galaxy resides. A single clump of only 1% of the total halo mass can reduce the density at $\lesssim 0.1$ halo scale radii by more than an order of magnitude (including the effect of a galactic wind as demonstrated in section 2.9), more than sufficient to explain the discrepancies between the rotation curves predicted (using gravity-only simulations) and observed for dark-matter dominated galaxies (e.g. Simon et al., 2005; de Blok et al., 2008).

The total amount of baryons is one sixth of all matter (i.e. the cosmic baryon fraction) Komatsu et al. (2011), i.e. 0.2 times the dark mass, 20 times more than our model clump. Thus, if the baryonic heating of a dark-matter halo is only $\sim 2\%$ efficient on average, the damage done to the halo is equivalent to that in our models, because any additional adiabatic inflow *and* outflow of baryons has no lasting effect on the dark matter.

This assumes, of course, that the baryonic sub-structures and clumps are able to heat the dark-matter particles which contribute to the central cusp. Our simple model of a

compact clump, which sinks to the centre of the dark-matter halo, is certainly somewhat unrealistic as baryonic structures are susceptible to disruption by tidal forces before they reach the innermost parts of the halo. However, owing to their dissipative nature baryons, unlike dark-matter, can form new sub-structures and clumps, which then continue to heat the dark-matter via dynamical friction. Moreover, as our simulations have shown, radial velocity anisotropy, which is typical for dark-matter haloes, make their innermost parts more vulnerable to perturbations from the outside. This is because much of the matter in the cuspy region is on eccentric orbits spending most of their time at much larger radii where they are prone to dynamic heating (see also Section 2.6.1).

2.11.1 Dark-matter contraction vs. expansion

A key process in the re-shaping of dark-matter haloes by non-gravitational baryonic physics is the transfer of energy via dynamical friction from baryonic sub-structures to the dark-matter particles⁵. The effect of this heating can be understood qualitatively by considering the Jeans equation of hydrostatic equilibrium

$$\nabla(\rho\sigma^2) = -\rho\nabla\Phi. \quad (2.17)$$

The heating of the dark matter by the non-adiabatic baryon infall raises the central σ^2 , which, at fixed ρ , increases the pressure gradient (left-hand side). At the same time, the arrival of the baryons increases the gravitational pull (right-hand side). If these two effects balance exactly, the dark-matter density ρ remains unaffected. If the heating dominates, as was the case in our maximally non-adiabatic simulations, then ρ must flatten to retain equilibrium. Conversely, if the gravitational pull dominates (especially for negligible heating, i.e. ‘adiabatic contraction’), then ρ has to steepen (and σ^2 will increase adiabatically due to the compression). The exact balance depends on the details and most likely

⁵While this process itself is, of course, purely gravitational, it is neglected in gravity-only simulations, which ignore the formation of baryonic sub-structures and unequivocally predict cuspy dark-matter haloes.

varies systematically with galaxy type, size, and environment, explaining the possibility of conflicting results from simulations which attempt to model baryon physics more directly (e.g. Romano-Diaz et al., 2008; Pedrosa et al., 2009).

An alternative way to look at this problem is to consider the effect on the dark-matter (coarse-grained) phase-space density, which arguably is dynamically more relevant than the space mass density, because it is conserved for adiabatic evolution. However, the process of baryon infall is inevitably non-adiabatic and reduces the dark-matter phase-space density⁶. As long as the accreted baryons remain at the centre, this may not necessarily result in a reduction of the dark-matter spatial density, because the additional gravitational potential of the newly arrived baryons increases the available bound velocity-space (phase-space at fixed position).

Of course, a galactic wind changes the situation: the loss of some or all of the accreted baryons tips the balance towards a reduction of the dark-matter density, as convincingly demonstrated by our models of satellite removal. In the Jeans-equation picture the wind removes the additional gravitational pull from the accreted baryons. In the phase-space interpretation, the wind reduces the bound velocity space for DM particles, thus pressing the dark-matter phase-space fluid out of the centre, like toothpaste out of its tube.

2.11.2 Application to dSph and GCs

For a dwarf spheroidal galaxy our simplistic model of baryon infall may apply even more directly. Given that their present-day baryonic mass is comparable to the dark mass that needs to be rearranged in order to convert their haloes from cusped to cored, it seems plausible that for a reasonable star formation efficiency one could build the stellar com-

⁶More precisely, it reduces the excess-mass function

$$D(f) \equiv \int_{\bar{f}(\mathbf{x}, \mathbf{v}) > f} d\mathbf{x} d\mathbf{v} [\bar{f}(\mathbf{x}, \mathbf{v}) - f] \quad (2.18)$$

with $\bar{f}(\mathbf{x}, \mathbf{v})$ the coarse-grained phase-space density (Dehnen, 2005).

ponent of the dSphs from a number of star clusters that fall to the centre by dynamical friction and in so doing generate a macroscopic core in the halo dark matter distribution of the dSph. For this to work, the clusters need to remain largely unscathed by tides before they reach $\sim 0.1r_2$. Peñarrubia et al. (2009) have investigated the tidal disruption of star clusters orbiting in a dSph, in particular the Sagittarius and Fornax satellites to the Milky Way, and used N -body simulations to confirm the following criterion for the tidal radius r_t of a globular cluster (GC) at radius r within a halo

$$\bar{\rho}_{\text{GC}}(r_t) \approx 3\bar{\rho}_h(r). \quad (2.19)$$

In particular they looked at the resilience of the five GCs in Fornax and found that GCs which retain bound masses of greater than approximately 95% of their total mass do not undergo tidal disruption by the halo. In our simulations the clump falls in to approximately $r = 0.1r_2$ at which point it has excavated the mass in the centre of the halo and reduced the central density. At a corresponding radius in the simulations of Peñarrubia et al., four of the GCs are still very stable against tidal disruption. The fifth one is only disrupted when it spends a large fraction of a Hubble time at a radius in the range corresponding to $0.1 - 0.2r_2$ of our model.

In a similar way we can look at the stability of GCs in Low Surface Brightness (LSB) galaxies. Kuzio de Naray et al. (2008, 2006) investigated the density profiles of a number of LSB galaxies and attempted to fit them using NFW and pseudo-isothermal halo models. Their best-fit NFW models should give an upper limit to the density in the inner halo and therefore the one most likely able to disrupt an infalling object. Using these we find a range of values for $\bar{\rho}_h(r)$ at 0.1 scale radii ranging from 0.012 to $0.080 \text{ M}_{\odot}\text{pc}^{-3}$. These are lower than the corresponding value for Fornax which is $\sim 0.13 \text{ M}_{\odot}\text{pc}^{-3}$. Based on the work of Peñarrubia et al. (2009) this implies that GCs would also be stable at $0.1r_2$ in LSB galaxies.

3

The mass distribution of the Fornax dSph: constraints from its globular cluster distribution

3.1 Introduction

The Milky Way's dwarf spheroidal (dSph) satellites are among the nearest, smallest and least luminous galaxies we know. They also exhibit the largest discrepancies between dynamical and luminous masses and as such represent a unique opportunity to study the affect of DM on stars and gas in galaxies. Fornax is the most massive undisrupted dwarf spheroidal satellite of the Milky Way (Walker et al., 2009), only challenged by the Sagittarius dwarf which is much closer to the centre of the Milky Way and undergoing strong

tidal stresses. It was discovered by Shapley (1938) and is one of the classical dSphs as opposed to the ultra faint dSphs which have all been discovered since 2005 from studies of the Sloan Digital Sky Survey (SDSS). Its half light radius is 668 ± 34 pc (Walker et al., 2009) and its mass within this radius has been estimated as $5.3 \pm 0.9 \times 10^7 M_{\odot}$ whereas its total mass is of the order of $10^8 M_{\odot}$ (Table 3.1). Fornax is approximately 135kpc from the Sun (Table 3.1) and it is estimated that it is currently near its galactic pericentre (Lux et al., 2010). Its orbit appears to have a relatively low eccentricity compared to other Milky Way dSphs. Like all dSphs it is dark matter dominated even in its central regions. It is unique among the Milky Way undisrupted dSphs in having globular clusters (GCs); it has five, with three of them at a projected distance outside of the half light radius (see table 3.1). There is also evidence of a shell structure at a distance of 670 pc in projection which, based on the age of the stellar population making up this structure, may be the remnant of a merger more than 2 Gyr ago when tidal stirring of gas produced the stars which form it (Coleman et al., 2004).

One apparent paradox about these GCs is that because they move in a massive background of dark matter they should be affected by dynamical friction which will reduce their energy causing their orbits to decay. Fornax's GCs are metal poor and very old, comparable with the oldest GCs in the Milky Way with ages of the order of a Hubble time (Buonanno et al., 1998, 1999; Mackey and Gilmore, 2003a; Greco et al., 2007). During their lifetime it would be expected that they would fall to the centre of Fornax and form a nuclear star cluster. Tremaine and collaborators have proposed this process as a mechanism for forming nuclear star clusters (Tremaine et al., 1975; Tremaine, 1976). However no bright stellar nucleus is observed in Fornax. This is known as the timing problem for Fornax's GCs because it seems highly improbable that Fornax's GCs would be observed so far from its centre at present. Several authors have proposed reasons for the observed current locations of Fornax's GCs. Oh et al. (2000) suggested two ideas. First

that a population of black holes transferred energy to the GCs through close encounters and second that a strong tidal interaction between the Milky Way and Fornax could inject energy into their orbits. There is no observational evidence for a population of black holes in the centre of Fornax and the observed proper motion indicates that the orbit of Fornax around the Milky Way never takes it closer than at present (Dinescu et al., 2004; Lux et al., 2010) probably ruling out this idea. Angus and Diaferio (2009) proposed that all but the most massive GC could orbit within the tidal radius and avoid falling to the centre of Fornax. Using numerical simulations and analytic arguments Goerdt et al. (2006) proposed that the current distribution of the Fornax GCs can be explained by the diminution of dynamical friction on the edge of a cored matter distribution which would cause the GCs to stall at the dark matter core radius. Support for this result was provided by Sánchez-Salcedo et al. (2006) who showed that a cored matter distribution in dwarf galaxies can significantly delay the infall times of GCs even if simple Chandrasekhar friction is used. Further confirmation of the reduction of dynamical friction at the edge of cored density profiles was provided by Inoue (2009) who studied this effect using N-body simulations.

The discovery that the dark matter density distribution of Fornax is cored would have significant implications for our ideas about how dwarf galaxies form. Collisionless cosmological simulations (which ignore the effects of baryons) based on the Λ CDM model predict that the density distribution of dark matter halos have a central cusp i.e. $\rho \propto r^{-n}$ where $n \approx 1$ (Dubinski and Carlberg, 1991; Navarro et al., 1996b). If Fornax has a cored density distribution we would need to find an explanation for how it formed. It is difficult to understand how a density core can be created by simply changing the nature of dark matter. Neither making it warm (e.g. Tremaine and Gunn (1979); Strigari et al. (2006); Villaescusa-Navarro and Dalal (2011)), nor self-interacting (e.g. Kochanek and White (2000); Hogan and Dalcanton (2000)) appears to change the halo density profile results

seen in cosmological simulations. By contrast, feedback from baryons during galaxy formation on these small scales might be expected to form dark matter cores. There are two key processes discussed in the literature: heating of the dark matter during baryonic infall due to dynamical friction (El-Zant et al., 2001; Goerdt et al., 2010; Cole et al., 2011, and see Chapter 2); or heating due to impulsive gas outflows (Navarro et al., 1996a; Read and Gilmore, 2005; Pontzen and Governato, 2011). Navarro et al. (1996a) were the first to point out that spherically symmetric adiabatic inflow of gas followed by *impulsive* outflow is not a time reversible process and will therefore pump heat into the dark matter halo. However, in their simple toy simulations, they require the baryons to collapse by a factor of ≈ 100 to produce any significant effect. Gnedin and Zhao (2002) refined this argument. They showed from the initial angular momentum of the baryons that it is very unlikely for the gas to collapse by more than a factor of 0.1. In this case (in agreement with Navarro et al. (1996a)), they find almost no effect on the dark matter profile. However, Read and Gilmore (2005) show that *repeating* the inflow/outflow phases can gradually turn a cusp into a core even when angular momentum barriers are taken into account. Pontzen and Governato (2011) show that this is most likely what is happening in recent cosmological simulations that (owing to strong simulated stellar feedback) have a very bursty star formation history (Mashchenko et al., 2008; Governato et al., 2010). In practice, both heating due to dynamical friction and heating due to impulsive gas outflow are likely to act in tandem during galaxy formation.

The first evidence that dSphs have a density core came from Kleyna et al. (2003) who found indirect evidence for a core in the Ursa Minor dwarf (UMi). UMi is a classical dSph and about one third as massive Fornax. It was discovered by A.G. Wilson of the Lowell Observatory in 1954 (Wilson, 1955). Its half light radius is 280 ± 15 pc (Walker et al., 2009) and its mass within this radius is $1.5 \pm 0.4 \times 10^7 M_{\odot}$. UMi is approximately 60 kpc from the Sun but its estimated galactic pericentre is 30 to 40 kpc (Lux et al., 2010).

The Milky Way dSphs have been observed intensively in recent years. This is primarily because these systems are the most dark matter dominated which we know. They are mostly intermediate or old stellar populations which are likely to be well mixed in the dark matter potential because star formation ceased many dynamical times ago. This in turn implies that they are ideal laboratories for studying the mass structure of their dark matter halos. The intense observational effort means that there is a wealth of kinematical data available to form the basis for theoretical models of these systems. One line of approach has been based on the Jeans equation where a parametric light profile for the stars is assumed and a velocity dispersion profile is derived based on a underlying parameterised dark matter profile (Peñarrubia et al., 2008; Strigari et al., 2008; Walker et al., 2009). Amorisco and Evans (2011) point out two flaws in this approach:

1. There is no guaranteed physical distribution function for the model. They give the example that it is not possible to embed an isotropic cored stellar profile in a NavarroFrenkWhite halo, even though the Jeans equations yield a solution.
2. The dark matter and stellar profiles are proposed a priori and so provide no new insight beyond what is assumed. There is no physical connection between the luminous and dark matter, other than the fact that the velocity dispersions can support the model against gravitational collapse.

Other approaches have been used including phase space modelling of two stellar sub-populations (Battaglia et al., 2008; Amorisco and Evans, 2011, 2012), and measuring the slopes of the mass profiles of two chemo-dynamically distinct stellar sub-populations (Walker and Peñarrubia, 2011). With the former approach the results of the basic Jeans modelling leave the mass weakly constrained and is consistent with both cusped and cored density distributions. Both of these approaches favour a cored density distribution but these results probably require further confirmation before a cusped density distribution can be ruled out.

In this chapter, we follow the work of Goerdt et al. (2006) by examining what the current location of the GCs can tell us about Fornax’s mass distribution. Our work improves on this previous analysis in several key respects: (i) we use six mass models for the underlying potential in Fornax that sample the full range consistent with the latest data; (ii) we consider triaxial as well as spherical mass distributions; (iii) we use the latest data for Fornax’s GCs as constraints on their phase space distribution; and (iv) we run thousands of N-body models to sample the uncertainties in the GC distribution and Fornax mass model. This large grid search of the available parameter space allows us to address whether or not there are multiple solutions to Fornax’s timing problem.

This chapter is organised as follows: section 3.2 will review the most up to date observations of Fornax and its GCs and describe the statistical approach we took to deal with uncertainties in the observations which provide the parameters needed when modelling the Fornax system. We also describe the method we have used for estimating the Fornax mass distribution which then form the basis for our Fornax mass models. In Section 3.3 we describe our results and in section 3.4 we discuss the implications of our results and draw our conclusions.

3.2 Modelling Approach

The basis for our approach is to take the most up to date observations of the Fornax’s GCs and combine these with plausible mass models based on the latest kinematic data for Fornax’s stars. We then create models of the Fornax system which we evolve over several Gyr to discover how the locations of the GCs change.

Table 3.1: Data for the Fornax system. The mass estimates from Mackey and Gilmore (2003b) are given as a logarithm and we show the most likely mass in column 3. r_c is the core radius for a King model ((King, 1962)). r_p is the projected distance of the cluster from the centre of Fornax. r_{los} is the distance to each cluster and v_{los} is the line of sight velocity relative to Fornax itself.

References: (a) Mackey and Gilmore (2003b), (b) Mackey and Gilmore (2003a), (c) Greco et al. (2007), (d) Mateo et al. (1991), (e) Walker et al. (2009), (f)Buonanno et al. (1999), (g)Mateo (1998).

¹ The radius given for Fornax is its half light radius.

Object	$\log M_{GC}$ (M_{\odot}) ^a	M_{GC} ($10^5 M_{\odot}$) ^a	r_c^1 (pc) ^a	r_p (kpc) ^a	r_{los} (kpc)	v_{los} (km s ⁻¹) ^d
Fornax	8.15 $^{+0.19e}_{-0.37}$	1420 ^e	668 ^e	-	137 \pm 13 ^{b,f} 138 \pm 8 ^g	-
GC1	4.57 \pm 0.13	0.37	10.03	1.6	130.6 \pm 3.0 ^b	-
GC2	5.26 \pm 0.12	1.82	5.81	1.05	136.1 \pm 3.1 ^b	-1.2 \pm 4.6
GC3	5.56 \pm 0.12	3.63	1.60	0.43	135.5 \pm 3.1 ^b	7.1 \pm 3.9
GC4	5.12 \pm 0.24	1.32	1.75	0.24	134 \pm 6 ^c	5.9 \pm 3.4
GC5	5.25 \pm 0.20	1.78	1.38	1.43	140.6 \pm 3.2 ^b	8.7 \pm 3.6

3.2.1 Observations of the Fornax globular clusters

Our principal sources for Fornax GC data are those published by Mackey and Gilmore (2003b,a) and Greco et al. (2007) who have carried out thorough surveys of the Fornax GCs. For our purposes the main data needed are accurate estimates of the masses, sizes, three dimensional positions and velocities of the globular clusters.

The best estimates for the relevant data are given in table 3.1. The values for the core radius of each GC (r_c) are based on the surface brightness profiles calculated in Mackey and Gilmore (2003b). These are Elson, Fall and Freeman (EFF) models ((Elson et al., 1987)) and the King core radius r_c is related to the EFF scale parameter a by

$$r_c = a(2^{2/\gamma} - 1)^{1/2} \quad (3.1)$$

where γ is the power law slope of the surface brightness at large radii.

If we compare the distance of the Sun to the Fornax dwarf Spheroidal (dSph) galaxy to the distances of its individual GCs from the Sun and the associated errors it can be seen

Table 3.2: Kinematic data for the Fornax dSph.

Reference	Approx. range of radii (kpc)	Approx range of σ (km s ⁻¹)	β
Walker et al. (2007)	< 0.1 - 1.7	7 - 12	-0.5
Łokas (2009)	0.1 - 1.3	9 - 11.5	-0.33 ^{+0.15} _{-0.19}

that the measurements of the distance of the Fornax GCs are not good enough to provide their accurate 3 dimensional locations relative to Fornax. They could not be used for orbit modelling which could distinguish between different matter distributions.

In order to make progress in modelling the evolution of the orbits of the Fornax GCs we will make use of statistical methods to select their velocities and their line of sight (LOS) distances. The methods are fully described in section 3.2.4 but in brief they consists of selecting velocities which agree with the measured LOS velocities and are also consistent with the stellar velocity distributions observed for Fornax and selecting a distribution of LOS distances consistent with observations.

The kinematics of the stellar component of Fornax itself have been widely studied. The data for Fornax is shown in table 3.2. The measured velocity dispersions are approximately flat over the range of radii observed so we have taken the velocity dispersion to be constant with radius and have chosen a value of 10.5 km s⁻¹. The velocity dispersion is observed to be mildly tangentially anisotropic (Walker et al., 2007; Łokas, 2009) and so we have chosen a value for the β parameter of $\beta \approx -0.33$. β is given by

$$\beta \equiv 1 - \frac{\sigma_{\theta}^2 + \sigma_{\phi}^2}{2\sigma_r^2} \quad (3.2)$$

From table 3.2 it can be seen that the stellar velocity dispersion anisotropy is subject to some uncertainty. However the difference in the radial and tangential velocity dispersions produced by using this value of β is small with $\sigma_r \approx 9.5 \text{ km s}^{-1}$ and $\sigma_t \approx 11 \text{ km s}^{-1}$ so this will not have a significant effect on our results.

3.2.2 Technicalities

To generate initial N -body conditions for the Fornax galaxy models, we sample positions from

$$\rho(r) = \rho_0 r^{-\gamma_0} (1 + (r/r_s)^\eta)^{-((\gamma_\infty - \gamma_0)/\eta)} \operatorname{sech}(r/r_t), \quad (3.3)$$

and velocities from self-consistent distribution functions of the form $L^{-2\beta} f(\varepsilon)$ for constant β models with $f(\varepsilon)$ obtained from an Abel inversion (Cuddeford, 1991). It is important to note that our models represent the overall mass distribution of Fornax including both the stars and the dark matter.

The resolution in the inner parts is enhanced by increasing the sampling probability by a factor $g(\varepsilon)^{-1}$ which is compensated by setting particle masses μ_i proportional to $g(\varepsilon_i)$. We used

$$g(\varepsilon) \propto \frac{1 + q r_{\text{circ}}^\eta(\varepsilon)}{r_{\text{circ}}^\eta(\varepsilon) + r_s^\eta} \quad (3.4)$$

with $q = 4$ the ratio between maximum and minimum particle mass and $r_{\text{circ}}(\varepsilon)$ the radius of the circular orbit with specific energy ε . The gravitational forces were computed using a softening kernel with density profile given in equation (3.5) below and r_s replaced by the softening length $\epsilon = 0.01$. Testing this method for our particular purposes we found that it allows a reduction of N to half at the same central resolution without any adverse effects.

$$\rho_s(r) = \frac{15}{8\pi} \frac{r_s^4 m_s}{(r^2 + r_s^2)^{7/2}}. \quad (3.5)$$

We use a unit system where $G = 1$, $1\text{kpc} = 1$, $222288M_\odot = 1$ which implies a time unit of 1 Gyr and velocity units where $1\text{kms}^{-1} \approx 1$ ($0.9778\text{kms}^{-1} = 1$).

3.2.3 Theoretical modelling

Our modelling technique has several stages. First we find a plausible range of mass models based on recent work done elsewhere (see below). We then perform a consistency check and test that these models produce stellar kinematics consistent with the observed kinematics of Fornax (Section 3.2.3). We establish a statistical method for setting the initial distances and velocities for the Fornax GCs which is consistent with the observations of the GCs and Fornax's stellar component (Section 3.2.4). We then use these techniques to run hundreds of simulations which sample the velocities and LOS distances appropriately.

Modelling the mass structure

Observations over the past decade have yielded an extensive data set of more than two thousand individual stellar velocities in Fornax (Walker et al., 2009). The richness of the data for this, and other dSphs justifies the development of more sophisticated modelling tools than the Jeans models typically used to date. For example, Wilkinson et al. (2002); Kleytna et al. (2002) demonstrated that distribution function modelling could be used to break the mass-anisotropy degeneracy inherent in kinematic modelling once sufficiently large kinematic data sets are available. To take full advantage of the new dSph data, Wilkinson et al. (in prep.) use a Markov-Chain-Monte-Carlo (MCMC) analysis with 13-parameter dynamical models to constrain the mass profile of Fornax. The models assume spherical symmetry and dynamical equilibrium. The mass profile and stellar luminosity profile are modelled independently using profiles of the form in equation (3) without the sech cut-off at large radii (10 parameters). The distribution functions are calculated numerically following the approach of Gerhard (1991) and Saha (1992) and contain three parameters which determine the velocity anisotropy profile of the stars. As in the earlier work Wilkinson et al. (2002); Kleytna et al. (2002), the models are compared to the data

on a star-by-star basis.

The details of the modelling will be presented elsewhere and in the present chapter we just use them to inform our choice of halo models. Rather than considering only a “best-fit” model of Fornax, we use the initial results to select a subset of four which span the range of models which are consistent with the kinematic data. This set comprises (1) a model with a logarithmic mass density slope of 1.3 at 100pc (this is the model with the highest overall likelihood in the MCMC analysis); (2) the highest likelihood model that exhibits a slope of 0.1 at 100pc (cored model); (3) the highest likelihood model that exhibits a slope of 0.5 at 100pc (intermediate model); (4) the highest likelihood model that exhibits a slope of 1.0 at 100pc (cusped model).

Table 3.3 shows the parameters for these four models. In all cases the value for γ_0 , γ_∞ , η , ρ_0 , the total mass M_∞ and the scale radius r_s were obtained from the MCMC chain outputs.

Creating mass models

On the basis of this modelling we have selected a number of mass distributions to explore how the different density profiles affect the evolution of the orbits of the Fornax GCs. Our main objective is to see if there are significant differences between a cusped dark matter profile as predicted by cosmological simulations (Dubinski and Carlberg, 1991; Navarro et al., 1997) and a more cored one. There is circumstantial evidence that the halos of dSphs are not strongly cusped but have a shallow cusp or core (Gilmore et al., 2007). For these reasons we have chosen a range of mass distributions which are all in close agreement with the modelling referred to above (see table 3.3).

In addition to the models based on the work described in section 3.2.3 we have included two more in order to more thoroughly explore the effects of the size and shape of Fornax. One is based on the parameters which have arisen from the mass modelling re-

ferred to above but has a triaxial shape. Its parameters are given in table 3.3. Its principal axis ratios are $c/a = 0.5$ and $b/a = 0.66$.

The final model is a spherical model with a large core. It is based on the work described in Walker and Peñarrubia (2011). They use a non-parametric statistical modelling technique and apply it to distinct stellar populations within Fornax to define the enclosed mass at the half light radii of the two populations.

The density profiles, mass distribution and variation of density slope with radius for these models are shown in figure 3.1.

Checking the stellar kinematics

Figure 3.2 shows the stellar velocity dispersion for each of our Fornax models plotted against the observed velocity dispersion as measured by Walker et al. (2007). These theoretical velocity dispersions were calculated by creating an N-body model of Fornax's stellar component based on a spherically symmetric and isotropic Plummer (Plummer, 1911) model of a tracer population of particles of negligible mass with density profile

$$\rho(r) = \rho_0 \left(1 + (r/r_s)^2\right)^{-5/2} \quad (3.6)$$

moving in the overall potential of our model mass distributions. It is important to note that our models represent the overall mass distribution of Fornax and not just the dark matter. However, as is well known dwarf spheroidal galaxies are dark matter dominated so our mass profiles are primarily representative of the distribution of dark matter. As can be seen from Figure 3.2 the models all produce a good fit to the data.

3.2.4 Establishing the globular cluster distribution

Velocity sampling

There are two sets of observations we can use to model the velocities of the Fornax GCs. We have observations of the LOS velocities for the GCs (see table 3.1) and we have data

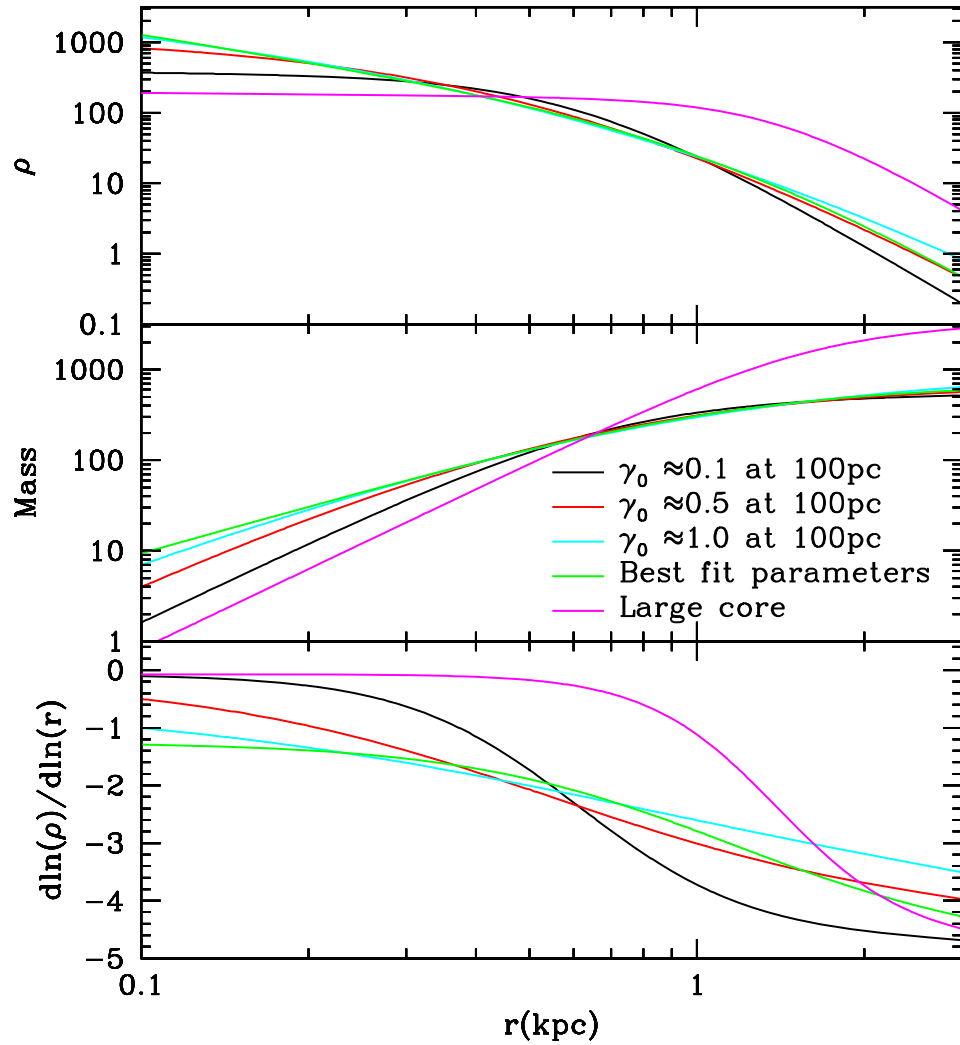


Figure 3.1: The mass structure for each halo used in our simulations. The top plot shows density versus radius, the middle plot shows mass versus radius and the bottom plot shows slope versus radius for each halo model.

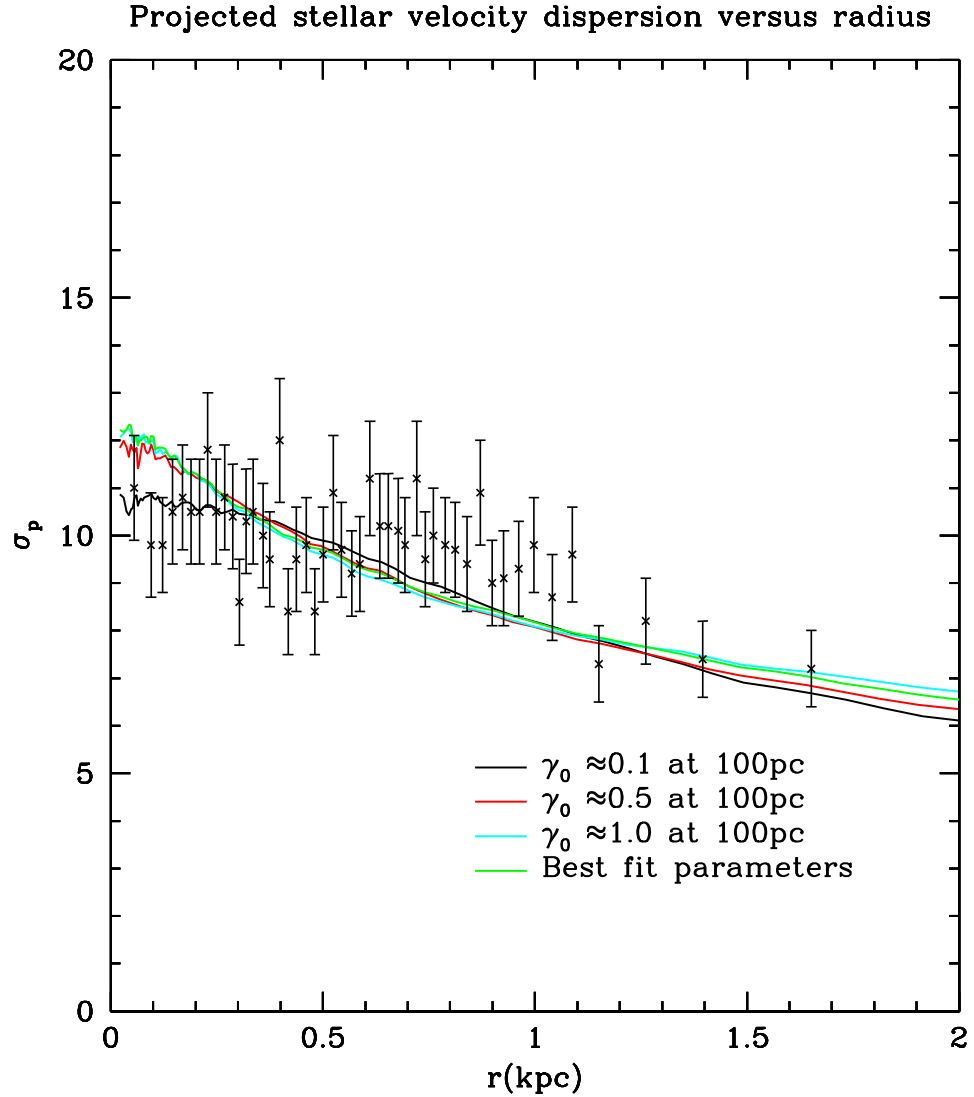


Figure 3.2: The observed stellar velocity dispersion (Walker et al., 2007) plotted against the theoretical velocity dispersion for each halo used in our simulations. The stellar velocity dispersion was derived assuming a tangentially biased stellar velocity distribution with a β parameter of $\beta \approx -0.33$ (see Table 3.2).

Table 3.3: Data for halos used in the simulations. γ_0 is the inner slope, γ_∞ is the outer slope and η is the transition parameter. γ_{100pc} is the slope at 100 pc. ρ_0 is the proportionality constant in equation 3.3. M_∞ is the total mass of the model, r_s is the scale radius and r_t is the truncation radius. c/a and b/a are the axis ratios.

Model	Name	γ_0	γ_∞	η	γ_{100pc}	M_∞ M_\odot	r_s kpc	r_t kpc	c/a	b/a
LC	Large core	0.07	4.65	3.7	0.1	8.00×10^8	1.4	10	1	1
SS	Shallow slope	0.08	4.65	2.77	0.1	1.23×10^8	0.62	10	1	1
IC	Intermediate cusp	0.13	4.24	1.37	0.5	1.51×10^8	0.55	10	1	1
TIC	Triaxial Intermediate cusp	0.13	4.24	1.37	0.5	1.51×10^8	0.55	10	0.5	0.67
SC	Steep cusp	0.52	4.27	0.93	1.0	1.98×10^8	0.80	10	1	1
BF	Best fit	1.25	4.68	1.82	1.3	1.52×10^8	1.13	10	1	1

on the velocity structure of the stars in Fornax (see table 3.2). It seems reasonable to assume that the GCs would follow a similar velocity structure to the stars in the bulk of the Fornax galaxy. Therefore we have constructed a statistical sampling scheme that produces velocities randomly such that the overall distribution matches the Fornax stellar velocity distribution while at the same time having the observed LOS velocities.

This process is as follows:

1. We select appropriate values for the one dimensional velocity dispersion and anisotropy parameter.
2. We transform the expressions for the velocity structure of the stellar component of Fornax from spherical polar coordinates to Cartesian coordinates. This is primarily to allow us to ensure that the LOS velocity can be taken into account easily in our analysis.
3. We separate the components of our variables along the LOS and in the plane of the sky so that the velocity distribution in the plane of the sky can be generated.

4. We generate the components of the appropriate normal velocity distribution in the plane of the sky.

This process is described in detail in Appendix A

Position sampling

The error in the distance estimates for the individual GCs are $\sim \pm 5\text{kpc}$ and so estimating the LOS distance to each GC accurately is not possible. One method for estimating the location relative to the centre of Fornax would be to assume that each component of the radial vector to the GC are equal in quadrature. The known projected distance to the centre of Fornax represents two of the spatial dimensions and so the square of the known spatial distance to the centre of Fornax would be \approx double the square of the unknown dimension. If R is the distance of a globular cluster (GC) from the centre of Fornax, z is the difference between the distance of the GC and the distance of Fornax and r_{proj} is the distance of the GC projected onto the sky then this would imply that

$$2\langle R^2 \rangle / 3 = \langle r_{proj}^2 \rangle \quad \langle z^2 \rangle = \langle r_{proj}^2 \rangle / 2 = \langle R^2 \rangle / 3 \quad \langle z \rangle = \pm \langle r_{proj} \rangle / \sqrt{2} \quad (3.7)$$

We could base our estimate for z on a normal distribution with mean zero and standard deviation $r_{proj} / \sqrt{2}$.

One weakness in this approach is that it does not explore a large range of distances of each GC from the centre of Fornax. Observations are consistent with the Fornax system being several kiloparsec across. We therefore have adopted a different method. First we have sampled the LOS distances uniformly in z between 0 and 2 kpc ($z \in [0, 2 \text{ kpc}]$). 2 kpc corresponds to the approximate tidal radius of the system (Walker and Peñarrubia, 2011) and see section 3.3.3. This allows us to create other interesting initial distributions afterwards by sampling appropriately. We have only used LOS distance in the range 0 to 2 kpc rather than -2 to 2 kpc because of the symmetry of our simulations. The majority

of models are spherical and so symmetric in the plane of the sky. This is also true for the triaxial model which is aligned so that the minor axis is parallel to the LOS.

3.2.5 Numerical convergence

In order to ensure that our simulations do not suffer from numerical noise we ran simulations with four different scenarios at different levels of resolution. We ran simulations with two different mass models, one cusped and one cored and for each mass model we ran two different orbits, one circular and one eccentric. In each case we created a model of Fornax with 4×10^5 , 1×10^6 and 4×10^6 particles and compared the evolution of one GC over 10 Gyrs. The evolution of the orbital radius of a single globular cluster moving on an eccentric orbit in a halo with a small core density profile (model SS from table 3.3) is shown in figure 3.3.

It can be seen that orbital evolution is very similar for each case with different numbers of particles. In particular the decay of the orbit follows the same timescales with the time and radius of the first stalling of the GC being the same. It has been shown that the 2-body noise in a simulation can cause the GC orbit to precess and cause artificial decay of the GC orbit once in the core (Read et al., 2006a). This combination of orbit and density profile was used because Read et al. (2006a) showed that convergence is most difficult for an eccentric orbit in a cored halo. This is the case where numerical friction caused by orbit precession has the largest effect on orbital decay. The simulations shown above give a strong indication that such effects are not significant at even lower resolutions than the one used for the main body of this work. We conclude that our simulations are strongly converged.

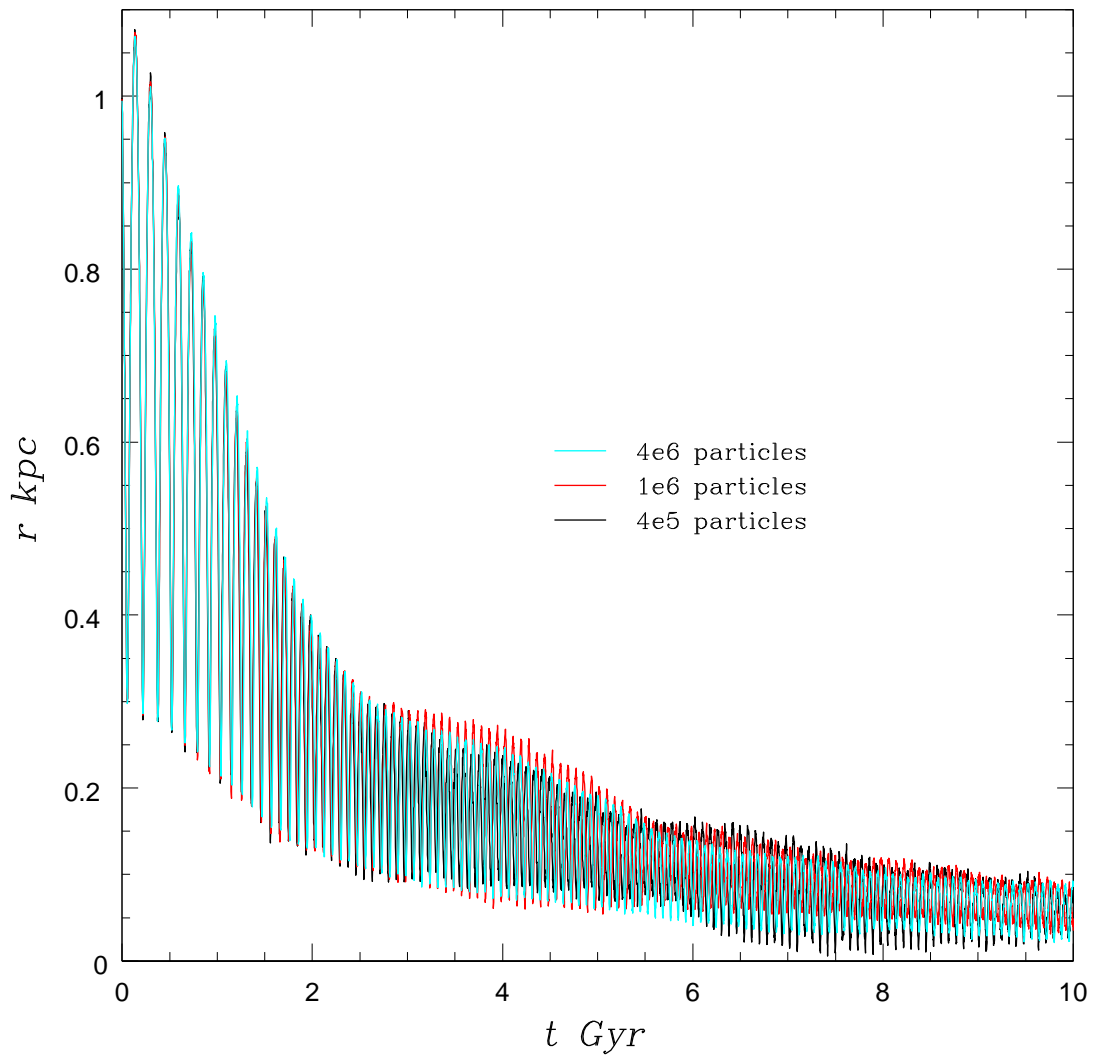


Figure 3.3: Plot of the evolution of a single globular cluster moving on an eccentric orbit in a halo with a small core density profile (model SS from table 3.3). The evolution of the distance from the centre of the galaxy is shown in different colours depending on the number of particles in the halo. Black corresponds to 500 thousand particles, red corresponds to 1 million particles and cyan corresponds to 4 million particles.

3.2.6 N-body simulations

We have taken the various mass models and run 700 simulations for each one. The velocities and positions were set up randomly as described above. We have fixed the position of the GC so that it has the correct projected distance but the LOS distance has a uniform distribution between 0 and 2 kpc relative to the distance of Fornax. This ensures that we explore the variation of the LOS distance thoroughly and allows us to investigate other distributions of LOS distance for each GC by filtering the simulations later. We have done this for a distribution which follows the stellar distribution function.

We have selected the velocities randomly so that the velocity distribution of the GCs is consistent with the velocity structure of the stellar component of Fornax and the observed LOS velocity of each GC.

3.3 Results

3.3.1 Main simulations

We have taken the instantaneous apocentre as our measure of the development of the orbits of the GCs. We have calculated this by taking the current energy and angular momentum of a GC and calculating the apocentre which corresponds to these values for the current halo potential (which will be modified by the infall of the GCs).

Figures 3.4 and 3.5 show the instantaneous apocentres of the GCs for each of seven hundred simulations for each mass model after 2 Gyr and 10 Gyr respectively.

Uniform distribution of LOS distances

First we will consider the complete set of results where the line of sight distances were distributed uniformly initially. After 2 Gyr (Figure 3.4) both GC1 or GC5 are only showing small evidence of falling to the centre of Fornax. At this stage the great majority of

cases for both GC1 and GC5 remain close to their initial radius in all models. GC1 is only showing a tendency to fall inwards in the cusped models SC (steep cusp) and BF (best fit). GC1 is the lightest ($3.7 \times 10^4 M_{\odot}$) and at the largest initial projected distance from the centre of Fornax. It will suffer the smallest dynamical friction and as dynamical friction force F is given by

$$F \propto M_{GC}^2 \quad (3.8)$$

where M_{GC} is the mass of a GC then its low mass will lead to much smaller torques driving it inwards. Though GC5 is much more massive (approximately 5 times more massive) it is at the second greatest projected distance from the centre of Fornax. The lower density here will lead to a reduction in the initial dynamical friction it undergoes. The other 3 GCs are all beginning to fall to the centre of Fornax at this time. How far in they have fallen depends strongly on the inner density profile of the mass model they orbit in.

Model BF shows the greatest evidence of undergoing the effects of dynamical friction. For GC3 and GC4 a significant proportion of the simulations have their instantaneous apocentres inside 30 pc with a smaller proportion of simulations showing this for GC4. GC2 does not show such a marked effect but a number of simulations already have an apocentre inside 100 pc. Model SC (steep cusp) shows similar results. Both of these models have a strongly cusped profile.

Model SS (shallow slope) shows much reduced signs of the effects of dynamical friction. GC3 shows the strongest effect and here the apocentres have only moved to the edge of the density core at worst. Many of the simulations show GC2 orbiting significantly further out still. GC2 and GC4 also show movement inwards but mainly to a few hundred parsecs from the centre. Model IC (intermediate cusp) shows results in between the cusped models and the cored ones as would be expected. It shows signs of inward migration for GC3 and GC4 but not as great as with models SC and BF.

After 10 Gyr (Figure 3.5) the trends shown at 2Gyr are continued. Four of the GCs show very similar behaviour. Only GC1 still shows no evidence of migrating to the centre of Fornax. All GCs have a small number of simulations where they remain at a large radius comparable with or greater than their initial location. GC5 has the largest probability of this occurring but even GC5 has only a small proportion of results which have not migrated inwards.

For the cusped models SC and BF the typical apocentre of their orbits is inside 10 pc and typically 3 pc which is comparable with their softening length meaning that they are at the very centre of the galaxy. The apocentres for the intermediate model IC are typically inside 10 pc but some have GCs still orbiting at finite distances of the order of 10 to 70 pc. Model SS shows the smallest reduction in apocentre with many orbits having an apocentre just inside the core radius of 100 pc. Many lie in the 20 to 100 pc range.

We highlight the behaviour of GC3 which falls to the centre of the galaxy in almost all cases. GC3 is the most massive GC ($3.63 \times 10^5 M_{\odot}$) and the second nearest to the centre of Fornax. It seems highly unlikely that this GC would not have fallen to a vanishingly small projected distance from the centre of Fornax in a Hubble time if the mass distribution in Fornax followed models IC, SC or BF.

The behaviour of the GCs in the different mass models is highlighted in Figure 3.6. Here we have plotted the instantaneous apocentres for all simulations with one Figure for each mass model with the GCs shown in different colours (red; GC1, blue; GC2 green; GC3, magenta; GC4 and cyan; GC5). It can clearly be seen that the GCs fall in earlier and further as the mass models become increasingly cusped. Figure 3.6 also shows the unusual behaviour of the large cored model (LC) where the GCs inside the core move out to the edge of the core but the GCs outside of the core fall in to the edge of the core.

Uniform distribution of LOS distances - large core mass model

We will now consider the behaviour of the GCs in mass model LC which has a large density core. This model shows very unusual behaviour. After 2 Gyr all GCs have apocentres which are closely clustered together with a strong peak at 1 kpc. This has become more pronounced at 10 Gyr. Detailed examination of the orbits of the GCs in individual simulations shows two behaviours. First orbits which have an apocentre outside of approximately 900 pc decay and the orbits move in quite rapidly (mostly in less than 2 Gyr) to approximately 900 pc. This behaviour confirms the work of Goerdt et al. (2006); Read et al. (2006a) which showed that massive satellites orbiting outside of an harmonic density core stall at the edge of the core. This behaviour is believed to be due to the reduction of dynamical friction due to the resonant effects of particles in the harmonic core. Second any GC which has an initial orbit within the harmonic core move *out* to the edge of the core. This behaviour is very unexpected and we do not believe that it has been reported previously though there is some evidence for orbital radii expanding again after falling in at the edge of harmonic cores in what has been called the kickback effect (Goerdt et al., 2010; Inoue, 2009). We will discuss this further in section 3.4.

3.3.2 Mass follows the light model

In order to further explore the effect of the initial orbits on the final locations of the GCs we modified the initial distribution of GC locations by sampling the initial radial distance and velocity of the GCs and filtering the simulations so that the GCs follow a Plummer distribution matching the GCs' distribution to the stellar one. This was done by filtering the results based on initial radius and velocity. The minimum distance which any GC can start from is the projected distance for that GC.

Figures 3.7 and 3.8 show the average instantaneous apocentre of the GCs for each of resulting simulations for each mass model after 2 Gyr and after 10 Gyr respectively. This

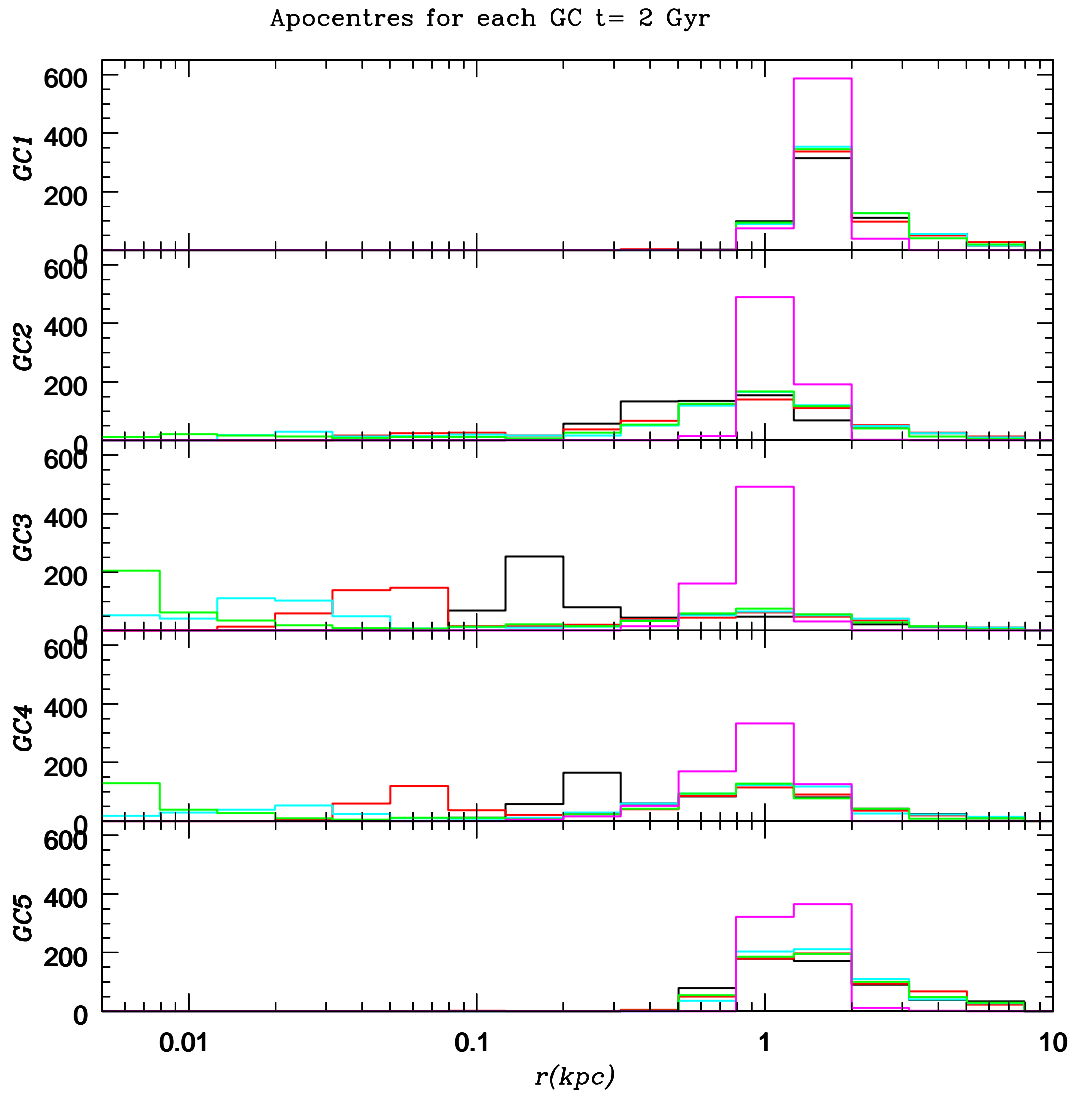


Figure 3.4: Uniform distribution of LOS distances. Plot of results for the apocentre of each Fornax globular cluster in 700 simulations after 2 Gyr. The models shown are SS (shallow core; black); IC (intermediate core; red); SC (steep cusp; cyan); BF (best fit; green); LC (Large core; magenta). See section 3.3.1.

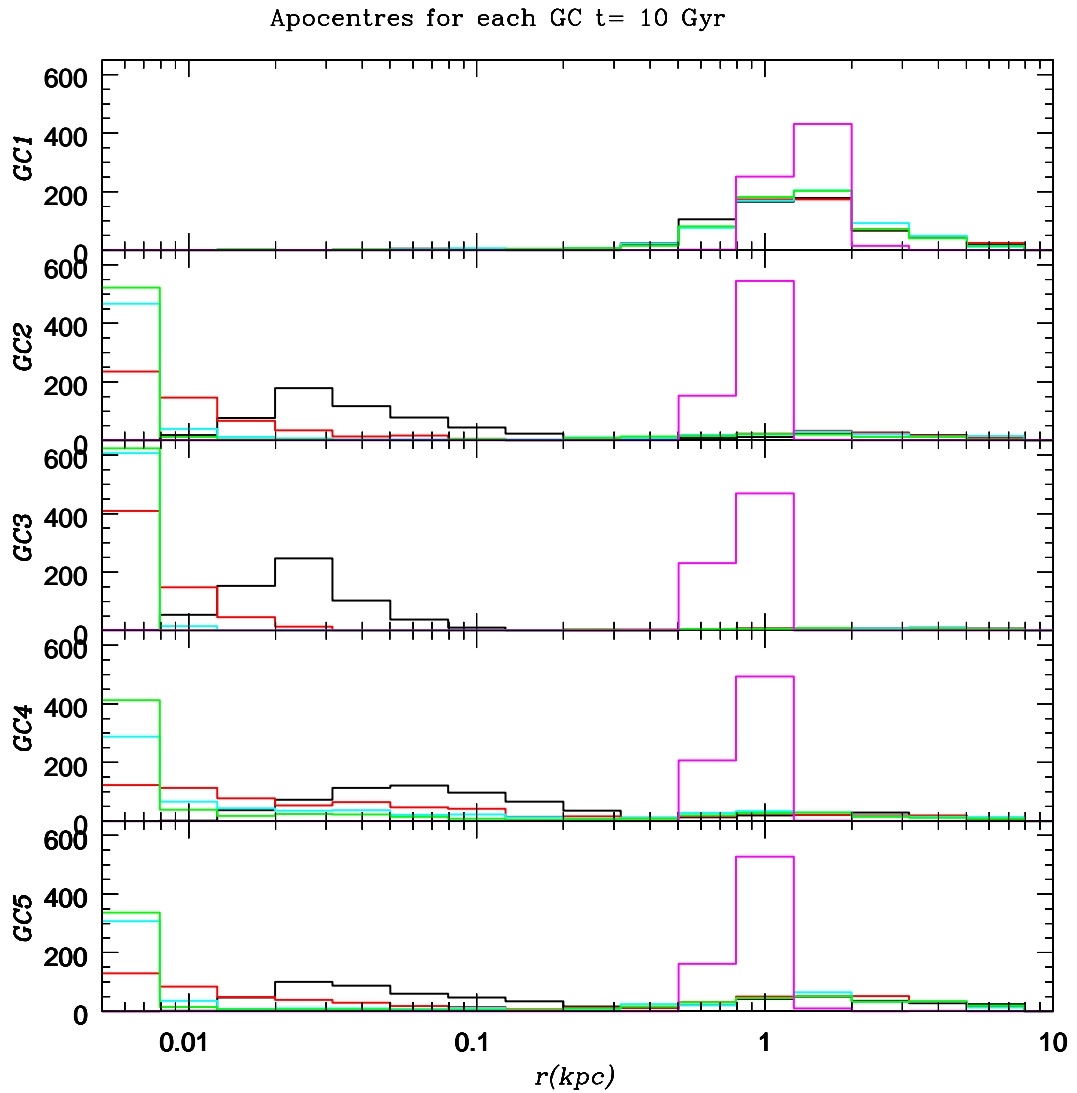


Figure 3.5: Uniform distribution of LOS distances. Plot of results for the apocentre of each Fornax globular cluster in 700 simulations after 10 Gyr. The models shown are SS (shallow core; black); IC (intermediate core; red); SC (steep cusp; cyan); BF (best fit; green); LC (Large core; magenta). See section 3.3.1.

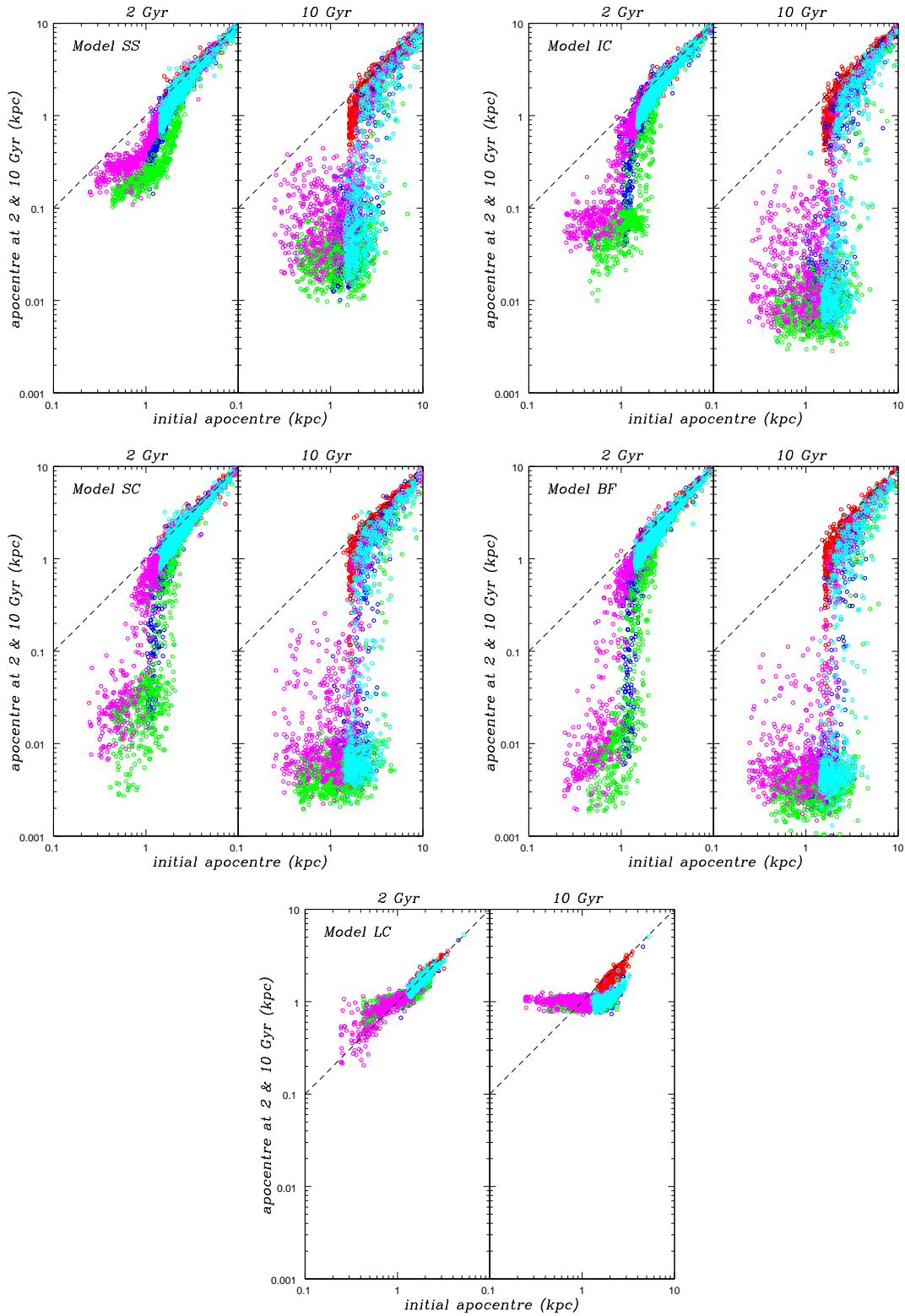


Figure 3.6: Instantaneous apocentres for all simulations by mass model with the GCs shown in different colours: red; GC1, blue; GC2 green; GC3, magenta; GC4 and cyan; GC5. The dashed line shows where the initial and later apocentres are equal.

results in a smaller sample but still large enough for the results to be significant.

The results are broadly similar to those where there is a uniform distribution of LOS distances. GCs in the cusped models SC and BF tend to fall in rapidly before 2 Gyr. Model LC with the large core shows the largest values of apocentre after 10 Gyr and the intermediate model IC show results which lie between the two extremes. The final distribution of apocentres is very similar to the results for the uniform distribution of LOS distances. This implies that over the period comparable with a Hubble time the final locations of the GCs are more sensitive to the density profile of Fornax than the initial distribution function of the GCs.

3.3.3 Initial GC position at the tidal radius of Fornax

A further variation we have tested is to look at the results if the initial distance is as large as possible to see if the current location of the Fornax GCs can be explained by a timing argument. Therefore we looked at the results sampled so that the initial apocentres of the GCs were comparable with the tidal radius of Fornax. We also applied a filter to the initial pericentres to make sure that the initial orbits were not too plunging.

We calculated the tidal radius for Fornax based on the method from Read et al. (2006b). We modelled Fornax as a spherical satellite orbiting around the Milky Way which was represented by a spherical host galaxy using a Hernquist model (Hernquist, 1990). It solves equation (7) of Read et al. (2006b) which accounts for the orbit of the satellite about the host, and the orbit of the stars within the satellite. This latter is controlled by the parameter $\alpha = [-1, 0, 1]$ for retrograde, radial and prograde orbits, respectively. We calculated a tidal radius for Fornax of between 1.8 and 2.8 kpc based on a the range of masses for Fornax given in table 3.3 using the extremal values for the the orbital data taken from Lux et al. (2010) and a total (extended) mass for the Milky Way of 1 to $2 \times 10^{12} M_{\odot}$. Figures 3.9 and 3.10 show the apocentres of the GCs for each of resulting simulations for

each mass model after 2 Gyr and after 10 Gyr respectively. The orbits were filtered so that the initial apocentres are greater than 1.75 kpc and the initial pericentres are greater than 0.5 kpc.

The results show that placing the initial GC orbit far out in the mass distribution does affect the proportion of results where the apocentre has not migrated to the centre of Fornax. This effect is particularly pronounced after 2 Gyr (Figures 3.9). At this time and with these initial conditions only a very small number of the simulations have fallen to the centre of Fornax. After 10 Gyr however we see the same behaviour as before with GC2, 3, 4 and 5 all showing a high probability that they would be found at the centre of Fornax when they are orbiting in a density distribution that has a cusped profile. One significant difference however is that a larger proportion of the simulations result in the GCs being found at large distances from the centre of Fornax. We have emphasised this by comparing the results after 10 Gyr for the SS model in Figure 3.11 which shows a comparison of the results from the uniform LOS distribution with those from our filtered distribution described above. This effect is particularly marked for GCs 2, 4 and 5 (with GC1 being largely unchanged in orbital radius). There is however still only a small probability of GC3 failing to migrate to the centre of Fornax in a cusped mass model.

We experimented with filtering more aggressively to see if we could prevent the GCs from falling to the centre of Fornax by limiting the initial apocentres and pericentres to be above minimum values. GC3 is the hardest to stop falling in in the way. For the most cusped model (BF) an initial pericentre of 1 kpc and an apocentre of 2.25 kpc ensured that all GCs except GC3 did not fall to the centre of Fornax in 10 Gyr. However to stop GC3 falling in these values needed to be changed to an initial pericentre of 0.75 kpc and an apocentre of 3.75 kpc or an initial pericentre of 1 kpc and an apocentre of 3.5 kpc. Quite similar values were found with the shallow slope model (SS).

In summary starting the GCs at a distance comparable with Fornax's tidal radius re-

sults in there being a higher probability that GCs 2 to 5 migrate to the centre of Fornax however there is now is a finite probability that the current locations can be explained by the GCs starting at the edge or even outside the Fornax system. However we need the GCs to have pericentres $\gtrsim 1$ kpc and apocentres $\gtrsim 3$ kpc to stop all the GCs falling in. To have a ratio of pericentres to apocentres consistent with the cosmological mean for accretion, we need apocentres ≈ 5 kpc. Apocentres in the range 3 kpc and 5 kpc seem unlikely given the observed distribution, however. Therefore the idea that the GCs originally orbited at large distances from the centre of Fornax may be ruled out.

3.3.4 Triaxial mass model

Figures 3.12 and 3.13 show a comparison of the results for models IC and TIC at 2 Gyr and 10 Gyr respectively. These models are identical (they are isotropic and have the same density profile) but model IC has spherical symmetry and model TIC is triaxial. Model TIC was generated using the made to measure method of Dehnen (2009) and has axis ratios of $c/a = 0.5$ and $c/a = 0.67$. It can be seen that the triaxial model TIC has led to a much reduced level of migration inwards. After 2 Gyr in most of the simulations with a triaxial halo the GCs have not fallen as far as when they are orbiting in a mass model with spherical symmetry. After 10 Gyr typically the GCs that do migrate inwards (GCs 3 to 5) have final radii of tens of parsecs and a significant number have orbits at 100 pc and more. Interestingly the number that do not migrate in is fairly similar. We conclude that triaxiality has a substantial effect on the effect of dynamical friction on satellites orbiting in any given matter distribution.

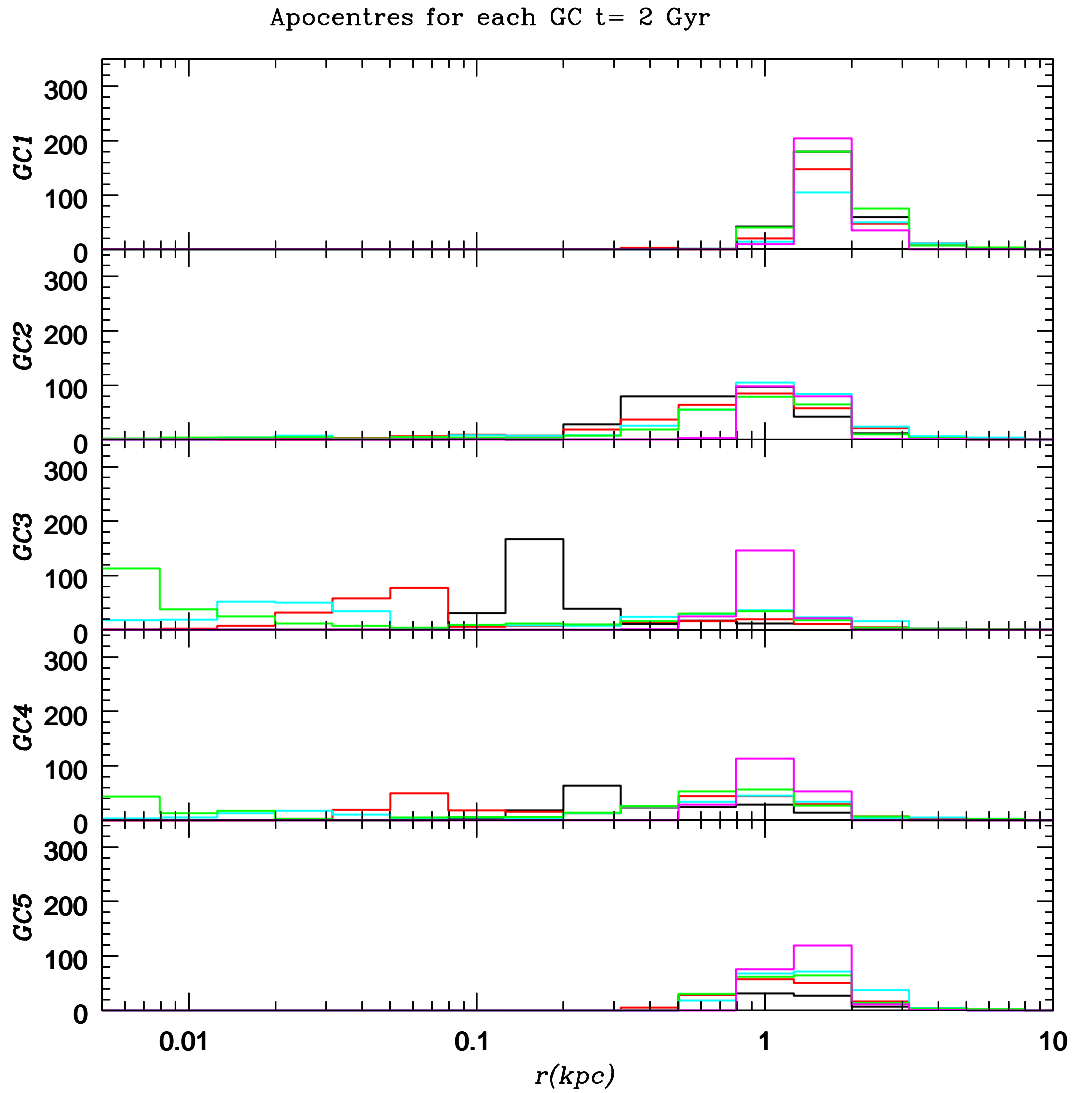


Figure 3.7: Mass follows light. Plot of results for the apocentre of each Fornax globular cluster after 2 Gyr. The models shown are SS (shallow core; black); IC (intermediate core; red); SC (steep cusp; cyan); BF (best fit; green); LC (Large core; magenta). See section 3.3.2.

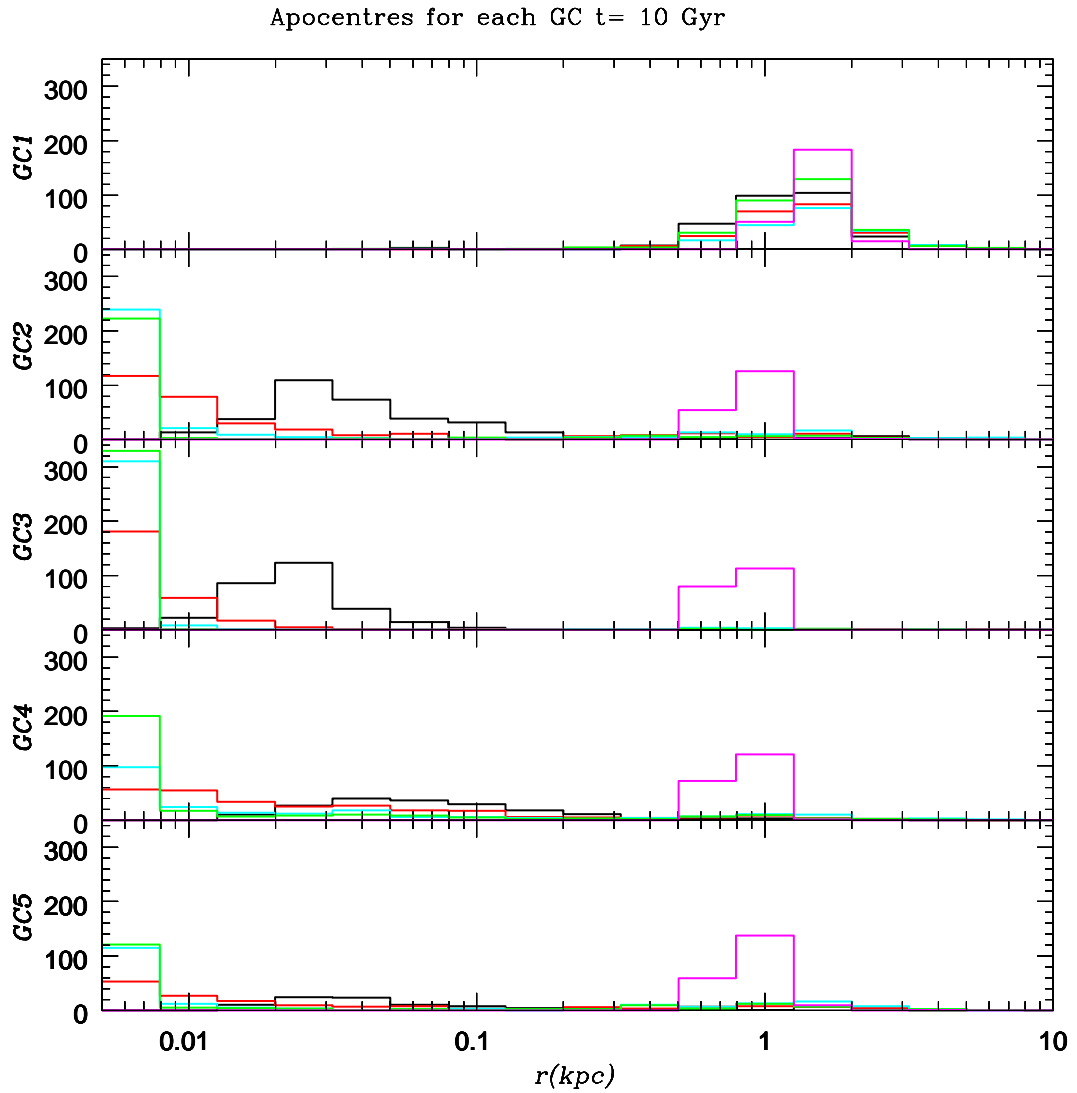


Figure 3.8: Mass follows light. Plot of results for the apocentre of each Fornax globular cluster after 10 Gyr. The models shown are SS (shallow core; black); IC (intermediate core; red); SC (steep cusp; cyan); BF (best fit; green); LC (Large core; magenta). See section 3.3.2.

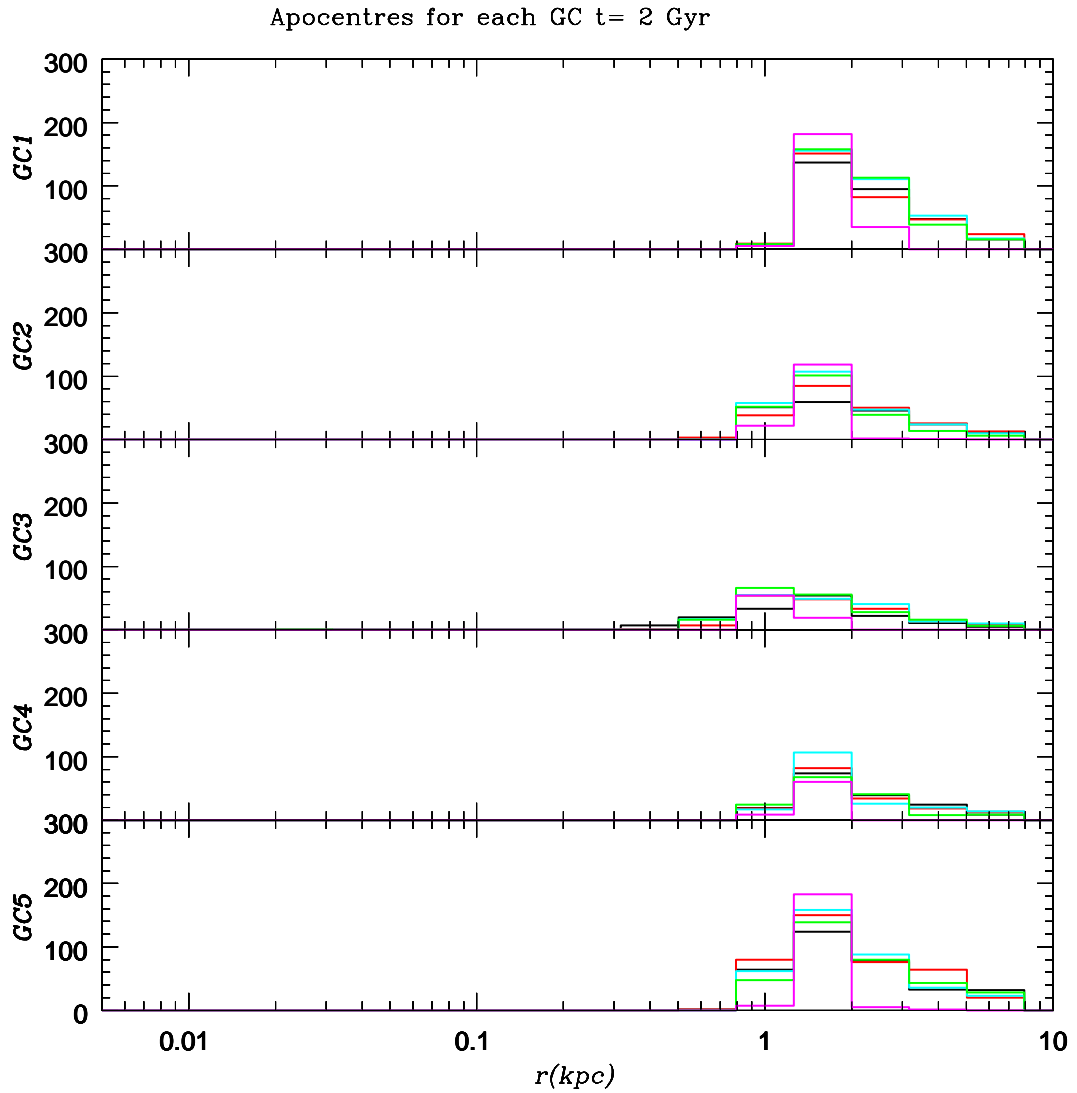


Figure 3.9: Starting on an orbit near the tidal radius. Plot of results for the apocentre of each Fornax GC after 2 Gyr. The models shown are SS (shallow core; black); IC (intermediate core; red); SC (steep cusp; cyan); BF (best fit; green); LC (Large core; magenta). See section 3.3.3.

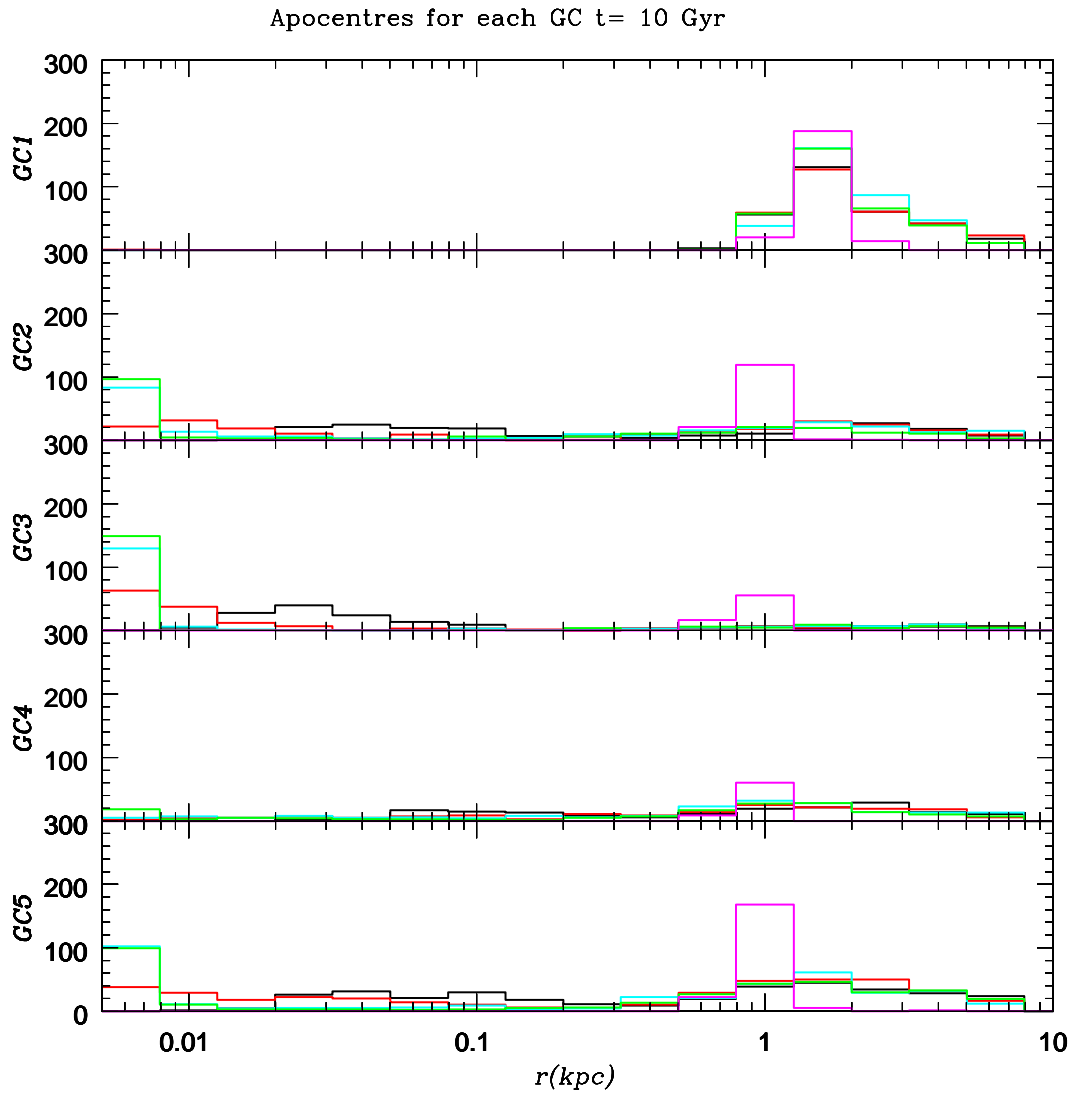


Figure 3.10: Starting on an orbit near the tidal radius. Plot of results for the apocentre of each Fornax GC after 10 Gyr. The models shown are SS (shallow core; black); IC (intermediate core; red); SC (steep cusp; cyan); BF (best fit; green); LC (Large core; magenta). See section 3.3.3.

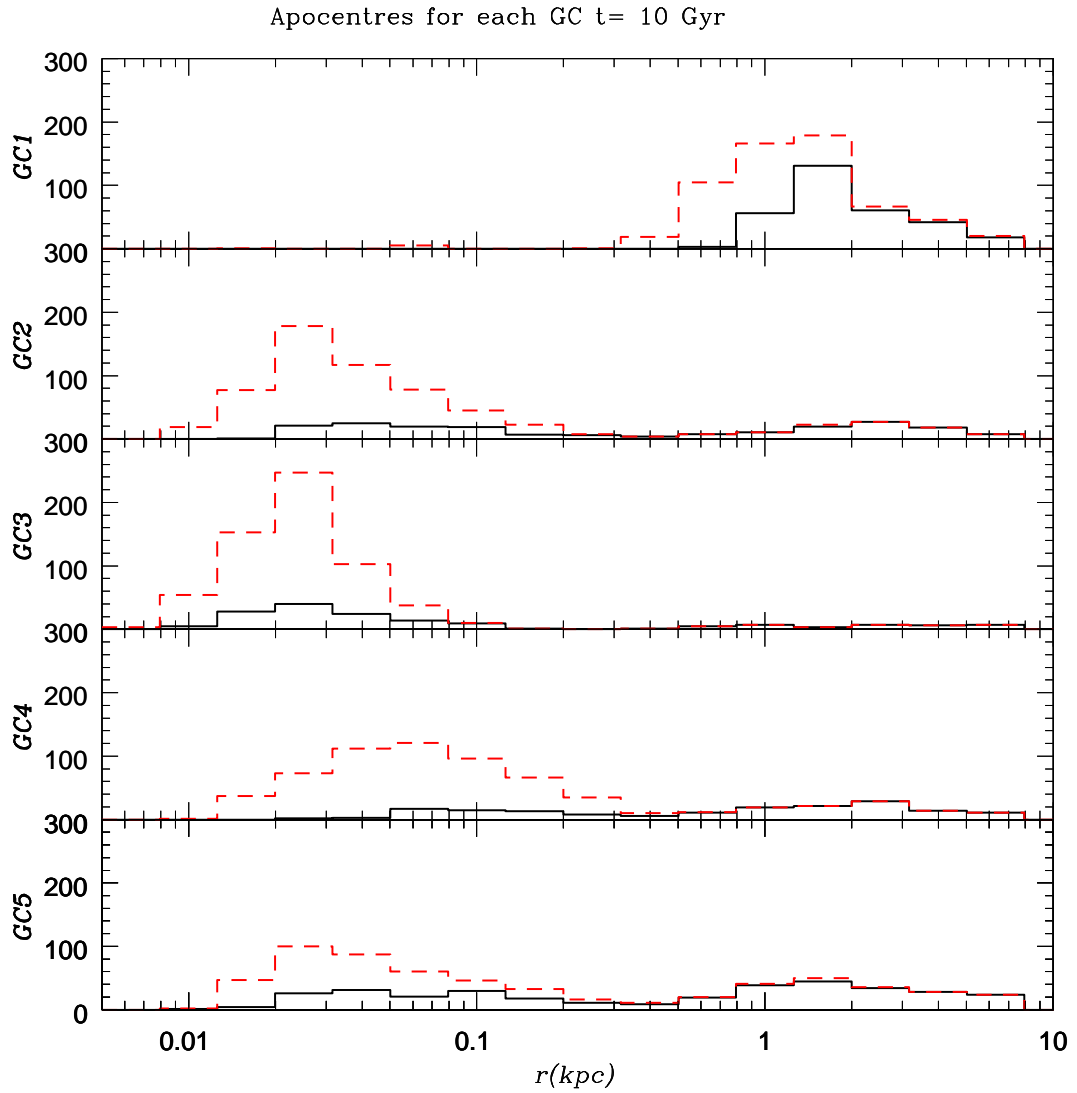


Figure 3.11: Starting on an orbit near the tidal radius. Plot of results for the apocentre of each Fornax globular cluster after 10 Gyr. The models shown is SS (shallow core) filtered so that the initial apocentre > 1.75 kpc and the initial pericentre > 0.5 kpc (black) and unfiltered (dashed red). See section 3.3.3.

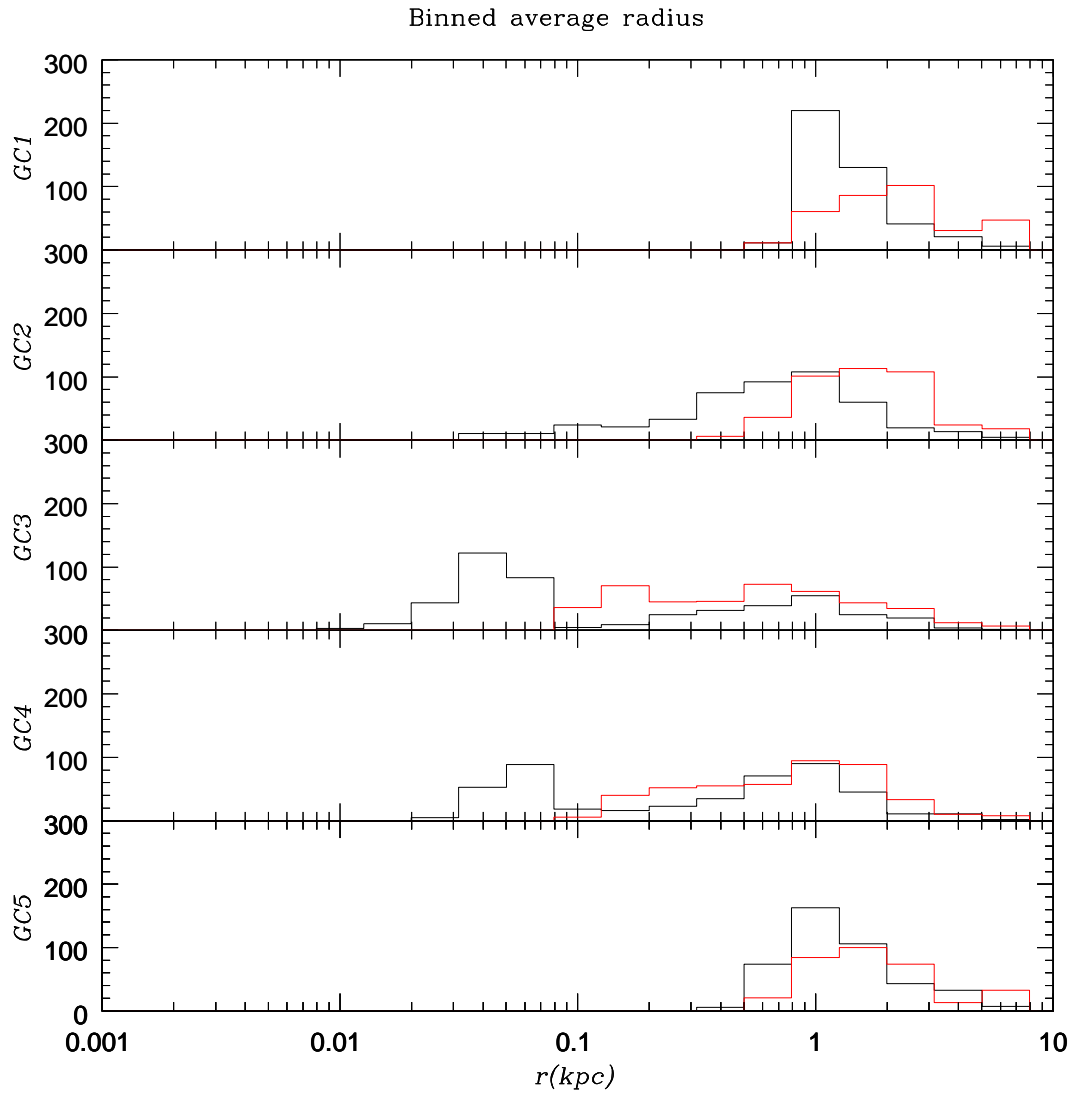


Figure 3.12: Uniform LOS distribution. Plot of results for the average final radius of each Fornax globular cluster in 700 simulations after 2 Gyr for spherical model IC (black) and triaxial model TIC (red). See section 3.3.4.

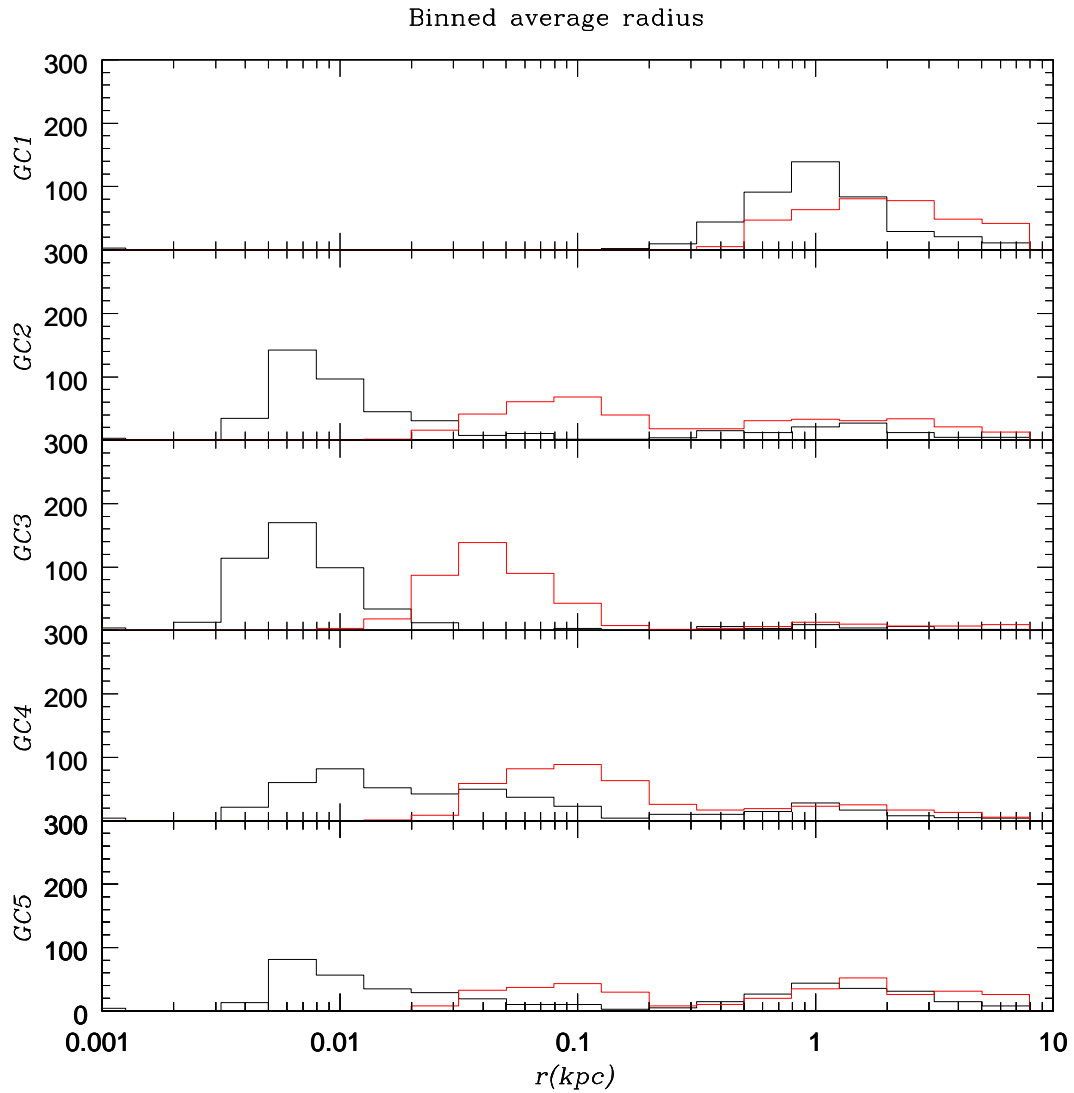


Figure 3.13: Uniform LOS distribution. Plot of results for the average final radius of each Fornax globular cluster in 700 simulations after 10 Gyr for spherical model IC (black) and triaxial model TIC (red). See section 3.3.4.

3.4 Conclusions

The Fornax galaxy is unique among the Milky Way dSphs in having five GCs at finite projected distances from its centre. These GCs are metal poor and very old comparable with the oldest GCs in the Milky Way. There is a timing problem with these GCs because it would be expected that they would fall to the centre of Fornax due to the action of dynamical friction and form a nuclear star cluster. No such star cluster is observed. Various proposals have been made to explain this and we have explored the idea that dynamical friction fails on the edge of a cored matter distribution which would cause the GCs to stall at the dark matter core radius thus providing evidence for a cored density distribution in Fornax. This would have strong implications for the way in which Fornax and other dSphs formed. Cosmological simulations based on Λ CDM predict that the density distribution of dark matter halos have a central cusp. Evidence for a cored matter distribution in Fornax would provide further impetus to find an explanation for why the predictions of Λ CDM are not always born out in practice.

We have extended previous work on what the current location of the GCs can tell us about Fornax's mass distribution in several ways. We use five mass models for the underlying potential in Fornax, we consider triaxial as well as spherical mass distributions, we use the latest data for Fornax's GCs as constraints on their phase space distribution and we run thousands of N-body models to sample the uncertainties in the GC distribution. This large grid search of the available parameter space allows us to address whether or not there are multiple solutions to Fornax's timing problem.

Our results show pronounced differences in the behaviour of GCs orbiting in the different mass models. However there are some clear trends in behaviour: cusped models have a high probability of causing the four most massive GCs to migrate to the centre of Fornax in a Hubble time. The more cored the models become the more likely it is that GCs 2 to 5 remain at a finite distance from the centre of Fornax. The mass model with a

small core with radius ≈ 100 pc keeps the GCs' orbits at tens of parsecs from the centre of Fornax. However this is not sufficient to explain the current projected distances of the GCs from its centre.

When the GCs have a uniform distribution of LOS distances the five GCs all show different behaviour. GC1 has an orbit that does not evolve greatly with time. Its location at the end of the simulations is very little changed from its initial location independent of the mass model it is placed in. GC1 tells us very little about the mass structure of Fornax. GC5's orbit does evolve and there are significant differences between its orbital behaviour in the different mass models. The final location of GC5 is bimodal with some instances of our simulations resulting in the GC falling in towards the centre of the galaxy and in others we find GC5 near its current location or even further out. Though this is true it would be difficult to draw conclusions about the mass distribution in Fornax based on its current location. In 10 Gyr GC5 has a finite probability of being found at its current projected distance from the centre of Fornax. GC2 and GC4 show significant differences between the different mass models in terms of their final distances from the centre of Fornax. GC2 and GC4 both show a very small probability of being found outside of 100 pc after 10 Gyr except for mass model LC with the large core. GC3 shows an even smaller probability of being found outside of the central regions of Fornax and in the majority of cases the inward migration has completed after 2 Gyr.

If we consider what happens if the GCs are initially located outside of the tidal radius of Fornax we find that though a fraction of the GCs fall to the centre of Fornax there is sufficiently large number that do not so that it seems possible that placing the GCs at this distance could be an explanation for their current distribution. However after examining the range of pericentres and apocentres needed to stop all the GCs falling in during 10 Gyr the ratio of apocentres to pericentres required are inconsistent with the cosmological mean for accretion. We therefore discard this as a possible explanation for the current

location of the GCs.

The mass model based on the non-parametric model of Walker and Peñarrubia (2011) shows some very interesting behaviour. Any GC starting outside the core falls in to the edge of the density core ($\lesssim 1$ kpc). However we also observe that GCs with orbits initially within the core *move out* to the edge of the core. The final instantaneous apocentres lie in the range 0.5 to 1.0 kpc. The orbital stalling may be explicable in terms of the mechanism described by Read et al. (2006a) (see also Inoue, 2009). However we are unaware of any general mechanism which would explain the dynamical “buoyancy” seen in our results. Tremaine and Weinberg (1984) carried out a thorough analytical treatment of dynamical friction in spherical systems and report that satellites moving slowly through resonance in a mass distribution with an harmonic core may have the sign of their dynamical friction reversed. We will carry out further analysis of these results to investigate the cause of this phenomenon.

Taken individually there is a strong case that the current locations of each GC cannot be explained if they orbit in a cusped mass distribution. Taken as a group it is even less likely that the GCs could be formed with the same distribution of initial locations as Fornax’s stellar component and remain at their current minimum distances. There is a high probability that the current distribution of GCs could not be sustained except in a density profile where there is a significant core out to several hundred parsecs.

Given these results it seems unlikely that the GCs could have been formed with a similar spatial distribution to the stellar component of the main body of Fornax and survived at their current projected distances except in a density profile where there is a significant core out to several hundred parsecs. In particular it is very difficult to explain the current location of GC3 other than by supposing that it is moving in a matter density distribution with a flat or very shallow profile out to several hundred parsecs.

The addition of triaxiality to the intermediate mass model IC (to create model TIC)

results in a slower and less pronounced migration inwards by the GCs. This may be a further mechanism which can help to provide an explanation for the current location of the GCs which we will explore further in future work.

Peñarrubia et al. (2009) studied the *tidal* disruption of GCs in Fornax and showed that only GC1 (see table 3.1) would be fully disrupted by Fornax's gravitational potential. This implies that GC1 is the only cluster that absolutely cannot have fallen to the centre otherwise we would not observe it at present. It does not sink to the centre of Fornax in almost all of our models, independently of the orbit distribution of GC1 or the underlying potential. This confirms that our models are consistent with observations since loosely bound clusters that pass near the centre would show no remaining trace of their existence after disruption. If there were more loosely bound clusters that we don't see now then they could have fallen to the centre of Fornax and been disrupted which implies a minimum central density for Fornax. The other clusters almost always sink to the centre unless the potential is cored or the GCs start very far out and are not on too plunging orbits. There inward motion would help to form a cored density profile and then they move out again due to the "dynamical buoyancy" effect. They would not have been disrupted because they are more tightly bound implying a maximum central density for Fornax. Thus if the potential of Fornax is cored then we can naturally understand the survival of the one loosely bound cluster GC1, and why the others haven't fallen to the centre and remained there (because the others did fall to the centre and then came out again).

If Fornax had originally had more GCs, perhaps twice as many, then the ones we do not see today would have had two possible fates. First they could have fallen in and been disrupted as described in the previous paragraph. The fact that we do not see a nuclear star cluster means that none of these potential GCs were tightly bound enough to survive. As the most massive clusters are most likely to fall in this seems unlikely. A second possible scenario is that missing GCs were tidally stripped from Fornax by the

Milky Way's gravitational potential. This is of course a possibility but our arguments rests on the fate of the observed GCs and so the existence of tidally stripped GCs does not invalidate our conclusions.

4

Can central mass concentrations prevent the formation of galactic bars?

4.1 Introduction

At least a third of all disc galaxies have strong bars and another third weak bars or oval distortions (Menéndez-Delmestre et al., 2007; Barazza, 2009; Masters et al., 2010; Nair and Abraham, 2010). These fractions increase when observing in the near-infrared, where the effect of dust and young stars is largely suppressed (Eskridge et al. 2000, Grosbøl et al. 2004). Bars can form spontaneously from an instability of the stellar disc (Miller et al., 1970; Toomre, 1981), but in reality, it seems more likely that external perturbations by interactions and mergers trigger a marginally stable stellar disc to form a bar (Byrd et al. 1986, Noguchi 1987, Berentzen et al. 2003, 2004, Gauthier et al. 2006,

Romano-Díaz et al. 2008). Bars may be considered standing spiral waves (Lynden-Bell and Kalnajs, 1972), but unlike spiral patterns they are long-lived phenomena, i.e. they are natural (non-linear) modes of rotating stellar discs and do not decay away. Theoretical considerations based on orbital dynamics imply that bars cannot extend beyond their co-rotation radius (Contopoulos, 1980; Athanassoula, 1992), and observationally determined bar pattern speeds (e.g. Kent 1987, Merrifield and Kuijken 1995, Weiner et al. 2001, Corsini et al. 2007, Zánmar Sánchez et al. 2008) suggest that bars extend almost out to their co-rotation radius, i.e. are rotating as fast as possible given their size, which is also in agreement with N -body simulations (Sellwood, 1980; Athanassoula, 1996).

Disc galaxies also often harbour central mass concentrations (CMCs) in form of super-massive black holes, central discs, and dense central star clusters. While super-massive black holes reach typically at most 0.1% of the disc mass (Magorrian et al. 1998, Ferrarese and Merritt 2000, Gebhardt et al. 2000, Kormendy and Richstone 1995), the corresponding CMC may be substantially more massive, since the black hole's gravitational influence can induce the formation of a steep central stellar cusp (Peebles, 1972; Young, 1980; Goodman and Binney, 1984; Quinlan et al., 1995; Leeuwinn and Athanassoula, 2000). By their non-axisymmetric force field bars affect the gas flow in the inner galaxy and often promote a gas-inflow (Sakamoto et al., 1999; Sheth et al., 2005), which can further add to the CMC, either in form of a nuclear gas disc or by forming stars in the central $\lesssim 100$ pc (Schinnerer et al., 2006).

The effect of a CMC on an *existing* galactic bar has been studied using N -body simulations (Norman et al., 1996; Shen and Sellwood, 2004; Athanassoula et al., 2005) with the result that a CMC affects the structure and appearance of the bar and, if it reaches several percent of the mass of the stellar disc itself, may even effectuate the destruction of the bar¹. Thus, while it is plausible that a growing CMC affects and weakens an established

¹ This result from fully self-consistent 3D N -body simulations (Athanassoula et al., 2005) is contradicted by a study of Hozumi and Hernquist (2005), who simulate a razor-thin (2D) disc without a bulge or dark-matter halo and find a CMC of only 0.5% the disc mass to destroy the bar. However, this finding is at

galactic bar, its destruction via secular growth of a CMC seems rather unlikely, albeit this may be possible when (bar-driven) gas-inflow creates a sufficiently massive CMCs (Berentzen et al., 2007).

In this study, we investigate the effect a *pre-existing* CMC has on the *formation* of a bar. This is motivated by the very real possibility that a CMC has been in place well before a stellar disc (and hence any possible bar) is established within a galaxy’s inner few kpc. The CMC could be originating from a gas-rich merger event, which may either form a dense nucleus via a starburst, or feed the growth of a super-massive black hole. (Note that contrary to some previous beliefs, a stellar-mass seed black hole may easily grow to a mass of a few $10^9 M_{\odot}$ by redshift $z = 6$, see King and Pringle 2006).

As mentioned above, bar formation may either occur spontaneously from gravitational instability, or be triggered by perturbations to the disc. Here, we will concentrate on the simpler first scenario and consider two different types of initial galaxy models. Model ‘MD’ starts with a maximum disc, i.e. the inner rotation curve is dominated by the contribution from the disc to the total gravitational attraction, while for model ‘MH’ the contribution from the halo to the rotation curve exceeds that from the disc at all radii, see Fig. 4.1 and 4.2. These models are conceptually similar to those used by Athanassoula and Misiriotis (2002), Athanassoula (2002, 2003), and Athanassoula et al. (2005), but have central dark-matter density cusps as predicted for CDM (model MH) or shallower (model MD), rather than a constant density core.

The dominance of the halo in model MH compared to model MD has two opposite effects. First, the halo reduces the importance of self-gravity for the disc and hence extends the linear instability which causes bar formation. (In low-resolution N -body simulations, this effect prevents bar formation altogether, which was used as indirect argument for the presence of massive dark-matter haloes in a bar-less galaxy, Ostriker and Peebles also at odds with observational evidence that bars can co-exist with such massive CMCs (Sakamoto et al., 1999).

1973). Second, the halo can absorb angular momentum of the bar via resonant interactions (Athanasoula, 1996, 2002, 2003; Holley-Bockelmann et al., 2005; Ceverino and Klypin, 2007). Since a bar is limited in size by its co-rotation radius, its ability to lose angular momentum is necessary for it to grow in size and strength. Without a massive dark halo, the bar can only exchange angular momentum with the outer parts of the stellar disc and hence remains small. Bars embedded in massive haloes, on the other hand, can grow to consume the whole stellar disc and grow much stronger (Athanasoula, 2002, 2003).

While a halo extenuates a bar initially but supports it eventually, a CMC only ever attenuates it, either by weakening an existing bar (as discussed above) or by hindering a bar from forming. This latter effect can be understood by the CMC moving the inner Lindblad resonance outwards (for a fixed bar pattern speed) and thus reducing the ability of the bar to form, since a linear bar-like perturbation can only exist between its inner Lindblad and co-rotation resonances (Contopoulos, 1980).

In this study, we compare the effects of a pre-existing CMC on the formation of a bar to the effect of a CMC introduced after formation of a bar in both types of galaxy models. In the linear regime of weak bar-like perturbations, these two effects are identical, so we are really looking for non-linear effects. To this end we run fully self-consistent N -body simulations. The models and numerical details are presented in section 4.2.

4.2 Modelling approach

4.2.1 The galaxy models

As already outlined in the introduction, we use two galaxy models: MD (for ‘massive disc’) and MH (for ‘massive halo’), following a terminology introduced by Athanasoula and Misiriotis (2002). Both models consist of an exponential stellar disc with density profile

$$\rho_d(R, z) = \frac{M_d}{4\pi R_d^2 z_d} \exp\left(-\frac{R}{R_d}\right) \operatorname{sech}^2\left(\frac{z}{z_d}\right), \quad (4.1)$$

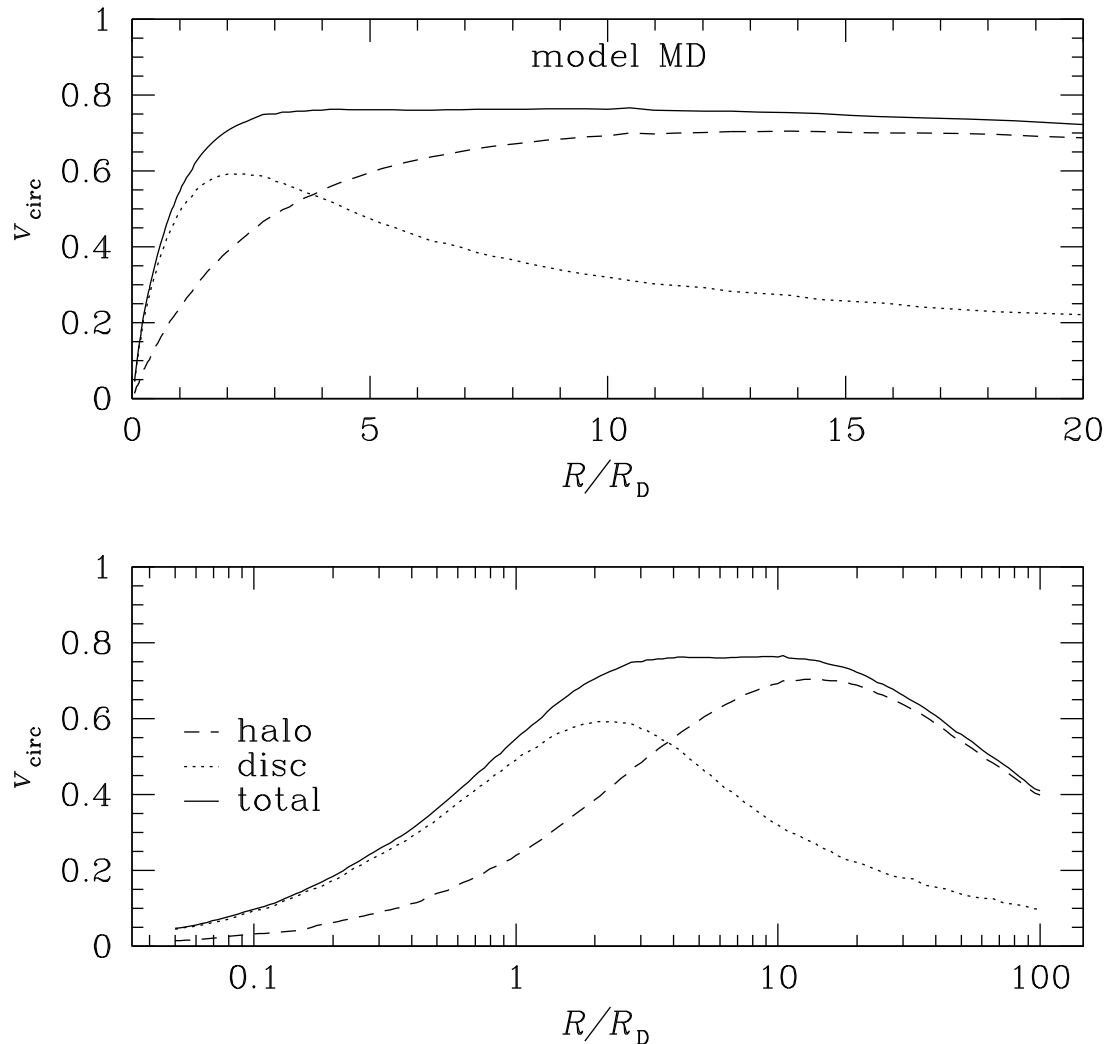


Figure 4.1: Rotation curves for a galaxy model used as initial conditions in our simulations. This is for the Model MD (“maximum disc”) galaxy model where the disc dominates the rotation curves in the inner region. Both panels show the same curves. The top one shows the rotation curves in the inner region of our model and the bottom panel shows these curves on a logarithmic scale at up to five times the radius. The solid line is the total rotation curve and the contributions from disc and halo are shown as dashed and dotted curves, respectively. Radii is given in units of the disc scale length and velocities in units of $\sqrt{GM_d/R_d}$ with M_d the total disc mass.

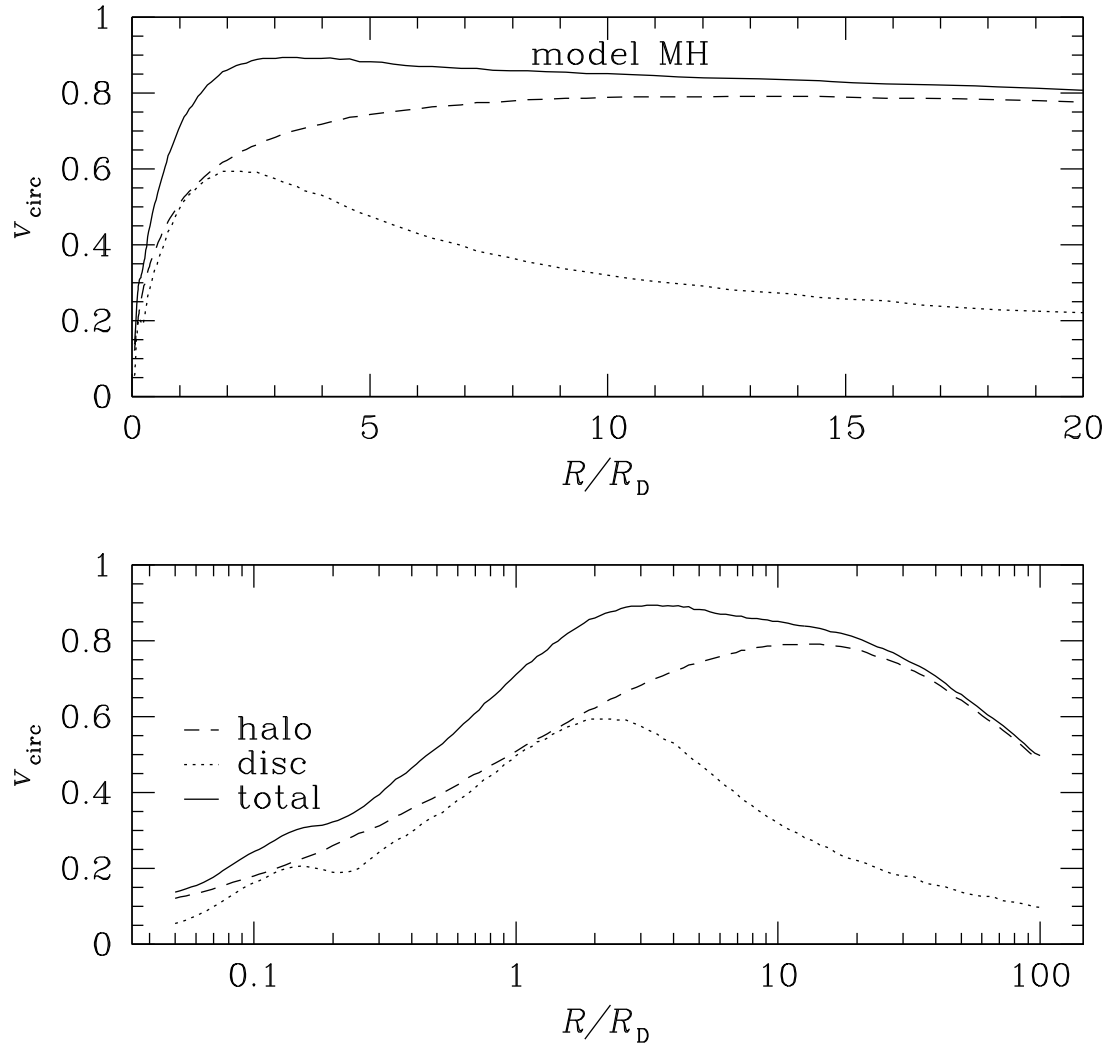


Figure 4.2: Rotation curves for a galaxy model used as initial conditions in our simulations. This is for the Model MH (“maximum halo”) galaxy model where the disc dominates the rotation curves in the inner region. Both panels show the same curves. The top one shows the rotation curves in the inner region of our model and the bottom panel shows these curves on a logarithmic scale at up to five times the radius. The solid line is the total rotation curve and the contributions from disc and halo are shown as dashed and dotted curves, respectively. Radii is given in units of the disc scale length and velocities in units of $\sqrt{GM_d/R_d}$ with M_d the total disc mass.

and a dark-matter halo, for which we adopt the density profile

$$\rho(r) \propto r^{-\gamma_0} (r^\eta + r_s^\eta)^{-(\gamma_\infty - \gamma_0)/\eta} \operatorname{sech}(r/r_t). \quad (4.2)$$

The parameter values for both models are given in Table 4.1. For model MH, the parameters for the dark-matter halo are those of a truncated Dehnen and McLaughlin (2005) model, which has a central density cusp with $\rho \propto r^{-7/9}$ as $r \rightarrow 0$ and gives an excellent fit to simulated CDM haloes, while model MD has a shallower central cusp with $\rho \propto r^{-2/9}$ and turns faster to steeper slopes at large radii (due to a larger η). We smoothly truncate both models at $r \sim r_t = 30R_d$. This reduces the number of particles at very large radii but does hardly affect the models in the range where resonant interaction with a bar may be important.

The rotation curves of both models, including the separate contributions from disc and halo, are plotted in Fig. 4.1 and 4.2. It shows that for model MH the halo contribution to v_{circ} dominates at all radii, while for model MD the halo contribution becomes important only at $r > 3.5R_d$, similar to the situation for the Milky Way today (e.g. Dehnen and Binney, 1998; McMillan, 2011).

From the mass models, self-consistent dynamical models are constructed following the method of McMillan and Dehnen (2007), which adapts the halo to the non-axisymmetric contributions of the disc gravity by adiabatically introducing them during a controlled N -body simulation. Unlike similar methods, this procedure does not seek to alter the radial density profile of the dark-matter halo to bring it into equilibrium with the disc but relaxes the halo in the potential of the disc resulting in a flatter shape. The disc velocity dispersion at each radius is set such that Toomre's $Q = 1.2$.

When generating the initial N -body model for the halo (before the aforementioned adaption to the disc non-axisymmetry), we sample positions from (4.2) and velocities from an ergodic distribution function. The resolution in the inner parts is enhanced by

increasing the sampling probability by a factor

$$g(\varepsilon) \propto \frac{1 + q r_{\text{circ}}^\eta(\varepsilon)}{r_{\text{circ}}^\eta(\varepsilon) + r_s^\eta} \quad (4.3)$$

with $q = 16$ the ratio between maximum and minimum particle mass and $r_{\text{circ}}(\varepsilon)$ the radius of the circular orbit with specific energy ε . This sampling is compensated by setting particle masses μ_i proportional to $g(\varepsilon_i)$. The particles were given individual gravitational softening lengths $\epsilon_i = 0.01(\mu_i/\bar{\mu})^{1/2}$ such that the maximum softened force exerted by each particle is a global constant. In equation (4.3) η and r_s can be chosen independently of the parameters of the same name in the mass model (4.2) but we have used the same values (see table 4.1).

For simulations with a CMC present from the beginning, the halo and disc equilibria are constructed taking the CMC gravity into account. We model the CMC by a softened N -body particle (which is allowed to move). This implies that the CMC is assumed to have spherical density

$$\rho(r) = \frac{15}{8\pi} \frac{M_{\text{CMC}} r_{\text{CMC}}^4}{(r^2 + r_{\text{CMC}}^2)^{7/2}} \quad (4.4)$$

with scale length r_{CMC} and mass M_{CMC} obeying

$$r_{\text{CMC}} = 0.1 R_d (M_{\text{CMC}}/M_d). \quad (4.5)$$

Our unit system is such that $G = M_d = R_d = 1$, which implies

$$\text{time unit} \approx 13 \left(\frac{R_d}{3.2 \text{ kpc}} \right)^{3/2} \left(\frac{M_d}{4 \times 10^{10} M_\odot} \right)^{-1/2} \text{ Myr}. \quad (4.6)$$

4.2.2 Technicalities

The N -body simulations were performed using the public N -body code `gyrfalCON` which uses the $O(N)$ force solver `falCON` (Dehnen, 2000, 2002) with minimum opening angle $\theta_{\text{min}} = 0.5$ and employs a scheme with individual adaptive time steps with minimum time-step of typically 2^{-10} time units. For some of the simulations shown in Table 4.3 we used

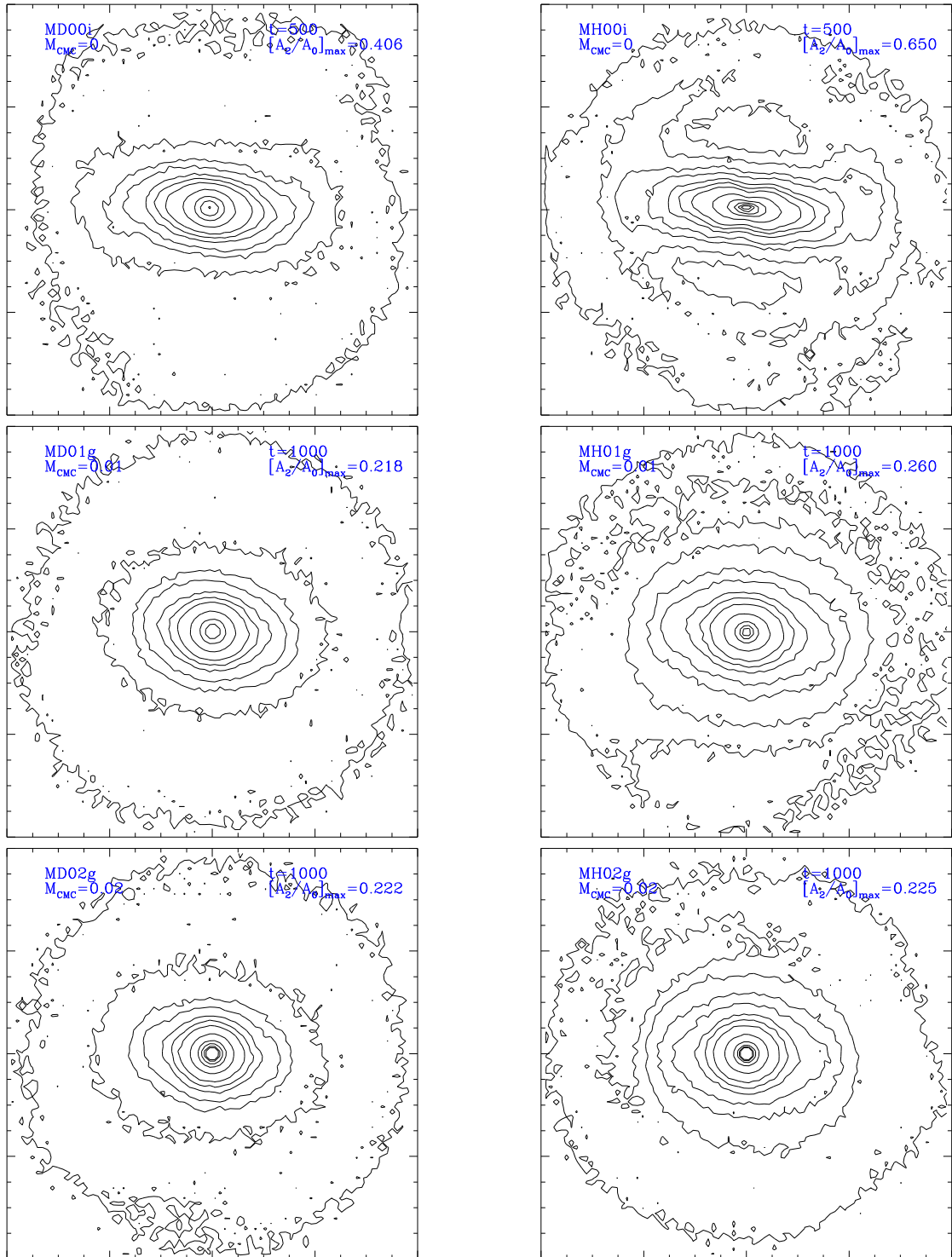


Figure 4.3: Surface density contours of the disc after 500 time units (top) for models MD (left panels) and MH (right panels). Rows 2 and 3 show the situation a further 500 time units later after the growth of a CMC at $t = 500$. The discs are oriented such that the maximum elongation occurs along the x -axis.

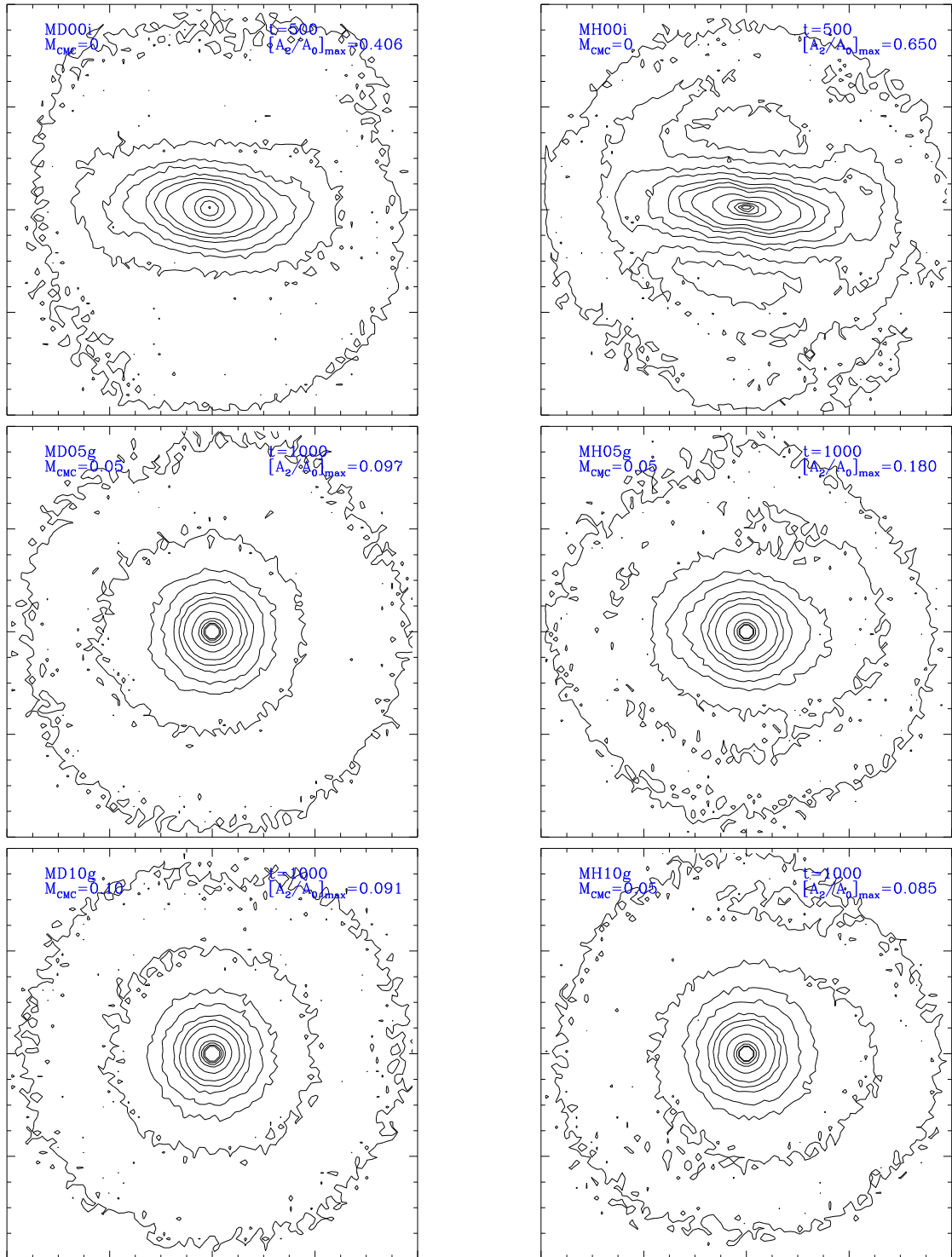


Figure 4.4: Surface density contours of the disc after 500 time units (top) for models MD (left panels) and MH (right panels). Rows 2 and 3 show the situation a further 500 time units later after the growth of a CMC at $t = 500$. The discs are oriented such that the maximum elongation occurs along the x -axis.

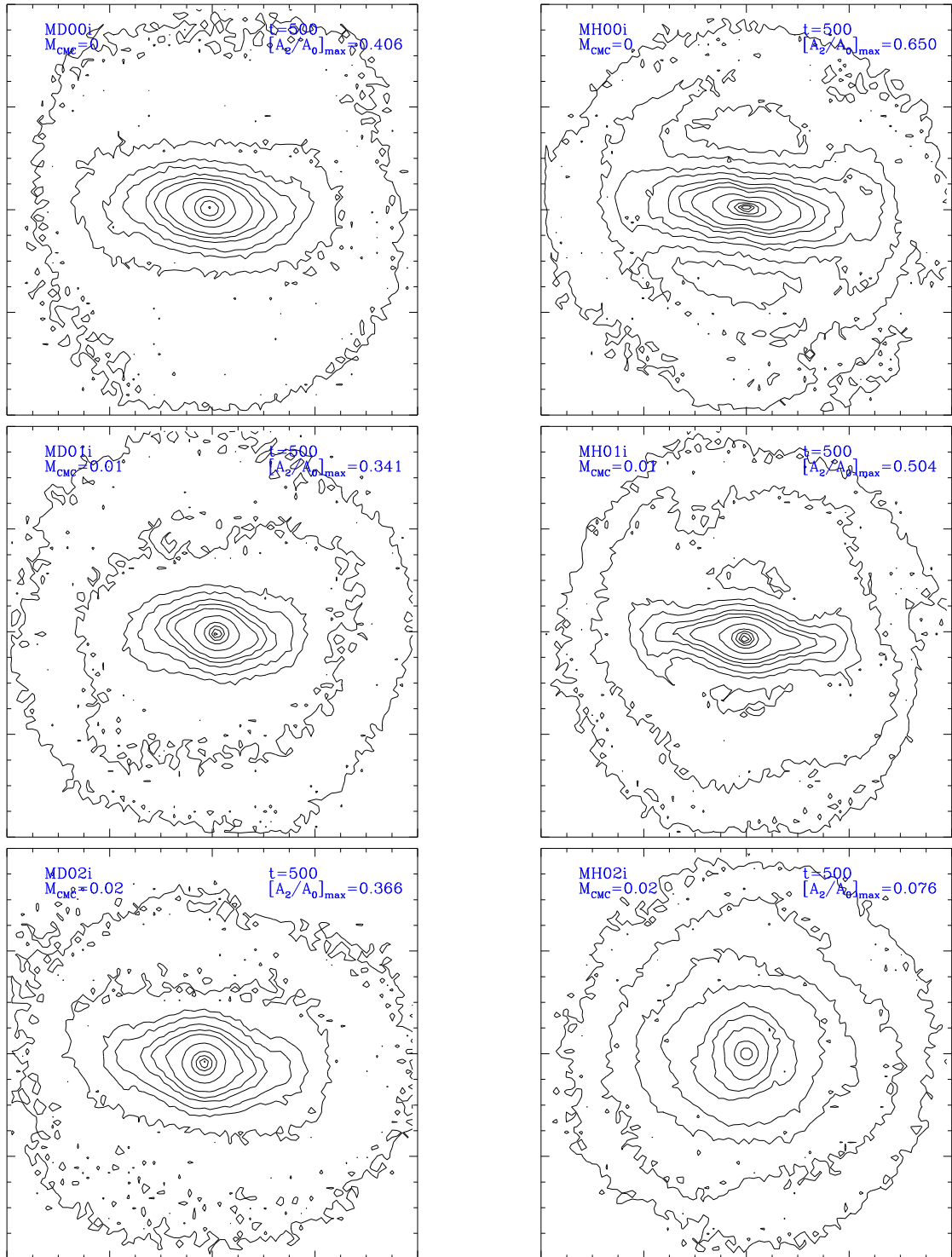


Figure 4.5: Surface density contours of the disc after 500 time units for models MD (left panels) and MH (right panels) with a CMC present from the start (except for the top row, which agrees with that of Figs. 4.3 and 4.4). The discs are oriented such that the maximum elongation occurs along the x -axis.

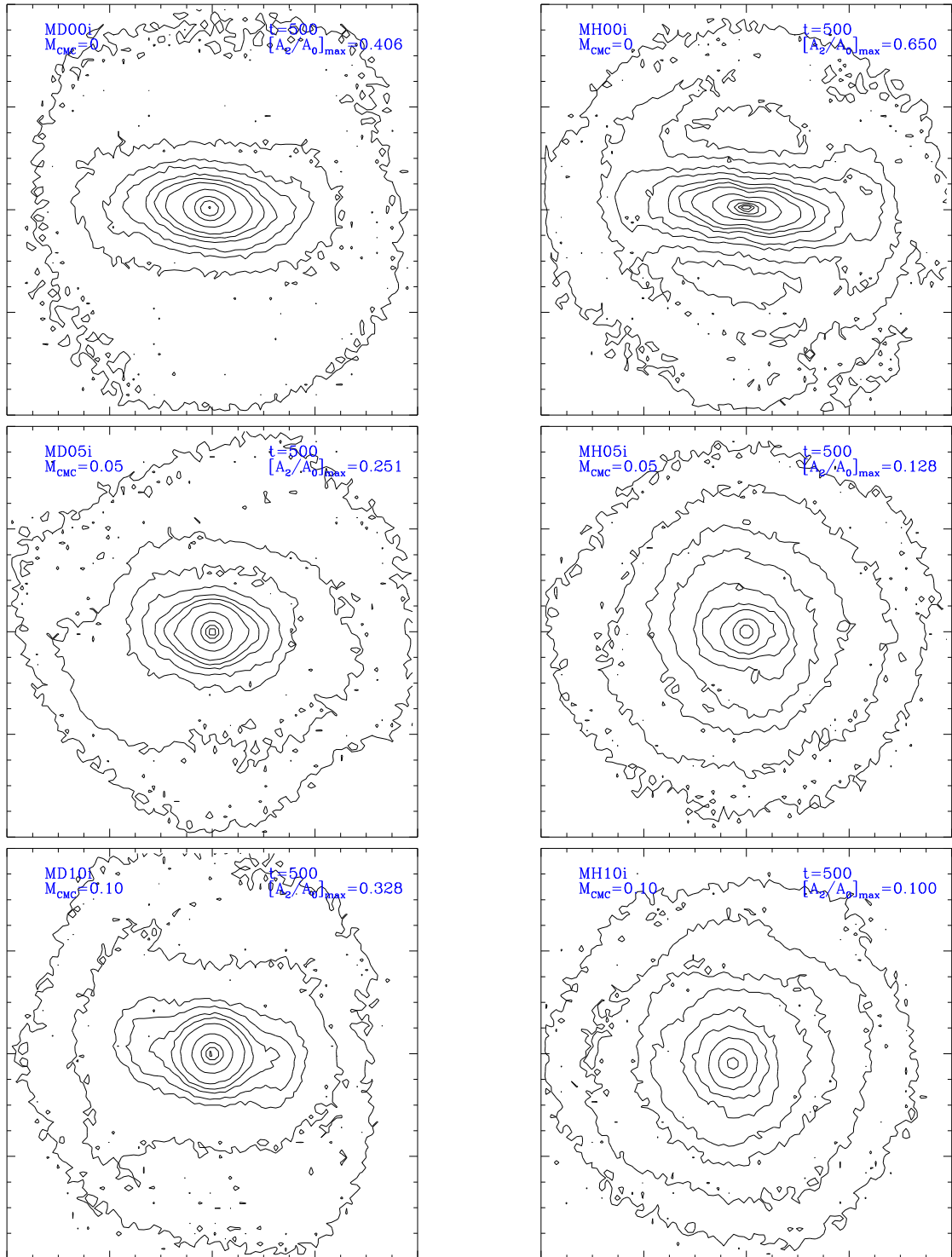


Figure 4.6: Surface density contours of the disc after 500 time units for models MD (left panels) and MH (right panels) with a CMC present from the start (except for the top row, which agrees with that of Figs. 4.3 and 4.4). The discs are oriented such that the maximum elongation occurs along the x -axis.

Model	M_d	R_d	z_d	M_h	r_s	r_t	γ_0	γ_∞	η
MD	1	1	0.1	16.8	6	30	2/9	31/9	1
MH	1	1	0.1	25.4	10	30	7/9	31/9	4/9

Table 4.1: Parameters of the two galaxy models used. M_d , R_d , and z_d are, respectively, the mass, scale length, and scale height of the stellar disc (equation 4.1). M_h , r_s , and r_t are, respectively, the total mass, scale radius, and truncations radius of the dark-matter halo, while γ_0 , γ_∞ and η parameterise its density-profile (equation 4.2), in particular $\rho_h \propto r^{-\gamma_0}$ as $r \rightarrow 0$.

shorter minimum time steps to achieve good energy conservation. The minimum time steps are shown in Table 4.3. Unless otherwise stated, we modelled the disc with 1 Mio particles of identical mass and the halo with 4.2 (MD) or 6.35 (MH) Mio particles of varying mass as outlined above.

The simulations were run for at least 500 time units, corresponding to ~ 6.5 Gyr when scaled to the Milky Way, which was typically much longer than the time (~ 150 time units) required for any bar to form. The energy was typically conserved to a few parts in 10000 (control simulations with more accurate time integration and force evaluation obtained the same results). A single run over 500 time units took about 360 CPU hours (on a single processor) in the MD case and 550 CPU hours in the MH case. (Some simulations required shorter time steps than 2^{-7} and hence more CPU time to complete.)

In order to ensure a careful modelling of the CMC, it was integrated with a time step ($\leq 2^{-11}$ time units) and its mutual forces with any other particles were approximated with a much reduced opening angle (by a factor of 0.7).

We also ran four additional simulations with increased resolution to test for convergences (the bottom four in table 4.2). For these, the number of disc particles was increased by a factor of four to 4 Mio, and the mass of the halo particles was reduced, but their number kept the same. In order to preserve the same halo profile in the inner galaxy, we used a smaller truncation radius of $r_t = 10R_d$.

name	initial	M_{CMC}	t_{start}	t_{end}	N_{d}	N_{h}
MD00i	MD	0	0	500	1 Mio	4.2 Mio
MD01i	MD+CMC	0.01	0	500	1 Mio	4.2 Mio
MD02i	MD+CMC	0.02	0	500	1 Mio	4.2 Mio
MD05i	MD+CMC	0.05	0	500	1 Mio	4.2 Mio
MD10i	MD+CMC	0.10	0	500	1 Mio	4.2 Mio
MH00i	MH	0	0	500	1 Mio	6.35 Mio
MH01i	MH+CMC	0.01	0	500	1 Mio	6.35 Mio
MH02i	MH+CMC	0.02	0	500	1 Mio	6.35 Mio
MH05i	MH+CMC	0.05	0	500	1 Mio	6.35 Mio
MH10i	MH+CMC	0.10	0	500	1 Mio	6.35 Mio
MD02iH	MD+CMC	0.02	0	1000	4 Mio	4.2 Mio
MD05iH	MD+CMC	0.05	0	1000	4 Mio	4.2 Mio
MH02iH	MH+CMC	0.02	0	1000	4 Mio	6.35 Mio
MH05iH	MH+CMC	0.05	0	1000	4 Mio	6.35 Mio

Table 4.2: Simulations with CMC present from the start. The last four simulations we run to test for convergence, but have a smaller halo truncation radius, see last paragraph of section 4.2.

4.3 Results

4.3.1 Bar Formation with a CMC present from the start

For both of the galaxy model described in section 4.2.1, we run simulations with initial CMC masses of $M_{\text{CMC}} = 0, 0.01, 0.02, 0.05$ and 0.1 , i.e. 0, 1, 2, 5, and 10 per cent of the disc mass, totalling ten simulations, see also table 4.2. In order to measure the behaviour of the disc, we perform, at each snapshot, an azimuthal Fourier analysis of the disc properties in radial annuli. In particular, we use the Fourier amplitude of the $m = 2$ component to the surface density to gauge the strength of the bar, while the pattern speed can be deduced from the evolution of the phase.

So that we can compare all our simulations we use the ratio between the amplitudes of the $m = 2$ and $m = 0$ Fourier components of the disc surface density as our estimate of bar strength thus eliminating any variations in total surface density. We find the maximum value of this ratio over the whole disc (maximum over all annuli). Figure 4.7 shows the

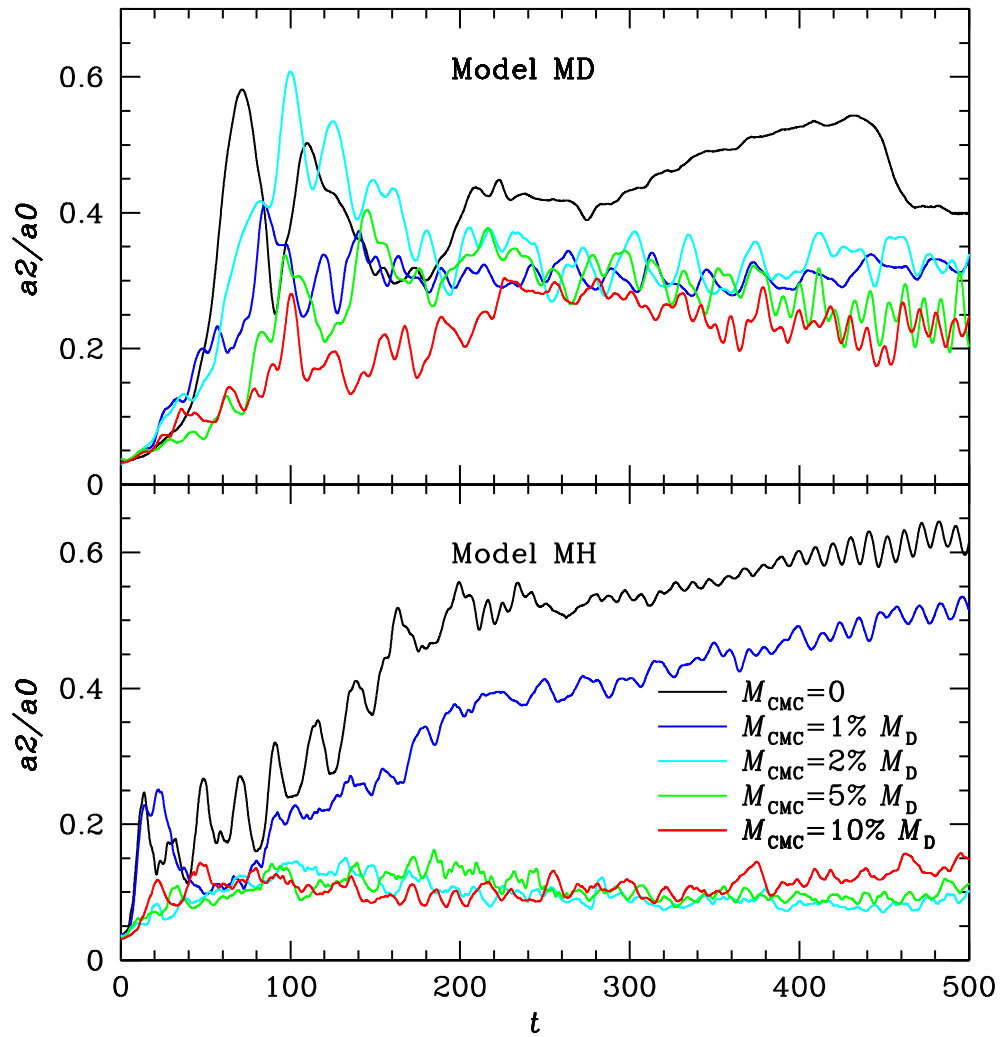


Figure 4.7: Time evolution of the ratio between the amplitudes of the $m = 2$ and $m = 0$ Fourier components of the disc surface density. See Section 4.3.1 for fuller description. The top and bottom panels show, respectively, the models MD00i to MD10i (using galaxy model MD) models MH00i to MH10i (using galaxy model MH), see table 4.2.

time evolution of this measure for the ten simulations of table 4.2 with typical resolution. Figures 4.5 and 4.6 show the surface density of the stellar discs at the final time $t = 500$. The cases without CMC (black curves) may be compared to the simulations of Athanassoula (2002).

The upper panel of figure 4.7 shows the growth of the $m = 2$ Fourier component for the model MD simulations. Several features can be noted.

All simulations form a bar and the bar strength grows readily from the start of the simulation. The simulation without a CMC forms a bar quickest and it forms the strongest bar. There is an initial peak between $t = 60$ and $t = 80$ which is followed by a deep minimum between $t = 80$ and $t = 100$ and then a second peak after $t = 100$. The deep minimum is due to a $m = 1$ asymmetry which can be seen in figure 4.11 (panel labelled $t = 100$).

The general shape of the growth of the $m = 2$ Fourier component is similar in all MD simulations. There is an initial main peak after 60 to 100 time units followed by a number of significant oscillations until the curve settle down to an approximately constant value with oscillations about a mean value. The simulation without a CMC shows the biggest difference from this pattern as it undergoes a second more extended period of secular growth between $t \approx 260$ and $t \approx 440$ before declining again and flattening out.

In general the larger the CMC the more slowly the bar forms and the weaker the bar becomes. However, as can be seen from Figure 4.5 and 4.6 the relationship between the size of the CMC and the strength of resulting bar is not completely monotonic. For instance the bar in the simulation with a CMC of mass $M_{\text{CMC}} = 2\% M_{\text{d}}$ forms a stronger bar than for the $M_{\text{CMC}} = 1\% M_{\text{d}}$ simulation. In addition the bar strength, as measured by the relative $m = 2$ Fourier component grows more quickly than the $M_{\text{CMC}} = 1\% M_{\text{d}}$ simulation. The bars in simulations with CMCs are all weakened compared to the one without a CMC.

The lower panel of figure 4.7 shows the growth of the $m = 2$ Fourier component for the model MH simulations. As with the model MD simulations we took five models with increasing CMC masses and evolved them.

The most notable result is clear from Figures 4.5 and 4.6 where it can be seen that for the three largest masses of the CMC the growth of a bar is completely suppressed. It is only where the CMC is less than 2% of the disc mass where a bar grows readily.

In the case with no CMC the bar grows from the start but not as rapidly as with the model MD simulations. Initially the model MH simulations are not prone to the the bar instability in the way the model MD simulations are due to the suppression of the disc self gravity by the stronger effect of the DM halo (Athanassoula, 2002). Significant growth of the bar is delayed until after $t = 100$.

Once the bar starts to grow there are a number of oscillations in the $m = 2$ Fourier component strength and there is an initial local peak of bar strength at about $t = 160$ ($a_2/a_0 \approx 0.55$). This is followed by a minimum and then a further maximum at $t = 200$ before a sustained period of secular growth starts until the end of the simulation. These minima are again due to $m = 1$ asymmetries caused by a spiral arm asymmetry originating on the end of the bar (as can be seen in figure 4.14 panel for $t = 200$).

A significant difference from the MD simulations is that the bar strength continues to grow after this until $t = 500$ and the bar is eventually longer and stronger than for the model MD discs ($a_2/a_0 \approx 0.65$ at $t = 500$ for the model MH simulations versus $a_2/a_0 \approx 0.406$ at $t = 500$ for the model MD simulations).

The simulations with the lowest mass CMC ($M_{\text{CMC}} = 1\% M_d$) also grows a bar. In this case the bar shows a similar pattern of growth to the simulation with no CMC but delayed until $t = 155$ and the the final value of the $m = 2$ Fourier component is significantly lower at the end of the simulation. In all other cases a bar does not form in the period of the simulation.

name	initial	M_{CMC}	t_{start}	t_{grow}	t_{end}	N_{d}	N_{h}	T_{min}
MD01g	MD+CMC	0.01	500	50	1000	1 Mio	4.2 Mio	2^{-12}
MD02g	MD+CMC	0.02	500	50	1000	1 Mio	4.2 Mio	2^{-12}
MD05g	MD+CMC	0.05	500	50	1000	1 Mio	4.2 Mio	2^{-11}
MD10g	MD+CMC	0.10	500	50	1000	1 Mio	4.2 Mio	2^{-10}
MH01g	MH+CMC	0.01	500	50	1000	1 Mio	6.35 Mio	2^{-12}
MH02g	MH+CMC	0.02	500	50	1000	1 Mio	6.35 Mio	2^{-12}
MH05g	MH+CMC	0.05	500	50	1000	1 Mio	6.35 Mio	2^{-11}
MH10g	MH+CMC	0.10	500	50	1000	1 Mio	6.35 Mio	2^{-10}

Table 4.3: Simulations with CMC present from the start. Note T_{min} is the minimum time step for a simulation.

In summary it can be seen that the presence of a CMC is potentially compatible with the growth of a bar in a galactic disc. For the model MD simulations a bar will develop in the presence of a CMC of all masses up to $M_{\text{CMC}} = 10\% M_{\text{d}}$. The bars in the simulations with the more massive CMCs have a tendency to be weaker but this is not a monotonic effect and the bars are all of similar strength. The model MH simulations show a much lower tolerance to the presence of a CMC and a bar only develops in a simulation with the lowest mass CMC ($M_{\text{CMC}} = 1\% M_{\text{d}}$). There is a strong implication that the suppression of the growth of a bar by a CMC is a non-linear effect.

4.3.2 Effect of a CMC grown in a disc with an existing bar

Several previous studies have looked at the effect if the introduction of a CMC into a disc with a pre-existing bar (Norman et al., 1996; Athanassoula and Misiriotis, 2002; Shen and Sellwood, 2004; Hozumi and Hernquist, 2005; Athanassoula et al., 2005). Generally these have shown that weaker bars are easier to destroy than stronger ones e.g. (Athanassoula et al., 2005). In order to compare our work with these studies we ran a series of simulations looking at the effect of the introduction of a CMC on the bars which developed in our simulations where no CMC was present.

We did this by taking the output from both the model MD and model MH simulations

with no CMC when a bar had evolved ($t = 500$). At this time both simulations have a bar which is sufficiently evolved for the effect of the introduction of a CMC to be studied. We then grew a CMC (in the form of an external potential) with the same range of masses used in the original simulations. The CMC potential was grown adiabatically over a period of 50 time units starting at $t = 500$. Its mass growth is given in equations 4.7 and 4.8.

$$M(t) = \left(\frac{3}{16}x^5 - \frac{5}{8}x^3 - \frac{15}{16}x + \frac{1}{2} \right) M_{CMC} \quad (4.7)$$

$$x = 2 \left(\frac{t - t_i}{t_f - t_i} \right) - 1 \quad (4.8)$$

Where $t_i = 500$ and $t_f = 550$. The details are given in Table 4.3.

The upper panel of figure 4.8 shows the growth of the $m = 2$ Fourier component for the model MD simulations. Several features can be noted. As can be seen in Figures 4.3 and 4.4 (left hand columns) the growth of a CMC destroys or significantly weakens the bar in every instance. The $M_{CMC} = 1\% M_d$ and $M_{CMC} = 2\% M_d$ simulations have a significant effect on the strength of the bar. The maximum strength of the bar reduces gradually over the period of the simulations leaving the bar weakened but not completely destroyed and bar strength is reduced to about half its initial value. The final surface density for the simulations with CMCs of mass $M_{CMC} = 1\% M_d$ and $M_{CMC} = 2\% M_d$ shows the bar has been reduced to a mildly oval bulge.

The introduction of the $M_{CMC} = 5\% M_d$ and $M_{CMC} = 10\% M_d$ CMCs have an immediate effect on bar strength which rapidly declines. By 60 time units after the introduction of the CMC the bar has essentially been destroyed in both cases though it takes a further 200 time units for the bar to fully dissipate in the simulation with a CMC of mass $M_{CMC} = 5\% M_d$.

The lower panel of figure 4.8 shows the growth of the $m = 2$ Fourier component for the model MH simulations. As can be seen in Figures 4.3 and 4.4 (right hand column) the introduction of a CMC has a similar effect to those seen in the model MD simulations. The

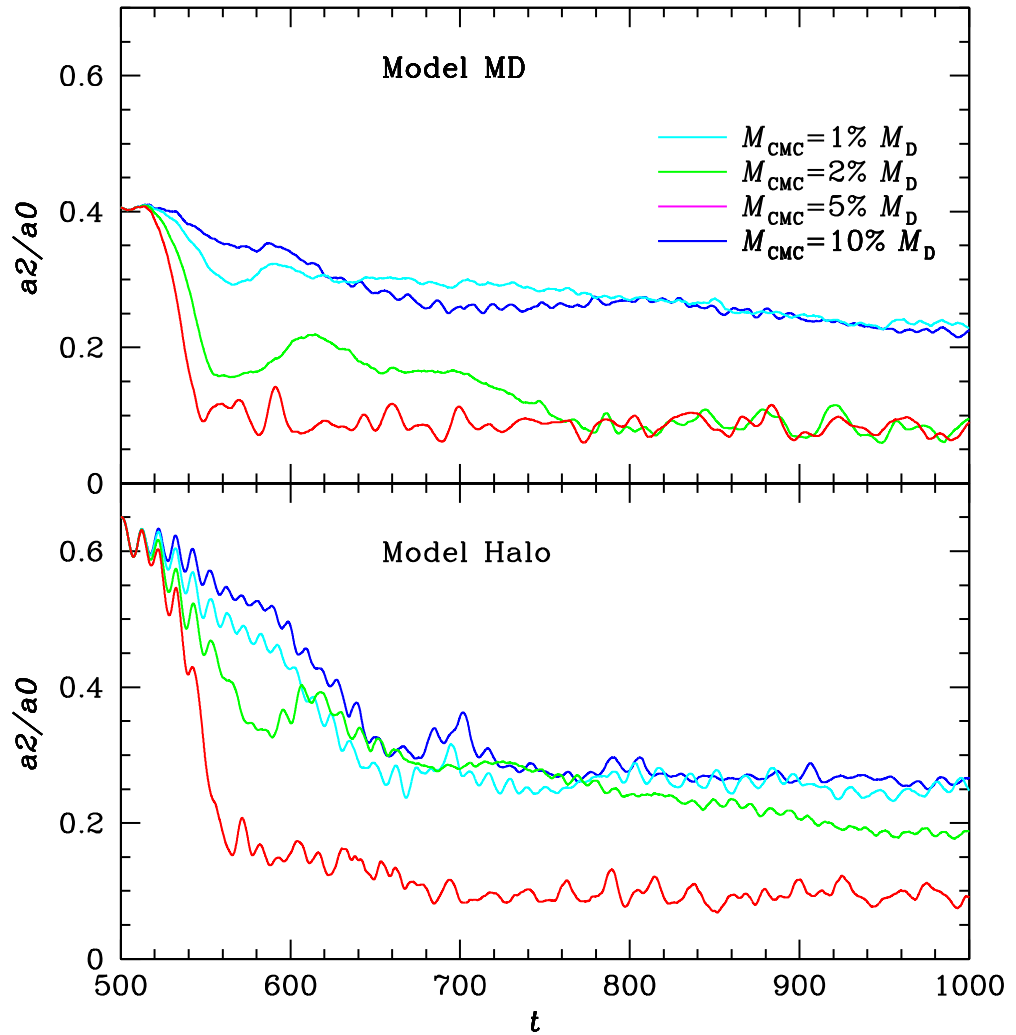


Figure 4.8: Simulations where a CMC is grown in a disc with a pre-existing bar. Time evolution of the (maximum over all annuli for) ratio between the amplitudes of the $m = 2$ and $m = 0$ Fourier components of the disc surface density. The top and bottom panels show, respectively, the models MD01g to MD10g (using galaxy model MD) models MH01g to MH10g (using galaxy model MH), see table 4.3.

initial bar is stronger than for the model MD simulations but the reduction in bar strength is relatively as great. In all cases the introduction of the CMC reduces the strength of the bar and in the case of the $M_{\text{CMC}} = 10\% M_{\text{d}}$ that the bar is destroyed.

The results for the introduction of a CMC are broadly in agreement with those found by Athanassoula et al. (2005). However particularly in the simulation where a CMC of mass $M_{\text{CMC}} = 1\% M_{\text{d}}$ is introduced the bar is reduced to such an extent that it is virtually destroyed. Our results indicate that a CMC of significantly lower mass than found in previous work can destroy a bar.

4.3.3 Comparison of methods of CMC growth

If we compare the results in Section 4.3.1 and 4.3.2 we see that there is a difference in the effect of a CMC depending on how it is introduced. In model MH simulations a CMC with a mass of 2% of the disc mass suppresses bar development when present prior to a bar forming. When a CMC of this mass is grown in a disc containing an evolved bar a weak bar remains. Thus the CMC has a bigger effect on the development of a bar than when destroying an evolved bar. For model MD simulations a CMC of 10% of the disc mass does not stop a bar developing (when present before a bar develops) whereas the introduction of a CMC of 5% of the disc mass destroys an evolved bar. Thus we see a difference in the effect of a CMC in our two different types of models (MD and MH).

In the model MD simulations there is a larger effect on a bar when a CMC is introduced to a pre-existing bar than when the bar grows with the CMC present. The CMCs with masses $M_{\text{CMC}} = 1\% M_{\text{d}}$ and $M_{\text{CMC}} = 2\% M_{\text{d}}$ have the smallest effect on the bar in both cases. However the relative strength of the bar is lower when the CMC is introduced than when it is present from the start. In the $M_{\text{CMC}} = 10\% M_{\text{d}}$ case and the $M_{\text{CMC}} = 5\% M_{\text{d}}$ case the bar is destroyed when a CMC is introduced to a disc with an existing bar *but* fail to suppress the bar when present before a bar is formed.

In the model MH simulations a reverse effect can be seen. Again the $M_{\text{CMC}} = 10\% M_{\text{d}}$ suppresses the bar in both cases but the other cases all show differences. In the case of the least massive CMC ($M_{\text{CMC}} = 1\% M_{\text{d}}$), the effect of the presence a CMC prior to bar formation is very small, and the disc develops a strong bar. However there is significant weakening of the bar when a CMC is introduced once the bar has formed. In the $M_{\text{CMC}} = 2\% M_{\text{d}}$ model the presence a CMC suppresses the formation of a bar. When a CMC of mass $M_{\text{CMC}} = 2\% M_{\text{d}}$ is introduced the bar is significantly weakened but not destroyed.

Our results imply that the CMC affects bar dynamics through different mechanisms in the two scenarios. When a CMC is present prior to bar formation, the model MH simulations appear to be more susceptible to the suppression of the bar by the CMC compared to the massive disc model. On the other hand when a CMC is introduced after the formation of a bar the model MD simulations are more susceptible to bar dissolution compared to the MH model.

4.3.4 Pattern speed CMC present from the start

A bar in a disc represents an non-axisymmetric distortion of the mass distribution in the disc with an $m = 2$ Fourier component symmetry. The angular speed Ω with which this distortion rotates is called the pattern speed. We measured the pattern speed of the bars in our simulations. The upper panel of figure 4.9 shows the evolution of the pattern speed of the bars for the model MD simulations discussed in section 4.3.1.

For the simulation without a CMC the pattern speed is quickly established. There is an initial peak corresponding to the initial peak in the $m = 2$ Fourier component followed by a minimum at $t = 110$ and then a decline during the remainder of the simulation as the bar strengthens. The simulation where $M_{\text{CMC}} = 1\% M_{\text{d}}$ shows a similar behaviour but at a higher pattern speed corresponding to its weaker $m = 2$ Fourier component. Other

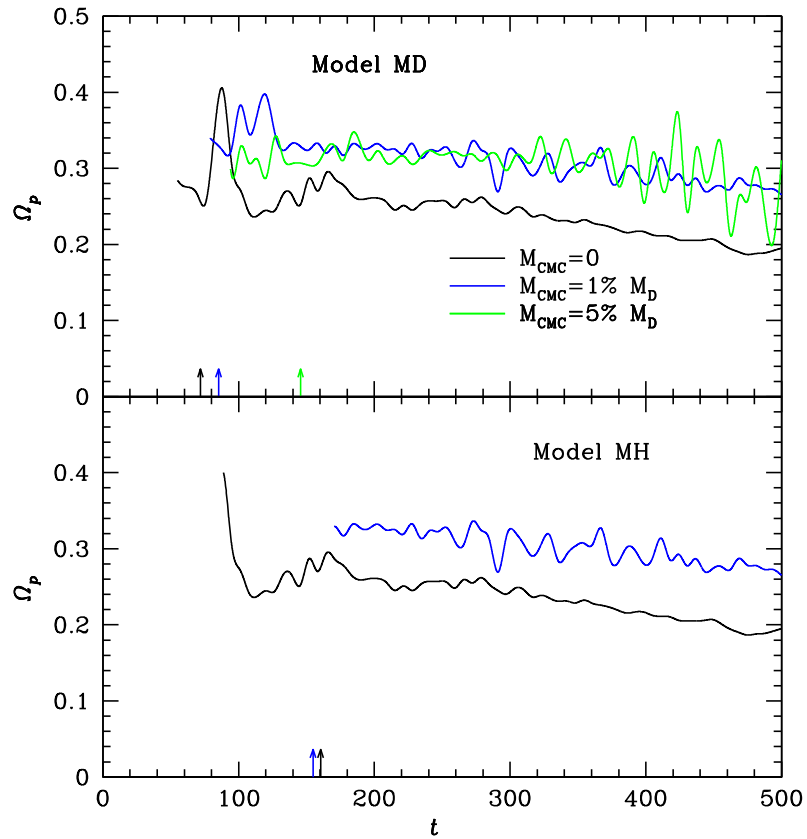


Figure 4.9: The upper panel shows the pattern speed for three typical cases of the MD simulations in units of radians per time unit. The mass of the CMC is given as a percentage of the disc mass. The arrows on the time axis mark the peak of the first major maximum value of the $m = 2$ Fourier component of the disc's surface density. The lower panel shows the pattern speed for the two MH simulations where a bar forms. As above the arrows on the time axis mark the peak of the first major maximum value of the $m = 2$ Fourier component of the disc's surface density.

simulations show this behaviour (the $M_{\text{CMC}} = 5\% M_{\text{d}}$ case is also shown for comparison).

Previous studies have found that when CMCs are introduced into discs with pre-existing bars the pattern speed increases as the bar weakens (Norman et al., 1996; Athanassoula et al., 2005). In addition when larger CMCs have produced weaker bars they have higher pattern speeds. One feature that can be seen in the $M_{\text{CMC}} = 0$ and $M_{\text{CMC}} = 1\% M_{\text{d}}$ simulations is that there is a peak in the pattern speed just after the initial peak in the maximum value of the $m = 2$ Fourier component of the disc's surface density. This corresponds to a minimum in the $m = 2$ Fourier component which occurs just after its initial peak emphasising the fact that the pattern speed increases as the bar weakens.

The lower panel of figure 4.9 shows the evolution of the bar's pattern speed for the model MH discs. For the simulation without a CMC the pattern speed is established by $t = 140$ and then declines until the end of the simulation. There is a steady fall throughout the remainder of the simulations. For the simulation where $M_{\text{CMC}} = 1\% M_{\text{d}}$, the pattern speed is established by $t = 230$ and then falls in a similar manner to the simulation without a CMC. Its pattern speed is always higher.

4.3.5 Pattern speed CMC is grown in a disc with an existing bar

We will now consider the development of the pattern speed for the simulations where a CMC is grown in a disc with an evolved bar. The upper panel of figure 4.10 shows the evolution of the pattern speed of the bar for all model MD simulations. For the simulations with $M_{\text{CMC}} = 1\% M_{\text{d}}$ and $M_{\text{CMC}} = 2\% M_{\text{d}}$ the pattern speed remains constant over the period of the simulation. The introduction of a CMC has had little effect on the pattern speed in these cases. For the simulations with $M_{\text{CMC}} = 5\% M_{\text{d}}$ and $M_{\text{CMC}} = 10\% M_{\text{d}}$ the pattern speed rises rapidly initially as the bar weakens until the bar is destroyed.

Comparing these results to the ones in sections 4.3.1 and 4.3.2 it can be seen that generally the pattern speed correlates inversely with the bar strength. The pattern speed

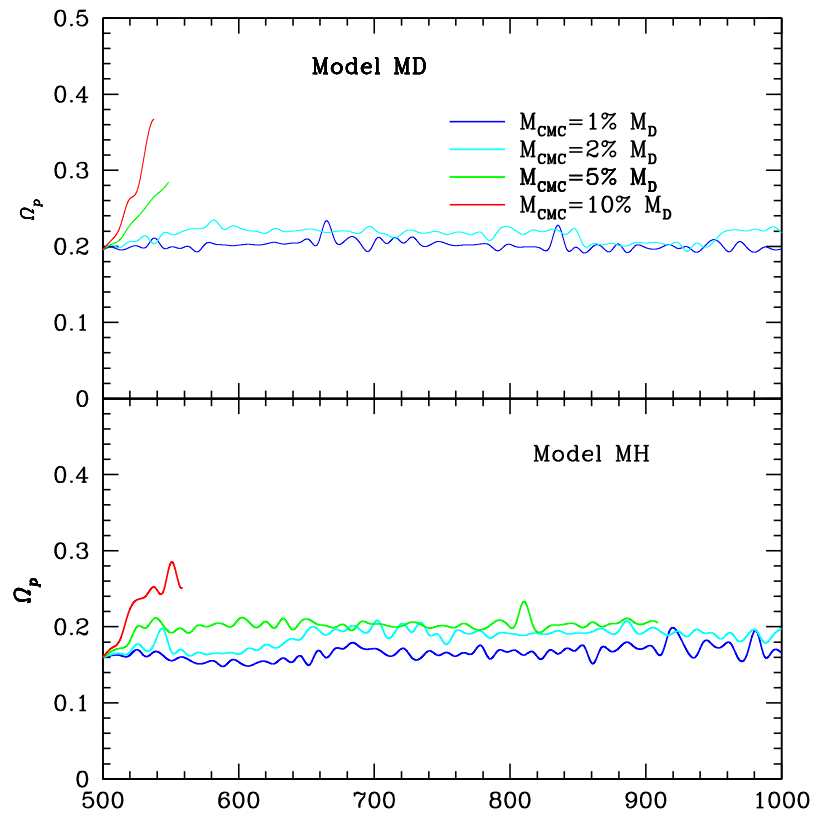


Figure 4.10: The upper panel shows the pattern speed for the MD simulations when a CMC was introduced into a disc with an existing bar. The units are radians per time unit. The mass of the CMC is given as a percentage of the disc mass. The lower panel shows the same plots for the MH simulations.

rises as a result of the bar decaying before the bar becomes too weak for us to measure a pattern speed.

The lower panel of figure 4.10 shows the evolution of the pattern speed for the model MH simulations. For the simulations with $M_{\text{CMC}} = 1\% M_{\text{d}}$, $M_{\text{CMC}} = 2\% M_{\text{d}}$ and $M_{\text{CMC}} = 5\% M_{\text{d}}$ the pattern speed rise slightly initially and then remains constant over the period of the simulation. For the simulations with $M_{\text{CMC}} = 10\% M_{\text{d}}$ the pattern speed rises rapidly just prior to the bar being destroyed.

4.3.6 Evolution with a CMC vs CMC introduction

Past studies have shown (Norman et al., 1996; Athanassoula et al., 2005) that as a bar grows in strength its pattern speed falls. Bars grow through the exchange of angular momentum between particles in the bar forming region of the disc and with resonant particles in the outer disc and DM halo. The inner disc particles are exchanging angular momentum which is absorbed by particles in the outer disc and DM halo. The bar grows in strength as more particles come into resonance with material further out in the outer disc and DM halo. The bar slows down because the particles at the extremities of the bar will have a lower angular speed. We have found that when a CMC is introduced there is an initial increase in pattern speed as the bar weakens but then the pattern speed remains approximately constant.

One explanation for this effect is the fact the the bar length does not change greatly even though the strength of the $m = 2$ Fourier component weakens considerably. When a bar is growing it gains length through more disc mass coming into resonance with material in the outer disc and DM halo. This means that the bar slows as it grows in length and strength. When it is weakened by the introduction of a CMC material is scattered from the bar by the influence of the CMC, but some material remains in resonance with the outer disc and halo, maintaining the bar speed at lower levels. Examination of the effect

of the CMC on bar strength shows that the bar is weakened from the inside outwards, preserving the bar further out and maintaining pattern speed.

4.4 Development of the Size and Shape of Bar

We will now consider some of the key changes in the bar morphology as bars develop or fail to do so. First we will consider the development of our two models (MD and MH) with no CMC and then look at some key models which have a CMC to see what differences the CMC makes.

4.4.1 Development of bars with no CMC

Figures 4.11 and 4.12 show density maps of the disc illustrating its evolution for the model MD simulation². The bar forms early in this case and is clearly visible by $t = 50$, though it does not have a boxy shape, and there is a large number of flocculent trailing spirals in the outer disc. The disc is still thin and shows no vertical structure. By $t = 100$ the bar has become asymmetric and the height of the disc has increased. There is a strong $m = 1$ Fourier component asymmetry visible in the spiral arms. At $t = 150$ the bar has a regular oval shape though the spiral arms have strong asymmetric features. The vertical height of the bar has increased further and buckling is clearly visible in the side on view.

Buckling plays an important role in the development and evolution of numerical stellar bars (see section 4.5.1). It is sometimes followed by a second episode of buckling (Martinez-Valpuesta et al., 2006) which occurs here. At $t = 500$ the bar is very prominent and has a softened boxy shape with significant vertical asymmetry. The bar is approximately 4 scale radii long.

²All of the density maps shown in this chapter were produced using glnemo an interactive visualization 3D program for N -body snapshots. Glnemo copyright Jean-Charles Lambert at The Astronomy Observatory of Marseilles Provence.

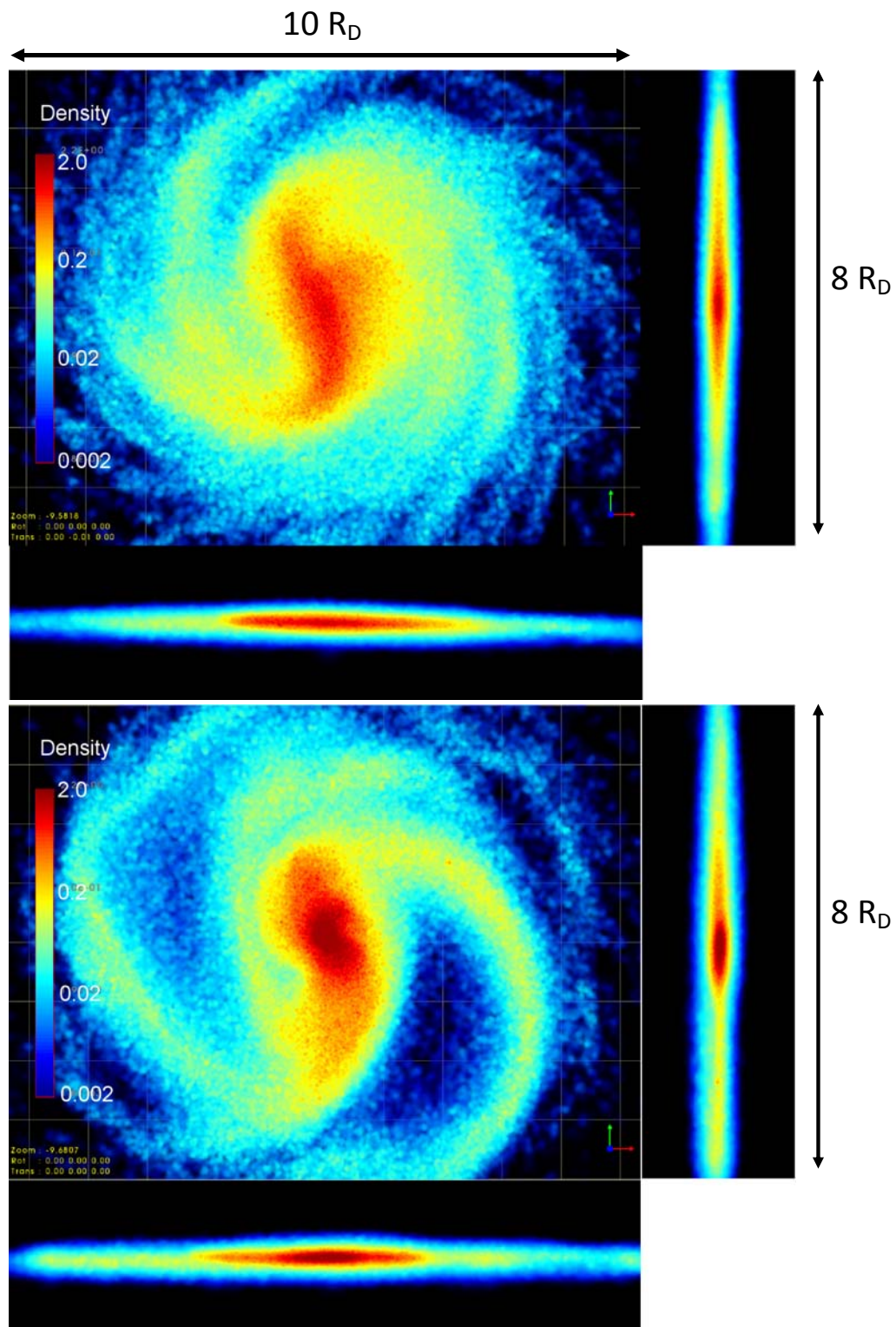


Figure 4.11: Model MD without a CMC. Density map for $t = 50$ (top) and $t = 100$ (bottom). Each set of density maps consists of face on view with bar side view underneath and bar end on view at the side.

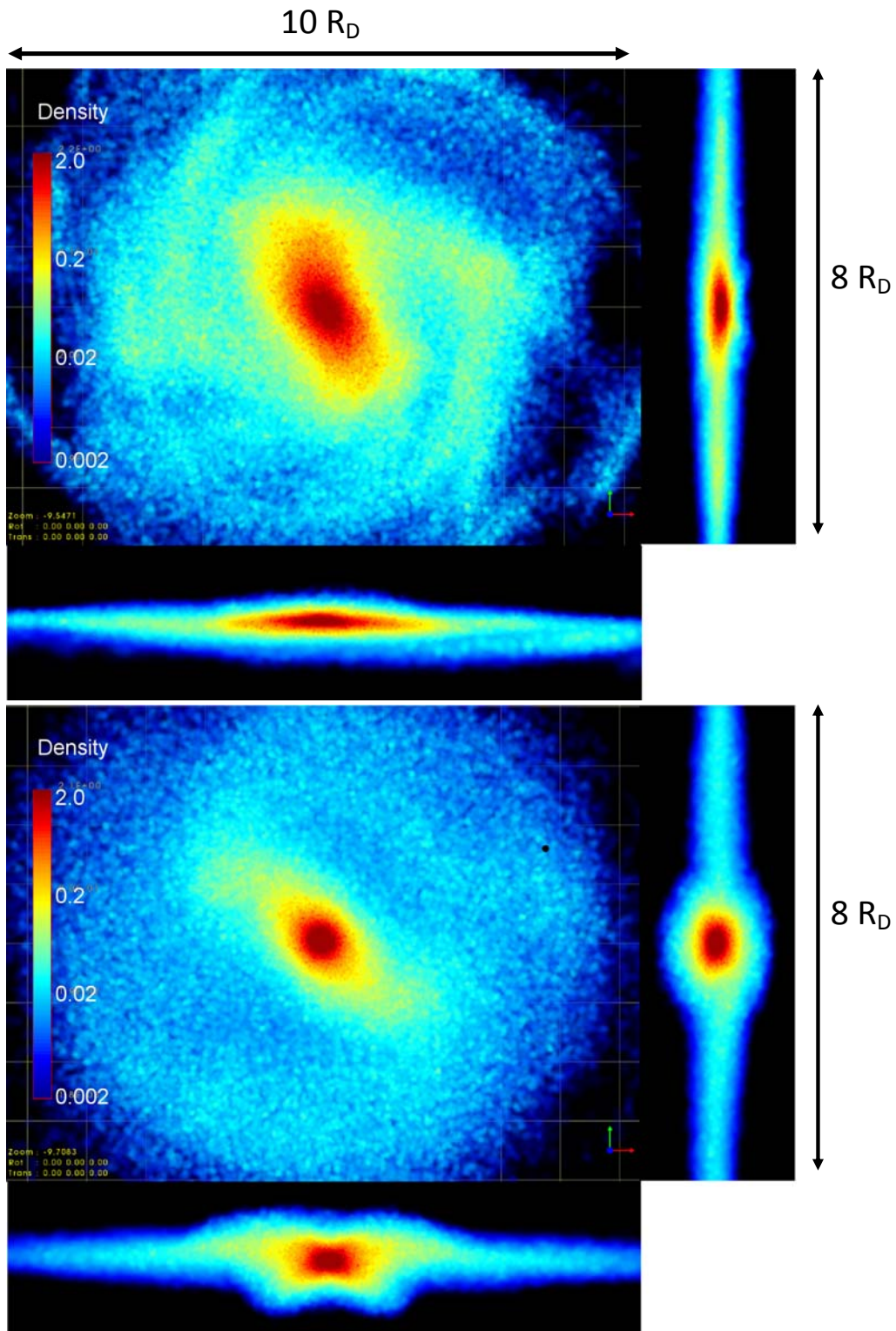


Figure 4.12: Model MD without a CMC. Density map for $t = 150$ (top) and $t = 500$ (bottom). Each set of density maps consists of face on view with bar side view underneath and bar end on view at the side.

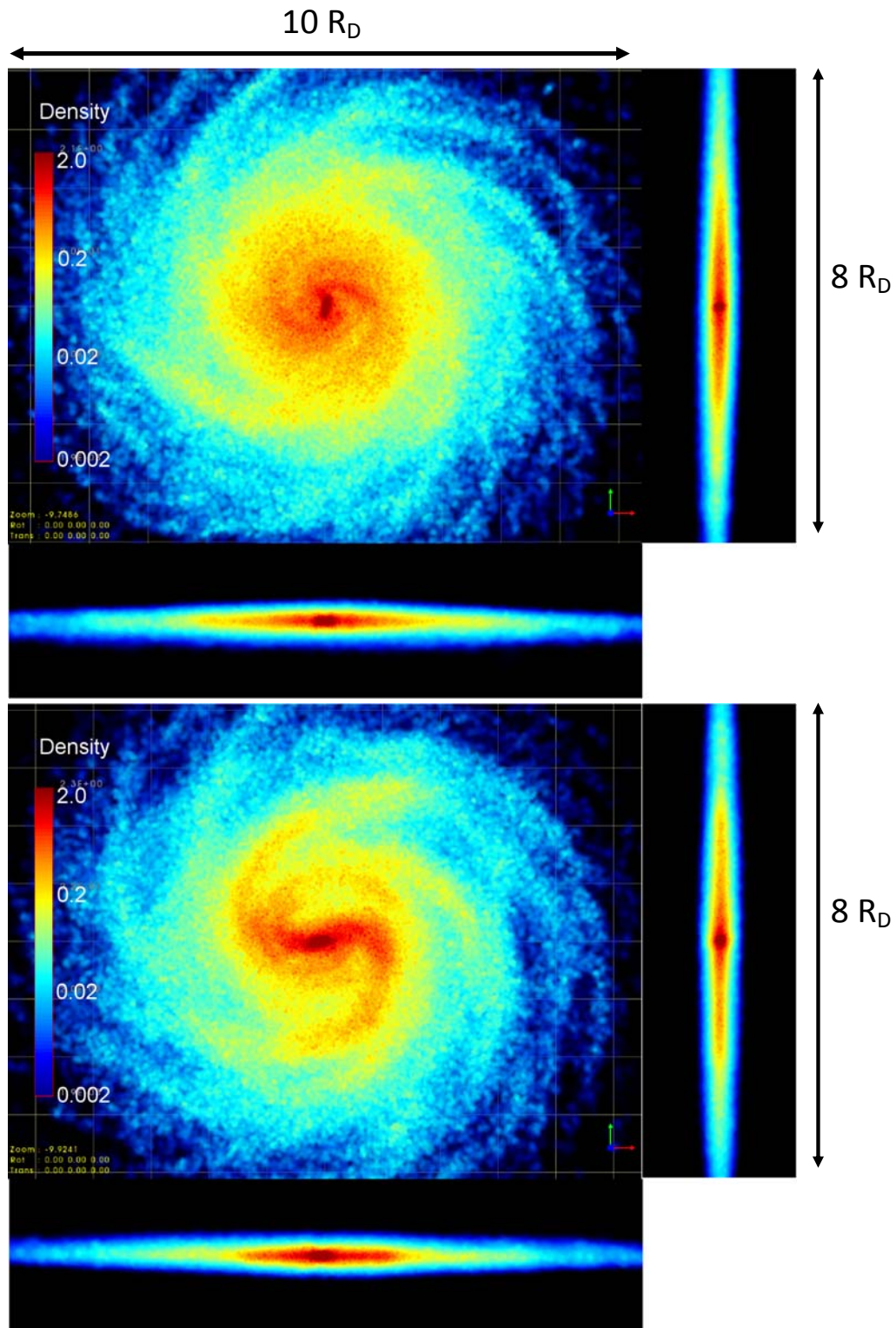


Figure 4.13: Model MH without a CMC. Density map for $t = 50$ (top) and $t = 125$ (bottom). Each set of density maps consists of face on view with bar side view underneath and bar end on view at the side.

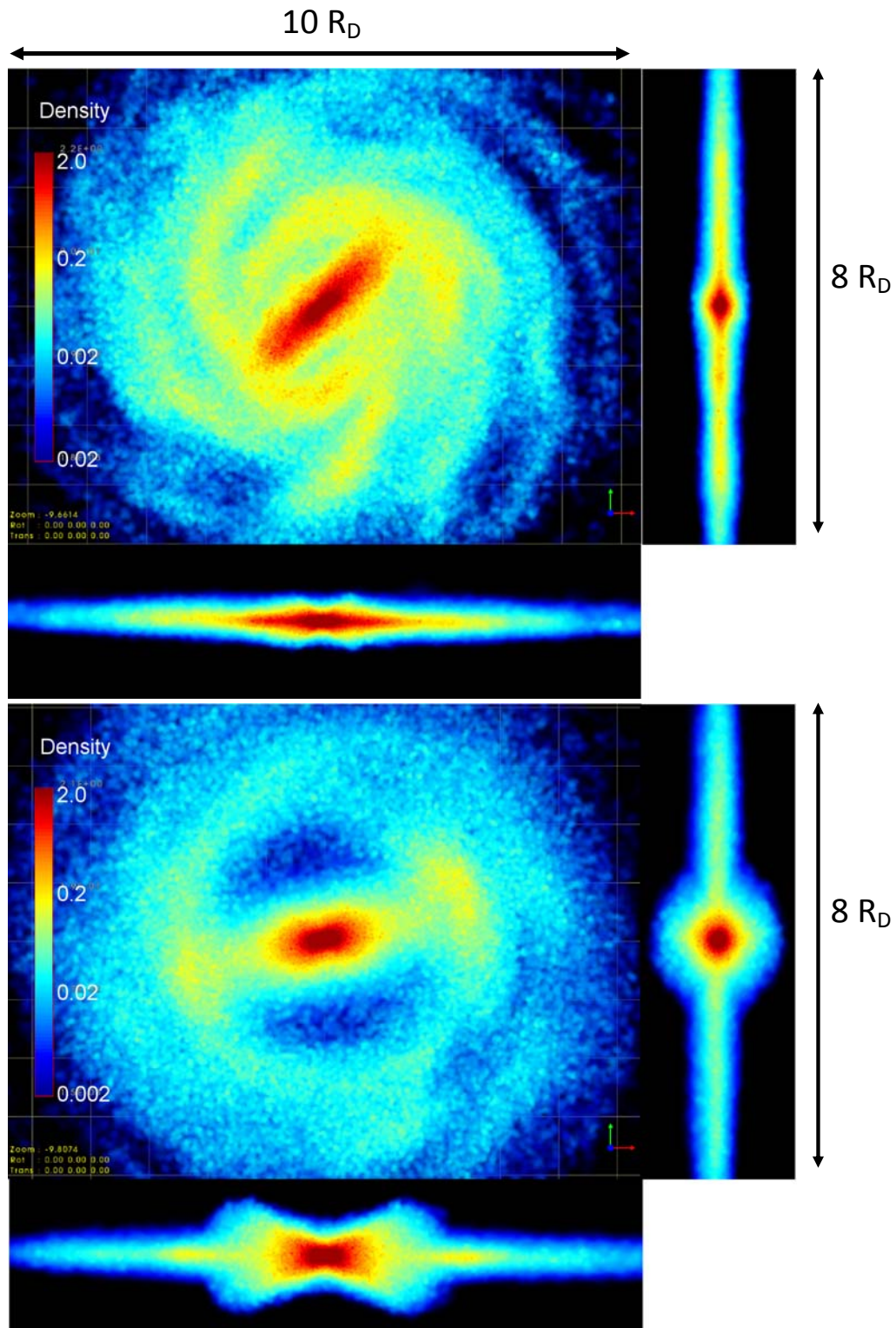


Figure 4.14: Model MH without a CMC. Density map for $t = 200$ (top) and $t = 500$ (bottom). Each set of density maps consists of face on view with bar side view underneath and bar end on view at the side.

Figures 4.13 and 4.14 show density maps of the disc illustrating its evolution for the model MH simulation. At $t = 50$ the bar is not visible, but a large number of flocculent trailing spirals can be seen. The disc remains thin and has no vertical structure. It is not until $t = 125$ that a very short bar begins to form in the centre of the disc (less than 2 disc scale radii long) and spiral arms are prominent. The bar then continues to strengthen ($t = 200$). A complex density structure is developing in the disc and the inner spiral arms have become less distinct. Vertical structure is becoming visible and a peanut shaped bulge is forming. At $t = 500$ the bar is now very prominent and has a strong peanut shape. The length of the bar is approximately 6 scale radii.

In summary, a bar forms much earlier in the model MD simulation (by $t = 50$) compared to $t = 125$ for model MH. Its evolution continues for the next 150 time units with the development of significant asymmetries in both the disc plane and the disc vertical thickness. It seems likely that this is due to non-linear growth modes which cause resonant density patterns in the disc and lead to the early development of the bar. By contrast the bar forms much later in the model MH simulation hinting at the suppression of non-linear growth modes. In addition, the model MH bar develops through secular growth. It evolves steadily and does not show the asymmetries seen in the model MD simulation or the asymmetric buckling which leads to the development of a boxy shape of the bar seen in the MD case at $t = 500$.

4.4.2 Development of bars with a CMC

Bars formed in all of the model MD simulations where a CMC was present. Let us consider the simulation with CMC mass $0.02M_d$ (Figure 4.15). The bar forms at $t = 100$ and is about 4 disc scale radii long. The upper panel of Figure 4.15 shows density maps for $t = 125$. There is a mildly peanut shape to the vertical structure. There is also a significant $m = 1$ Fourier component asymmetry visible in the spiral arms which is probably the

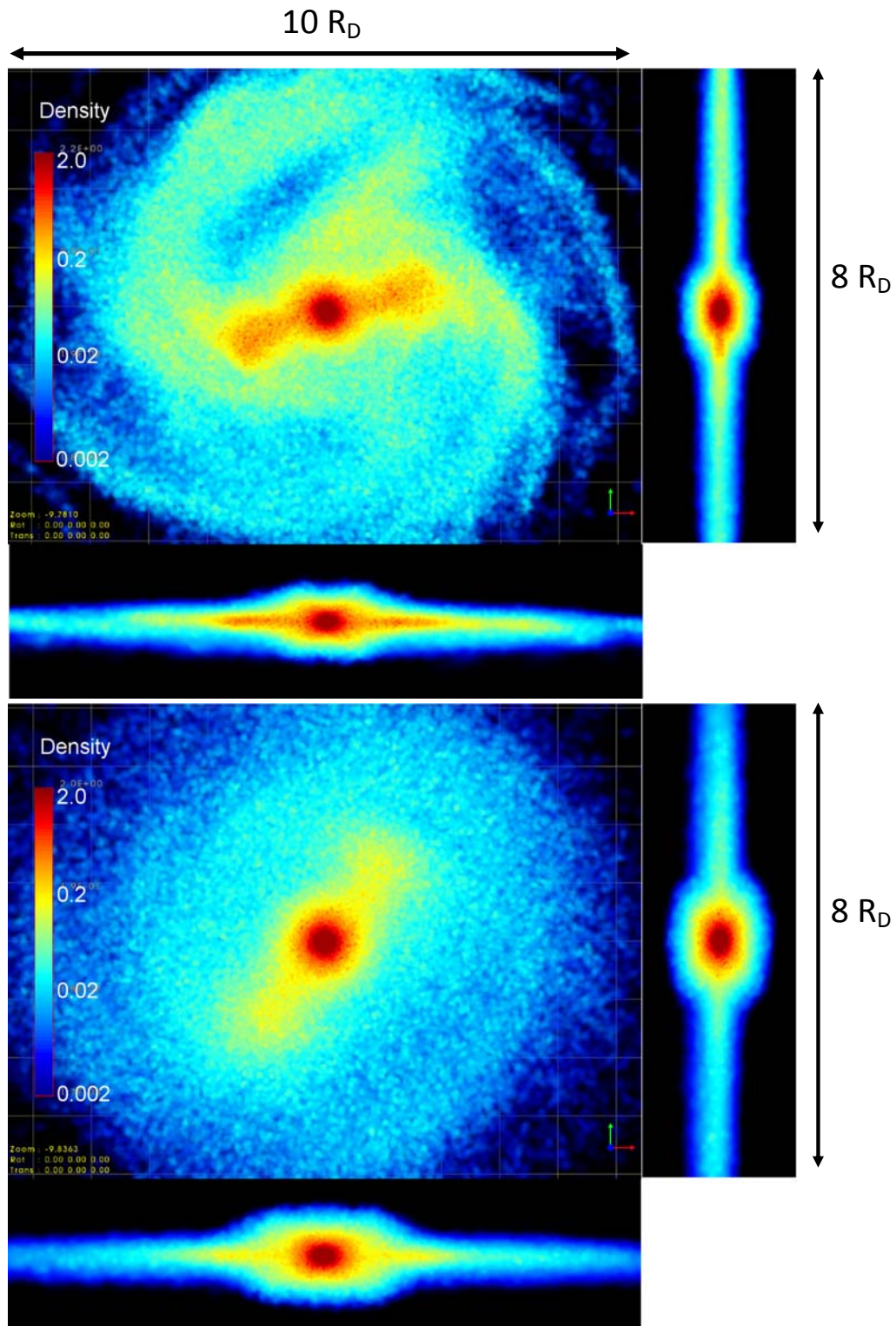


Figure 4.15: Model MD with CMC of mass $0.02M_d$. Density map for $t = 125$ (top) and $t = 500$ (bottom). Each set of density maps consists of face on view with bar side view underneath and bar end on view at the side.

reason for the falling strength of the bar at this time. At $t = 500$ the bar is 5 disc scale radii long and has no strong boxy or peanut structure. The main differences to the model MD simulation with no CMC is that the disc is thicker and the bar narrower. Development of the bar is very similar to the simulation with no CMC but fewer asymmetries develop in the disc implying that non-linear growth modes are damped. This damping can also be seen in the relative size of the fluctuations in the relative $m = 2$ Fourier component (Figure 4.7).

Bars formed in only one of the MH simulations where a CMC was present, the one with a CMC of $0.01M_d$. Bar development is very similar to the simulation with no CMC. By $t = 250$ a bar and a peanut are clearly developing. By $t = 500$ a strong bar has grown and a strong peanut has developed. The main effect of the CMC is to slow the development of the bar and reduce its strength.

Bar formation was suppressed in the model MH simulation which had a CMC of $0.02M_d$. Figure 4.16 shows the surface density maps of the disc at $t = 500$ (equivalent to 6.5 Gyr for a galaxy with the mass of the Milky Way) and clearly a bar has not developed.

For model MD simulations a CMC slows the development of a bar and weakens its final size and shape possibly by suppressing the non-linear growth modes. However it does not suppress bar formation completely even for very large CMC masses ($0.1M_d$). For the MH simulations with CMC mass $0.01M_d$ the CMC delays the start of bar growth but once started the bar grows at a similar rate and though it is smaller at $t = 500$ it has a strong peanut shape and is still growing. For the other masses bar growth is suppressed for a much longer period.

4.4.3 Evolution of Bars when a CMC introduced

Figures 4.3 and 4.4 shows the surface density maps when growing a CMC in a disc with an evolved bar. The density plots are taken 450 time units after the CMC has grown to its

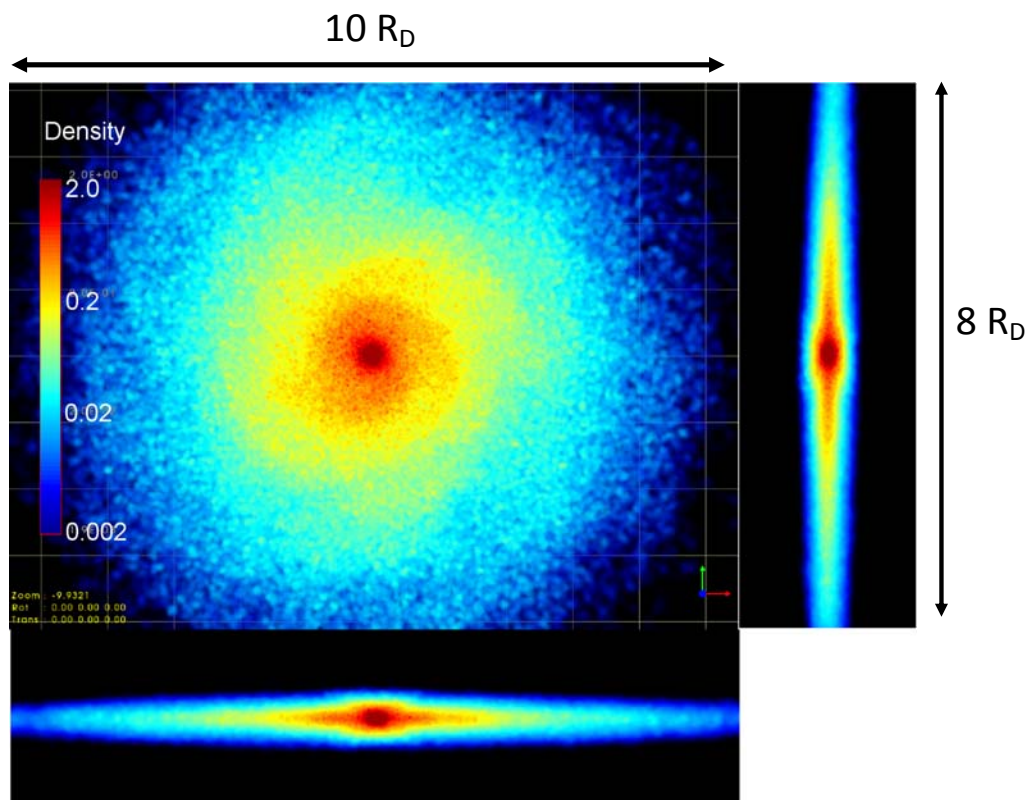


Figure 4.16: Model MH with CMC of mass $0.02M_d$. Density map for $t = 500$. The set of density maps consists of face on view with bar side view underneath and bar end on view at the side.

full mass. If we consider the model MD results (left hand column) for CMC mass $0.02M_d$ and CMC mass $0.05M_d$ the bar has been destroyed. Introducing a CMC into a model MD disc with an existing bar has a very significant effect on the bar destroying it even for low CMC masses. The model MH simulations (right hand column) for CMC mass $0.02M_d$ and CMC mass $0.05M_d$ show a short weak bar but it has been greatly diminished. In both MD and MH simulations the growth of a CMC has a significant effect on the strength of a pre-existing bar.

4.5 Evolution of Disc Parameters

4.5.1 Disc buckling and velocity dispersion

Past studies have shown that numerical stellar bars undergo a dynamical instability called vertical buckling (Combes et al., 1990; Pfenniger and Friedli, 1991; Raha et al., 1991; Berentzen et al., 1998; Patsis et al., 2002b). This is an out of plane instability where the bar bends out of the plane of the disc initially into a banana shape which is asymmetric perpendicular to the plane of the disc. Following this instability the bar thickens, and acquires a characteristic boxy peanut shape. Buckling is important in bar formation as it has a profound effect on bar development. In addition it heats the disc and can destroy the bar. The origin of boxy/peanut shaped bulges has two possible explanations. One is the so called fire-hose instability (Toomre, 1966; Raha et al., 1991; Merritt and Sellwood, 1994) and the other is resonance heating (Combes et al., 1990; Pfenniger and Friedli, 1991; Patsis et al., 2002a). The fire-hose instability occurs when bending waves in the disc become unstable when their wavelength is sufficiently short (Binney and Tremaine, 2008). Resonance heating occurs when stars undergoing the instability are in resonance with bar itself.

Buckling is most easily quantified through the $m=1$ Fourier component of the disc

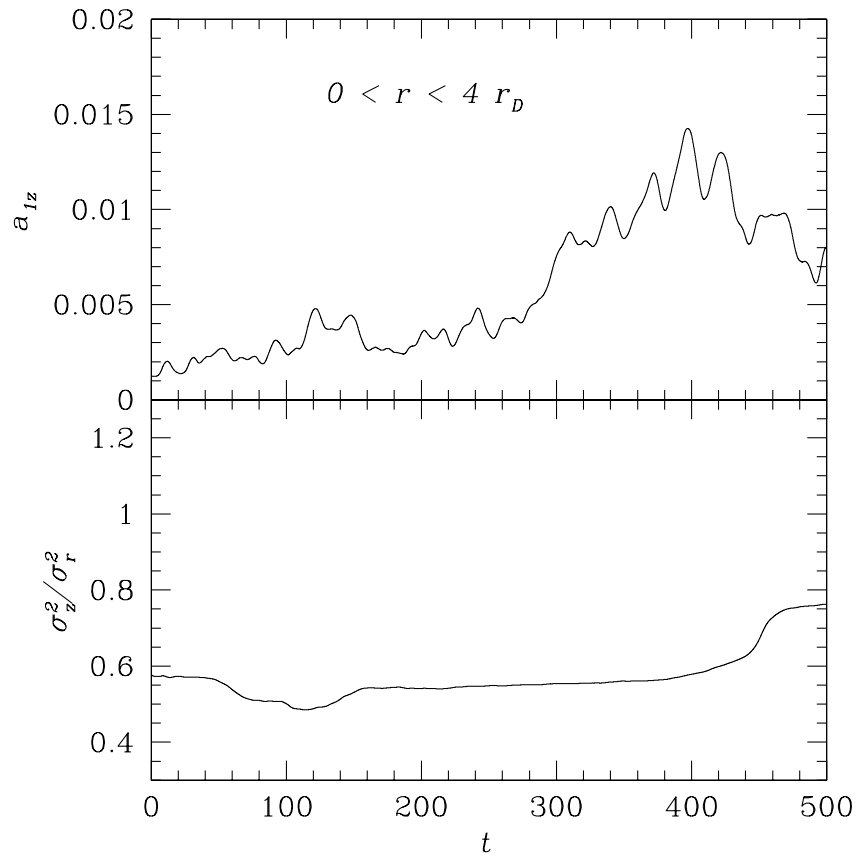


Figure 4.17: Evolution of the vertical buckling amplitude (magnitude of the $m = 1$ Fourier component of the disc surface density in the rz -plane) (top) and the vertical to radial dispersion velocity in the disc (bottom) for the massive disc model with no CMC.

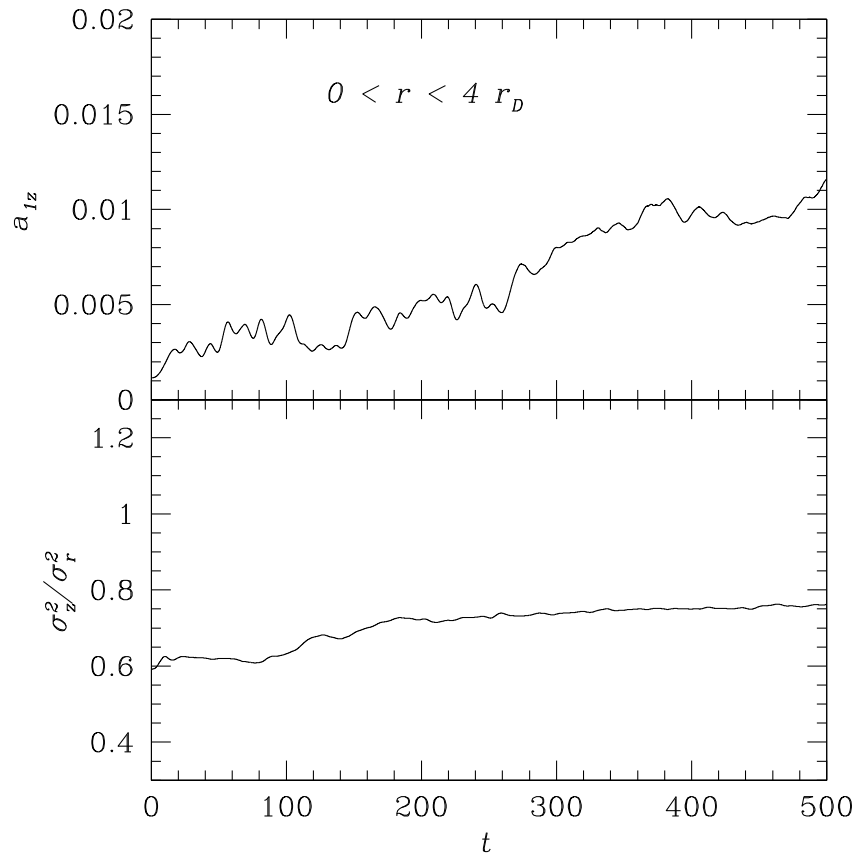


Figure 4.18: Evolution of the vertical buckling amplitude (magnitude of the $m = 1$ Fourier component of the disc surface density in the rz -plane) (top) and the vertical to radial dispersion velocity in the disc (bottom) for the model MD disc with a CMC with a mass of 2% of the mass of the disc.

surface density in the rz -plane (a_{1z}). For the model MD simulation with no CMC the evolution of this parameter is shown in figure 4.17. It can be seen that there are two periods of buckling, one beginning at $t \approx 100$ with a peak at $t \approx 140$ and one at starting at $t \approx 220$ with a peak at $t \approx 400$. The first of these can be seen in the top panel of Figure 4.12 and the second in the bottom panel of Figure 4.12. The second episode initially grows the strength of the bar which then reduces dramatically after $t=440$ (see figure 4.7).

Figure 4.17 also shows the evolution of the vertical to radial dispersion velocity in the disc. The buckling instability is a breaking of the vertical symmetry in the bar. Toomre (1966) has shown that the coupling between the vertical and radial motion is the main cause of this instability and the result is that the vertical and radial velocity dispersions become equal (the fire hose instability). The expected evolution of σ_z^2/σ_r^2 is that it initially falls due to the onset of the bar instability as σ_r grows. It then rises again due to the coupling between the vertical and radial motion which marks the onset of disc buckling. The critical value of σ_z^2/σ_r^2 at which buckling starts has been estimated at various values from 0.06 to 0.6 (Raha et al., 1991; Sotnikova and Rodionov, 2005; Sellwood, 1996) but clearly depends on the form and status of the disc. Figure 4.17 shows that this ratio starts to fall at $t \approx 40$ marking the onset of the bar instability. It falls to a value of ≈ 0.5 at $t \approx 110$ where it starts to rise again but stabilises at between 0.55 and 0.6 until $t \approx 380$ when it rises again to $\gtrsim 0.75$.

Examination of the density profiles of section 4.4.1 reveal two episodes of buckling. One starting at $t \approx 100$ and ending at $t \approx 150$ and the second more significant one at $t \approx 400$. This corresponds with the changes in the $m=1$ Fourier component of the disc surface density in the rz -plane and the evolution of σ_z^2/σ_r^2 .

Figure 4.18 shows the evolution of a_{1z} and the evolution of σ_z^2/σ_r^2 for the MD model with a CMC of mass $0.02M_d$. Here the evolution of the a_{1z} is quite different to the MD model with no CMC. There is no obvious early peak and later growth is more gradual,

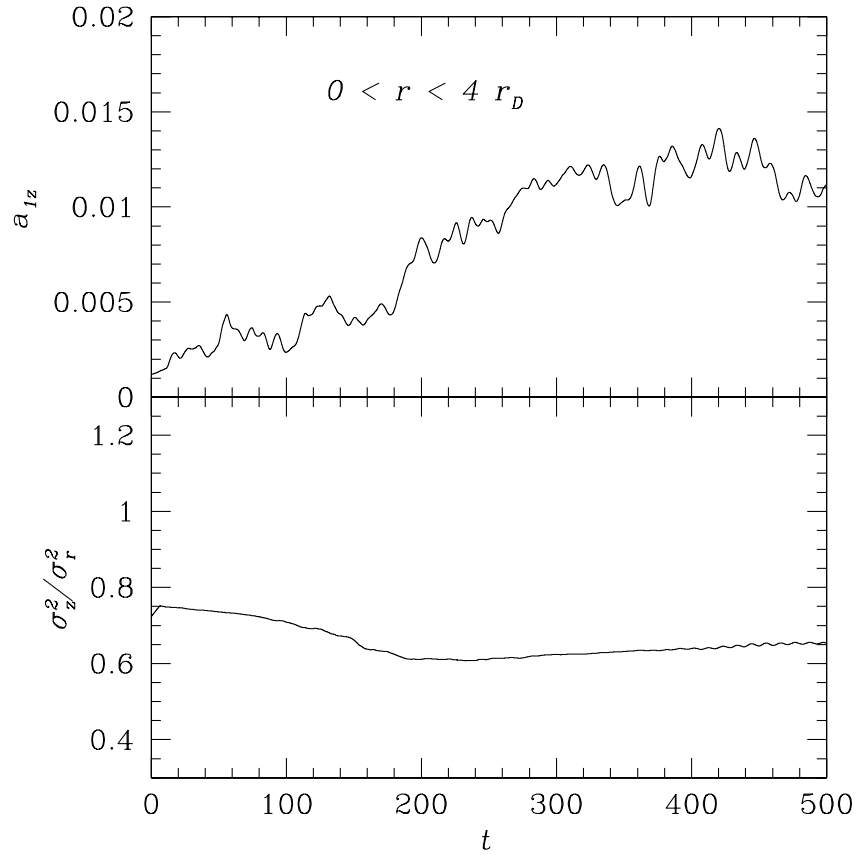


Figure 4.19: Evolution of the vertical buckling amplitude (magnitude of the $m = 1$ Fourier component of the disc surface density in the rz -plane) (top) and the vertical to radial dispersion velocity in the disc (bottom) for the MH model with no CMC.

continuing to grow throughout the simulation. The evolution of the σ_z^2/σ_r^2 ratio is even more noticeably different to the no CMC model. There is no fall initially though the ratio rises from $t \approx 70$ stabilising at $\gtrsim 0.75$.

Figure 4.19 shows the evolution of a_{1z} and σ_z^2/σ_r^2 for the model MH disc with no CMC. The $m = 1$ Fourier component of the disc surface density in the rz -plane shows secular growth starting at $t \approx 170$ and continuing until the end of the simulation. The σ_z^2/σ_r^2 ratio is quite different to the evolution of the no CMC model MD. It falls gradually from ≈ 0.75 until $t \approx 180$ and then stabilises before recovering slowly until it reaches ≈ 0.65 at $t = 500$. This simulation grows a strong boxy peanut (see section 4.4.1). The

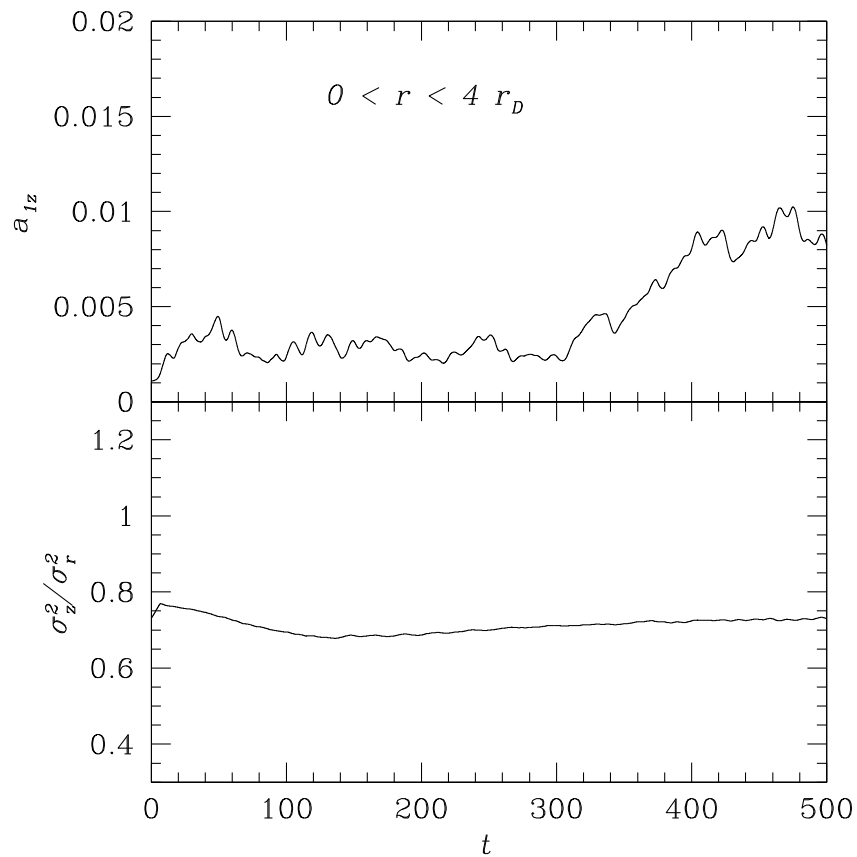


Figure 4.20: Evolution of the vertical buckling amplitude (magnitude of the $m = 1$ Fourier component of the disc surface density in the rz -plane) (top) and the vertical to radial dispersion velocity in the disc (bottom) for the model MH disc with a CMC of mass of 1% of the mass of the disc.

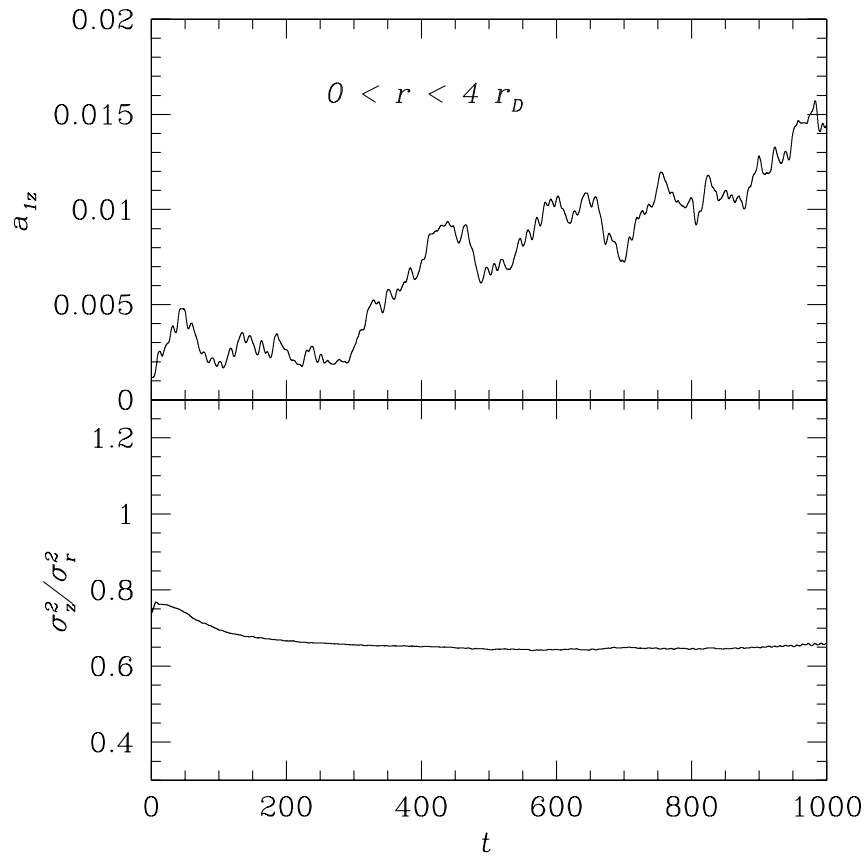


Figure 4.21: Evolution of the vertical buckling amplitude (magnitude of the $m = 1$ Fourier component of the disc surface density in the rz -plane) (top) and the vertical to radial dispersion velocity in the disc (bottom) for the model MH disc with a CMC of mass of 2% of the mass of the disc.

start of the growth of the peanut begins at $t \approx 175$ which corresponds to the start of the growth of a_{1z} and the minimum in σ_z^2/σ_r^2 .

Figure 4.20 shows the evolution of a_{1z} and σ_z^2/σ_r^2 for the model MH disc with a CMC of mass of 1% of the mass of the disc. The evolution of a_{1z} and the minimum in σ_z^2/σ_r^2 shows a similar pattern to the model MH disc with no CMC. The secular growth starts somewhat later at $t \approx 300$. The σ_z^2/σ_r^2 ratio falls gradually from ≈ 0.75 until $t \approx 140$ and then stabilises before recovering slowly until it reaches ≈ 0.73 at $t = 500$. This simulation grows a less strong boxy peanut (see section 4.4.2).

In both of the above cases the growth of the boxy peanut does not require a strong buckling phase to initiate it and the growth of the peanut is a secular phenomenon (Villa-Vargas et al., 2009).

Figure 4.21 shows the evolution of a_{1z} and that of σ_z^2/σ_r^2 for the model MH disc with a CMC of mass of 2% of the mass of the disc. The evolution of a_{1z} shows a similar pattern to the previous two MH cases but the secular growth starts at $t \approx 300$ as in the model with a mass of $0.01M_d$. However the σ_z^2/σ_r^2 ratio falls from ≈ 0.75 until $t \approx 150$ and then continues to subside never recovering significantly.

4.5.2 Evolution of angular momentum

Figure 4.22 shows the evolution of the z component of the angular momentum of the disc for two model MD discs in three radial ranges. The inner range is $r < 1$, the central range correspond to the region where the bar tends to be strongest and is $1 < r < 3$ and the outer range is outside this region, $r > 3$. For the model MD disc with no CMC it can be seen that the angular momentum in the bar region drops rapidly between $t = 40$ and $t = 120$ which is the main period of bar formation. This corresponds to the early onset of the bar instability and corresponds to the establishment of resonances which allow the inner part of the disc to transfer angular momentum to the outer disc. More than 75% of the angular

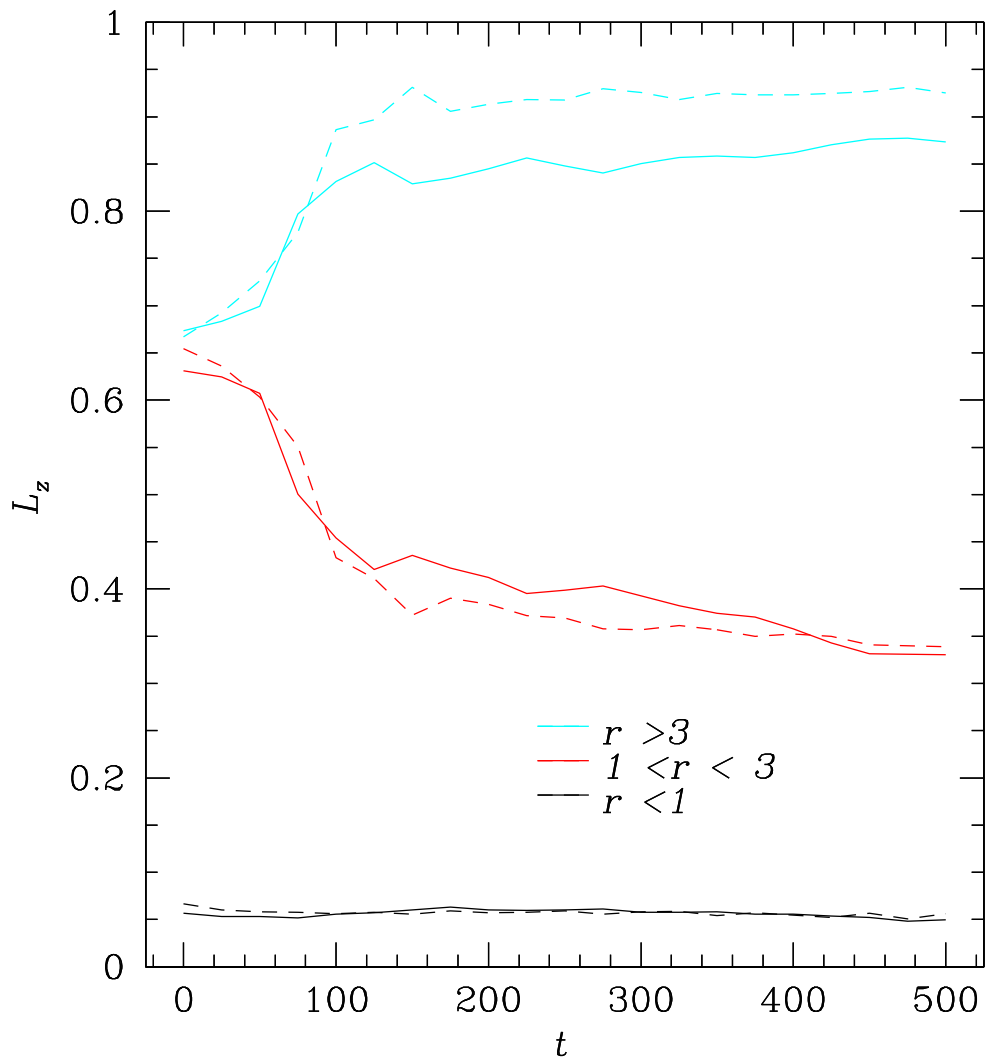


Figure 4.22: Evolution of the z component of the angular momentum of the disc in three radial bins for model MD discs. The solid lines are the with no CMC and the dashed lines are the MD model with a CMC of mass 2% of the disc.

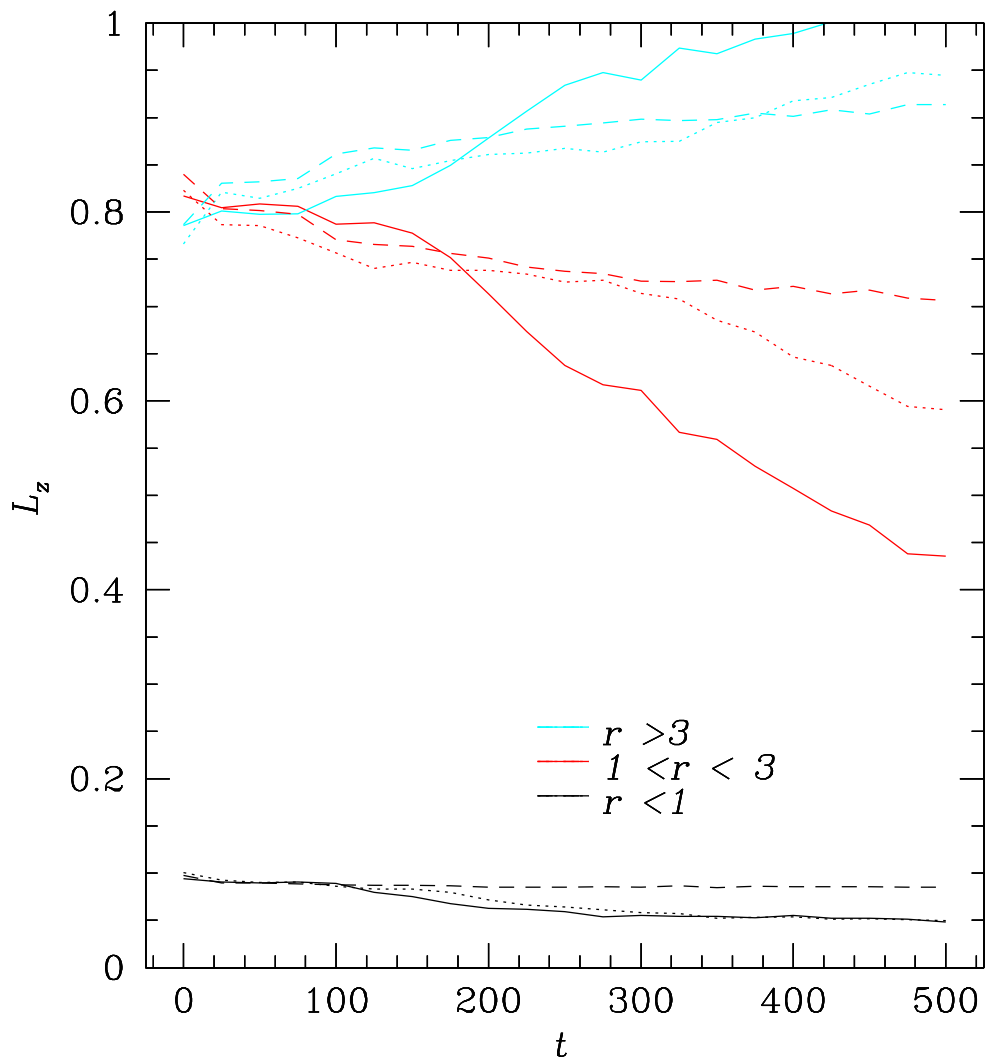


Figure 4.23: Evolution of the z component of the angular momentum of the disc in three radial bins for model MH discs. The solid lines are with no CMC, the dotted lines are with with a CMC of mass 1% of the disc and the dashed lines are with a CMC of mass 2% of the disc.

momentum exchanged by the bar region is absorbed by the outer disc. There is then a much longer period of secular exchange of angular momentum of the bar region with the outer disc and to a greater extent the halo (more than 55% of the angular momentum exchanged by the bar region is absorbed by the halo during this period). The dashed line in figure 4.22 shows the z component of the angular momentum for the model with a CMC with 2% of the mass of the disc. The main effect of the CMC is to delay the onset of the disc instability slightly and to make the step change smaller, both of which contribute to a weaker bar forming. Over 90% of the initial rapid exchange of momentum from the inner disc is absorbed by the outer disc but all of the remaining angular momentum exchanged by the bar region of the disc is absorbed by the halo.

Figure 4.23 shows the evolution of the z component of the angular momentum of the disc in three radial ranges for two model MH discs. The three ranges are the same as for the model MD discs described above. For the model MH disc with no CMC it can be seen that the angular momentum exchange is delayed until $t = 100$ and then the angular momentum in the bar region changes much more gradually. The changes start slowly and then become more rapid by $t = 170$ which corresponds to the growth of the boxy peanut. About 55% of the angular momentum exchanged by the bar region is absorbed by the outer disc during the secular exchange of angular momentum of the bar region with the outer disc and the halo.

The dotted lines in figure 4.23 shows the z component of the angular momentum for the model with a CMC with 1% of the mass of the disc. For the CMC with 1% of the mass of the disc the main effect of the CMC is to delay the onset of the angular momentum exchange and make the rate of exchange smaller, both of which contribute to a weaker bar forming.

The dashed lines in figure 4.23 shows the z component of the angular momentum for the model with a CMC with 2% of the mass of the disc. Here there is still an exchange of

angular momentum but the rate of exchange is smaller. In both the $M_{\text{CMC}} = 0$ and $M_{\text{CMC}} = 0.01M_{\text{d}}$ there is a noticeable acceleration in the rate of transfer of angular momentum from the bar region of the disc a $t \approx 150$ in the $M_{\text{CMC}} = 0$ model and at $t \approx 300$ for the $M_{\text{CMC}} = 0.01M_{\text{d}}$ model. No such acceleration is seen in the rate of transfer of angular momentum for the $M_{\text{CMC}} = 0.02M_{\text{d}}$ model. It seems likely that this acceleration corresponds to the rapid growth of orbital resonances and that the presence of the CMC suppresses the growth of orbital resonances needed to grow the bar.

4.6 Discussion and Conclusions

Model MH discs are more susceptible to the suppression of bar formation than model MD discs which is the reverse of the effect seen when a CMC is grown in a disc with a pre-existing bar. Figure 4.24 shows the value to the second Fourier component of the surface density averaged over the final 50 time units for all our simulations. It seems highly likely that the mechanism for the suppression of a bar is different from the mechanism for the destruction of a bar. Athanassoula et al. (2005) found that strong bars are less prone to dissolution than weak ones. Our simulations show that MD models are more prone to the bar instability than MH models. In model MD discs the bar develops earlier and grows more rapidly than those seen in model MH discs. This is clearly illustrated by the step change in the angular momentum discussed in section 4.5.2. However the exchange of angular momentum continues for longer and the bar thus grows stronger in model MH discs due to the greater mass in the dark matter halo to absorb angular momentum.

In the model MD discs the bar forms spontaneously due to the bar instability however the growth of the bar is limited by its ability to transfer angular momentum to the outer disc or the dark matter (DM) halo. In these models there is not enough mass in the DM halo to absorb angular momentum beyond a certain level and so the bar cannot grow further. This is true for all masses of CMC *where* the bar forms.

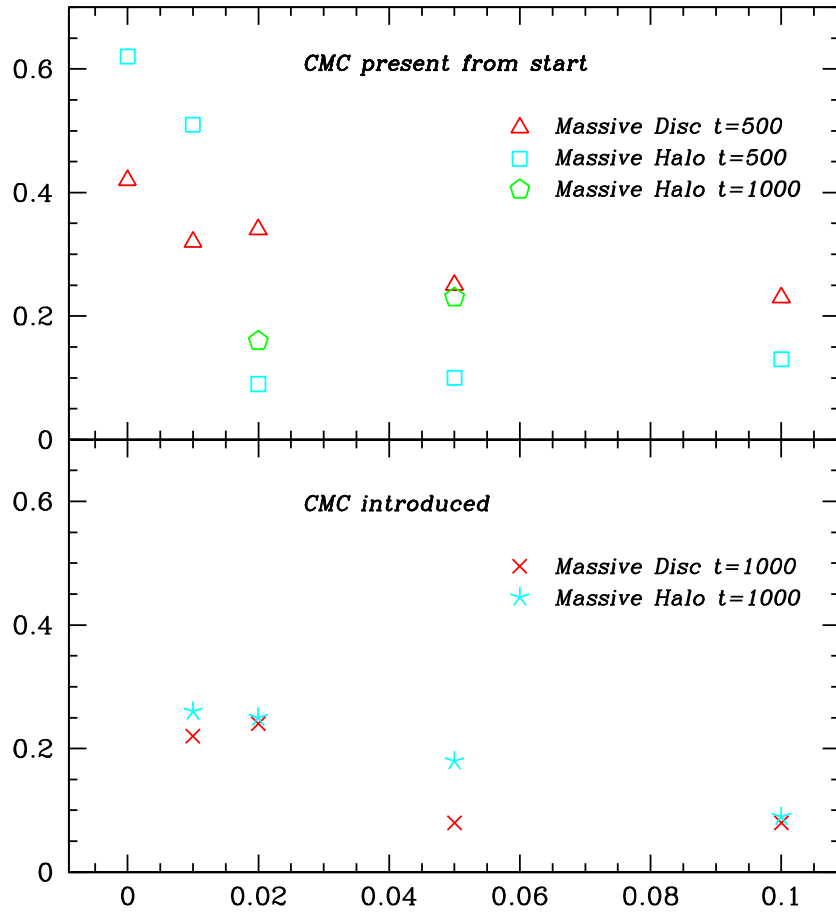


Figure 4.24: The final value of the second Fourier component of the surface density ($\frac{a_2}{a_0}$) averaged over the final 50 time units of our simulations. The upper panel shows the results when the CMC is present from the beginning and the lower panel shows the results what a CMC is introduced when a bar has evolved.

As the model MH discs are already less susceptible to the formation of a bar then the addition of CMC will dilute the disc self gravity which will increase the damping of the disc instability. The presence of the CMC acts against the resonant orbit coupling between the inner disc and the outer disc and dark matter halo.

The growth of the strong peanut shaped bulge in the model MH discs appears to proceed through a secular and not a dynamical buckling mechanism (Villa-Vargas et al., 2009) and proceeds without the onset of the buckling instability. Buckling can be seen in the model MD discs but it does not appear to be caused by the fire hose instability. The ratio of σ_z^2/σ_r^2 does not fall to the levels at which the instability is predicted to be triggered (Raha et al., 1991; Sotnikova and Rodionov, 2005; Sellwood, 1996). This implies that the evolution of this ratio is an outcome of the buckling and not a cause. As has been suggested by Athanassoula and Martínez-Valpuesta (2008) it seems likely that in this case the formation of a bar is due to the changes in the orbital structure of the stars in the disc.

5

Conclusions

Over the last 30 years great advances have been made in our understanding of cosmology and the growth of structure in the universe. During that time it has become clear that most of the matter in the Universe is dark, only detectable through its gravitational influence on luminous matter. Our standard cosmological model, Λ CDM, makes detailed predictions on the scale of galaxy clusters and larger (Mpc) scales and is in excellent agreement with a number of observations (Springel et al., 2006). However Λ CDM does not tell us what dark matter (DM) is. The nature of this dark matter is one of the biggest problems in fundamental physics and cosmology today. Theoretically it is believed that the dark matter is a non-baryonic Cold Dark Matter (CDM). The predictions of the CDM model have been explored in great detail using cosmological N-body simulations. All dark matter models predict the formation of massive self-gravitating structures called halos, and these halos are important because they are where galaxies form.

On the scale of galaxies there are many challenges. The CDM model makes a clear prediction that dark matter haloes should have divergent central densities (cusps), yet observations of galaxies strongly suggest that haloes in the real Universe have finite central densities (cores) (de Blok, 2010, and references therein). Does this tension between theory and observation signal a fundamental problem for the CDM model, or are there astrophysical processes that could explain naturally why we see dark matter cores instead of cusps? One of our objectives has been to provide an answer to this important question and to investigate some of the key problems of galaxy formation in a rigorous way and build a deep understanding of the key processes involved.

Baryons play an important role in the formation and early evolution of galaxies but the predictions of cusped profiles are based on purely dark matter simulations. If baryons are introduced, they can have a profound effect on halo structure, but it is far from clear what kind of effect they will have because the physics of galaxy formation is still poorly understood. Therefore cosmological simulations are not very useful for developing insight and it is better to use controlled simulations that allow you to study parts of a problem in detail and to build the physical understanding of how a particular process works.

However baryons interact in much more complex ways than DM. Gas physics is a multiscale problem with a dynamic range of many orders of magnitude. Including full baryonic physics is too difficult for the computing power available to us today. We have not attempted to model the complexities of baryonic physics but instead use dynamical models of baryonic matter moving in dark-matter halos.

We have found that one key process in the re-shaping of dark-matter haloes by baryons is the transfer of energy via dynamical friction from baryonic sub-structures to the dark-matter. The dark matter is heated by the non-adiabatic infall of the baryons. We have demonstrated that this raises the central velocity dispersion which will tend to drive matter out. However the arrival of the baryons also raises the gravitational force pulling matter

in. Which of these two effects wins out depends on the details of such “mergers”. If the infall is rapid and non-adiabatic then the pressure due to heating wins and the central dark matter density will fall. If the heating is small, the gravitational pull will dominate and the density will increase. The latter occurs in the case of adiabatic contraction. Which effect dominates will depend on the specific situation and this fact probably explains some of the conflicting results reported in the literature (e.g. Romano-Diaz et al., 2008; Pedrosa et al., 2009).

A good way to envisage this problem is to look at the effect on the dark-matter coarse-grained phase-space density which is conserved for adiabatic evolution. However it seems highly likely that in the early universe the baryonic infall is a violent non-adiabatic process which reduces the dark-matter phase-space density. If the accreted baryons fall in and then remain at the centre of the galaxy this may not result in a reduction of the dark-matter spatial density, because the additional gravitational potential of the newly arrived baryons increases the available bound velocity-space (phase-space at this position). However we have demonstrated (see Chapter 2) that if the baryons are driven out of the galaxy by a galactic wind this will result in a reduction in available phase space which in turn will result in the dark matter moving out, reducing the central density. Another way to look at this is that the wind removes the additional gravitational pull from the accreted baryons. In the phase-space interpretation, the wind reduces the bound velocity space meaning that the dark matter must expand.

Our model has implications for the formation of dwarf galaxies. Their present day baryonic mass within the half light radius (of the order of a few percent of the total mass) is of the order of the mass of DM which needs to be rearranged in order to convert their halos from cusped to cored. This opens up the scenario that their stellar component could be built from a number of star clusters that fall to their centres due to the action of dynamical friction (assuming a plausible star formation efficiency).

This brings us to the subject of the density profile of dwarf galaxies. There is strong evidence that Low Surface Brightness (LSB) galaxies have a central core or shallow slope (e.g. Oh et al., 2008). However, though there is some good evidence that the central density of dwarf spheroidal galaxies are not cusped, the evidence is not as conclusive (see Chapter 3). Can observations of the dynamical state of the dwarfs provide evidence to distinguish whether they have a cored or cusped density profile? Here the situation with the Fornax dwarf provides some clues. It is unique in having five globular star clusters which present us with a paradox. Why have they not fallen to the centre of the galaxy creating a nuclear star cluster? Our approach here is to model Fornax and the clusters plausibly in agreement with the best observations and see how they develop in mass models for Fornax with differing density profiles.

Our results show that the timing problem can be solved in three ways:

1 Fornax has a large core such that the GCs stall at its edge. We have shown that a shell-like distribution for the GCs can be expected in this case independently of the initial conditions (because of "dynamical buoyancy"). Furthermore, this can naturally explain why there is only one low density GC that could have been disrupted in the Fornax core, and it is located on an orbit which means that it is extremely unlikely to have ever fallen into the core.

2 The GCs were accreted only very recently. However, this solution seems unlikely because it is not clear where would they accrete from.

3 The GCs are a long way from the centre of Fornax. This could be consistent with the GCs having been accreted long ago, leaving them on high-apocentre orbits. However we have shown that to avoid them falling to the centre over a Hubble time, the GCs require a pericentre of $\gtrsim 1$ kpc and an apocentre of $\gtrsim 2-3$ kpc (if this solution is to work for cusped Fornax mass distributions). The former is theoretically odd, while the latter is at strong tension with the observed distribution of GCs.

Solutions 2 and 3 are essentially strongly disfavoured. This leaves only the strong probability that Fornax has a large core such that the GCs stall at its edge. From our work in Chapter 2 and that of others reported in the literature it seems likely that such a core can form naturally as a result of baryonic processes. Warm dark matter / self-interacting dark matter can lead to core formation too, but only if very exotic and unusual versions of these dark matter models are employed. If Fornax has a core, then this strongly affects the mapping from the measured velocity dispersion to the maximum velocity of the halo. This invalidates any results based on abundance matching on these small scales which have led some to conclude that warm dark matter may provide a better alternative to cold dark matter in explaining the kinematic properties of the local group (Lovell et al., 2012).

A coherent picture is building where galaxies in the universe form by the gravitational infall of baryons into cusped dark matter halos. This infall heats the dark matter increasing the available phase space. As the gas contracts stars form creating stellar winds which are augmented by winds from supernovae as the most massive stars reach the ends of their lives. This in turn removes baryons reducing the available phase space which in turn reduces the real space density and turns the dark matter density into a cored one. This process may happen many times, each one contributing to the reduction in central density.

One other major process which effects galactic evolution is the growth of the super-massive black holes (SMBHs) at the centre of galaxies. These objects can grow very rapidly during the early universe and have a profound effect on the evolution of their galaxy. The relative rate of growth of SMBHs compared to other formation and secular processes which go on in galaxies could have observational implications at low red-shift.

We have studied how CMCs affect the development of bars in galaxies. The existence of a bar is an important diagnostic tool for interpreting the developmental history of a galaxy. We find that the pre-existence of a large enough CMC in a galaxy could lead to the suppression of a galactic bar. In addition the relative dominance of dark-matter in a

disc galaxy affects the likelihood that a bar will be suppressed by a CMC of any given mass. We find significant differences between the effect a CMC has on a bar that already exists and that when a CMC has grown prior to a galactic bar developing.

Bars develop in different ways depending on the relative contribution of the DM halo to the inner galactic rotation curve (where the gas and stars are found). We distinguish two scenarios for the development of galactic bars, one where baryons dominate the inner rotation curve (model MD) and one where the DM makes an equivalent contribution (model MH). In the model MD a bar forms quickly and grows by transferring angular momentum from the inner disc to the outer disc and DM halo. In the model MH the bar grows more slowly due to the suppression of the disc self gravity by the halo. However the bar can continue to grow and become stronger than the model MD because there is more available matter in the DM halo to absorb angular momentum from the inner disc.

Our findings show that the pre-existence of a CMC can suppress the growth of a bar more easily in the model MH. This is likely to be due to the further suppression of the bar instability in the disc by the CMC. Thus the resonances which lead to the transfer of angular momentum in the disc are suppressed. The model MD on the other hand develops a bar even with a very massive (10% of the mass of the disc) CMC in place.

We conclude that Λ CDM is a very successful theory but at galactic scales it requires careful interpretation in terms of baryonic physics. The interactions between baryons and dark matter play a very significant role in shaping galaxies. Future careful modelling with careful interpretation can provide useful insights into the nature of galaxy formation and evolution.

A

Generating Fornax's Globular Cluster Distribution

A.1 Transformation of coordinates

Normally we would consider the velocity dispersion for a system such as Fornax in terms of its components in spherical polar coordinates. If we assume we have a dynamical model for Fornax which has a velocity dispersion structure

$$(\sigma_r, \sigma_\theta, \sigma_\phi) \tag{A.1}$$

Here $\sigma_r, \sigma_\theta, \sigma_{phi}$ may all depend on r . We want to convert this to a Cartesian frame shown in figure A.1 with velocity dispersion components

$$(\sigma_x, \sigma_y, \sigma_z) \tag{A.2}$$

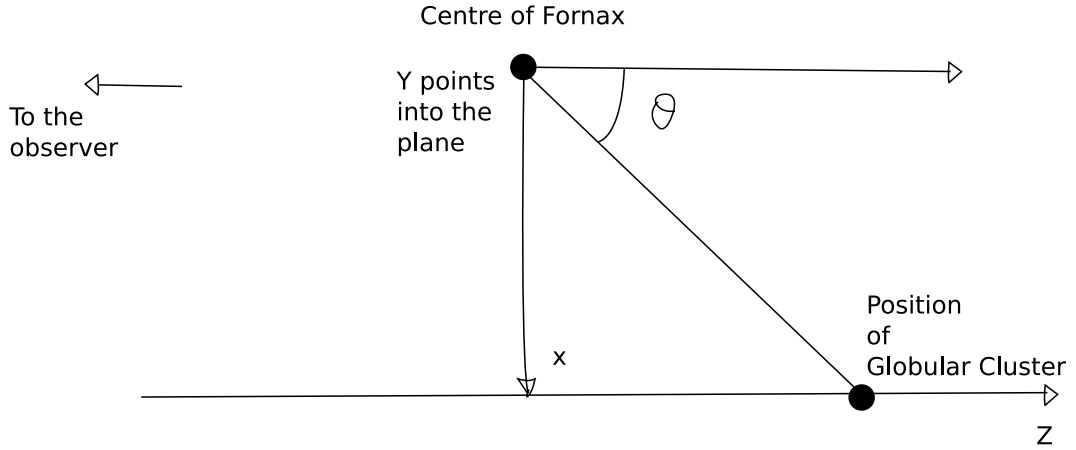


Figure A.1: Cartesian coordinate axes for the globular cluster relative to the centre of Fornax.

The distribution of velocities in each of the r , θ and ϕ coordinates will be normally distributed with a mean value of 0 and standard deviation of σ_r , σ_θ , σ_ϕ respectively. The overall distribution $f(\mathbf{w})$ may be expressed as

$$f(\mathbf{w}) \propto \exp(-1/2 (\mathbf{w}\mathbf{W}\mathbf{w})) \quad (\text{A.3})$$

where $\mathbf{w} = (v_r, v_\theta, v_{phi})$ and \mathbf{W} is a 3×3 matrix given by

$$\mathbf{W} = \begin{pmatrix} 1/\sigma_r^2 & 0 & 0 \\ 0 & 1/\sigma_\theta^2 & 0 \\ 0 & 0 & 1/\sigma_\phi^2 \end{pmatrix} \quad (\text{A.4})$$

If we now transform into a Cartesian frame as shown in figure A.1 then $\mathbf{v} = (v_x, v_y, v_z)$ and

$$f(\mathbf{v}) \propto \exp(-1/2 (\mathbf{v}\mathbf{R}^{-1}\mathbf{W}\mathbf{R}\mathbf{v})) \quad (\text{A.5})$$

where \mathbf{R} is the transformation matrix. We are at liberty to chose a frame where $\phi = 0$ then

$$\mathbf{R} = \begin{pmatrix} \sin\theta & 0 & \cos\theta \\ \cos\theta & 0 & -\sin\theta \\ 0 & 1 & 0 \end{pmatrix} \quad (\text{A.6})$$

$$\mathbf{R}^{-1} = \begin{pmatrix} \sin\theta & \cos\theta & 0 \\ 0 & 0 & 1 \\ \cos\theta & -\sin\theta & 0 \end{pmatrix} \quad (\text{A.7})$$

and

$$\mathbf{R}^{-1}\mathbf{W}\mathbf{R} = \begin{pmatrix} \sin^2\theta/\sigma_r^2 + \cos^2\theta/\sigma_\theta^2 & 0 & \sin\theta\cos\theta/\sigma_r^2 - \sin\theta\cos\theta/\sigma_\theta^2 \\ 0 & 1/\sigma_\phi^2 & 0 \\ \sin\theta\cos\theta/\sigma_r^2 - \sin\theta\cos\theta/\sigma_\theta^2 & 0 & \cos^2\theta/\sigma_r^2 + \sin^2\theta/\sigma_\theta^2 \end{pmatrix} \quad (\text{A.8})$$

We can separate out the dependency on v_y due to choosing $\phi = 0$ and the velocity distribution then becomes

$$f(\mathbf{v}) \propto \exp\left(-1/2\left(\mathbf{v}'\mathbf{R}'^{-1}\mathbf{W}'\mathbf{R}'\mathbf{v}'\right)\exp\left(-1/2\left(v_y^2/\sigma_\phi^2\right)\right)\right) \quad (\text{A.9})$$

with $\mathbf{v}' = (v_x, v_z)$ and \mathbf{R}', \mathbf{W}' and given by

$$\mathbf{R}' = \begin{pmatrix} \sin\theta & \cos\theta \\ \cos\theta & -\sin\theta \end{pmatrix} \quad (\text{A.10})$$

$$\mathbf{W}' = \begin{pmatrix} 1/\sigma_r^2 & 0 \\ 0 & 1/\sigma_\theta^2 \end{pmatrix} \quad (\text{A.11})$$

A.1.1 Separation of variables

We now have an expression for the velocity distribution which depends simply on v_y and in a more complex way on v_x and v_z . We can express the v_x and v_z dependency of $f(\mathbf{v})$ as

$$f(\mathbf{v}) \propto \exp\left(-1/2\left(v_x^2 a_{xx} + v_z^2 a_{zz} + 2v_x v_z a_{xz}\right)\right) \quad (\text{A.12})$$

The constants a_{xx} , a_{zz} and a_{xz} are derived from the multiplication of the 2 x 2 matrices \mathbf{R}'^{-1} , \mathbf{W}' and \mathbf{R}' and given by the expressions

$$a_{xx} = \sin^2\theta/\sigma_r^2 + \cos^2\theta/\sigma_\theta^2 \quad (\text{A.13})$$

$$a_{zz} = \cos^2\theta/\sigma_r^2 + \sin^2\theta/\sigma_\theta^2 \quad (\text{A.14})$$

$$a_{xz} = \sin\theta\cos\theta/\sigma_r^2 - \sin\theta\cos\theta/\sigma_\theta^2 \quad (\text{A.15})$$

We can equate a_{xx} to the normal exponent of the x component of the velocity dispersion

$$1/\sigma'_x{}^2 = a_{xx} \quad (\text{A.16})$$

In addition we have an estimate for $v_z = V_{los}$ and so we can simplify this distribution by completing the square for the exponent as shown in equation A.17.

$$v_x^2 a_{xx} + v_z^2 a_{zz} + 2v_x v_z a_{xz} = C + (v_x - V_0)^2 / \sigma'_x{}^2 \quad (\text{A.17})$$

where

$$V_0 = \left[(\sigma_r^2 - \sigma_\theta^2) \sin\theta\cos\theta / (\sin^2\theta\sigma_\theta^2 + \cos^2\theta\sigma_r^2) \right] V_{los} \quad (\text{A.18})$$

We can now express the velocity distribution in a form which has separated the dependence on v_y and a new variable v'_x which is offset by V_0 from v_x . The velocity distribution is then given by

$$f(\mathbf{v}) \propto \exp\left(-1/2\left(v'_x{}^2/\sigma'_x{}^2\right)\right) \exp\left(-1/2\left(v_y^2/\sigma_\phi^2\right)\right) \quad (\text{A.19})$$

where

$$v'_x = v_x - V_0 \quad (\text{A.20})$$

The dependence on C which is a function of V_{los} has been absorbed into the constant of proportionality.

A.1.2 Generation of the velocity distribution

To complete the process for choosing the velocities for the globular clusters we introduce variables ρ and ψ such that v_x and v_y depend on them as shown

$$v_y = \sigma_\phi \rho \sin\psi \qquad v_x = \sigma_x \rho \cos\psi + V_0 \qquad (\text{A.21})$$

If we substitute these expressions back into equation A.19 we obtain

$$f(\mathbf{v}) dv_x dv_y \rightarrow \exp(-\rho^2/2) \rho d\rho d\psi \qquad (\text{A.22})$$

We define the cumulative probability $P(\rho)$ of selecting a value ρ which is given by the expression

$$P(\rho) = 1 - \exp(-\rho^2/2) \qquad (\text{A.23})$$

ρ itself can then be calculated from the expression

$$\rho = \sqrt{-2 \ln(1 - P(\rho))} \qquad (\text{A.24})$$

We can now use $P(\rho)$ and ψ to generate our velocity distribution. If we select these as uniformly distributed random numbers they can be used to calculate the normally distributed velocities v_x and v_y using equation A.21.

A.2 Velocity structure

As shown in table 3.2 the velocity dispersion of Fornax is approximately constant with radius. We use a constant value of 10.5 km s^{-1} (Walker et al., 2007) for the one dimensional velocity dispersion and a value of β of -0.33 (Łokas, 2009) making the stellar velocity structure mildly tangential. We can then calculate the different components of the spherical velocity dispersion using the following expressions

$$\beta = 1 - \sigma_\theta^2 / \sigma_r^2 \qquad 3\sigma_{1D}^2 = \sigma_{Total}^2 \implies \sigma_r^2 = \sigma_{1D}^2 / (1 - 2/3\beta) \qquad (\text{A.25})$$

and

$$\sigma_{\theta}^2 = \sigma_{\phi}^2 = (1 - \beta) \sigma_r^2 \quad (\text{A.26})$$

This gives the following values for the spherical components of the velocity dispersion

$$\sigma_r = 9.51\text{kms}^{-1} \quad \sigma_{\theta} = 10.96\text{kms}^{-1} \quad \sigma_{\phi} = 10.96\text{kms}^{-1} \quad (\text{A.27})$$

REFERENCES

- Amorisco, N. C. and Evans, N. W. (2011). Phase-space models of the dwarf spheroidals. *MNRAS*, 411:2118–2136.
- Amorisco, N. C. and Evans, N. W. (2012). Dark matter cores and cusps: the case of multiple stellar populations in dwarf spheroidals. *MNRAS*, 419:184–196.
- Angus, G. W. and Diaferio, A. (2009). Resolving the timing problem of the globular clusters orbiting the Fornax dwarf galaxy. *MNRAS*, 396:887–893.
- Arena, S. E. and Bertin, G. (2007). Slow evolution of elliptical galaxies induced by dynamical friction. III. Role of density concentration and pressure anisotropy. *A&A*, 463:921–935.
- Athanassoula, E. (1992). Morphology of bar orbits. *MNRAS*, 259:328–344.
- Athanassoula, E. (1996). Evolution of Bars in Isolated and in Interacting Disk Galaxies. In *Astronomical Society of the Pacific Conference Series*, pages 309–+.
- Athanassoula, E. (2002). Bar-Halo Interaction and Bar Growth. *ApJ*, 569:L83–L86.
- Athanassoula, E. (2003). What determines the strength and the slowdown rate of bars? *MNRAS*, 341:1179–1198.
- Athanassoula, E., Lambert, J. C., and Dehnen, W. (2005). Can bars be destroyed by a central mass concentration? - I. Simulations. *MNRAS*, 363:496–508.
- Athanassoula, E. and Martínez-Valpuesta, I. (2008). Formation and Evolution of Bulges. In J. H. Knapen, T. J. Mahoney, & A. Vazdekis, editor, *Pathways Through an Eclectic Universe*, volume 390 of *Astronomical Society of the Pacific Conference Series*, pages 454–+.
- Athanassoula, E. and Misiriotis, A. (2002). Morphology, photometry and kinematics of N -body bars - I. Three models with different halo central concentrations. *MNRAS*, 330:35–52.
- Barazza, F. D. e. a. (2009). Frequency and properties of bars in cluster and field galaxies at intermediate redshifts. *A&A*, 497:713–728.
- Battaglia, G., Helmi, A., Tolstoy, E., Irwin, M., Hill, V., and Jablonka, P. (2008). The Kinematic Status and Mass Content of the Sculptor Dwarf Spheroidal Galaxy. *ApJ*, 681:L13–L16.
- Belokurov, V., Zucker, D. B., Evans, N. W., Kleyna, J. T., Koposov, S., Hodgkin, S. T., Irwin, M. J., Gilmore, G., Wilkinson, M. I., Fellhauer, M., Bramich, D. M., Hewett, P. C., Vidrih, S.,

- De Jong, J. T. A., Smith, J. A., Rix, H., Bell, E. F., Wyse, R. F. G., Newberg, H. J., Mayeur, P. A., Yanny, B., Rockosi, C. M., Gnedin, O. Y., Schneider, D. P., Beers, T. C., Barentine, J. C., Brewington, H., Brinkmann, J., Harvanek, M., Kleinman, S. J., Krzesinski, J., Long, D., Nitta, A., and Snedden, S. A. (2007). Cats and Dogs, Hair and a Hero: A Quintet of New Milky Way Companions. *ApJ*, 654:897–906.
- Belokurov, V., Zucker, D. B., Evans, N. W., Wilkinson, M. I., Irwin, M. J., Hodgkin, S., Bramich, D. M., Irwin, J. M., Gilmore, G., Willman, B., Vidrih, S., Newberg, H. J., Wyse, R. F. G., Fellhauer, M., Hewett, P. C., Cole, N., Bell, E. F., Beers, T. C., Rockosi, C. M., Yanny, B., Grebel, E. K., Schneider, D. P., Lupton, R., Barentine, J. C., Brewington, H., Brinkmann, J., Harvanek, M., Kleinman, S. J., Krzesinski, J., Long, D., Nitta, A., Smith, J. A., and Snedden, S. A. (2006). A Faint New Milky Way Satellite in Bootes. *ApJ*, 647:L111–L114.
- Bennett, C. L., Hill, R. S., Hinshaw, G., Larson, D., Smith, K. M., Dunkley, J., Gold, B., Halpern, M., Jarosik, N., Kogut, A., Komatsu, E., Limon, M., Meyer, S. S., Nolta, M. R., Odegard, N., Page, L., Spergel, D. N., Tucker, G. S., Weiland, J. L., Wollack, E., and Wright, E. L. (2011). Seven-year Wilkinson Microwave Anisotropy Probe (WMAP) Observations: Are There Cosmic Microwave Background Anomalies? *ApJS*, 192:17.
- Benson, A. J., Lacey, C. G., Baugh, C. M., Cole, S., and Frenk, C. S. (2002). The effects of photoionization on galaxy formation - I. Model and results at $z=0$. *MNRAS*, 333:156–176.
- Berentzen, I., Athanassoula, E., Heller, C. H., and Fricke, K. J. (2003). Numerical simulations of interacting gas-rich barred galaxies: vertical impact of small companions. *MNRAS*, 341:343–360.
- Berentzen, I., Athanassoula, E., Heller, C. H., and Fricke, K. J. (2004). The regeneration of stellar bars by tidal interactions: numerical simulations of fly-by encounters. *MNRAS*, 347:220–236.
- Berentzen, I., Heller, C. H., Shlosman, I., and Fricke, K. J. (1998). Gas-driven evolution of stellar orbits in barred galaxies. *MNRAS*, 300:49–63.
- Berentzen, I., Shlosman, I., Martinez-Valpuesta, I., and Heller, C. H. (2007). Gas Feedback on Stellar Bar Evolution. *ApJ*, 666:189–200.
- Binney, J. J. and Tremaine, S. (2008). *Galactic dynamics. 2nd ed.* Princeton, NJ, Princeton

- University Press.
- Blumenthal, G. R., Faber, S. M., Flores, R., and Primack, J. R. (1986). Contraction of dark matter galactic halos due to baryonic infall. *ApJ*, 301:27–34.
- Bosma, A. and van der Kruit, P. C. (1979). The local mass-to-light ratio in spiral galaxies. *A&A*, 79:281–286.
- Buonanno, R., Corsi, C. E., Castellani, M., Marconi, G., Fusi Pecci, F., and Zinn, R. (1999). Hubble Space Telescope Photometry of the Fornax Dwarf Spheroidal Galaxy: Cluster 4 and Its Field. *AJ*, 118:1671–1683.
- Buonanno, R., Corsi, C. E., Zinn, R., Fusi Pecci, F., Hardy, E., and Suntzeff, N. B. (1998). The Ages of the Globular Clusters in the Fornax Dwarf Galaxy. *ApJ*, 501:L33.
- Byrd, G. G., Valtonen, M. J., Valtaoja, L., and Sundelius, B. (1986). Tidal triggering of Seyfert galaxies and quasars - Perturbed galaxy disk models versus observations. *A&A*, 166:75–82.
- Ceverino, D. and Klypin, A. (2007). Resonances in barred galaxies. *MNRAS*, 379:1155–1168.
- Chandrasekhar, S. (1943). Dynamical Friction. I. General Considerations: the Coefficient of Dynamical Friction. *ApJ*, 97:255–+.
- Clowe, D., Gonzalez, A., and Markevitch, M. (2004). Weak-Lensing Mass Reconstruction of the Interacting Cluster 1E 0657-558: Direct Evidence for the Existence of Dark Matter. *ApJ*, 604:596–603.
- Cole, D. R., Dehnen, W., and Wilkinson, M. I. (2011). Weakening dark matter cusps by clumpy baryonic infall. *MNRAS*, 416:1118–1134.
- Coleman, M., Da Costa, G. S., Bland-Hawthorn, J., Martínez-Delgado, D., Freeman, K. C., and Malin, D. (2004). Shell Structure in the Fornax Dwarf Spheroidal Galaxy. *AJ*, 127:832–839.
- Combes, F., Debbasch, F., Friedli, D., and Pfenniger, D. (1990). Box and peanut shapes generated by stellar bars. *A&A*, 233:82–95.
- Contopoulos, G. (1980). How far do bars extend. *A&A*, 81:198–209.
- Corsini, E. M., Aguerri, J. A. L., Debattista, V. P., Pizzella, A., Barazza, F. D., and Jerjen, H. (2007). The Bar Pattern Speed of Dwarf Galaxy NGC 4431. *ApJ*, 659:L121–L124.
- Cuddeford, P. (1991). An analytic inversion for anisotropic spherical galaxies. *MNRAS*, 253:414–

- 426.
- de Blok, W. J. G. (2010). The Core-Cusp Problem. *Advances in Astronomy*, 2010.
- de Blok, W. J. G., Walter, F., Brinks, E., Trachternach, C., Oh, S.-H., and Kennicutt, Jr., R. C. (2008). High-Resolution Rotation Curves and Galaxy Mass Models from THINGS. *AJ*, 136:2648–2719.
- Dehnen, W. (2000). A Very Fast and Momentum-conserving Tree Code. *ApJ*, 536:L39–L42.
- Dehnen, W. (2002). A Hierarchical O(N) Force Calculation Algorithm. *J. Comp. Phys.*, 179:27–42.
- Dehnen, W. (2005). Phase-space mixing and the merging of cusps. *MNRAS*, 360:892–900.
- Dehnen, W. (2009). Tailoring triaxial N-body models via a novel made-to-measure method. *MNRAS*, 395:1079–1086.
- Dehnen, W. and Binney, J. J. (1998). Mass models of the Milky Way. *MNRAS*, 294:429–+.
- Dehnen, W. and McLaughlin, D. E. (2005). Dynamical insight into dark matter haloes. *MNRAS*, 363:1057–1068.
- Diemand, J., Kuhlen, M., and Madau, P. (2007). Dark Matter Substructure and Gamma-Ray Annihilation in the Milky Way Halo. *ApJ*, 657:262–270.
- Dinescu, D. I., Keeney, B. A., Majewski, S. R., and Girard, T. M. (2004). Absolute Proper Motion of the Fornax Dwarf Spheroidal Galaxy from Photographic and Hubble Space Telescope WFPC2 Data. *AJ*, 128:687–699.
- Dubinski, J. and Carlberg, R. G. (1991). The structure of cold dark matter halos. *ApJ*, 378:496–503.
- Efstathiou, G. (1992). Suppressing the formation of dwarf galaxies via photoionization. *MNRAS*, 256:43P–47P.
- Einasto, J. and Einasto, L. (1972). Modified exponential models of stellar systems. *Tartu Astrofüüsika Observatoorium Teated*, 36:3–45.
- El-Zant, A., Shlosman, I., and Hoffman, Y. (2001). Dark Halos: The Flattening of the Density Cusp by Dynamical Friction. *ApJ*, 560:636–643.
- El-Zant, A. A., Hoffman, Y., Primack, J., Combes, F., and Shlosman, I. (2004). Flat-cored Dark

- Matter in Cuspy Clusters of Galaxies. *ApJ*, 607:L75–L78.
- Elson, R. A. W., Fall, S. M., and Freeman, K. C. (1987). The structure of young star clusters in the Large Magellanic Cloud. *ApJ*, 323:54–78.
- Eskridge, P. B., Frogel, J. A., Pogge, R. W., Quillen, A. C., Davies, R. L., DePoy, D. L., Houdashelt, M. L., Kuchinski, L. E., Ramírez, S. V., Sellgren, K., Terndrup, D. M., and Tiede, G. P. (2000). The Frequency of Barred Spiral Galaxies in the Near-Infrared. *AJ*, 119:536–544.
- Ferrarese, L. and Merritt, D. (2000). A Fundamental Relation between Supermassive Black Holes and Their Host Galaxies. *ApJ*, 539:L9–L12.
- Freeman, K. C. (1970). On the Disks of Spiral and so Galaxies. *ApJ*, 160:811.
- Gao, L., White, S. D. M., Jenkins, A., Stoehr, F., and Springel, V. (2004). The subhalo populations of Λ CDM dark haloes. *MNRAS*, 355:819–834.
- Gauthier, J.-R., Dubinski, J., and Widrow, L. M. (2006). Substructure around M31: Evolution and Effects. *ApJ*, 653:1180–1193.
- Gebhardt, K., Bender, R., Bower, G., Dressler, A., Faber, S. M., Filippenko, A. V., Green, R., Grillmair, C., Ho, L. C., Kormendy, J., Lauer, T. R., Magorrian, J., Pinkney, J., Richstone, D., and Tremaine, S. (2000). A Relationship between Nuclear Black Hole Mass and Galaxy Velocity Dispersion. *ApJ*, 539:L13–L16.
- Gerhard, O. E. (1991). A new family of distribution functions for spherical galaxies. *MNRAS*, 250:812–830.
- Gilmore, G., Wilkinson, M. I., Wyse, R. F. G., Klypin, J. T., Koch, A., Evans, N. W., and Grebel, E. K. (2007). The Observed Properties of Dark Matter on Small Spatial Scales. *ApJ*, 663:948–959.
- Gnedin, O. Y., Kravtsov, A. V., Klypin, A. A., and Nagai, D. (2004). Response of Dark Matter Halos to Condensation of Baryons: Cosmological Simulations and Improved Adiabatic Contraction Model. *ApJ*, 616:16–26.
- Gnedin, O. Y. and Zhao, H. (2002). Maximum feedback and dark matter profiles of dwarf galaxies. *MNRAS*, 333:299–306.
- Goerdt, T., Moore, B., Read, J. I., and Stadel, J. (2010). Core Creation in Galaxies and Halos Via

- Sinking Massive Objects. *ApJ*, 725:1707–1716.
- Goerdt, T., Moore, B., Read, J. I., Stadel, J., and Zemp, M. (2006). Does the Fornax dwarf spheroidal have a central cusp or core? *MNRAS*, 368:1073–1077.
- Goodman, J. and Binney, J. (1984). Adding a point mass to a spherical stellar system. *MNRAS*, 207:511–515.
- Governato, F., Brook, C., Mayer, L., Brooks, A., Rhee, G., Wadsley, J., Jonsson, P., Willman, B., Stinson, G., Quinn, T., and Madau, P. (2010). Bulgeless dwarf galaxies and dark matter cores from supernova-driven outflows. *Nature*, 463:203–206.
- Greco, C., Clementini, G., Catelan, M., Held, E. V., Poretti, E., Gullieuszik, M., Maio, M., Rest, A., De Lee, N., Smith, H. A., and Pritzl, B. J. (2007). Variable Stars in the Fornax dSph Galaxy. I. The Globular Cluster Fornax 4. *ApJ*, 670:332–345.
- Green, A. M., Hofmann, S., and Schwarz, D. J. (2004). The power spectrum of SUSY-CDM on subgalactic scales. *MNRAS*, 353:L23–L27.
- Grosbøl, P., Patsis, P. A., and Pompei, E. (2004). Spiral galaxies observed in the near-infrared K band. I. Data analysis and structural parameters. *A&A*, 423:849–859.
- Hansen, S. H. and Moore, B. (2006). A universal density slope Velocity anisotropy relation for relaxed structures. *New Astronomy*, 11:333–338.
- Hernquist, L. (1990). An analytical model for spherical galaxies and bulges. *ApJ*, 356:359–364.
- Hogan, C. J. and Dalcanton, J. J. (2000). New dark matter physics: Clues from halo structure. *Phys. Rev. D*, 62(6):063511.
- Holley-Bockelmann, K., Weinberg, M., and Katz, N. (2005). Bar-induced evolution of dark matter cusps. *MNRAS*, 363:991–1007.
- Hozumi, S. and Hernquist, L. (2005). *PASJ*, submitted.
- Inoue, S. (2009). The test for suppressed dynamical friction in a constant density core of dwarf galaxies. *MNRAS*, 397:709–716.
- Irwin, M. J., Belokurov, V., Evans, N. W., Ryan-Weber, E. V., de Jong, J. T. A., Koposov, S., Zucker, D. B., Hodgkin, S. T., Gilmore, G., Prema, P., Hebb, L., Begum, A., Fellhauer, M., Hewett, P. C., Kennicutt, Jr., R. C., Wilkinson, M. I., Bramich, D. M., Vidrih, S., Rix, H.,

- Beers, T. C., Barentine, J. C., Brewington, H., Harvanek, M., Krzesinski, J., Long, D., Nitta, A., and Snedden, S. A. (2007). Discovery of an Unusual Dwarf Galaxy in the Outskirts of the Milky Way. *ApJ*, 656:L13–L16.
- Jardel, J. R. and Sellwood, J. A. (2009). Halo Density Reduction by Baryonic Settling? *ApJ*, 691:1300–1306.
- Johansson, P. H., Naab, T., and Ostriker, J. P. (2009). Gravitational Heating Helps Make Massive Galaxies Red and Dead. *ApJ*, 697:L38–L43.
- Kent, S. M. (1987). The pattern speed in the SB0 galaxy NGC 936. *AJ*, 93:1062–1069.
- King, A. R. and Pringle, J. E. (2006). Growing supermassive black holes by chaotic accretion. *MNRAS*, 373:L90–L92.
- King, I. (1962). Density Law in Spherical Stellar Systems. *AJ*, 67:274–275.
- Kleyna, J., Wilkinson, M. I., Evans, N. W., Gilmore, G., and Frayn, C. (2002). Dark matter in dwarf spheroidals - II. Observations and modelling of Draco. *MNRAS*, 330:792–806.
- Kleyna, J. T., Wilkinson, M. I., Gilmore, G., and Evans, N. W. (2003). A Dynamical Fossil in the Ursa Minor Dwarf Spheroidal Galaxy. *ApJ*, 588:L21–L24.
- Klypin, A., Kravtsov, A. V., Valenzuela, O., and Prada, F. (1999). Where Are the Missing Galactic Satellites? *ApJ*, 522:82–92.
- Knebe, A., Devriendt, J. E. G., Mahmood, A., and Silk, J. (2002). Merger histories in warm dark matter structure formation scenarios. *MNRAS*, 329:813–828.
- Kochanek, C. S. and White, M. (2000). A Quantitative Study of Interacting Dark Matter in Halos. *ApJ*, 543:514–520.
- Komatsu, E., Smith, K. M., Dunkley, J., Bennett, C. L., Gold, B., Hinshaw, G., Jarosik, N., Larson, D., Nolte, M. R., Page, L., Spergel, D. N., Halpern, M., Hill, R. S., Kogut, A., Limon, M., Meyer, S. S., Odegard, N., Tucker, G. S., Weiland, J. L., Wollack, E., and Wright, E. L. (2011). Seven-year Wilkinson Microwave Anisotropy Probe (WMAP) Observations: Cosmological Interpretation. *ApJS*, 192:18.
- Kormendy, J. and Richstone, D. (1995). Inward Bound—The Search For Supermassive Black Holes In Galactic Nuclei. *ARA&A*, 33:581–+.

- Kuzio de Naray, R., McGaugh, S. S., and de Blok, W. J. G. (2008). Mass Models for Low Surface Brightness Galaxies with High-Resolution Optical Velocity Fields. *ApJ*, 676:920–943.
- Kuzio de Naray, R., McGaugh, S. S., de Blok, W. J. G., and Bosma, A. (2006). High-Resolution Optical Velocity Fields of 11 Low Surface Brightness Galaxies. *ApJS*, 165:461–479.
- Lacey, C. and Cole, S. (1993). Merger rates in hierarchical models of galaxy formation. *MNRAS*, 262:627–649.
- Leeuwijn, F. and Athanassoula, E. (2000). Central cusp caused by a supermassive black hole in axisymmetric models of elliptical galaxies. *MNRAS*, 317:79–96.
- Lokas, E. L. (2009). The mass and velocity anisotropy of the Carina, Fornax, Sculptor and Sextans dwarf spheroidal galaxies. *MNRAS*, 394:L102–L106.
- Lovell, M. R., Eke, V., Frenk, C. S., Gao, L., Jenkins, A., Theuns, T., Wang, J., White, S. D. M., Boyarsky, A., and Ruchayskiy, O. (2012). The haloes of bright satellite galaxies in a warm dark matter universe. *MNRAS*, 420:2318–2324.
- Lukić, Z., Heitmann, K., Habib, S., Bashinsky, S., and Ricker, P. M. (2007). The Halo Mass Function: High-Redshift Evolution and Universality. *ApJ*, 671:1160–1181.
- Lux, H., Read, J. I., and Lake, G. (2010). Determining orbits for the Milky Way’s dwarfs. *MNRAS*, 406:2312–2324.
- Lynden-Bell, D. and Kalnajs, A. J. (1972). On the generating mechanism of spiral structure. *MNRAS*, 157:1–+.
- Mackey, A. D. and Gilmore, G. F. (2003a). RR Lyrae stars in four globular clusters in the Fornax dwarf galaxy. *MNRAS*, 343:747–761.
- Mackey, A. D. and Gilmore, G. F. (2003b). Surface brightness profiles and structural parameters for globular clusters in the Fornax and Sagittarius dwarf spheroidal galaxies. *MNRAS*, 340:175–190.
- Magorrian, J., Tremaine, S., Richstone, D., Bender, R., Bower, G., Dressler, A., Faber, S. M., Gebhardt, K., Green, R., Grillmair, C., Kormendy, J., and Lauer, T. (1998). The Demography of Massive Dark Objects in Galaxy Centers. *AJ*, 115:2285–2305.
- Markevitch, M., Gonzalez, A. H., Clowe, D., Vikhlinin, A., Forman, W., Jones, C., Murray, S.,

- and Tucker, W. (2004). Direct Constraints on the Dark Matter Self-Interaction Cross Section from the Merging Galaxy Cluster 1E 0657-56. *ApJ*, 606:819–824.
- Martinez-Valpuesta, I., Shlosman, I., and Heller, C. (2006). Evolution of Stellar Bars in Live Axisymmetric Halos: Recurrent Buckling and Secular Growth. *ApJ*, 637:214–226.
- Mashchenko, S., Wadsley, J., and Couchman, H. M. P. (2008). Stellar Feedback in Dwarf Galaxy Formation. *Science*, 319:174–.
- Masters, K. L., Nichol, R. C., Hoyle, B., Lintott, C., Bamford, S., Edmondson, E. M., Fortson, L., Keel, W. C., Schawinski, K., Smith, A., and Thomas, D. (2010). Galaxy Zoo: Bars in Disk Galaxies. *ArXiv e-prints*.
- Mateo, M., Olszewski, E., Welch, D. L., Fischer, P., and Kunkel, W. (1991). A kinematic study of the Fornax dwarf spheroidal galaxy. *AJ*, 102:914–926.
- Mateo, M. L. (1998). Dwarf Galaxies of the Local Group. *ARA&A*, 36:435–506.
- McMillan, P. J. (2011). Mass models of the Milky Way. *MNRAS*, 414:2446–2457.
- McMillan, P. J. and Dehnen, W. (2007). Initial conditions for disc galaxies. *MNRAS*, 378:541–550.
- Menéndez-Delmestre, K., Sheth, K., Schinnerer, E., Jarrett, T. H., and Scoville, N. Z. (2007). A Near-Infrared Study of 2MASS Bars in Local Galaxies: An Anchor for High-Redshift Studies. *ApJ*, 657:790–804.
- Merrifield, M. R. and Kuijken, K. (1995). The pattern speed of the bar in NGC 936. *MNRAS*, 274:933–938.
- Merritt, D. and Sellwood, J. A. (1994). Bending instabilities in stellar systems. *ApJ*, 425:551–567.
- Miller, R. H., Prendergast, K. H., and Quirk, W. J. (1970). Numerical Experiments on Spiral Structure. *ApJ*, 161:903.
- Moore, B., Quinn, T., Governato, F., Stadel, J., and Lake, G. (1999). Cold collapse and the core catastrophe. *MNRAS*, 310:1147–1152.
- Nair, P. B. and Abraham, R. G. (2010). On the Fraction of Barred Spiral Galaxies. *ApJ*, 714:L260–L264.
- Navarro, J. F., Eke, V. R., and Frenk, C. S. (1996a). The cores of dwarf galaxy haloes. *MNRAS*, 283:L72–L78.

- Navarro, J. F., Frenk, C. S., and White, S. D. M. (1995). The assembly of galaxies in a hierarchically clustering universe. *MNRAS*, 275:56–66.
- Navarro, J. F., Frenk, C. S., and White, S. D. M. (1996b). The Structure of Cold Dark Matter Halos. *ApJ*, 462:563–+.
- Navarro, J. F., Frenk, C. S., and White, S. D. M. (1997). A Universal Density Profile from Hierarchical Clustering. *ApJ*, 490:493–+.
- Navarro, J. F., Hayashi, E., Power, C., Jenkins, A. R., Frenk, C. S., White, S. D. M., Springel, V., Stadel, J., and Quinn, T. R. (2004). The inner structure of Λ CDM haloes - III. Universality and asymptotic slopes. *MNRAS*, 349:1039–1051.
- Navarro, J. F., Ludlow, A., Springel, V., Wang, J., Vogelsberger, M., White, S. D. M., Jenkins, A., Frenk, C. S., and Helmi, A. (2009). The diversity and similarity of simulated cold dark matter haloes. *MNRAS*, pages 1918–+.
- Navarro, J. F., Ludlow, A., Springel, V., Wang, J., Vogelsberger, M., White, S. D. M., Jenkins, A., Frenk, C. S., and Helmi, A. (2010). The diversity and similarity of simulated cold dark matter haloes. *MNRAS*, 402:21–34.
- Nipoti, C., Treu, T., Ciotti, L., and Stiavelli, M. (2004). Galactic cannibalism and cold dark matter density profiles. *MNRAS*, 355:1119–1124.
- Noguchi, M. (1987). Close encounter between galaxies. II - Tidal deformation of a disc galaxy stabilized by massive halo. *MNRAS*, 228:635–651.
- Norman, C. A., Sellwood, J. A., and Hasan, H. (1996). Bar Dissolution and Bulge Formation: an Example of Secular Dynamical Evolution in Galaxies. *ApJ*, 462:114–+.
- Oh, K. S., Lin, D. N. C., and Richer, H. B. (2000). Globular Clusters in the Fornax Dwarf Spheroidal Galaxy. *ApJ*, 531:727–738.
- Oh, S.-H., de Blok, W. J. G., Walter, F., Brinks, E., and Kennicutt, R. C. (2008). High-Resolution Dark Matter Density Profiles of Things Dwarf Galaxies: Correcting for Noncircular Motions. *AJ*, 136:2761–2781.
- Ostriker, J. P. and Peebles, P. J. E. (1973). A Numerical Study of the Stability of Flattened Galaxies: or, can Cold Galaxies Survive? *ApJ*, 186:467–480.

- Patsis, P. A., Athanassoula, E., Grosbøl, P., and Skokos, C. (2002a). Edge-on boxy profiles in non-barred disc galaxies. *MNRAS*, 335:1049–1053.
- Patsis, P. A., Skokos, C., and Athanassoula, E. (2002b). Orbital dynamics of three-dimensional bars - III. Boxy/peanut edge-on profiles. *MNRAS*, 337:578–596.
- Peñarrubia, J., McConnachie, A. W., and Navarro, J. F. (2008). The Cold Dark Matter Halos of Local Group Dwarf Spheroidals. *ApJ*, 672:904–913.
- Peñarrubia, J., Walker, M. G., and Gilmore, G. (2009). Tidal disruption of globular clusters in dwarf galaxies with triaxial dark matter haloes. *MNRAS*, 399:1275–1292.
- Pedrosa, S., Tissera, P. B., and Scannapieco, C. (2009). The impact of baryons on dark matter haloes. *MNRAS*, 395:L57–L61.
- Peebles, P. J. E. (1972). *Ge. Rel. Gravitation*, 3:61–61.
- Perlmutter, S., Aldering, G., Goldhaber, G., Knop, R. A., Nugent, P., Castro, P. G., Deustua, S., Fabbro, S., Goobar, A., Groom, D. E., Hook, I. M., Kim, A. G., Kim, M. Y., Lee, J. C., Nunes, N. J., Pain, R., Pennypacker, C. R., Quimby, R., Lidman, C., Ellis, R. S., Irwin, M., McMahon, R. G., Ruiz-Lapuente, P., Walton, N., Schaefer, B., Boyle, B. J., Filippenko, A. V., Matheson, T., Fruchter, A. S., Panagia, N., Newberg, H. J. M., Couch, W. J., and The Supernova Cosmology Project (1999). Measurements of Omega and Lambda from 42 High-Redshift Supernovae. *ApJ*, 517:565–586.
- Pfenniger, D. and Friedli, D. (1991). Structure and dynamics of 3D N-body barred galaxies. *A&A*, 252:75–93.
- Plummer, H. C. (1911). On the problem of distribution in globular star clusters. *MNRAS*, 71:460–470.
- Pontzen, A. and Governato, F. (2011). How supernova feedback turns dark matter cusps into cores. *ArXiv e-prints*.
- Quinlan, G. D., Hernquist, L., and Sigurdsson, S. (1995). Models of Galaxies with Central Black Holes: Adiabatic Growth in Spherical Galaxies. *ApJ*, 440:554–+.
- Raha, N., Sellwood, J. A., James, R. A., and Kahn, F. D. (1991). A dynamical instability of bars in disk galaxies. *Nature*, 352:411–+.

- Read, J. I. and Gilmore, G. (2005). Mass loss from dwarf spheroidal galaxies: the origins of shallow dark matter cores and exponential surface brightness profiles. *MNRAS*, 356:107–124.
- Read, J. I., Goerdt, T., Moore, B., Pontzen, A. P., Stadel, J., and Lake, G. (2006a). Dynamical friction in constant density cores: a failure of the Chandrasekhar formula. *MNRAS*, 373:1451–1460.
- Read, J. I., Wilkinson, M. I., Evans, N. W., Gilmore, G., and Kleyna, J. T. (2006b). The tidal stripping of satellites. *MNRAS*, 366:429–437.
- Reed, D. S., Bower, R., Frenk, C. S., Jenkins, A., and Theuns, T. (2007). The halo mass function from the dark ages through the present day. *MNRAS*, 374:2–15.
- Romano-Díaz, E., Shlosman, I., Heller, C., and Hoffman, Y. (2008). Disk Evolution and Bar Triggering Driven by Interactions with Dark Matter Substructure. *ApJ*, 687:L13–L16.
- Romano-Díaz, E., Shlosman, I., Hoffman, Y., and Heller, C. (2008). Erasing Dark Matter Cusps in Cosmological Galactic Halos with Baryons. *ApJ*, 685:L105–L108.
- Rubin, V. C., Ford, W. K. J., and Thonnard, N. (1980). Rotational properties of 21 SC galaxies with a large range of luminosities and radii, from NGC 4605 / $R = 4\text{kpc}$ / to UGC 2885 / $R = 122\text{kpc}$ /. *ApJ*, 238:471–487.
- Saha, P. (1992). Constructing stable spherical galaxy models. *MNRAS*, 254:132–138.
- Sakamoto, K., Okumura, S. K., Ishizuki, S., and Scoville, N. Z. (1999). Bar-driven Transport of Molecular Gas to Galactic Centers and Its Consequences. *ApJ*, 525:691–701.
- Sánchez-Salcedo, F. J., Reyes-Iturbide, J., and Hernandez, X. (2006). An extensive study of dynamical friction in dwarf galaxies: the role of stars, dark matter, halo profiles and MOND. *MNRAS*, 370:1829–1840.
- Schinnerer, E., Böker, T., Emsellem, E., and Lisenfeld, U. (2006). Molecular Gas Dynamics in NGC 6946: A Bar-driven Nuclear Starburst “Caught in the Act”. *ApJ*, 649:181–200.
- Sellwood, J. A. (1980). Galaxy models with live halos. *A&A*, 89:296–307.
- Sellwood, J. A. (1996). Bar Formation, Evolution and Destruction. In R. Buta, D. A. Crocker, & B. G. Elmegreen, editor, *IAU Colloq. 157: Barred Galaxies*, volume 91 of *Astronomical Society of the Pacific Conference Series*, pages 259–+.

- Shapley, H. (1938). Two Stellar Systems of a New Kind. *Nature*, 142:715–716.
- Shen, J. and Sellwood, J. A. (2004). The Destruction of Bars by Central Mass Concentrations. *ApJ*, 604:614–631.
- Sheth, K., Vogel, S. N., Regan, M. W., Thornley, M. D., and Teuben, P. J. (2005). Secular Evolution via Bar-driven Gas Inflow: Results from BIMA SONG. *ApJ*, 632:217–226.
- Simon, J. D., Bolatto, A. D., Leroy, A., Blitz, L., and Gates, E. L. (2005). High-Resolution Measurements of the Halos of Four Dark Matter-Dominated Galaxies: Deviations from a Universal Density Profile. *ApJ*, 621:757–776.
- Smoot, G. F., Bennett, C. L., Kogut, A., Wright, E. L., Aymon, J., Boggess, N. W., Cheng, E. S., de Amici, G., Gulkis, S., Hauser, M. G., Hinshaw, G., Jackson, P. D., Janssen, M., Kaita, E., Kelsall, T., Keegstra, P., Lineweaver, C., Loewenstein, K., Lubin, P., Mather, J., Meyer, S. S., Moseley, S. H., Murdock, T., Rokke, L., Silverberg, R. F., Tenorio, L., Weiss, R., and Wilkinson, D. T. (1992). Structure in the COBE differential microwave radiometer first-year maps. *ApJ*, 396:L1–L5.
- Sotnikova, N. Y. and Rodionov, S. A. (2005). Bending Instability of Stellar Disks: The Stabilizing Effect of a Compact Bulge. *Astronomy Letters*, 31:15–29.
- Spano, M., Marcelin, M., Amram, P., Carignan, C., Epinat, B., and Hernandez, O. (2008). GHASP: an H α kinematic survey of spiral and irregular galaxies - V. Dark matter distribution in 36 nearby spiral galaxies. *MNRAS*, 383:297–316.
- Springel, V., Frenk, C. S., and White, S. D. M. (2006). The large-scale structure of the Universe. *Nature*, 440:1137–1144.
- Springel, V., White, S. D. M., Jenkins, A., Frenk, C. S., Yoshida, N., Gao, L., Navarro, J., Thacker, R., Croton, D., Helly, J., Peacock, J. A., Cole, S., Thomas, P., Couchman, H., Evrard, A., Colberg, J., and Pearce, F. (2005). Simulations of the formation, evolution and clustering of galaxies and quasars. *Nature*, 435:629–636.
- Strigari, L. E., Bullock, J. S., Kaplinghat, M., Kravtsov, A. V., Gnedin, O. Y., Abazajian, K., and Klypin, A. A. (2006). A Large Dark Matter Core in the Fornax Dwarf Spheroidal Galaxy? *ApJ*, 652:306–312.

- Strigari, L. E., Bullock, J. S., Kaplinghat, M., Simon, J. D., Geha, M., Willman, B., and Walker, M. G. (2008). A common mass scale for satellite galaxies of the Milky Way. *Nature*, 454:1096–1097.
- Taylor, A. N., Dye, S., Broadhurst, T. J., Benitez, N., and van Kampen, E. (1998). Gravitational Lens Magnification and the Mass of Abell 1689. *ApJ*, 501:539–+.
- Thoul, A. A. and Weinberg, D. H. (1996). Hydrodynamic Simulations of Galaxy Formation. II. Photoionization and the Formation of Low-Mass Galaxies. *ApJ*, 465:608.
- Tollerud, E. J., Bullock, J. S., Strigari, L. E., and Willman, B. (2008). Hundreds of Milky Way Satellites? Luminosity Bias in the Satellite Luminosity Function. *ApJ*, 688:277–289.
- Toomre, A. (1966). *Notes on the 1966 Summer Study Program at the Woods Hole Oceanogr. Inst. Geophysical Fluid Dynamics No. 66-46 p 111.*
- Toomre, A. (1981). What amplifies the spirals. In S. M. Fall & D. Lynden-Bell, editor, *Structure and Evolution of Normal Galaxies*, pages 111–136.
- Tremaine, S. and Gunn, J. E. (1979). Dynamical role of light neutral leptons in cosmology. *Physical Review Letters*, 42:407–410.
- Tremaine, S., Henon, M., and Lynden-Bell, D. (1986). H-functions and mixing in violent relaxation. *MNRAS*, 219:285–297.
- Tremaine, S. and Weinberg, M. D. (1984). Dynamical friction in spherical systems. *MNRAS*, 209:729–757.
- Tremaine, S. D. (1976). The formation of the nuclei of galaxies. II - The local group. *ApJ*, 203:345–351.
- Tremaine, S. D., Ostriker, J. P., and Spitzer, Jr., L. (1975). The formation of the nuclei of galaxies. I - M31. *ApJ*, 196:407–411.
- van Albada, T. S., Bahcall, J. N., Begeman, K., and Sancisi, R. (1985). Distribution of dark matter in the spiral galaxy NGC 3198. *ApJ*, 295:305–313.
- Villa-Vargas, J., Shlosman, I., and Heller, C. (2009). Dark Matter Halos and Evolution of Bars in Disk Galaxies: Collisionless Models Revisited. *ApJ*, 707:218–232.
- Villaescusa-Navarro, F. and Dalal, N. (2011). Cores and cusps in warm dark matter halos. , 3:24.

- Walker, M. G., Mateo, M., Olszewski, E. W., Gnedin, O. Y., Wang, X., Sen, B., and Woodroffe, M. (2007). Velocity Dispersion Profiles of Seven Dwarf Spheroidal Galaxies. *ApJ*, 667:L53–L56.
- Walker, M. G., Mateo, M., Olszewski, E. W., Peñarrubia, J., Wyn Evans, N., and Gilmore, G. (2009). A Universal Mass Profile for Dwarf Spheroidal Galaxies? *ApJ*, 704:1274–1287.
- Walker, M. G. and Peñarrubia, J. (2011). A Method for Measuring (Slopes of) the Mass Profiles of Dwarf Spheroidal Galaxies. *ArXiv e-prints*.
- Walsh, S. M., Jerjen, H., and Willman, B. (2007). A Pair of Boötes: A New Milky Way Satellite. *ApJ*, 662:L83–L86.
- Warren, M. S., Quinn, P. J., Salmon, J. K., and Zurek, W. H. (1992). Dark halos formed via dissipationless collapse. I - Shapes and alignment of angular momentum. *ApJ*, 399:405–425.
- Weinberg, M. D. and Katz, N. (2002). Bar-driven Dark Halo Evolution: A Resolution of the Cusp-Core Controversy. *ApJ*, 580:627–633.
- Weiner, B. J., Sellwood, J. A., and Williams, T. B. (2001). The Disk and Dark Halo Mass of the Barred Galaxy NGC 4123. II. Fluid-Dynamical Models. *ApJ*, 546:931–951.
- White, S. D. M. and Frenk, C. S. (1991). Galaxy formation through hierarchical clustering. *ApJ*, 379:52–79.
- Wilkinson, M. I., Kleyna, J., Evans, N. W., and Gilmore, G. (2002). Dark matter in dwarf spheroidals - I. Models. *MNRAS*, 330:778–791.
- Willman, B., Dalcanton, J. J., Martinez-Delgado, D., West, A. A., Blanton, M. R., Hogg, D. W., Barentine, J. C., Brewington, H. J., Harvanek, M., Kleinman, S. J., Krzesinski, J., Long, D., Neilsen, Jr., E. H., Nitta, A., and Snedden, S. A. (2005). A New Milky Way Dwarf Galaxy in Ursa Major. *ApJ*, 626:L85–L88.
- Wilson, A. G. (1955). Sculptor-Type Systems in the Local Group of Galaxies. *PASP*, 67:27–29.
- York, D. G., Adelman, J., Anderson, Jr., J. E., Anderson, S. F., Annis, J., Bahcall, N. A., Bakken, J. A., Barkhouser, R., Bastian, S., Berman, E., Boroski, W. N., Bracker, S., Briegel, C., Briggs, J. W., Brinkmann, J., Brunner, R., Burles, S., Carey, L., Carr, M. A., Castander, F. J., Chen, B., Colestock, P. L., Connolly, A. J., Crocker, J. H., Csabai, I., Czarapata, P. C., Davis, J. E.,

- Doi, M., Dombeck, T., Eisenstein, D., Ellman, N., Elms, B. R., Evans, M. L., Fan, X., Federwitz, G. R., Fiscelli, L., Friedman, S., Frieman, J. A., Fukugita, M., Gillespie, B., Gunn, J. E., Gurbani, V. K., de Haas, E., Haldeman, M., Harris, F. H., Hayes, J., Heckman, T. M., Hennessy, G. S., Hindsley, R. B., Holm, S., Holmgren, D. J., Huang, C., Hull, C., Husby, D., Ichikawa, S., Ichikawa, T., Ivezić, Ž., Kent, S., Kim, R. S. J., Kinney, E., Klaene, M., Kleinman, A. N., Kleinman, S., Knapp, G. R., Korienek, J., Kron, R. G., Kunszt, P. Z., Lamb, D. Q., Lee, B., Leger, R. F., Limmongkol, S., Lindenmeyer, C., Long, D. C., Loomis, C., Loveday, J., Lucinio, R., Lupton, R. H., MacKinnon, B., Mannery, E. J., Mantsch, P. M., Margon, B., McGehee, P., McKay, T. A., Meiksin, A., Merelli, A., Monet, D. G., Munn, J. A., Narayanan, V. K., Nash, T., Neilsen, E., Neswold, R., Newberg, H. J., Nichol, R. C., Nicinski, T., Nonino, M., Okada, N., Okamura, S., Ostriker, J. P., Owen, R., Pauls, A. G., Peoples, J., Peterson, R. L., Petravick, D., Pier, J. R., Pope, A., Pordes, R., Prosapio, A., Rechenmacher, R., Quinn, T. R., Richards, G. T., Richmond, M. W., Rivetta, C. H., Rockosi, C. M., Ruthmansdorfer, K., Sandford, D., Schlegel, D. J., Schneider, D. P., Sekiguchi, M., Sergey, G., Shimasaku, K., Siegmund, W. A., Smee, S., Smith, J. A., Snedden, S., Stone, R., Stoughton, C., Strauss, M. A., Stubbs, C., SubbaRao, M., Szalay, A. S., Szapudi, I., Szokoly, G. P., Thakar, A. R., Tremonti, C., Tucker, D. L., Uomoto, A., Vanden Berk, D., Vogeley, M. S., Waddell, P., Wang, S., Watanabe, M., Weinberg, D. H., Yanny, B., and Yasuda, N. (2000). The Sloan Digital Sky Survey: Technical Summary. *AJ*, 120:1579–1587.
- Young, P. (1980). Numerical models of star clusters with a central black hole. I - Adiabatic models. *ApJ*, 242:1232–1237.
- Zánmar Sánchez, R., Sellwood, J. A., Weiner, B. J., and Williams, T. B. (2008). Modeling the Gas Flow in the Bar of NGC 1365. *ApJ*, 674:797–813.
- Zucker, D. B., Belokurov, V., Evans, N. W., Kleyna, J. T., Irwin, M. J., Wilkinson, M. I., Fellhauer, M., Bramich, D. M., Gilmore, G., Newberg, H. J., Yanny, B., Smith, J. A., Hewett, P. C., Bell, E. F., Rix, H., Gnedin, O. Y., Vidrih, S., Wyse, R. F. G., Willman, B., Grebel, E. K., Schneider, D. P., Beers, T. C., Kniazev, A. Y., Barentine, J. C., Brewington, H., Brinkmann, J., Harvanek, M., Kleinman, S. J., Krzesinski, J., Long, D., Nitta, A., and Snedden, S. A. (2006a). A Curious

- Milky Way Satellite in Ursa Major. *ApJ*, 650:L41–L44.
- Zucker, D. B., Belokurov, V., Evans, N. W., Wilkinson, M. I., Irwin, M. J., Sivarani, T., Hodgkin, S., Bramich, D. M., Irwin, J. M., Gilmore, G., Willman, B., Vidrih, S., Fellhauer, M., Hewett, P. C., Beers, T. C., Bell, E. F., Grebel, E. K., Schneider, D. P., Newberg, H. J., Wyse, R. F. G., Rockosi, C. M., Yanny, B., Lupton, R., Smith, J. A., Barentine, J. C., Brewington, H., Brinkmann, J., Harvanek, M., Kleinman, S. J., Krzesinski, J., Long, D., Nitta, A., and Snedden, S. A. (2006b). A New Milky Way Dwarf Satellite in Canes Venatici. *ApJ*, 643:L103–L106.
- Zwicky, F. (1933). Die Rotverschiebung von extragalaktischen Nebeln. *Helvetica Physica Acta*, 6:110–127.
- Zwicky, F. (1937). On the Masses of Nebulae and of Clusters of Nebulae. *ApJ*, 86:217.